# Colloidal dispersions of repulsive nanoparticles

Tunable effective interactions, phase behaviour and anisotropy

**Jeffrey Everts**

# Colloidal dispersions of repulsive nanoparticles: tunable effective interactions, phase behaviour and anisotropy

J. C. Everts

# Colloidal dispersions of repulsive nanoparticles: tunable effective interactions, phase behaviour and anisotropy

**Colloïdale dispersies van repulsieve nanodeeltjes: afstembare effectieve wisselwerkingen, fasengedrag en anisotropie**

(met een samenvatting in het Nederlands)

## Proefschrift

ter verkrijging van de graad van doctor aan de Universiteit Utrecht op gezag van de rector magnificus, prof. dr. G. J. van der Zwaan, ingevolge het besluit van het college voor promoties in het openbaar te verdedigen op maandag 19 september 2016 des middags te 4.15 uur

door

## Jeffrey Christopher Everts

geboren op 1 april 1988 te Roermond

Promotor: Prof. dr. R. H. H. G. van Roij

# Contents

# Contents

# Publications

The content of the following chapters is based on the following publications:

- <u>J. C. Everts</u>, N. Boon and R. van Roij, *Density-induced reentrant melting of colloidal Wigner crystals*, Phys. Chem. Chem. Phys., **18**, 5211 (2016) (Chapter 2).

- <u>J. C. Everts</u>, M. N. van der Linden, A. van Blaaderen, and R. van Roij, *Alternating strings and clusters in suspensions of charged colloids*, Soft Matter, **12**, 6610 (2016) (Chapter 4).

- <u>J. C. Everts</u>, S. Samin and R. van Roij, *Tuning colloid-interface interactions by salt partitioning*, Phys. Rev. Lett. **117**, 098002 (2016) (Chapter 5).

- <u>J. C. Everts</u>, M. T. J. J. M. Punter, S. Samin, P. van der Schoot and R. van Roij, *A Landau-de Gennes theory for hard colloidal rods: defects and tactoids*, J. Chem. Phys., **144**, 194901 (2016) (Chapter 7).

- <u>J. C. Everts</u> and R. van Roij, *Demixing in a binary mixture of repulsive charged colloids*, in preparation (Chapter 3)

- <u>J. C. Everts</u>, S. Samin and R. van Roij, *Salt effects on the lateral interaction of wetting colloids at an oil-water interface*, in preparation (Chapter 5)

- <u>J. C. Everts</u>, N. A. Elbers, J. E. S. van der Hoeven, S. Samin, A. van Blaaderen and R. van Roij, *Colloid-interface interactions in the presence of multiple ion species: charge regulation and dynamics*, in preparation (Chapter 6)

Other publications by the author:

- W. Beugeling, <u>J. C. Everts</u> and C. Morais Smith, *Topological phase transitions driven by next-nearest-neighbor hopping in two-dimensional lattices*, Phys. Rev. B, **86**, 195129 (2012).

- S. Cantekin, Y. Nakano, <u>J. C. Everts</u>, P. van der Schoot, E. W. Meijer, and A. R. A. Palmans, *A stereoselectively deuterated supramolecular motif to probe the role of solvent during self-assembly processes*, Chem. Comm., **48**, 3803 (2012).

- P. J. M. Stals, <u>J. C. Everts</u>, R. de Bruijn, I. A. W. Filot, M. M. J. Smulders, R. Martin-Rapun, E. A. Pidko, T. F. A. de Greef, A. R. A. Palmans and E. W. Meijer, *Dynamic supramolecular polymers based on benzene-1,3,5-tricarboxamides: The influence of amide connectivity on aggregate stability and amplification of chirality*, Chem. Eur. J., **16**, 810 (2010).

# 1

# Introduction

*We introduce the notion of nanoparticles and colloids and set out the general concepts that we will use in this thesis. The length scales and theories that are important in understanding suspensions of charged spherical and charge-neutral rod-shaped colloids are discussed.*

## 1.1 The classical world under the microscope

Whenever we zoom in on a piece of matter, various building blocks can be observed depending on the length scale that one is looking at. For example, if we consider snow, we observe ice crystals on a mesoscopic scale, which in turn consist of water molecules arranged in some lattice on the nanoscale. The water molecules themselves consist of atoms, which are built up of protons, neutrons and electrons. When we zoom in even further than this, we find quarks and particles that mediate their interactions, such as gluons. The conceptual complexity of the governing theories almost seems to be inversely proportional to the relevant length scale that one is looking at, ranging from classical physics on the largest length scales, to quantum mechanics or quantum field theory on the subnanometer scales, and (who knows) string theory or quantum gravity for even smaller length scales.

Going back to our example of snow, we see that the ordering and structure of the ice crystals that make up these aggregates can actually be quite complex, and can be understood by using classical physics. The complexity in structure arises because of the interplay of *many* smaller building blocks [1], that may or may not be actually quantum objects. This should be contrasted to, for example, the relative "simple" structure of a water molecule being "just" two hydrogen (H) atoms bound to a single oxygen (O) with a H-O-H bond angle of 104.55 degrees [2], which can only be understood by applying quantum mechanics [3]. We can find a rough estimate whether quantum effects are important by using the thermal de Broglie wavelength $\Lambda$ [4], which for a particle with mass $m$ without any internal degrees of freedom is given by

$$\Lambda = \frac{h}{\sqrt{2\pi m k_B T}},$$

(1.1)

with $k_B = 1.38064852... \cdot 10^{-23}$J K$^{-1}$ the Boltzmann constant, the Planck constant $h = 6.626070040...\cdot 10^{-34}$ J·s and $T$ temperature. When $\Lambda$ is larger than the particle size or interparticle spacing, classical physics breaks down. When we apply this hypothesis to spherical particles of diameter $D$ with mass density $\rho = 1 - 10$ kg m$^{-3}$, we find that $\Lambda/D \sim 10^{-9} - 10^{-4}$, for $D$ ranging from 10 nm to 1 $\mu$m at room temperature. Particles with sizes in this range are thus essentially classical, and can be viewed under the (optical) microscope. This is the so-called colloidal regime, and the particles with these sizes are called colloids (particle sizes of a few microns) as coined by Graham [5], or nanoparticles (particle sizes of a few nanometers)[1]. The concept of a colloidal particle can be very broad: these can be metallic or polymeric spheres, but also fat droplets, red blood cells or ice crystals, as long as they fall in the correct range of particle sizes.

Often viewed as models for atomic systems when they are spherical and charged, they can be described by classical statistical physics: because colloidal particles are almost always suspended in a medium (often a liquid), Brownian motion occurs [6, 7], which allows them to explore all of their phase space, such that the ergodic principle applies (except for glasses). Their shape is, however, not limited to that of a sphere: the advances in chemical synthesis make it possible to synthesize colloids with all kinds of shapes and material properties [8]. Unlike atoms, the intrinsic *particle* properties are thus highly tunable. Magnetic colloids can, for example, be produced, which show collective behaviour when driven by an alternating external magnetic field [9], forming magnetic snake-like swimmers. Another example is that of a sphere with a hemisphere that is negatively charged, while the other hemisphere is positively charged. Named after the two-faced god in Roman mythology, this is the so-called (dipolar) Janus particle, which can self-assemble into chains [10], clusters [11] and rings [12]. Shape can also have a large impact on the phase behaviour. For example, in Ref. [13] the phase diagram is constructed by changing the shape of a particle from a hard cube to a hard sphere by a gradual truncation of the edges, giving rise to various non-trivial crystalline phases and close-packed structures. Finally, colloidal particles also show possible applications in material science, being promising candidates for *e.g.* photonic bandgap materials [14]. These examples show that colloids are more than just a classical analogue of an atom, even from a fundamental point of view.

Not only the shape and material properties of the colloidal particles matter, but also the properties of the *medium* plays an important role. This is why colloids are almost always investigated as a colloidal dispersion. For example, fat droplets in water is called milk, red blood cells in water (together with some other "stuff") is blood, water droplets in air form a cloud, and gold nanoparticles in a glass is known as cranberry glass[2]. The above examples show liquid-liquid, solid-liquid, liquid-gas, and glass-solid

---

[1]Because the particle size as such is not a fundamental parameter in the theories that we will consider in this thesis, we do not make a strict distinction between nanoparticles and colloids, and just view them as the same type of classical systems that could be mapped onto each other by a suitable rescaling of the length scales that will be discussed later.

[2]This is an expensive red-coloured glass that obtains its colour due to the presence of gold nanoparticles, as was found out by Faraday [15]. Microscopically, the rubyish colour comes from the

dispersions, respectively, and many more types of dispersions can be considered, as long as the colloidal particles are immiscible with the surrounding medium (which is often the case if the colloidal particle is a solid). Not only does the medium affect the colloid, for example, by making them charged as we shall see later, the colloidal particles themselves can also affect the medium. As an example we will consider a suspension of colloidal particles in a (molecular) liquid crystalline medium. Topological defects are generated in the liquid crystalline phase due to the presence of the colloids, that can range from disclination loops and point defects [18], to director field realizations of mathematical knots [19]. These examples show that the tunability of the *particle* properties and that of the *medium* make colloidal dispersions interesting systems to study, which often reveal surprising phenomena.

Out of the endless possibilities of colloidal systems, we will focus in this thesis on repulsive colloidal spheres and rods. The repulsions can be short-ranged (such as hard spheres or hard rods), but we will also consider repulsions of a tunable range and strength for like-charged spheres in an electrolyte solution. To establish the necessary knowledge to understand these systems, we will first focus on the electrostatics of ionic systems, and how these concepts translate to charged colloidal dispersions. Finally, we briefly discuss hard rod-like systems and their phase behaviour, ending with an outline of this thesis.

## 1.2 Electrostatics of ionic systems

The medium in which the colloidal particles reside consist often of a solvent with ions residing in it. Being actually (at least) a quaternary solvent-ions-colloid mixture, the solvent is often described as a structureless medium, characterized by a dielectric constant $\epsilon$ at temperature $T$. The Coulomb pair interaction $\Phi_c(r)$ between two like-charged monovalent ions separated by a distance $r$ larger than the hard-core separation, is then given by

$$\beta\Phi_c(r) = \frac{\beta e^2}{4\pi\epsilon_{\text{vac}}\epsilon r}, \tag{1.2}$$

with $\epsilon_{\text{vac}} = 8.854187817...\cdot 10^{-12}$ F·m$^{-1}$ the vacuum permittivity and $e = 1.6021766208...$ C the elementary charge. Eq. (1.2) defines a length scale for which the Coulomb interaction between these two ions equals the thermal energy $\beta^{-1} = k_B T$, which is the Bjerrum length $\lambda_B = \beta e^2/4\pi\epsilon_{\text{vac}}\epsilon$. It is therefore a measure for the strength of the electrostatic interaction: if $\lambda_B$ is small, the Coulomb interaction is weak, if $\lambda_B$ is large, the interaction is strong. At room temperature, we find $\lambda_B = 55.6/\epsilon$ [nm]. For a medium with a high dielectric constant, such as water ($\epsilon = 80$), we find $\lambda_B = 0.7$ nm, while an oil with $\epsilon = 2$ gives $\lambda_B = 28$ nm. The effects of these various values can be seen

---

adsorption of visible light that originates from the collective oscillation of the free (conduction-band) electrons, the so-called surface plasmon resonance [16], for optimal particle sizes of 5-60 nm [17]. This mechanism should be contrasted to the adsorption of photons with the correct energy that promotes bound electrons from a ground state to an excited state, that gives the colour to, for example, dyes.
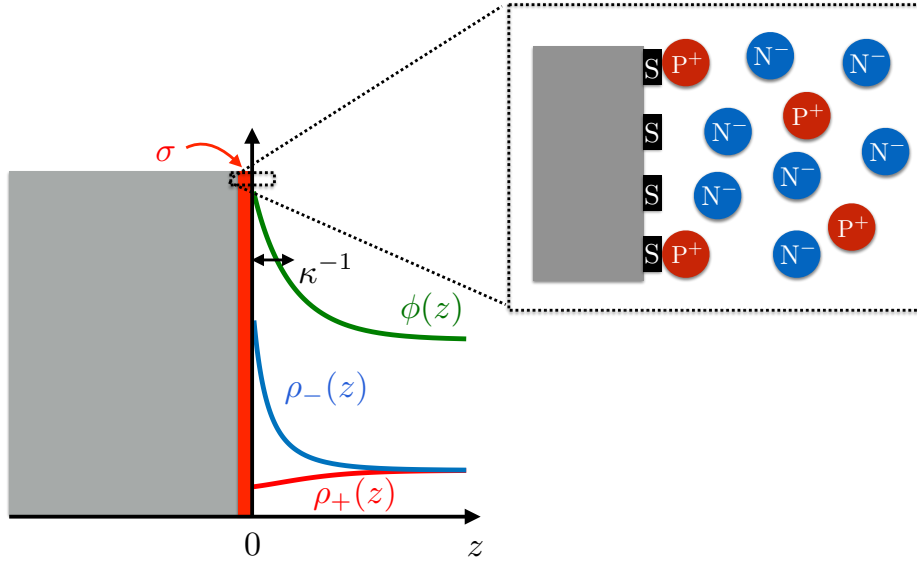
**Figure 1.1:** Schematic presentation of a charged wall at $z < 0$ with positive surface charge density $\sigma$, that results from the adsorption of positive ions $P^+$ to neutral sites S. The resulting (dimensionless) electrostatic potential $\phi(z)$ and ion densities $\rho_+(z)$ for the positive ions $P^+$ and $\rho_-(z)$ for the negative ions $N^-$ are then shown to decay with a decay length called the Debye screening length $\kappa^{-1}$.

on, for example, table salt NaCl, where the $Na^+$ and $Cl^-$ in a crystalline state have a centre-to-centre separation of 0.28 nm. Compared to the above Bjerrum lengths, we conclude that it is easier to dissociate NaCl in water, but is much harder to do so in an oil.

Ignoring fluctuations in local density, and assuming that the ions are homogeneously distributed, we learn from the Poisson equation

$$\nabla^2 \phi(\mathbf{r}) = -4\pi\lambda_B[\rho_+(\mathbf{r}) - \rho_-(\mathbf{r})], \qquad (1.3)$$

that the electrostatic potential $\phi(\mathbf{r})/(\beta e)$ is constant, since the density of positive $\rho_+(\mathbf{r})$ and negative ions $\rho_-(\mathbf{r})$ are constant in space. For non-trivial potential profiles at the mean-field level, let us consider the canonical example of a charged surface with surface area $A$ positioned in an electrolyte solution at the $xy$ plane at $z = 0$, with a positive surface charge density $e\sigma$. In Fig. 1.1 we show schematically this system.

Because $\sigma > 0$, negative ions will accumulate near the surface, while positive ions are depleted from it. The resulting diffuse ion layer together with the surface charge form two types of layers containing ionic charges, and is hence called the electrical double layer. Its width determines the range of the Coulomb interactions in an electrolyte solution. Because the range is smaller than it would be in the absence of ions, we say that the electrostatic potential is being *screened*.

The surface charge density is of the same nature as the (bulk) ions, because microscopically it stems from the ionic adsorption on, or ionic desorption from the surface, and therefore, $\sigma$ depends on the salt concentration $\rho_s$. The fact that a surface charge density in a broader sense depends on the thermodynamic state of the system is called

*charge regulation.* Let us for simplicity assume that only the cations can adsorb on sites that reside on the colloidal surface. The entropy of the ions, the Coulomb interactions and the coupling between bulk and surface can be captured within the so-called intrinsic Helmholtz free energy functional using classical density functional theory [20]

$$\frac{\beta \mathcal{F}[\rho_\pm]}{A} = \sum_{\alpha=\pm} \int_{-\infty}^{\infty} dz \, \{\rho_\alpha(z)\ln[\rho_\alpha(z)\Lambda_\alpha^3] - 1\} + \frac{1}{2}\int_{-\infty}^{\infty} dz \, Q(z)\phi(z)$$

$$+ \sigma[\ln(\sigma a^2) + F_b] + (\sigma_m - \sigma)\ln[(\sigma_m - \sigma)a^2], \quad (1.4)$$

where $\Lambda_\alpha$ is the thermal de Broglie wavelength of an ion with sign $\alpha$, $Q(z) = \rho_+(z) - \rho_-(z) + \sigma\delta(z)$, $a$ is a microscopic length scale associated with the area occupied by a surface site, and $\sigma_m$ is the surface density of chargeable sites. Finally, $F_b$ is a free energy of binding given by the internal partition sum

$$\exp\left(-\beta F_b\right) = \frac{1}{\Lambda_+^3}\int_{v_b} d^3\mathbf{r}\exp[-\beta H_b(\mathbf{r})], \quad (1.5)$$

assuming a classical binding Hamiltonian $H_b(\mathbf{r})$ that describes the adsorption of positive ions on the charged surface. According to Eq. (1.5) an ion is defined as being adsorbed, if it resides within a binding volume $v_b$ near the surface.

The system with the surface is assumed to be in osmotic contact with a reservoir with salt concentration $2\rho_s$ and we gauge the electrostatic potential to be zero in this reservoir. For this reason, it makes sense to consider the osmotic ensemble in which the ions are treated grand-canonically, via the Legendre transformation

$$\Omega[\rho_\pm, \sigma] = \mathcal{F}[\rho_\pm, \sigma] - A\int dz \left\{\sum_{\alpha=\pm} u_\alpha(z)\rho_\alpha(z) + u_+(z)\sigma\delta(z)\right\}, \quad (1.6)$$

where $u_\alpha(z) = \mu_\alpha - V_{\text{ext}}(z)$, with the ion chemical potential $\mu_\alpha = \log(\rho_s\Lambda_\alpha^3)$. For the external potential $V_{\text{ext}}(z)$ we use the hard-wall potential

$$V_{\text{ext}}(z) = \begin{cases} \infty, & (z < 0), \\ 0, & (z > 0). \end{cases} \quad (1.7)$$

Within mean-field the density profiles are found by $\delta\Omega[\rho_\pm, \sigma]/\delta\rho_\pm(z) = 0$, which result in the Boltzmann distributions, $\rho_\pm(z) = \rho_s\exp[\mp\phi(z)]$ for $z > 0$, which combined with Eq. (1.3) gives the Poisson-Boltzmann equation

$$\phi''(z) = \kappa^2 \sinh[\phi(z)], \quad (z > 0), \quad (1.8)$$

with $\kappa = \sqrt{8\pi\lambda_B\rho_s}$ and a prime denotes the derivative with respect to $z$. The boundary conditions follow by appropriate use of Gauss' law,

$$\phi'(0^+) = -4\pi\lambda_B\sigma, \quad (1.9)$$

$$\phi'(z \to \infty) = 0. \quad (1.10)$$

Eqs. (1.8)-(1.10) are solved by,

$$\phi(z) = 2\ln\frac{1 + C\exp(-\kappa z)}{1 - C\exp(-\kappa z)} \xrightarrow{(\kappa z \gg 1)} 4C\exp(-\kappa z). \qquad (1.11)$$

The asymptotic behaviour for $\kappa z \gg 1$ shows that $\kappa^{-1}$ is a length scale for which $\phi(z)$ is being screened (shown schematically in Fig. 1.1), hence it is called the Debye screening length. It is also the decay length for the diffuse ion layer, as can be seen by evaluating the densities with Eq. (1.11). The integration constant $C$ can be derived by evaluating $\partial\Omega[\rho_{\pm},\sigma]/\partial\sigma = 0$, which results in the Langmuir adsorption isotherm

$$\sigma = \frac{\sigma_m}{1 + \exp[\beta F_b - \beta\mu_+ + \phi(0^+)]}. \qquad (1.12)$$

Another, but equivalent, way to derive $\sigma$ is by applying the law of mass action to the charging of a single site S by adsorption of a positive ion P$^+$, according to the equilibrium S+P$^+ \leftrightarrows$ SP$^+$ with equilibrium constant $K$. This results in

$$\sigma = \sigma_m\left\{1 + \frac{K}{\rho_s}\exp[\phi(0^+)]\right\}^{-1} = \sigma_m\left\{1 + \frac{K}{\rho_+(0^+)}\right\}^{-1}. \qquad (1.13)$$

Comparison of Eq. (1.12) with Eq. (1.13) provides the relation $K = \rho_s\exp[\beta F_b - \beta\mu_+]$, or in other words,

$$K = \left\{\int_{v_b} d^3\mathbf{r}\exp[-\beta H_b(\mathbf{r})]\right\}^{-1}. \qquad (1.14)$$

For the approximation $H_b(\mathbf{r}) = \epsilon_b$, this results in $K = v_b^{-1}\exp(\beta\epsilon_b)$, giving insight in the microscopic nature of $K$. Furthermore, we see that $K$ depends only on temperature and on material properties through $\epsilon_b$. The integration constant $C$ can be derived from

$$\frac{4C}{1 - C^2} = \frac{4\pi\lambda_B\sigma_m}{\kappa}\left[1 + \frac{K}{\rho_s}\left(\frac{1+C}{1-C}\right)^2\right]^{-1}, \qquad (1.15)$$

which can be solved analytically in principle, but the expression is lenghty. Hence, for a given $\rho_s$, we can find $C$, and from this not only the surface potential follows,

$$\phi(0^+) = 2\ln\left(\frac{1+C}{1-C}\right), \qquad (1.16)$$

which depends on $\rho_s$, but also $\sigma$ by using Eq. (1.13). This should be contrasted to other boundary conditions, such as (i) the constant-charge boundary condition where $\sigma$ is a given constant, but $\phi(0^+)$ depends on $\rho_s$, and (ii) the constant-potential boundary condition where $\phi(0^+)$ is fixed and $\sigma$ varies as function of $\rho_s$ (and is thus also a form of charge regulation).

Finally, we define the Gouy-Chapman length $\xi = (2\pi q\lambda_B\sigma)^{-1}$, which is the distance for which the Coulomb interaction of a single counter ion of valency $q$ with the charged

plate in the absence of other ions equals $k_B T$. Using $\xi$, we can define the (Netz-Moreira) coupling parameter $\Xi = q^2 \lambda_B / \xi = 2\pi q^3 \lambda_B \sigma$. Within a field-theoretical treatment of ionic systems in the presence of charged surfaces, it can be shown that the Poisson-Boltzmann theory is actually the saddle point theory with respect to a fluctuating electrostatic potential. Systematic corrections to the mean-field solution can be found by a weak coupling expansion in terms of $\Xi$ [21], in a similar spirit to the loop expansion in quantum field theory in terms of $\hbar$ [22]. The same $\Xi$ is also the relevant parameter in a strong coupling expansion [23, 24]. Therefore, $\Xi$ is a measure for the importance of electrostatic correlations, and these become more important for high surface charges and/or multivalent ions, giving rise to phenomena such as like-charge attraction and the formation of highly correlated two-dimensional layers of ions close to a charged surface [25]. Throughout this thesis, however, we will only focus on monovalent ions such that $\Xi \ll 1$ and therefore Poisson-Boltzmann theory applies.

## 1.3 Charged colloidal suspensions and their tunability

Having discussed a single charged plate in an electrolyte, we now go to the more complex situation of a colloidal suspension. For charge-regulating particles, it is more convenient to retain the particle nature of the colloids and to not use density profiles to describe them, as was done for the ions. There are two main differences compared to the charged plate. First of all, the non-linear Poisson-Boltzmann equation is much harder to study than for a single charged plate. Even for a fixed configuration of colloids, solving the full three-dimensional Poisson-Boltzmann equation (with suitable boundary conditions),

$$\nabla^2 \phi(\mathbf{r}) = \kappa^2 \sinh[\phi(\mathbf{r})], \quad \mathbf{r} \in \text{outside colloids} \tag{1.17}$$

$$\nabla^2 \phi(\mathbf{r}) = 0, \quad \mathbf{r} \in \text{inside colloids}, \tag{1.18}$$

requires a lot more numerical effort than for a single charged plate. To illustrate qualitatively the behaviour of the above equations, we solved the Poisson-Boltzmann equation Eqs. (1.17) and (1.18) in Fig. 1.2 for a two-dimensional system of constant-potential spheres with surface potential $\phi_0 = 3$ at various $\kappa^{-1}$, showing that the spatial structure of the various screening clouds not only depends on the precise local configuration of colloids, but also on the Debye screening length via $\rho_s$. For small screening lengths the double layers do not overlap and the system can be viewed as a hard-sphere system with an "inflated" hard-core diameter (Fig. 1.2(a)). By increasing $\kappa^{-1}$ some double layers start to overlap (Fig. 1.2(b)-(c)), and if the particles are sufficiently far apart, the system can still be viewed as hard-sphere like. Significant double layer overlapping occurs when $\kappa^{-1}$ is increased even further (Fig. 1.2(d)), while at very long screening lengths the double layer overlapping is so significant that the screening ions are homogeneously distributed throughout the sample (Fig. 1.2(e)). Such a system is essentially a one-component plasma: a system of charged point-particles in a homogeneous neutralizing background. This example shows that it is not hard to imagine that
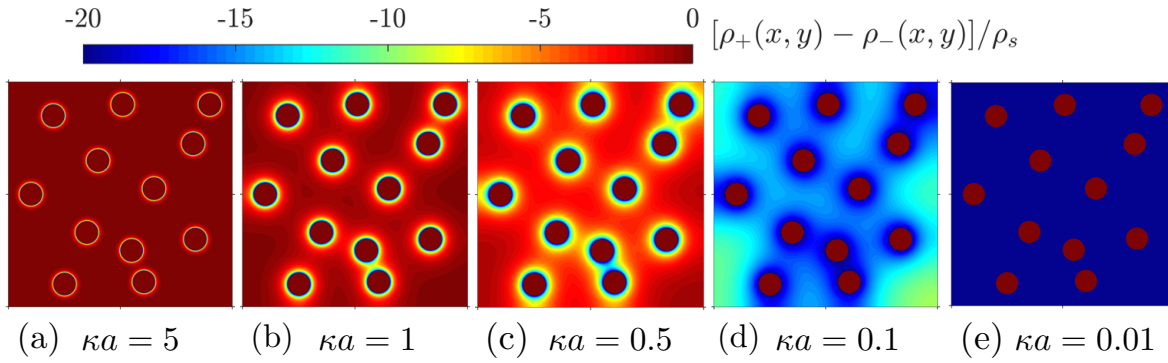
**Figure 1.2:** Numerical results for the net ionic charge density $(\rho_+ - \rho_-)/\rho_s$ with $\rho_s$ the reservoir salt concentration, to visualize the double layers of twelve two-dimensional constant-potential colloids of radius $a$ and surface potential $\phi_0 = 3$ in a box of $20a \times 20a$ for various Debye lengths $\kappa^{-1}$. By decreasing $\rho_s$ the particles can be tuned (a) from hard-sphere like to (b)-(d) a suspension with increasing double layer overlaps and (e) a one-component plasma where the extended double layers from a homogeneous background.

charge-regulating particles have a surface-charge distribution that does not only depend on salt concentration and the dielectric constant of the surrounding medium, but also on the precise configuration of colloids and hence on the (local) density. Moreover, these are properties that can be *tuned*. Finally, we also see from the dependence on local density and $\kappa^{-1}$, that the value of the electrostatic potential at particle separations where the double layers start to overlap depends on the thermodynamic state. This is the Donnan potential, and can be seen as the mean potential difference compared to a hypothetical ion reservoir with no colloids in it.

Secondly, colloidal particles undergo Brownian motion by the random "kicks" of the surrounding solvent (or gas), and should therefore be viewed as thermal systems as opposed to the (stationary) plate of the example in the previous section. If we denote a fixed colloidal configuration by $\mathbf{R}^N = (\mathbf{R}_1, ..., \mathbf{R}_N)$, we can write down a grand potential functional in the same spirit as for the single charged plate $\Omega[\rho_\pm, \{\sigma_i\}_{i=1}^N; \mathbf{R}^N]$. From the minimum condition $\min_{\rho_\pm,\sigma_i} \Omega[\rho_\pm, \{\sigma_i\}_{i=1}^N; \mathbf{R}^N]$ we obtain the ionic grand potential in the external field of $N$ colloids, which defines the many-body effective Hamiltonian

$$H_{\text{eff}}(\mathbf{R}^N) = H_{\text{bare}}(\mathbf{R}^N) + \min_{\rho_\pm,\sigma_i} \Omega[\rho_\pm, \{\sigma_i\}_{i=1}^N; \mathbf{R}^N], \tag{1.19}$$

with $H_{\text{bare}}(\mathbf{R}^N)$ a non-electrostatic (many-body) Hamiltonian that can include the effects of, for example, hard-sphere repulsions and van der Waals attractions. From Eq. (1.19) the free energy $F = F(N, V, T, \mu_s)$ can be extracted

$$\exp(-\beta F) = \int \frac{d\mathbf{R}^N}{N!\mathcal{V}^N} \exp[-\beta H_{\text{eff}}(\mathbf{R}^N)], \tag{1.20}$$

with $\mathcal{V}$ the thermal volume of a colloid that results from the integration over internal degrees of freedom and the momenta. It is straightforward to extend the above formalism to describe also non-trivial dielectric profiles of the medium (such as an oil-water
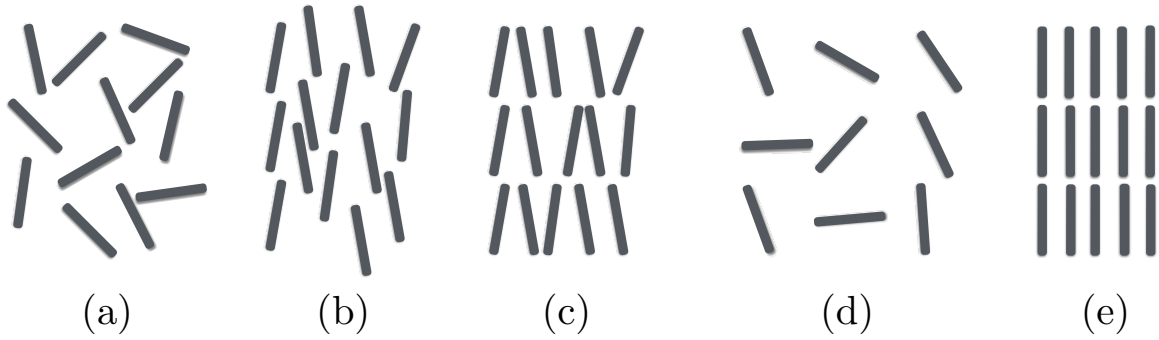
**Figure 1.3:** A few examples of phases that rod-like systems can form, ranging from (a) an isotropic fluid, to (b) a nematic state, and (c) smectic phase, (d) plastic crystal, and finally (e) a crystal.

interface), various shapes etc. Both the effective Hamiltonian and the free energy of the system will be studied in this thesis, within a suitable approximation depending on the specific application.

## 1.4 Rod-like systems

The phases of a system with spherical particles that interact via an isotropic pair potential can range from a (dilute) gas, via an isotropic liquid, to an ordered crystal upon increasing the density. The ordering of the particles can be completely described by the positional ordering of their centre-of-masses. In the case of rods many more phases can be formed, because the particle orientation is a new degree of freedom, such that also orientational order can occur without the need of positional order (or vice versa). For example, an isotropic liquid is found for rods whenever the system is completely translational and rotational symmetric (Fig. 1.3(a)). When the rods break rotational symmetry by aligning towards a common direction, the phase is called a nematic state (Fig. 1.3(b)). It is different from, for example, a ferromagnet, since every rod can be rotated by 180 degrees without change the state of the system, which is called up-down symmetry. When translational symmetry is broken in one direction, the state is called a smectic phase (Fig. 1.3(c)), which is easily recognized by the formation of layers, in which the rods behave as a two-dimensional fluid. The smectic and nematic phase are liquid crystal phases. If, however, the rotational symmetry stays intact, but translational symmetry is broken in all three dimensions, a plastic crystal is formed, as shown in Fig. 1.3(d) for rods that position their centre-of-masses in a cubic lattice, with every lattice site occupied by a rod with a random orientation. When both rotational and translational symmetry is broken in all dimensions, the crystalline phase is formed (Fig. 1.3(e)). More phases than these can be found depending on the dimensionality of the broken rotational and positional degrees of freedom [26], but we will not discuss them here.

With the exception of the plastic crystal that needs long-ranged repulsion, all phases can occur in hard-rod systems. The excluded volume interactions of such systems are

elegantly captured in the so-called Onsager theory [27], which is essentially a second virial theory where the rods interact via hard-core repulsions. Within density functional theory, we ascribe a density field $\rho(\mathbf{r}, \hat{\omega})$, viewing each orientation $\hat{\omega}$ as a distinct species, to find the grand potential functional

$$
\begin{aligned}
\beta\Omega[\rho] = \int d\mathbf{r} d\hat{\omega} \rho(\mathbf{r}, \hat{\omega}) \{\log[\rho(\mathbf{r}, \hat{\omega})\mathcal{V}] - 1 - \mu + V_{\text{ext}}(\mathbf{r}, \hat{\omega})\} \\
- \frac{1}{2} \int d\mathbf{r} d\hat{\omega} d\mathbf{r}' d\hat{\omega}' f(\mathbf{r}, \hat{\omega}, \mathbf{r}', \hat{\omega}') \rho(\mathbf{r}, \hat{\omega}) \rho(\mathbf{r}', \hat{\omega}'),
\end{aligned}
\tag{1.21}
$$

with the Mayer function of a hard-sphere potential $\phi_{\text{HS}}(\mathbf{r}, \hat{\omega}, \mathbf{r}', \hat{\omega}')$ given by

$$
f(\mathbf{r}, \hat{\omega}, \mathbf{r}', \hat{\omega}') = -1 + \exp[-\beta\phi_{\text{HS}}(\mathbf{r}, \hat{\omega}, \mathbf{r}', \hat{\omega}')],
\tag{1.22}
$$

and $V_{\text{ext}}(\mathbf{r}, \hat{\omega})$ an external potential that can be used to, for example, describe hard walls or external fields. Although we will not try to attempt to solve it in this thesis, the appropriate Euler-Lagrange equation can be found to be

$$
\log[\rho(\mathbf{r}, \hat{\omega})\mathcal{V}] - \int d\mathbf{r}' d\hat{\omega}' f(\mathbf{r}, \hat{\omega}, \mathbf{r}', \hat{\omega}') \rho(\mathbf{r}', \hat{\omega}') + V_{\text{ext}}(\mathbf{r}, \hat{\omega}) = \beta\mu.
\tag{1.23}
$$

A numerical solution to this non-linear integral equation for bulk is rather straightforward [28], however, a lot more numerical effort is needed to describe for example an isotropic-nematic interface [29]. The situation becomes even more complex for systems that host topological defects, confined systems or liquid-crystalline droplets. Therefore, it is desirable to have a simplification for this theory to extract useful qualitative behaviour. We will propose such a theory later in this thesis.

## 1.5  Outline of this thesis

The above concepts will be applied in this thesis to repulsive colloidal particles. The main part will be about charged colloids that are suspended in an oily environment. Already in one-component systems such dispersions give interesting phase behaviour, as we shall see in Chapter 2. There we lay out various frameworks to give accurate predictions for the crystallization transition that is driven by electrostatic repulsions. Moreover, we will show how the macroscopic phase diagram can give information on the microscopic charging mechanism of a single colloid. In Chapter 3, we make the system more complex by considering binary mixtures of charge-asymmetric colloids. We find demixing in such a system, which may have direct consequences in sedimentation profiles. In Chapter 4, we investigate whether a binary mixture can form alternating strings or compact clusters, via a directional effective pair potential. For this to occur it turns out that charge regulation and many-body effects are important. In Chapter 5 we take a step back in complexity regarding the many-body nature of a colloidal dispersion by investigating only a single charge-regulating sphere. Instead, we make the

medium more complex by considering the presence of an oil-water interface. We calculate the effective interaction of an oil-dispersed particle with such an interface and show that the nature of the colloid-interface interaction is highly tunable by salt. Finally, we investigate the lateral colloid-colloid interaction for particles that penetrate the oil-water interface. In Chapter 6, we show how the effective colloid-interface potential is changed when multiple ion species are present in the medium and how this interaction is influenced by various charge-regulation mechanisms. Finally, the influence of ion dynamics will be discussed in view of recent experiments. In Chapter 7, we consider anisotropy in the particle shape, by constructing an effective Landau theory for hard rods that mimicks Onsager theory, but needs a lot less numerical effort to solve. We apply this theory to topological defects and liquid crystalline droplets (tactoids).

# 2

# Density-induced reentrant melting of colloidal Wigner crystals

*Electrostatic repulsions can drive crystallization in many-particle systems. For charged colloidal systems, the phase boundaries as well as crystal structure are highly tunable by experimental parameters such as salt concentration and pH. By using projections of the colloid-ion mixture to a system of (soft) repulsive spheres and the one-component plasma (OCP), we study the hitherto unexplained experimentally observed reentrant melting of electrostatically repelling colloids upon increasing the colloid density. Our study shows that the surface chemistry should involve a competition between adsorption of cations and anions to explain the observed density-induced reentrant melting.*

## 2.1 Introduction

Crystalline ordering is observed in systems with building blocks as small as electrons [30, 31], and as big as granular particles [32]. The crystallization of a many-body system is a direct result of the forces between the particles, and relating these forces to the observed ordering in the system is a challenging problem in general. For example, crystallization can be driven by attractive interactions between the individual components, such as in the gas-crystal transition for a Lennard-Jones system below the triple-point temperature [4]. A purely repulsive interaction can also result in crystalline order, a text-book example being the self-assembly of colloidal hard spheres into a face-centered cubic crystal at high densities [33–35]. In systems of charged particles, where Coulomb interactions are pivotal for understanding the crystallization transition, the inherent structure may also either form due to the attractions between oppositely charged species [36], or due to mutual repulsion between like-charged particles. Crystallization due to electrostatic repulsions has been studied extensively for colloidal systems [37–44]. These colloidal Wigner crystals [45] are very interesting from a engineering perspective as they can have extraordinary optical [46] or mechanical properties [47].

Due to the relatively large size of the particles, the transition to a crystal can be studied using an optical microscope. Interestingly, the charge of these particles is usually not fixed, but regulated [48–50], as it results from the chemical equilibrium between the ionizable surface and the ions in the solvent [51], which causes the effective forces between the particles to be highly tunable by experimentally controllable parameters. The ordering of the particles therefore shows strong dependence on parameters such as pH and salt concentration. This opens up a vast parameter space in which various crystalline structures can be found.

In earlier studies the formation of charge-induced crystallization was described within Poisson-Boltzmann theory [52] in the spherical- cell approximation. The resulting electrostatic potential and ionic diffuse screening layer around the central particle are then mapped through a renormalized colloidal charge to effective one-component systems for which the phase diagram is known empirically from e.g. simulations of point-Yukawa particles [53]. Recently, it was shown that the cell approach can also be used to define a mapping to a one-component plasma (OCP) [54], such that the freezing criterion for the classical OCP can be applied. Combining explicit models for the surface chemistry of the colloidal particles with the OCP mapping yields a model that fits very well with experiments and provides insight not only at the level of molecular details of the charging mechanism and the equilibrium constant, but also at the macroscopic scale of phase diagrams [54]. In this work we build on Ref. [54] by considering how various crystallization mechanisms affect the phase diagrams of colloidal particles that are subject to charge regulation. We will also connect our theoretical results with the experimental phase diagrams of Refs. [49, 55, 56]. We will highlight the well-understood reentrant melting as function of salt concentration, and the less understood reentrant melting as function of colloid density. We will show here that the latter can only be explained by a sufficiently strong density dependence of the colloidal charge and the screening length [49, 56], that results from a binary adsorption model.

## 2.2  Model

Our description of the colloidal suspension invokes the spherical cell approximation as was introduced by Alexander *et al.* in 1984 [57]. In this approximation the suspension is divided into spherical cells, each containing one colloidal particle of radius $a$. These cells are all identical with radius $R$, which is related to the colloidal packing fraction via $\eta = (a/R)^3$. Within mean-field theory the ion-density profiles $\rho_\pm(r)$ are related to the electrostatic potential $\phi(r)/(\beta e)$ by $\rho_\pm(r) = \rho_s \exp[\mp\phi(r)]$, with $r$ the radial coordinate, $e$ the proton charge, $\beta^{-1} = k_B T$ the thermal energy and $\rho_s$ the salt concentration of a reservoir with which the system is assumed to be in osmotic equilibrium. Notice that varying $\rho_s$ is equivalent to varying the chemical potential of the ions. Apart from the particle radius $a$, there are two length scales in our problem. These are the Bjerrum length $\lambda_B = \beta e^2/4\pi\epsilon_{\mathrm{vac}}\epsilon$ and the Debye screening length $\kappa^{-1} = (8\pi\lambda_B\rho_s)^{-1/2}$. Here $\epsilon_{\mathrm{vac}}$ is the vacuum dielectric constant and $\epsilon$ is the relative dielectric constant in the solvent. Combining the mean-field density profiles with the Poisson equation results
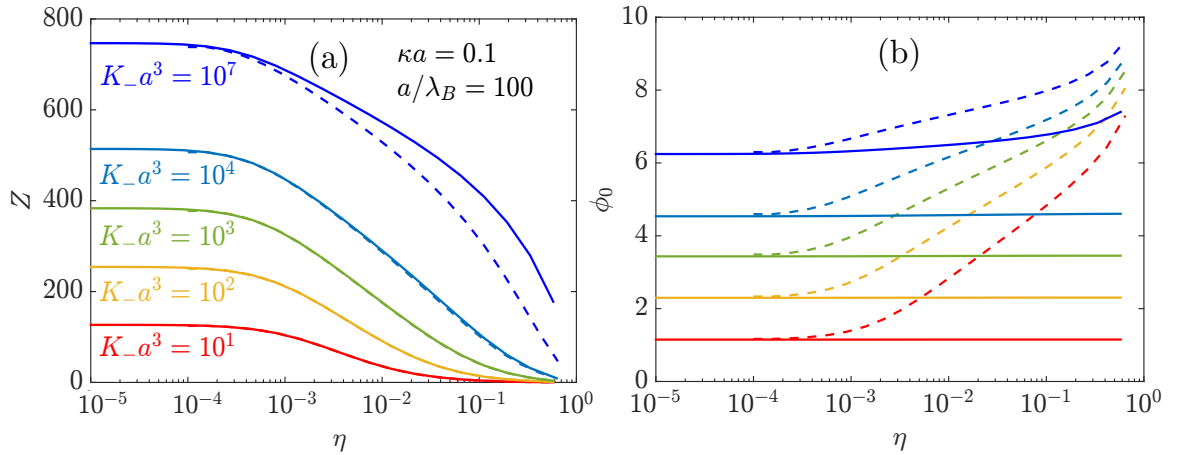
**Figure 2.1:** The full curves represent (a)the particle charge $Z$ and (b) the dimensionless surface potential $\phi_0$ as function of packing fraction $\eta$ for various values of the equilibrium constant $K_-$, while keeping $K_+ a^3 = 1$ and the total number of surface sites $M = 10^7$ fixed. The dashed lines in (a) are the result of a constant-potential system where we chose $\phi_0$ such that the resulting $Z$ coincides in the dilute limit. The reverse is done in (b) but then for a constant-charge system that has a $Z$ such that the resulting $\phi_0$ coincides in the dilute limit. The lines for $K_- a^3 = 10^7$ are essentially the same as for the limit $K_- a^3 \to \infty$, in which no anions can adsorb.

in the non-linear spherically symmetric Poisson-Boltzmann (PB) equation

$$\frac{d^2\phi}{dr^2} + \frac{2}{r}\frac{d\phi}{dr} = \kappa^2 \sinh[\phi(r)], \quad r \in [a, R], \tag{2.1}$$

with boundary conditions $\phi'(a) = -Z\lambda_B/a^2$ and $\phi'(R) = 0$, where a prime denotes a radial derivative and $Ze$ is the colloidal charge. From the solution of the PB equation the surface potential $\phi_0 = \phi(a)$ and the Donnan potential $\phi_D = \phi(R)$ are found self-consistently once $Z$ is known. Here we do not only consider the constant-charge case where $Z$ is a known input parameter, but we will also calculate $Z$ self-consistently for charge regulation cases where we consider an associative charging mechanism in which a single surface site S can be occupied by negative ions N⁻ and positive ions P⁺. These are governed by the reactions $S + P^+ \leftrightarrows SP^+$ with equilibrium constant $K_+ = [S][P^+]/[SP^+]$ and $S + N^- \leftrightarrows SN^-$ with equilibrium constant $K_- = [S][N^-]/[SN^-]$. This results in an adsorption isotherm that relates the surface charge to the surface potential [51] via

$$\frac{Z}{M} = \frac{K_- \exp(-\phi_0) - K_+ \exp(\phi_0)}{\sum_\sigma K_\sigma \exp(z_\sigma \phi_0) + K_+ K_-/\rho_s}, \tag{2.2}$$

with $z_\pm = \pm 1$, which reduces to the familiar Langmuir form

$$\frac{Z}{M} = \frac{1}{1 + K_+/\rho_s \exp(\phi_0)}, \tag{2.3}$$

in the limit where $K_- \to \infty$. Here $M$ is the number of sites available for adsorption and we will set it to $M = 10^7$, which is equivalent to roughly one surface group per 1 nm²

for a micron-sized particle. Note that high values for $K_\pm/\rho_s$ yield little tendency for the ions to adsorb, while small values for $K_\pm/\rho_s$ results in a significant fraction of occupied surface groups. In Figure 2.1 we plot some results for (a) $Z$ and (b) $\phi_0$ obtained from the cell model as function of $\eta$ for $M = 10^7$, $a/\lambda_B = 100$ and $\kappa a = 0.1$. We see that the colloidal particle always discharges as function of $\eta$, while the corresponding $\phi_0$ increases or is approximately constant for the case in which both positive as well as negative ions can adsorb. The observed constant potential in the latter case is because both the chargeabilities $Y_\pm = \kappa a M/(8\pi K_\pm a^3)$ are much larger than unity for these parameters, as we shall show in the Appendix.

From the cell model it is possible to extract effective pair potentials, which we will use in various freezing criteria. The best known route towards an effective pair potential for (highly) charged particles uses charge renormalization [58, 59] in combination with DLVO theory [60, 61] . An effective charge $Z^*$ is defined by extrapolating the linear screening solution fitted to the numerical solution for the far-field electrostatic potential to $r = a$ [57],

$$Z^* = \frac{\tanh \phi_D}{\bar{\kappa} \lambda_B} \left[ (\bar{\kappa}^2 aR - 1) \sinh(\bar{\kappa}R - \bar{\kappa}a) + (\bar{\kappa}R - \bar{\kappa}a) \cosh(\bar{\kappa}R - \bar{\kappa}a) \right]. \tag{2.4}$$

Here $\bar{\kappa}^{-1}$ is a colloid-density dependent screening length given by $\bar{\kappa}^2 = \kappa^2 \cosh \phi_D$. From this so-called renormalized charge $Z^*$, we can define the effective DLVO pair potential

$$\beta U_{\mathrm{DLVO}}(r) = \begin{cases} \infty, & r < 2a, \\ \left( \dfrac{Z^* \exp(\bar{\kappa}a)}{1 + \bar{\kappa}a} \right)^2 \dfrac{\lambda_B \exp(-\bar{\kappa}r)}{r}, & r \geq 2a. \end{cases} \tag{2.5}$$

We remark here that this DLVO-based method is known to become inaccurate for dense systems [62–67], due to many-body effects resulting from a significant overlap between double layers with the hard core of other particles. Nevertheless, in case the double layers constitute a relatively thin shell around the individual particles, the DLVO form is deemed accurate.

Alternatively, one can choose to calculate effective point-Yukawa charges by fitting the linearized solution for the "far-field" electrostatic potential in the cell to the non-linear solution that follows from the Poisson-Boltzmann model. By extrapolating the linear solution to $r = 0$ , an effective Yukawa point charge $Q$ can be identified in the origin [67], which is found to depend on the cell-boundary parameters via

$$Q = \frac{\tanh \phi_D}{\bar{\kappa} \lambda_B} \left[ \bar{\kappa}R \cosh(\bar{\kappa}R) - \sinh(\bar{\kappa}R) \right]. \tag{2.6}$$

Using this effective point charge, the effective pair interaction can be expressed as the sum of the non-electrostatic hard-core repulsion and a Yukawa potential

$$\beta U_{\mathrm{Y}}(r) = \begin{cases} \infty, & r < 2a, \\ \dfrac{Q^2 \lambda_B \exp(-\bar{\kappa}r)}{r}, & r \geq 2a. \end{cases} \tag{2.7}$$

By means of computer simulations of these point particles [67] it has been confirmed recently that this approach yields a very accurate estimate for the colloid-colloid pair-correlation functions and the pressure for both dilute and dense colloidal systems when compared with a mixture of colloids and ions.

## 2.3 Crystallization criteria

There are various approaches towards determining the location of the charge-induced crystallization transition that we will discuss in this work. As it has been proposed earlier by other authors, it is tempting to view the charged system as an effective hard-sphere system, with an effective hard-core diameter $\sigma_{\text{eff}}$ that is larger than the original diameter of the particle due to the electrostatic repulsions [68–71]. This can, for example, be achieved by defining the second virial coefficient $B_2 = (1/2) \int d\mathbf{r} \{1 - \exp[-\beta U_{\text{DLVO}}(\mathbf{r})]\}$ and imposing the second virial coefficient of the hard-sphere fluid $B_2 = (2/3)\pi\sigma_{\text{eff}}^3$. By using that the hard-sphere system crystallizes at packing fraction $(\pi/6)\sigma_{\text{eff}}^3\rho > 0.5$ [35], we arrive at the freezing criterion $B_2\rho > 2$, with $\rho$ the colloid density.

Another approach that does not rely on any pair potential can be found by comparing the osmotic pressure $\Pi$ to that of a system of hard spheres. Within the cell model, the osmotic pressure is given by summing the ionic and the hard-core contributions. This results in $\beta\Pi/\rho = 2\rho_s(\cosh\phi_D - 1)/\rho + (1 + \eta + \eta^2 - \eta^3)/(1-\eta)^3$, where we have used the Carnahan-Starling expression for the second term. The criterion $\beta\Pi/\rho > 13$ can now be applied in analogy to the hard-sphere system.

Both hard-sphere like criteria that are described above are expected to be accurate at high salt concentration, where the double layers and hence the repulsive interactions are short-ranged. On the other hand, when the interactions are longer ranged the effective hard-core model is expected to break down and other approaches are needed. Recent work describes a method to map the suspension to a system of point-Coulomb particles in a neutralizing background. The latter system is known as the one-component plasma (OCP). The mapping to an OCP constitutes a partitioning of the full ionic charge into individual double layers that (partially) neutralize the charged particles and a homogeneous background of ionic charge that neutralizes the remaining charge. Within the cell model, this background is identified as the ionic charge density on the cell boundary, $\rho_+(R) - \rho_-(R)$. It defines an equivalent OCP-point charge $Z_{\text{OCP}}$ via the charge-neutrality requirement, i.e., $Z_{\text{OCP}} = -[\rho_+(R) - \rho_-(R)]/\rho$, such that the OCP coupling parameter $\Gamma_{\text{OCP}} = Z_{\text{OCP}}^2\lambda_B\rho^{1/3}$, which is the dimensionless parameter that fully characterizes the OCP, takes the form

$$\Gamma_{\text{OCP}} = \frac{1}{16\pi^2}\frac{\tanh^2\phi_D}{\bar{\kappa}\lambda_B}(\bar{\kappa}D)^5, \qquad (2.8)$$

where we used the mean interparticle distance $D = \rho^{-1/3}$, given within the cell model by $D^3 = 4\pi R^3/3$. For $\Gamma_{\text{OCP}} < 106$ the OCP is in the disordered fluid state, yet for $\Gamma_{\text{OCP}} > 106$ it favours a body-centered cubic (BCC) crystalline state [72, 73].

17

The empirical criterion $\Gamma_{\mathrm{OCP}} > 106$ was very recently shown to be very successful in describing experiments on colloidal systems [54] and is an attractive option due to its simplicity.

The OCP, however, does not feature a face-centered cubic (FCC) phase, such that it cannot capture the experimentally observed BCC-FCC phase transition. The effective Yukawa point charges defined by Eq. (2.6) and Eq. (2.7) form an alternative approach to calculating the freezing lines in a charged colloidal system. We can use the Lindemann criterion for the effective pair potential [74] and find that crystalline order is expected if the so-called Yukawa coupling parameter

$$\Gamma_{\mathrm{Y}} \equiv \beta U_{\mathrm{Y}}(D) \left[ 1 + \bar{\kappa} D + \frac{1}{2}(\bar{\kappa} D)^2 \right] \tag{2.9}$$

exceeds 106. Eq. (2.9), together with Eq. (2.6) can be expanded in powers of $\kappa D$ to find

$$\Gamma_{\mathrm{Y}} = \frac{1}{16\pi^2} \frac{\tanh^2 \phi_D}{\bar{\kappa} \lambda_B} \left[ (\bar{\kappa} D)^5 + \mathcal{O}((\bar{\kappa} D)^7) \right] . \tag{2.10}$$

Interestingly, up to 5th order in $\bar{\kappa} D$ this is just the coupling parameter $\Gamma_{\mathrm{OCP}}$ from Eq. (2.8) obtained by mapping the cell model to the one component plasma (OCP). Point-Yukawa particles, however, do exhibit an FCC phase at sufficiently large $\bar{\kappa} D$, so it is interesting that the fluid-crystal lines from the OCP and point-Yukawa criteria coincide within numerical accuracy. Computer simulations of Yukawa systems [75, 76] have shown that the fluid-crystal transition (either to FCC or BCC) is accurately described by the condition

$$\log[\beta U_{\mathrm{Y}}(D)] = 4.670 - 1.0417\bar{\kappa} D + 0.1329(\bar{\kappa} D)^2 - 0.01043(\bar{\kappa} D)^3 + 0.0004343(\bar{\kappa} D)^4$$
$$- 0.000006924(\bar{\kappa} D)^5, \tag{2.11}$$

for $0 < \bar{\kappa} D < 12$, which is up to minor deviations equivalent to the Lindemann criterion of Eq. (2.9). The criterion for the transition between a BCC to an FCC phase was found to be

$$\log[\beta U_{\mathrm{Y}}(D)] = 97.65 - 151.469499\bar{\kappa} D + 106.626405(\bar{\kappa} D)^2 - 41.67136(\bar{\kappa} D)^3 \tag{2.12}$$
$$+ 9.639931(\bar{\kappa} D)^4 - 1.3150249(\bar{\kappa} D)^5 + 0.09784811(\bar{\kappa} D)^6 - 0.00306396(\bar{\kappa} D)^7,$$

for $1.85 < \bar{\kappa} D < 6.8$. We remark that instead of the point-Yukawa approach we could also have used $U_{\mathrm{DLVO}}(r)$ as was done in Ref. [53]. Recent work, however, has shown that DLVO-based approaches underestimate the effective repulsion at high packing fractions, even if combined with methods such as charge renormalization. Indeed, $U_{\mathrm{DLVO}}(r)$ was not able to accurately describe the experiments in Ref. [54]. The point-Yukawa approach therefore yields a more direct and accurate route to the effective screened-Coulomb interactions at any density.
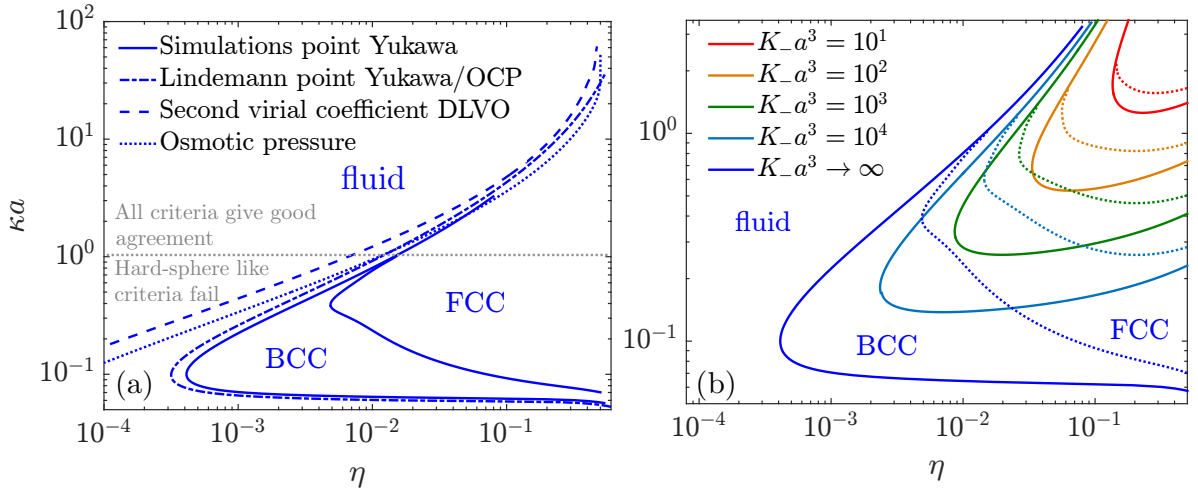
**Figure 2.2:** (a) Phase diagram in the $(\eta, \kappa a)$ representation for particles that acquire their charge through cationic adsorption only. We fix the Bjerrum length $\lambda_B = 0.01a$ and equilibrium constant $K_+ a^3 = 1$. The full lines stem from the extrapolated point charge $Q$ of the cell model, which was used as the point-Yukawa charge in the computer simulation criterion from Ref. [76]. For this criterion, it is possible to obtain the crystal-crystal transition line from a FCC to BCC lattice. The dashed-dotted line is obtained by applying the Lindemann criterion for point-Yukawas ($\Gamma_Y = 106$); this line overlaps with the result of a OCP criterion ($\Gamma_{OCP} = 106$). The dashed line uses a second virial coefficient result ($B_2 \rho = 2$). Finally the dotted line uses an osmotic pressure criterion ($\beta \Pi / \rho = 13$). A dotted grey line indicates the region below which the hard-sphere like criteria using $B_2$ and $\Pi$ are expected to fail. (b) Same as full lines in (a), but now we allow negative ions to adsorb, tuned by the equilibrium constant $K_-$. Notice that the full blue line is the same as in (a), yet here we use dotted lines for the FCC-BCC transitions for clarity. We use the same color coding as in Fig. 2.1.

## 2.4 Phase diagrams

To get a better idea of the reliability of the various crystallization criteria for colloidal particles that are subjected to charge regulation, we will compare them first for the case when only positive ions can adsorb ($K_- \to \infty$). In Fig. 2.2(a), we plot a few phase boundaries in the $(\eta, \kappa a)$ representation for a variety of crystallization criteria for $a/\lambda_B = 100$ and $K_+ a^3 = 1$, featuring FCC, BCC and fluid phases. Note that only $\eta < 0.5$ is shown. For these system parameters, we see that the BCC only appears in a finite "pocket" of in intermediate packing fractions $10^{-3} \lesssim \eta \lesssim 10^{-1}$ and $10^{-1} \lesssim \kappa a \lesssim 1$. The fluid-BCC line and the fluid-FCC line at $\kappa a \gtrsim 1$, as predicted by the Lindemann criterion Eq. (2.9), are very close to the slightly more accurate simulation-based criterion of Eq. (2.11) for all $\kappa a$. Notice furthermore that the FCC-BCC line is connected only to the fluid-crystal line of Eq. (2.11). Finally, as was mentioned in the previous section, the Lindemann criterion Eq. (2.9) is indeed equivalent to the OCP criterion of Eq. (2.8): we found that they essentially overlap within the numerical accuracy, and hence we have drawn them as a single line.

The good predictive power of the OCP-like criteria of Eqs. (2.8) and (2.9) does not come as a surprise for the regime of $\kappa a < 1$, where the screening length is large

compared to the particle size. However, the good quality of the OCP criterion of Eq. (2.8) at $\kappa a > 1$ and even at $\kappa a > 10$ is quite striking. Likewise, it should not come as a surprise that the hard-sphere freezing criteria based on $B_2\rho > 2$ of the DLVO potential and the osmotic pressure $\Pi > 13k_BT\rho$ of the cell model perform well at $\kappa a > 10$ and reasonably well at $\kappa a \approx 1$. However, at $\kappa a < 1$ they deviate substantially and are, therefore, not capable of predicting the empirical OCP-type criteria in this weak screening regime. In particular, the hard-sphere like criteria cannot capture the "back-bending" of the crystallization line to high $\eta$ at $\kappa a \lesssim 10^{-1}$, which is caused by the discharging of the particles at low salt concentrations, such that repulsions weaken and melting occurs [53, 54]. The hard-sphere like criteria actually do show this bending-back phenomenon far below the scale of Fig. 2.2(a). The "up-bending" of the crystallization line to high $\eta$ at $\kappa a \gtrsim 10^{-1}$ is due to the reduced repulsions which comes from the enhanced screening of the (increasing) colloidal charge. The resulting shape of the crystallization line of Fig. 2.2(a) describes a fluid-BCC-fluid or fluid-BCC-FCC-fluid phase sequence upon increasing $\kappa a$ at fixed $\eta \in (10^{-3}, 10^{-1})$, a reentrant melting that was also found in the constant-potential calculations of Ref. [53] and in the experiments and calculations of Ref. [54]. However, particles described by the adsorption isotherm Eq. (2.3) cannot account for the reentrant melting that was observed in Ref. [49] upon increasing the colloid density. Below we will show that an extension of the existing theories to include adsorption of a second ionic species does give rise to such a density-induced reentrant melting phenomenon.

On the basis of the superior performance of the OCP-based rather than the hard-sphere based crystallization criteria, we will now only consider the criteria of Eqs. (2.11) and (2.12), which includes input from Eq. (2.7). We focus on the effect of anionic and cationic adsorption by setting $K_+a^3 = 1$ as before, together with setting a finite equilibrium constant $K_-$ (rather than the $K_- \to \infty$ limit which prevents anionic adsorption).

In Fig. 2.2(b) we show a set of phase diagrams, again in the $(\eta, \kappa a)$-representation, for a variety of $K_-$, showing fluid, BCC, and FCC states as expected. However, the crystallization lines at finite $K_-$ all exhibit a regime of $\kappa a$ where the phase sequence fluid-BCC-fluid appears upon increasing $\eta$. This density-induced reentrant melting is absent in the line for $K_- \to \infty$, which is the lowest-lying curve in Fig. 2.2(b). In other words, the feature of a reentrant fluid with increasing colloid concentration depends crucially on the existence of multiple charging mechanisms. Finally, we remark that for results with a non-zero $K_-^{-1}$, the crystallization boundary at $\eta = 0.5$ is not correctly predicted because point particles do not exhibit hard-sphere crystallization.

We now try to rationalize the occurrence of a reentrant fluid as function of $\rho$. For this we investigate the OCP criterion, since it approximates the freezing lines of the Yukawa result (Eq. (2.11)) accurately and it has the added advantage of providing a physical mechanism. In order to get a reentrant fluid, $\Gamma_{\mathrm{OCP}}$ must be non-monotonous as function of density. For this we calculate

$$\frac{\partial \Gamma_{\mathrm{OCP}}}{\partial \rho} = \Gamma_{\mathrm{OCP}} \left( \frac{1}{3} Z_{\mathrm{OCP}} \rho^{-1} + 2\frac{\partial Z_{\mathrm{OCP}}}{\partial \rho} \right), \qquad (2.13)$$
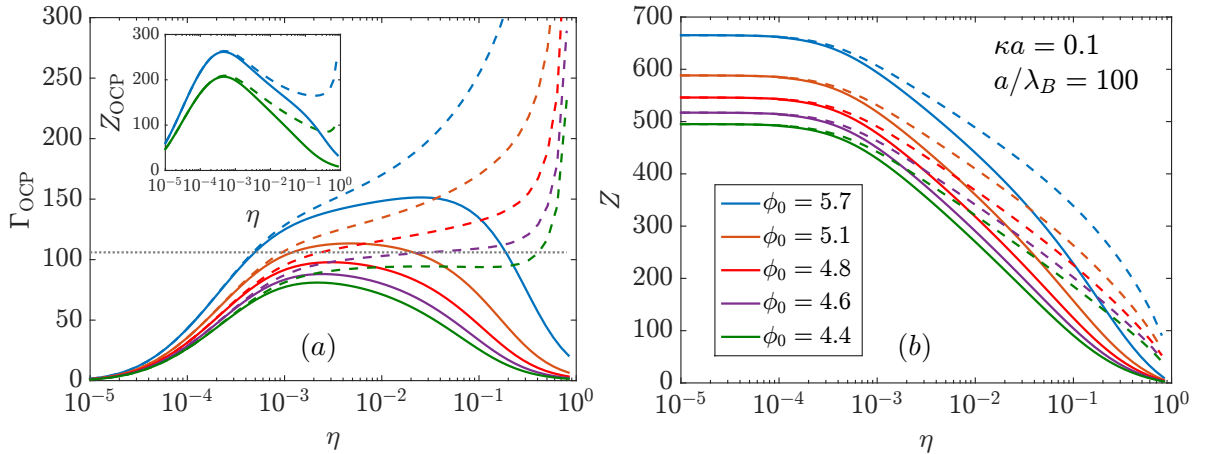
**Figure 2.3:** (a) The OCP coupling parameter $\Gamma_{\text{OCP}}$ (see Eq. (2.8)) as function of packing fraction $\eta$ for a charging mechanism $S + P^+ \leftrightarrows SP^+$ with equilibrium constant $K_+ = [S][P^+]/[SP^+]$ (dashed lines), compared to a constant-potential system (full lines) with a chosen surface potential such that $Z$ (shown in (b)) coincides in the dilute limit. Observe that only for constant-potential particles $\Gamma_{\text{OCP}}$ can intersect the dotted grey line $\Gamma_{\text{OCP}} = 106$ twice, showing that these systems exhibit reentrant melting as function of $\eta$. This is because constant-potential particles have the strongest tendency to decrease $Z_{\text{OCP}}$ for $\eta \gtrsim 10^{-3}$, as can be seen in the inset of (a) where $Z_{\text{OCP}}$ as function of $\eta$ is shown for the highest and lowest surface potential. This decrease in $Z_{\text{OCP}}$ occurs because constant-potential particles have a larger tendency to discharge, which is shown in (b) where we plot $Z$ as function of $\eta$.

and investigate its sign. The first term in Eq. (2.13) is always positive. In the dilute limit the first term dominates in Eq. (2.13), hence $\Gamma_{\text{OCP}}$ increases with $\rho$. Compressing the system tends to reduce the mutual repulsions, the particles discharge and this reduces $Z_{\text{OCP}}$. This effect is not strong enough to drive $\partial_\rho \Gamma_{\text{OCP}} < 0$ for particles that acquire their charge through adsorption of only a single ion species. However, $Z_{\text{OCP}}$ has a much stronger tendency to decrease for $\eta \gtrsim 10^{-3}$ if the particles have significant adsorption affinities for *both* cations and anions, and therefore have a fairly constant surface potential. This is illustrated in Fig. 2.3(a), where $\Gamma_{\text{OCP}}$ is shown (with $Z_{\text{OCP}}$ in the inset) as function of $\eta$ for particles on which only positive ions can adsorb, and we compare these quantities with constant-potential particles. Indeed, we see that $\Gamma_{\text{OCP}}$ can intersect the line $\Gamma_{\text{OCP}} = 106$ twice as function of $\eta$ for constant-potential particles. This can be rationalized from the fact that these type of particles have a larger tendency to discharge for $\eta \gtrsim 10^{-3}$ as is shown in Fig. 2.3(b), which reveals $Z$ as function of $\eta$ for constant-potential particles and for particles that acquire their charge by cationic adsorption. We conclude that for constant-potential particles the second term in Eq. (2.13) can become sufficiently negative for a reentrant fluid to occur.

## 2.5 Comparison with experiments

To verify our approach towards reentrant melting in suspensions of charged colloids, we compare our results with experiments on poly(methyl methacrylate) spheres ($a =$

1 $\mu$m) in a solvent mixture of 20% cis-decaline and 80% cyclohexylbromide where a hitherto unexplained reentrant fluid was observed upon varying $\rho$, see Ref. [49, 56]. We use a Bjerrum length that is close to the experimental value $a/\lambda_B = 125$ and vary the values of $\kappa a$ and $K_\pm a^3$ until good agreement with the experimental phase boundaries was obtained. It should be noted that in the parameter regime where we found a good fit, the last term in the denominator of Eq. (2.2) is small compared to the other terms in the denominator. This effectively means that we can only determine the ratio of $K_+/K_-$ rather than their individual values. Moreover, notice that Eq. (2.2) is independent of $\rho_s$ in this limit if $\phi_0$ is taken as an input parameter. This means that the calculated fluid-crystal boundary can also be explained by a constant-potential system for all salt concentrations. The experimentally obtained fluid-BCC phase boundary at $\eta = 0.0415$ and that of the BCC-reentrant fluid phase at $\eta = 0.1165$ are represented by the dashed vertical lines in Fig. 2.4(a) and (b). The full vertical lines represent the corresponding phase boundary as predicted from our theory, using $\kappa a = 0.6$ and $K_-/K_+ = 51$ as fit parameters, for which the dimensionless zeta potential reads $\phi_0 = 1.96$. Given that our theory is capable of predicting a reentrant fluid phase, it should not come as a surprise that we can fit the two experimentally observed phase boundaries in terms of these two fit parameters rather accurately.

Interestingly, however, the structure of various state points in both fluid phases and the BCC phase was also investigated in Ref. [49] by means of simulations of a system with a pairwise DLVO potential of the form of Eq. (2.5). The contact potential $U_{\mathrm{DLVO}}(2a) \equiv \epsilon_c$ and the effective screening length $\bar{\kappa}^{-1}$ were obtained from fits to the experimentally observed radial distribution function, and are represented by the open symbols in Fig. 2.4(a) and (b), respectively, where the error bars stem from Ref. [49]. The parameters $\epsilon_c$ and $\bar{\kappa}a$ for the crystal are shown as filled symbols, and were obtained from estimations by using the Yukawa phase diagram. The full curves in Fig. 2.4 (a) and (b) represent our prediction of $\bar{\kappa}^{-1}$ and $\epsilon_c$, given within our calculation by $\epsilon_c = U_Y(2a)$, with the fit parameters obtained from the phase boundaries as discussed above. The agreement is very satisfactory and is an indication that the underlying charging mechanism indeed involves a competing cation and anion process.

Further evidence for the predictive power of the present theory is provided by comparing the experimentally observed fluid-FCC phase boundary of the very same system but at a much higher salt concentration, as presented in Ref. [55]. Although no reentrant fluid was found here we can check whether $K_-/K_+ = 51$ that was determined for the parameters in Fig. 2.4 is also able to describe this experiment. At large $\kappa$, we have $\bar{\kappa} \approx \kappa$ and for this reason we use for $\kappa a$ the value of $\bar{\kappa}a = 2.5$ as was determined from the simulations in Ref. [55]. In Fig. 2.5 a plot is shown for the state points of the fluid (open symbols) and FCC crystal (filled symbols). For completeness we also add the state points of Fig. 2.4. We find a very good agreement of the fluid-FCC state points with the phase diagram calculated from the cell model with $K_-/K_+ = 51$. In Ref. [55] the radial distribution function $g(r)$ of these state points could be described by Monte-Carlo simulations with a DLVO contact potential of $\beta\epsilon_c = 140$. However, we find a slightly higher contact potential from our cell model calculations, $\beta\epsilon_c \approx 200$.
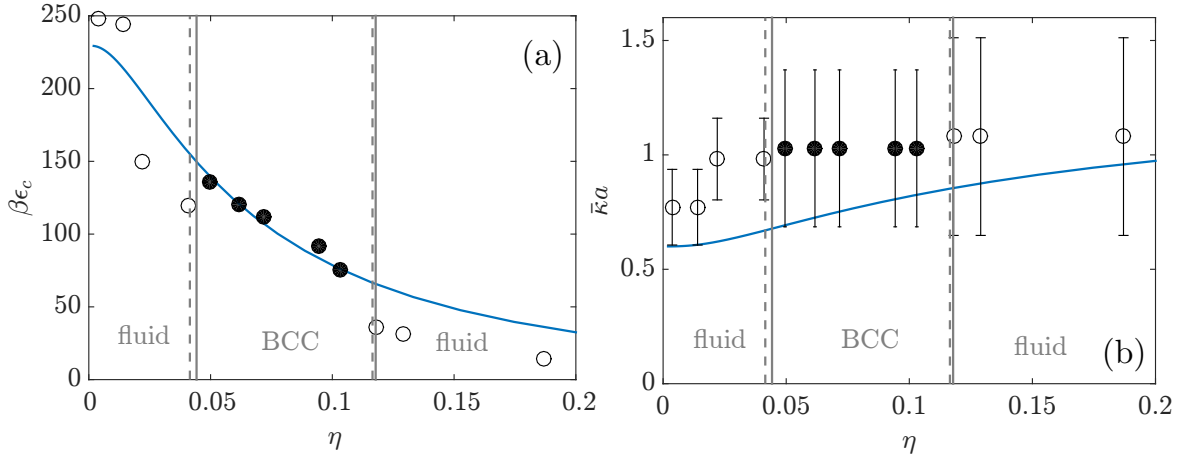
**Figure 2.4:** Comparison of the phase boundaries (fluid-BCC-fluid) and Yukawa parameters from Ref. [49]. The full grey lines are obtained from a cell-model calculation using $\kappa a = 0.6$, $a/\lambda_B = 125$, $K_-/K_+ = 51$ (equivalently $\phi_0 = 1.96$), while the dashed grey lines are from experiments. The equivalent contact value $\epsilon_c$ of the pair interaction potential from the cell model is shown as the full blue line in (a) and we compare them with Monte-Carlo simulations of Ref. [49] using a DLVO potential, shown as the symbols. Open symbols correspond to fluid state points, while filled symbols are BCC state points. A similar comparison is made in (b) for $\bar{\kappa}a$, with error bars calculated from the data provided in Ref. [49]. We remark that the values of $\epsilon_c$ and $\bar{\kappa}$ for the BCC state points in Ref. [49] were estimated using the Yukawa phase diagram and not directly determined from simulation.
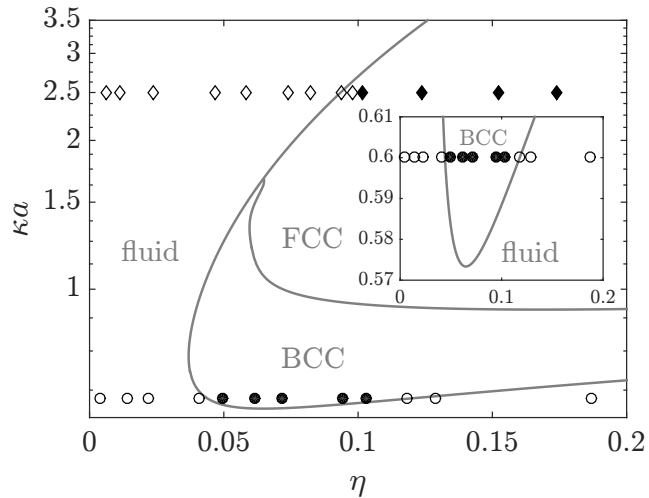


**Figure 2.5:** The phase diagram calculated using the cell model in combination with Eqs. (2.11) and (2.12), where we use the parameters $a/\lambda_B = 125$ and $K_-/K_+ = 51$ (or equivalently $\Delta pK = pK_- - pK_+ = -1.7$) . The experimentally obtained state points of the fluid-FCC transition from Ref. [55] are shown as the open and filled diamonds for the fluid and FCC phase, respectively. The reentrant fluid phase of Ref. [49] are labeled by the open circles, while the BCC state points are shown as filled circles. A zoomed-in version of the phase diagram around these BCC state points are shown in the inset, to emphasize the reentrant nature of the phase transition.

## 2.6 Discussion and conclusions

We investigated various crystallization criteria that are based on hard spheres, the OCP and Yukawa point particles. We have seen that the point-particle criteria are reliable in a large parameter regime, while the considered hard-sphere criteria should only be trusted at high salt concentrations. Moreover, we have seen that adsorption of multiple ion species on the colloidal surface can explain the occurrence of a density-induced reentrant fluid at fixed (reservoir) salt concentration. In contrast, the crystal phase is always reentrant as function of salt concentration for the charge regulation mechanisms that we investigated. We tested this result against the experiments of Refs [49, 55, 56] and found good agreement with the phase boundaries.

There are some caveats, however. In particular, we assume that the density of colloids is varied at a fixed reservoir salt concentration $\rho_s$ and hence a fixed $\kappa a$. In other words, all our calculations are based on the grand-canonical treatment of the salt. However, in experiments the ions are often treated canonically and the salt concentration is expected to change with the density of colloids. In Ref. [56], this effect has been accounted for by defining $\tilde{\kappa}^2 = 8\pi\lambda_B\rho_{\mathrm{ion}}$, where $\rho_{\mathrm{ion}} = Z\rho + 2\tilde{\rho}_s$ and $\tilde{\rho}_s$ the initial salt concentration without colloids. Here the authors interpreted the value of the inverse screening length determined from simulations of DLVO particles as $\tilde{\kappa}$, while this is $\bar{\kappa}$ within our treatment. This latter quantity does depend on colloidal density even if the ions are treated grand canonically. However, since $\bar{\kappa} \neq \tilde{\kappa}$ in general, we should perform our calculations in the canonical ensemble, by fixing the initial salt concentration and changing $\kappa$ accordingly if $\eta$ is varied. Nevertheless, we expect that this will not change the qualitative features of our result and this may only alter the precise values of the $\epsilon_c$ and $\bar{\kappa}$ obtained from the cell model. This means that the density dependent $Z$ and $\kappa$ that was observed in Ref. [49, 56] can still be attributed to an underlying charge regulation mechanism where multiple ions are involved, regardless of this caveat. Finally, we note that there are experimental systems for which the grand-canonical treatment is justified, see for example Ref. [54].

As an outlook we wish to state that our work also suggests that microscopic details of charging mechanisms can possibly be inferred from macroscopic measurements of phase boundaries and/or structural mesoscopic measurements of $g(r)$. The model that we presented here provides a simple of way to investigating these charge regulation effects, which are sometimes underestimated in charged colloidal suspensions.

# Appendix: Relation between constant-potential and binary-adsorption model

In this Appendix we rationalize the constant potential behaviour that was observed in Fig. 2.1(b). Typically, only a small fraction of the surface sites actually contains an ion, i.e. $[\text{SP}^+]$, $[\text{SN}^-] \ll [\text{S}]$, and in this case we may approximate Eq. (2.2) as

$$y = Y_+ \exp(-\phi_0) - Y_- \exp(\phi_0), \tag{2.14}$$

where $y = Z\lambda_B/(\kappa a^2)$ and $Y_\alpha = \kappa a M/(8\pi K_\alpha a^3)$ are the dimensionless charge density and *chargeability* [54] respectively, and we assume the surface to be positively charged, i.e. $Y_+ > Y_-$. The point of zero charge is given by $\bar{\phi}_0 = \log(Y_+/Y_-)/2$. Expanding Eq. (2.14) around this iso-electric point, gives

$$y = -2\sqrt{Y_+ Y_-}[\phi_0(\eta) - \bar{\phi}_0] + \mathcal{O}\{[\phi_0(\eta) - \bar{\phi}_0]^3\}, \tag{2.15}$$

and we also find $|(\phi_0(\eta) - \bar{\phi}_0)| < |y/\sqrt{4Y_+ Y_-}|$, with $\Delta\phi_0 = (\phi_0(\eta) - \bar{\phi}_0)$. We are now interested in the maximal deviation $\Delta\phi_0 = \phi_0(\eta \downarrow 0) - \bar{\phi}_0$. To estimate it, we use the Gouy-Chapman relation and use it for our colloids. In this case, $y = 2\sinh(\phi_0/2)$. This relation underestimates the charge at infinite dilution that comes from the cell model, but it is still a good estimate. This results in

$$y < 2\sinh(\bar{\phi}_0/2) < (Y_+/Y_-)^{1/4} - (Y_-/Y_+)^{1/4}, \tag{2.16}$$

and thus $|\Delta\phi_0| < \frac{1}{2}\left(Y_-^3 Y_+\right)^{-1/4} < 1/(2Y_-)$, showing that significant chargeabilities for *both* the dominant (+) as well as the competing (-) charge mechanism will lead to constant-potential like behaviour. For the light blue curves in Fig. 2.1(b) we have $|\Delta\phi_0| = 0.07$, while the estimate in Eq. (2.16) gives $|\Delta\phi_0| = 0.13$. The red curve has $|\Delta\phi_0| = 0.001$, while Eq. (2.16) gives $|\Delta\phi_0| = 0.0001$. The blue curve is not at constant potential anymore, since $|\Delta\phi_0| > 1$, and this is supported by Eq. (2.16) which gives $|\Delta\phi_0| = 10^2$. Indeed the linearization in Eq. (2.15) breaks down, and the system is not described by a constant potential.

# 3

# Demixing in a binary mixture of repulsive charged colloids

*Phase separation in a binary mixture of repulsive charged colloidal spheres is investigated within the binary cell model. This approach allows for the investigation of charge-regulation effects, such as cationic adsorption on the colloidal surface or constant-potential boundary conditions. The repercussions of the spinodal instabilities on sedimentation profiles are discussed within the local-density approximation in the context of the colloidal Brazil nut effect.*

## 3.1 Introduction

Colloidal suspensions are characterized by a large size asymmetry between the basic constituents: the colloids are large compared to the solvent molecules and the ions surrounding it. In such suspensions the solvent is often approximated as a dielectric continuum, and on the mean-field level the ions are coarse-grained and treated on the level of their density profiles, such as in Poisson-Boltzmann (PB) theory. The ions can have large impact on the effective colloid-colloid interactions. It is, for example, known that ionic correlations can induce an attraction between like-charged colloids [77]. Interestingly, an effective attractive contribution to the free energy can also occur on the mean-field level, which can lead to phenomena such as gas-liquid separation. This was theoretically found within linear screening theory [63] where the cohesive energy originates from the so-called volume terms. These are one-body contributions to the many-body effective potential that do depend on the colloid density, but not on the colloidal centre-of-mass coordinates. Interestingly, the gas-liquid separation was absent in the spherical-cell model [66], which automatically includes non-linear screening effects that are absent in linear screening theory, at the expense of losing the multi-centered nature of the colloidal particles. Interestingly, an approach that combined the cell and linear-screening model showed that a gas-liquid separation could

still be possible [78], although to date there is still no strict consensus whether such an instability can really occur in one-component suspensions of charged colloids.

Binary colloidal suspensions are even more complex, since the two species can differ in size and in charge, and this can lead to, for example, the formation of various colloidal analogues of ionic crystals for oppositely charged colloids [36, 79–84]. In contrast, purely repulsive charge-asymmetric mixtures have a tendency to demix. This can be understood if we draw an analogy with the known phase separations in binary hard-sphere systems [85–88], and in charged mixtures of $He^{++}$ and $H^{+}$ in the atmosphere [89]. Such a phase separation is rather unexpected: the repulsions in one of the two phases is always stronger than in the mixed state. Even so, spinodal instabilities were shown to exist in binary Yukawa systems within the hypernetted chain closure to the Ornstein-Zernike equations [90], but only when a non-additivity parameter is introduced. The non-additivity parameter was also needed in computer simulations of charged macroions in the primitive model[1] to fit the simulated effective pair potentials accurately [91], and this approach turned out to be very successful. Based on Ref. [89] for the $He^{++}$ and $H^{+}$ mixture, we can hypothesize that the non-additivity is due to a less efficient charge neutralization in the mixture than in the pure phases. This argument is, however, vague and we are not aware of any microscopic derivation of the non-additivity parameter from first principles. Furthermore, it was shown that a binary mixture of charged colloids within many-body linear screening theory is actually an additive Yukawa system [92], and these contributions to the two-body terms of the free energy should be added to the one-body volume terms. Furthermore, using again the analogy with binary hard spheres, we mention that non-additivity is not required for hard spheres to demix. The demixing for additive hard spheres can be understood from packing arguments: although the repulsions in the pure phase of the large particles are stronger, the packing is more efficient, leading to a high-density crystalline phase of large particles in coexistence with a fluid with predominantly small particles [88]. This lack of a need for non-additivity in binary hard-sphere mixtures is the reason that we are not convinced about the requirement of non-additivity in Yukawa systems for a spinodal instability to occur. However, to show that non-additivity is not needed one needs simulations or theories that go beyond the hypernetted-chain approximation of Ref. [90].

The possibility for phase separation in a mixture of charged colloids is not only investigated theoretically: phase separation is also experimentally observed [93–96]. When charge regulation is included, micro-phase separation can even occur [97], which will be discussed more in depth in the next chapter. Furthermore, understanding the bulk phase behaviour is necessary to understand, for example, sedimentation of binary charged colloids [98–101], for which the precise sedimentation profiles could hint to an underlying phase separation, and is therefore also of relevance in sedimentation experiments.

This motivates us to have a closer look at phase separation in binary suspensions of

---

[1]In the primitive model ions are treated as charged hard spheres, but the solvent is a dielectric continuum.

repulsive charged colloids. Most approaches to these systems [92, 102] are based on effective pair potentials of the Yukawa type. In this chapter we will, however, focus on the phase behaviour of binary mixtures of charge-asymmetric repulsive colloidal particles on the level of Poisson-Boltzmann theory within the cell approximation, which makea it easier to include the effects of charge regulation. We will provide the framework of calculating thermodynamic properties in such a model in Sec. 3.2 and we investigate the possibility for phase separation of charge-asymmetric, but size-symmetric particles in Sec. 3.3. We will conclude this chapter by applying our theory to a binary colloidal suspension in an external gravitational field in Secs. 3.4, and make comparisons with recent experiments [103]. We conclude with suggestions to improve on the LDA result, which can be important close to a binodal or spinodal.

## 3.2 Binary cell model

We consider a binary mixture of charged colloids with radii $a_i$, particle numbers $N_i$ and densities $\rho_i$ for $i = 1, 2$. We describe every fixed configuration of colloids within the spherical-cell approximation [57, 104], where every colloid is situated in a spherical cell with radius $R$, with the cells filling the system volume. Consequently, we may relate the packing fraction $\eta_i$ to the number fraction $x_i = N_i/(N_1 + N_2)$ via $\eta_i = x_i(a_i/R)^3$. Within the spherical-cell approximation, the free energy $F$ per unit volume $V$ is given by

$$\beta f(\rho_1, \rho_2, T, \mu_s) = \sum_{i=1}^{2} \rho_i \{\ln(\rho_i \mathcal{V}_i) - 1 + \min_{\rho_\pm^i, Z_i} \beta \omega_i[\rho_\pm^i, Z_i]\} + \beta f_{\mathrm{HS}}. \quad (3.1)$$

Here $\mathcal{V}_i$ is the colloidal thermal volume and $f_{\mathrm{HS}}$ is an excess free energy describing the hard-sphere repulsions, and as usual $\beta^{-1} = k_B T$ is the thermal energy. The grand potential $\omega_i[\rho_\pm^i, Z_i]$ of a single cell for $i = 1, 2$ is given by

$$\beta \omega_i[\rho_\pm^i, Z_i] =$$
$$\sum_{\alpha=\pm} \int_{a_i < r < R} d\mathbf{r} \rho_\alpha^i(r) \left[\ln \frac{\rho_\alpha^i(r)}{\rho_s} - 1\right] + \frac{1}{2} \int_{a_i < r < R} d\mathbf{r} \, Q_i(r) \phi_i(r) + \beta \omega_{\mathrm{surf},i}(Z_i), \quad (3.2)$$

with $\rho_\pm^i(r)$ the ion density profiles in a cell of type $i$, $eZ_i$ is the total colloidal charge ($e$ being the elementary charge), $Q_i(r) = \rho_+^i(r) - \rho_-^i(r) + (Z_i/4\pi a_i^2)\delta(r - a_i)$ and where $\phi_i(r)/(\beta e)$ is the electrostatic potential for a cell of type $i$. The term $\omega_{\mathrm{surf}}(Z_i)$ encodes for the type of boundary conditions that we impose on the colloidal surface. We will consider constant-charge (CC), constant-potential boundary conditions (CP), and a single cationic adsorption model (CR). The CP case and CR case describe charge-regulating colloids. For all the various cases, we have

$$\beta \omega_{\mathrm{surf},i}(Z_i) = \begin{cases} 0, & (\mathrm{CC}), \\ Z_i \left[\ln Z_i + \ln\left(\frac{K_i}{\rho_s}\right)\right] + (M_i - Z_i)\ln(M_i - Z_i), & (\mathrm{CR}), \\ -Z_i \phi_i(a_i), & (\mathrm{CP}). \end{cases} \quad (3.3)$$

Note that the CP case in Eq. (3.3) is just a Legendre transformation. The CR case describes a lattice gas with $M_i$ surface sites that can become charged via cationic adsorption, $S_i + P^+ \leftrightarrows S_iP^+$, with equilibrium constant $K_i = [S_i][P^+]/[S_iP^+]$. In the remaining we set $M_i/10^7 = 4\pi$ for $i = 1, 2$, which corresponds to 1 surface site per nm$^2$ for a micronsized colloid.

From the Euler-Lagrange equations $\delta\omega_i[\rho_\pm^i, Z_i]/\delta\rho_\pm^i(r) = 0$, we find the Boltzmann distributions $\rho_\pm^i(r) = \rho_s \exp[\mp\phi_i(r)]$. Together with the Poisson equation for $\phi_i(r)$, it results in the Poisson-Boltzmann equation

$$\phi_i''(r) + \frac{2}{r}\phi_i'(r) = \kappa^2 \sinh[\phi_i(r)], \tag{3.4}$$

where $\kappa^{-1} = (8\pi\lambda_B\rho_s)^{-1}$ is the Debye screening length. Henceforth, a prime denotes the derivative with respect to the radial coordinate $r$. We express global charge neutrality by the boundary condition $x\phi_1'(R) + (1-x)\phi_2'(R) = 0$, where $x = x_1$. Notice that in our formulation a single cell is not necessarily charge neutral, however the weighted average of all the cells is, in contrast to the approach in Ref. [105][2]. Moreover, we impose the continuity condition $\phi_1(R) = \phi_2(R) =: \phi_D$, with $\phi_D/(\beta e)$ the Donnan potential. Finally, we have the boundary conditions,

$$\phi_i'(a_i) = \begin{cases} -\dfrac{Z_i\lambda_B}{a_i^2}, & Z_i \text{ given constant,} \quad \text{(CC)}, \\ -\dfrac{M_i\lambda_B}{a_i^2}\left\{1 + \dfrac{K_i}{\rho_s}\exp[\phi_i(a_i)]\right\}^{-1}, & \text{(CR)}, \end{cases} \tag{3.5}$$

$$\phi_i(a_i) = \text{constant}, \quad \text{(CP)}, \tag{3.6}$$

where we derived the CR boundary condition using Eq. (3.3) from $\partial\omega_{\text{surf},i}/\partial Z_i = 0$ and we used Gauss' law applied to the colloidal surface. For the CP case we can find the charge by evaluating $Z_i = -a_i^2\phi'(a_i)/\lambda_B$ when $\phi_i(r)$ is known.

We determine the minimized functional,

$$\min_{\rho_\pm^i, Z_i} \beta\omega_i[\rho_\pm^i, Z_i] = \frac{1}{2}Z_i\phi_i(a_i) + 4\pi\rho_s \int_{a_i}^R dr\, r^2\{\phi_i(r)\sinh\phi_i(r) - 2[\cosh\phi_i(r) - 1]\}$$

$$+ \begin{cases} 0, & \text{(CC)}, \\ -Z_i\phi_i(a_i) - M_i\ln\left\{1 + \dfrac{\rho_s}{K_i}\exp[-\phi_i(a_i)]\right\}, & \text{(CR)}, \\ -Z_i\phi_i(a_i), & \text{(CP)}. \end{cases} \tag{3.7}$$

From the free energy Eq. (3.1) with insertion of Eq. (3.7), we can extract various thermodynamic properties. The osmotic pressure is given by $\Pi = -(\partial F/\partial V)_{N_1,N_2,T,\mu_s}$, which results in

$$\beta\Pi = \rho + \rho_s\left[2(\cosh\phi_D - 1) - \kappa^{-2}\sum_{i=1}^2 x_i|\phi_i'(R)|^2\right] + \beta p_{\text{HS}}, \tag{3.8}$$

---

[2]In our case one does not need to perform a minimization procedure with respect to the cell radii.

with $p_{\text{HS}}$ the excess (hard-sphere) pressure and $\rho = \rho_1 + \rho_2$ the total colloid density. The colloidal chemical potential $\mu_i = (\partial F/\partial N_i)_{N_{i\neq j},T,\mu_s}$ takes some more numerical effort to calculate

$$\beta\mu_i = \ln\eta_i + \frac{\partial}{\partial\eta_i}\sum_{j=1}^{2}\eta_j\beta\omega_j\left(\frac{a_i}{a_j}\right)^3 + \beta\mu_{\text{HS},i}, \qquad (3.9)$$

with $\mu_{\text{HS},i}$ the excess (hard-sphere) chemical potential of species $i$. From Eq. (3.9) we determine the possibility for demixing by calculating the spinodal. The spinodal is given by the condition $\det(\partial\mu_i/\partial\rho_j) = 0$, and the critical point can be determined from Eq. (3.8) by the condition, $\partial\Pi(x_{\text{sp}},\eta_{\text{sp}})/\partial x_{\text{sp}} = 0$, with $(x_{\text{sp}},\eta_{\text{sp}})$ being points situated on the spinodal. Phase coexistence between a phase $\alpha$ and a phase $\beta$ can be calculated from diffusive and mechanical equilibrium,

$$\mu_i\left(\rho_1^{(\alpha)},\rho_2^{(\alpha)}\right) = \mu_i\left(\rho_1^{(\beta)},\rho_2^{(\beta)}\right), \quad (i=1,2), \qquad (3.10)$$

$$\Pi\left(\rho_1^{(\alpha)},\rho_2^{(\alpha)}\right) = \Pi\left(\rho_1^{(\beta)},\rho_2^{(\beta)}\right), \qquad (3.11)$$

respectively. The resulting curve for $i = \alpha,\beta$ given by $\rho_2^{(i)}\left(\rho_1^{(i)}\right)$ in the $\left(\rho_1^{(i)},\rho_2^{(i)}\right)$ plane is called the binodal, but also other representations are possible (such as in the plane of chemical potentials).

An added advantage of the cell model is that we can give a crude estimate whether crystallization can occur. Since we define the cell radius according to the the point for which a Donnan potential can be defined, there is a simple mapping to the OCP, that is given by

$$\Gamma = \frac{1}{16\pi^2}\frac{(\kappa D)^5}{\kappa\lambda_B}\sinh^2\phi_D, \qquad (3.12)$$

where $D^3 = 4\pi R^3/3$ (see Chapter 2). The system crystallizes for $\Gamma > 106$ and this crystallization estimate interpolates between the one-component limits $\eta_1 \to 0$ or $\eta_2 \to 0$ of the suspension.

## 3.3 Spinodal instabilities and crystallization estimates

For simplicity, we will only focus on the phase behaviour of charge-asymmetric colloidal species that have the same colloid radii for all $i$, $a_i = a$. We can therefore use the Carnahan-Starling expression $\beta f_{\text{HS}}/\rho_c = (4\eta - 3\eta^2)/(1-\eta)^2$ for the excess part of the free energy, from which also $\beta p_{\text{HS}}/\rho_c = (1 + \eta + \eta^2 - \eta^3)/(1-\eta)^3$ and $\mu_{\text{HS,i}} = (8\eta - 9\eta^2 + 3\eta^3)/(1-\eta)^3$ for all $i$ follow. In the remainder of the text, we will set $\kappa a = 0.1$ and $a/\lambda_B = 100$, which are typical values for charged colloids in oil with $\epsilon \sim 8$. First, we investigate the effect of a charge asymmetry in the CC case. In Fig. 3.1 we find the spinodals and their critical points for various charge combinations $(Z_1, Z_2)$. Furthermore, we plot the crystallization estimate using $\Gamma > 106$ together with
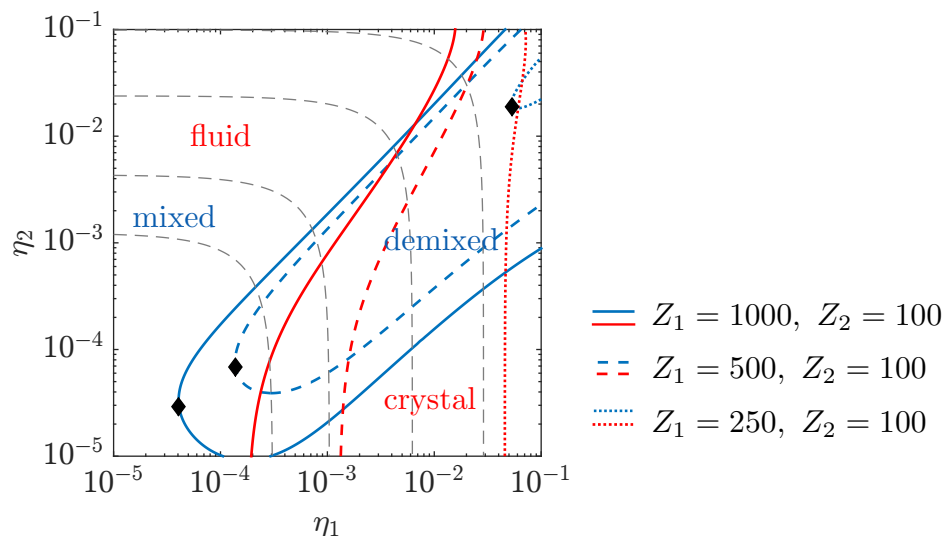
**Figure 3.1:** Phase separation for a binary charge-asymmetric, but size-symmetric, colloidal dispersion of constant-charge particles of radii $a$. The Debye length $\kappa^{-1}$ is given by $\kappa a = 0.1$ and the Bjerrum length $\lambda_B$ by $a/\lambda_B = 100$. A mixture of colloids of type $i$ with charge $Z_i$ and volume fraction $\eta_i$ are shown to demix within the binary cell model, for various charge asymmetries $Z_1/Z_2$ as indicated by the spinodals (blue lines). The black diamonds are the critical points and the grey dashed lines are tie lines for the $Z_1 = 500$, $Z_2 = 100$ case. In red we show a crystallization estimate based on mapping the binary cell model to a one-component plasma, which is accurate for the one-component limits $\eta_1 \to 0$ or $\eta_2 \to 0$.

Eq. (3.12). We clearly see that there is a spinodal for the charge asymmetries $(Z_1, Z_2) = (1000, 100)$, $(500, 100)$ and $(250, 100)$, and the extend of the demixing region is reduced when this asymmetry between $Z_1$ and $Z_2$ is larger. Interestingly, the formation of a pure 1-phase is within our theory always associated with crystallization, as was also found in experiment [96]. Indeed, this supports the analogy with phase separation in binary-hard sphere systems, where the better packing of particles in the pure phases is preferred over a reduced repulsion in the mixed phase [88]. The demixing occurs in a large region of the $(\eta_1, \eta_2)$ plane due to the long-ranged screening of the interactions, since $\kappa a = 0.1$. This is different from the experiments of Ref. [96], which have been performed in water and are thus systems with a much smaller screening length.

Surprisingly, these findings are based on a theory that is constructed for fluids. So strictly speaking, the spinodal instability within the cell model results is a fluid-fluid demixing. The spherical-cell approximation cannot predict crystallization in itself: we need mappings to other theories for that, see Chapter 2. Apparently, the packing in a pure high-charged fluid is still better than the packing in a mixed state, presumably because of the long-ranged interactions involved. Such a situation is different from hard spheres, where the fluid-fluid coexistence turned out to be metastable [87].

In Fig. 3.1, the one-component system of low-charged particles (species 2) did not crystallize, however, if we increase $Z_2$, they can also crystallize. The OCP mapping then interpolates the two crystallization boundaries as can be seen in Fig. 3.2(a). However, since the theory is meant as indication, it is hard to assess how the crystal-

crystal coexistence (if any) will look like in a true system. For this we need more accurate mappings of the cell model to simulation results, but unfortunately, we are not aware of simulation work on repulsive charged particles that relates the crystallization boundaries to the values of the respective effective pair interactions evaluated at the typical interparticle distance (which are known for one-component systems, see Chapter 2).

In Fig. 3.2(a) we also compare the various boundary conditions (CC, CR, and CP), see Eqs. (3.5) and (3.6). For a proper comparison, we choose the parameters such that $Z_1$ and $Z_2$ from the CP and CR calculation match the charges for the CC case $(Z_1, Z_2) = (750, 250)$ in the dilute limit. The resulting charges (CP and CR) are shown in Fig. 3.2(b)-(e) as function of $\eta_1$ and $\eta_2$. We see that the demixed region of the CR case is larger than the CC case. Alhough the charges in the demixed region are lower than that of the CC case due to discharging of the particles, it turns out that the charge asymmetry becomes larger compared to the dilute limit. Along the diagonal $\eta_2 = \eta_1$ in the $(\eta_1, \eta_2)$ plane, we find for $\eta_1 = 10^{-5}$, $10^{-4}$, $10^{-3}$, $10^{-2}$ and $10^{-1}$ that $Z_1/Z_2 = 3$, 3.1, 4, 8.6 and 40, respectively. Larger charge asymmetries are associated with a larger tendency for demixing, as was shown in Fig. 3.1, explaining the larger region for phase separation for the CR case compared with the CC case. Finally, iso-$Z_i$ ($i = 1, 2$) lines seem to coincide with the tie lines (iso-$\Pi$ lines), compare Fig. 3.2(a) with Fig. 3.2(d) and (e). This means that phases in coexistence with each other nearly have the same charges.

For the CP case the line $\det(\partial\mu_i/\partial\eta_j) = 0$ is more extended than the spinodal of the CC and CR cases. There is a demixing region where the tie lines cross the spinodal line, and the larger extent of this region is because of the larger charge asymmetries at these volume fractions than the CR and CC case. There is, however, also a region where the tie lines do not seem the cross the "spinodal", this is clarified in Fig. 3.2(f), where a few iso-$\Pi$ lines are plotted in the $(\eta_1, \eta_2)$ plane. There is a region where these lines bend to higher volume fractions of species 1 *or* 2, and $\Pi$ can become also negative at high $(\eta_1, \eta_2)$. The latter observation is associated with attraction, because species 2 is negatively charged for these thermodynamic state points, while species 1 stays positive, see Fig. 3.2(b)-(c). The bending of the isolines to higher $\eta_1$ or higher $\eta_2$ is associated with a spinodal that bends towards low $\eta_1$ or low $\eta_2$. On the eye, this seems like a gas-liquid separation, but for smaller volume fractions we see that the spinodal is dominated by the ideal gas contributions, $\det(\partial\mu_i/\partial\eta_j) \sim (\eta_i\eta_j)^{-1} > 0$. This ensures that there are no spinodal instabilities in the one-component limits. This is also expected, since the one-component cell model does not predict a gas-liquid separation in charged colloidal suspensions [66].

The large extension of the "spinodal" for the CP case is, however, not well understood. Certainly it has to do with the tendency of species 2 becoming negative and the fact that $Z_1$ increases again for an increasing $\eta_2$ at fixed $\eta_1$, see Fig. 3.2(b). This non-monotonous behaviour of $Z_1$ is easily understood mathematically within the cell model, because increasing $\eta_2$ has two effects. (i) The value of $\phi_D$ is increased, and since the surface potential is fixed, it is easier to reach this asymptotic value at the cell boundary
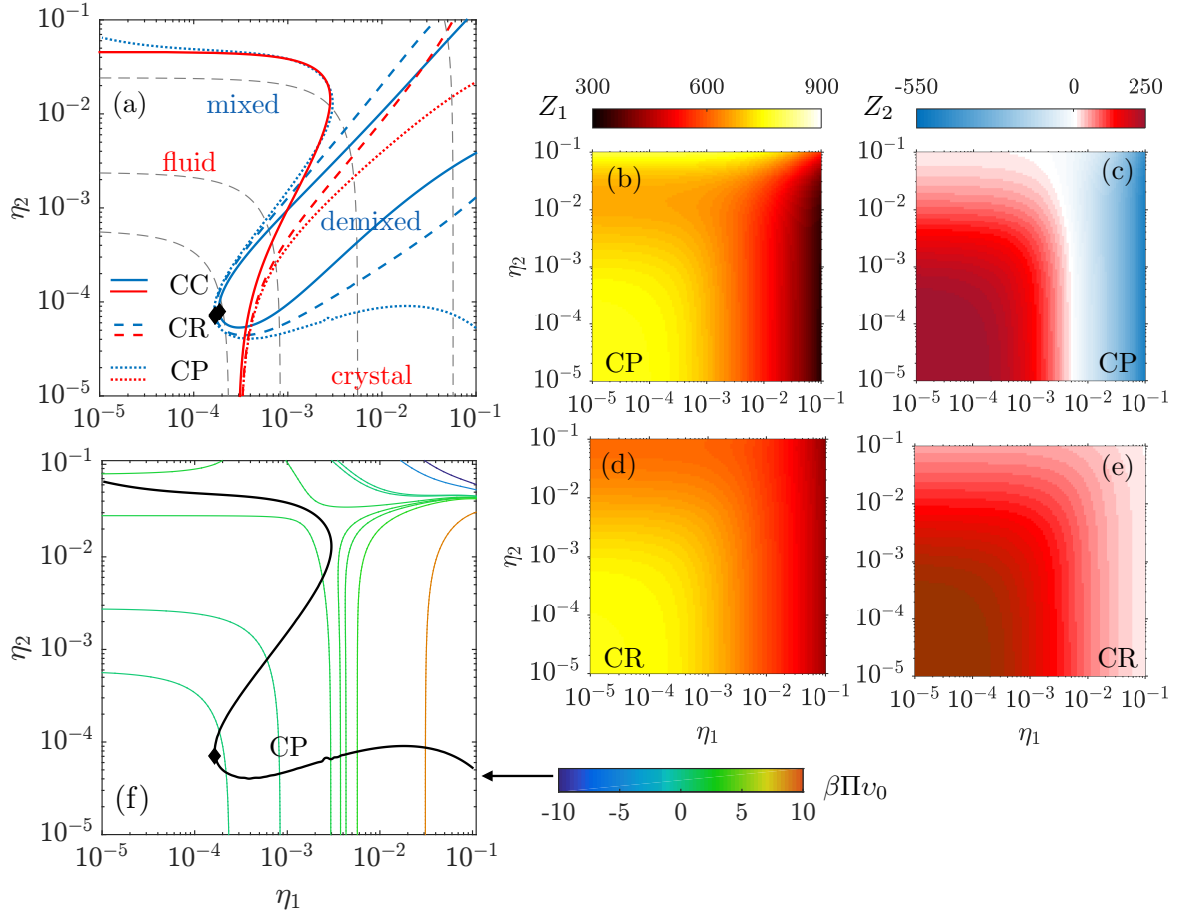
**Figure 3.2:** (a) Phase separation in a binary mixture of charge-asymmetric, but size-symmetric, colloids of species $i = 1, 2$, for constant-charge (CC) particles, a single cationic-adsorption charge-regulation model (CR) and a constant-potential model (CP). All calculations are at $\kappa a = 0.1$, $a/\lambda_B = 100$, with $\kappa^{-1}$ the Debye length and $\lambda_B$ the Bjerrum length. The blue lines are the spinodals, red lines are crystallization estimates, the grey dashed lines are tie lines for the CR case, and the black diamonds are the critical points. In all curves the charges in the dilute limit equal $Z_1 = 750$ and $Z_2 = 250$ (by suitable tuning the surface potentials (CP) or equilibrium constants (CR)), as shown by the colormaps in (b)-(c) for the CP case and in (d)-(e) for the CR case. To understand the "strange" form of the CP spinodal, we also show the constant-osmotic pressure lines for the CP case in (f), which are the same as the tie lines, with $\Pi$ the osmotic pressure and $v_0$ the colloidal volume (which is the same for $i = 1$ and $i = 2$. Note that $\Pi$ can become negative and that it has a non-trivial density dependence in contrast to the CR and CC cases, see the tie lines in (a) and in Fig. 3.1, respectively.

in a cell of type 1. The slope at the colloid is therefore smaller in absolute value and the particle discharges. (ii) Introducing more particles of species 2 decreases $R$, and this results in charging by a similar reasoning to (i). Physically, we can understand these two phenomena by recalling that the constant-potential model is an approximation to a binary adsorption model (see previous chapter). Above reasons (i) and (ii) can then be interpreted physically as, (i) particles discharge to reduce mutual repulsion and (ii) the ions that are desorbed from particle species 2 become available for species 1. These cations can readsorb to particles of species 1 due to mass action. We believe that (a) $Z_2$ becoming negative and (b) the non-monotonous behaviour of $Z_1$ as function of $\eta_1$ and $\eta_2$ are the reasons why $\Pi$ shows the bending behaviour to higher $\eta_i$, a phenomenon that is absent for the CR and CC cases. The resulting instability should therefore not be viewed as demixing, and we speculate that it hints towards a tendency for microphase separation, which was also observed in experiment [97]. This hypothesis will be tested in the next chapter, where we shall indeed see that constant-potential particles can microphase separate in clusters and alternating strings. Finally, our calculations show that the CC case has a larger tendency to crystallize than the CR case, which in turn has a larger tendency to crystallize than the CP case. Indeed, particle discharging can impede crystallization, as we have already seen in the previous chapter.

## 3.4 Sedimentation profiles within the local density approximation

In this section we will investigate how demixing of the bulk reveals itself in sedimentation profiles. In a sedimentation experiment a colloidal suspensions is put in a capillary, and depending on the buoyant mass the particles settle to (i) the bottom if the mass density of the particles is larger than that of the solvent (sedimentation), or (ii) to the top of the capillary when the mass density is lower than that of the solvent (creaming). The sedimentation profiles in these experiments can possibly have non-trivial stackings, even for simple phase diagrams [106]. Charged colloids, in contrast, show also non-trivial behaviour. For example, the density profiles can be more extended than the barometric distribution due to a charge separation between bottom and top of the capillary that results in a macroscopic electric field [107, 108]. Furthermore, sedimentation experiments on charged colloids are interesting because information on the charge regulation mechanism can possibly be inferred from measurements of the colloid-density profile [109].

Theoretically, it has been shown that binary systems of charged colloids can segregate because of the formation of an inhomogeneous macroscopic electric field [99]. The segregation can manifest itself as the colloidal Brazil nut effect: larger particles float on top of smaller particles in the case of sedimentation, or are found beneath the smaller particles in the case of creaming. In other words, their height distribution is opposite to the distribution that one expects based on buoyancy alone. The colloidal Brazil nut effect was experimentally observed for large and small charged polymethylmethacrylate
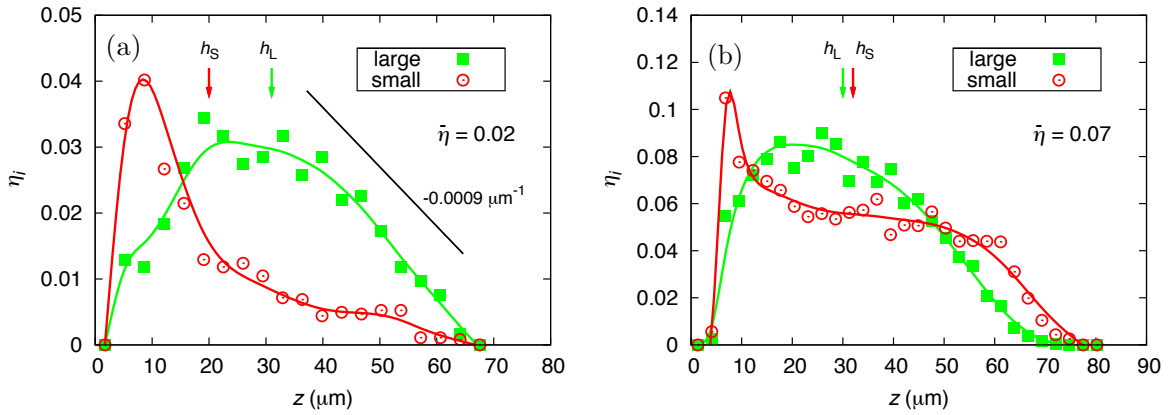
**Figure 3.3:** Experimentally observed sedimentation profiles (taken from Ref. [103]) for large ($L$, radius $a_L = 0.99$ $\mu$m) and small ($S$, radius $a_S = 0.79$ $\mu$m) PMMA particles with gravitational lengths $L_S = 1.39$ $\mu$m and $L_L = 0.71$ $\mu$m, with charge number of the large particles $Z_L \sim 450 - 750$ and for the small particles $Z_S \sim 250$. (a) and (b) differ in overall volume fraction $\bar{\eta}$. The mean height $h_i$ is indicated by arrows, showing that (a) is an example of the colloidal Brazil nut effect, while (b) is on the transition between Brazil nut and non-Brazil nut. The experiments are conducted in CHB with dielectric constant $\epsilon = 7.92$ and Debye screening length $\kappa^{-1} = 6$ $\mu$m.

(PMMA) particles in cyclohexylbromide (CHB) [103], see Fig. 3.3. Interestingly, by tuning the overall colloid density (without changing the type of particles or medium), one can go from a situation where the colloidal Brazil nut effect was observed to a situation where it was absent. As measured from the top of the capillary by the coordinate $z$ (the density of CHB is larger than that of PMMA), the smaller particles where present at low $z$, while the larger particles were present at higher $z$ at low overall density, see Fig. 3.3(a). The mean height of large particles $h_L$ in this particular case is larger than that of small particles $h_S > h_L$, where

$$h_i = \frac{\int_0^\infty dz \, z\eta_i(z)}{\int_0^\infty dz\eta_i(z)}, \quad (i = L, S). \tag{3.13}$$

At larger overall densities, this situation changes: at large $z$ the small particles become again the dominant species, such that $h_S \approx h_L$, see Fig. 3.3(b). We tried to see if these phenomena could be captured using the theory of Ref. [99], but for the experimental parameters we found no numerical solution. This can now be rationalized in light of the previous sections, because at these charges the particles demix. Furthermore, the reentrance of the low-charged particles being the majority species at a given $z$ has not been found for other system parameters where a numerical solution was possible for the theory in Ref. [99].

This motivates us to have a look at the cell model calculations in an external gravitational field. For this we consider an external potential for the colloids, $V_{\text{ext},i}(\mathbf{r})$, with $i = 1, 2$. The free energy of the cell model Eq. (3.1) is treated within a local density approximation (LDA) for the colloids and their charges, followed by a Legendre transform to a grand-canonical (rather than a canonical) description of the colloids. The

corresponding grand potential density functional is

$$\Omega_{\text{LDA}}[\rho_1, \rho_2] = \int d\mathbf{r} \left[ f(\{\rho_j(\mathbf{r})\}_{j=1}^2) + \sum_{i=1}^{2} \rho_i(\mathbf{r})(V_{\text{ext},i}(\mathbf{r}) - \mu_i) \right], \qquad (3.14)$$

where we introduced the colloid chemical potential $\mu_i$. The equilibrium density profiles can now be found by minimizing this functional, which is equivalent to solving the Euler-Lagrange equations for $i = 1, 2$,

$$\mu_i - V_{\text{ext},i}(\mathbf{r}) = \frac{\partial}{\partial \rho_i(\mathbf{r})} f(\{\rho_j(\mathbf{r})\}_{j=1}^2), \qquad (3.15)$$

which follow from $\delta\Omega_{\text{LDA}}[\rho_1, \rho_2]/\delta\rho_i(\mathbf{r}) = 0$. We choose the external potential $\beta V_{\text{ext},i} = z/L_i$, with $L_i = (\beta m_i g)^{-1}$ the gravitational length, $m_i$ the buoyant mass and $g = 9.81$ m$^2$/s the gravitational acceleration. The interpretation of the $z$ direction depends on the buoyant mass: (i) for creaming $z = 0$ corresponds to the top of the capillary, and (ii) for sedimentation $z = 0$ is the bottom of the capillary. Both are captured within our formalism.

In order to include phase separation in the LDA model, we need the binodal, which can be calculated from Eqs. (3.10) and (3.11). The binodal is shown for the $(Z_1, Z_2) = (750, 250)$ CC case in Fig. 3.4(a). The binodal has an asymmetric shape, and this is also observed for charged silica particles in water [96], but with the difference that the more asymmetric side is towards the higher-charged (crystalline) phase, rather than the fluid phase. Currently, we do not understand this qualitative difference. An example of a sedimentation profile as calculated from (3.15) is shown in Fig. 3.4(b) and (c) in the full lines for parameters $L_1 = 0.7a$, $L_2 = 1.4a$ and $(Z_1, Z_2) = (750, 250)$, where we take into account the phase separation. The two plots differ in overall packing fraction. The phase separation manifests itself as a discontinuous jump in the density profiles, and we observe a segregation of particles: particles of type 2 reside dominantly at low $z$, while particles of type 1 reside mainly at large $z$. Since $L_2/L_1 = 2$, it is an example of the colloidal Brazil nut effect: the mean height $h_i$ satisfies $h_2 > h_1$ although $m_2 < m_1$. For $z > 250a$ the system is essentially a one-component system of type 1, and the density decays exponentially with a decay length of $(Z_1 + 1)L_1$ for $\eta_1 > (1/3)(a/\lambda_B)(\kappa a)^2/Z_1 = 4 \cdot 10^{-4}$, which is known from a Donnan equilibrium model [107]. We observe therefore that this scaling is reproduced by the cell model. Furthermore, there should be a crossover to a linear regime and a barometric regime, however, this occurs beyond the scale of the plots of Fig. 3.4(b) and (c), and we also found this within our theory (not shown in figure). For the same initial conditions $\eta_i(z = 0)$ and parameters, we also calculate the sedimentation profile for the $(Z_1, Z_2) = (250, 100)$ (dotted lines in (b) and (c)), where phase separation is not expected at these volume fractions, see Fig. 3.1. We again find the colloidal Brazil nut effect, showing that segregation within the LDA is not necessarily a consequence of an underlying phase separation.

The LDA results, however, show a significant discrepancy with the experiments. Not only the shapes and extent of the sedimentation profiles shapes are not accurately
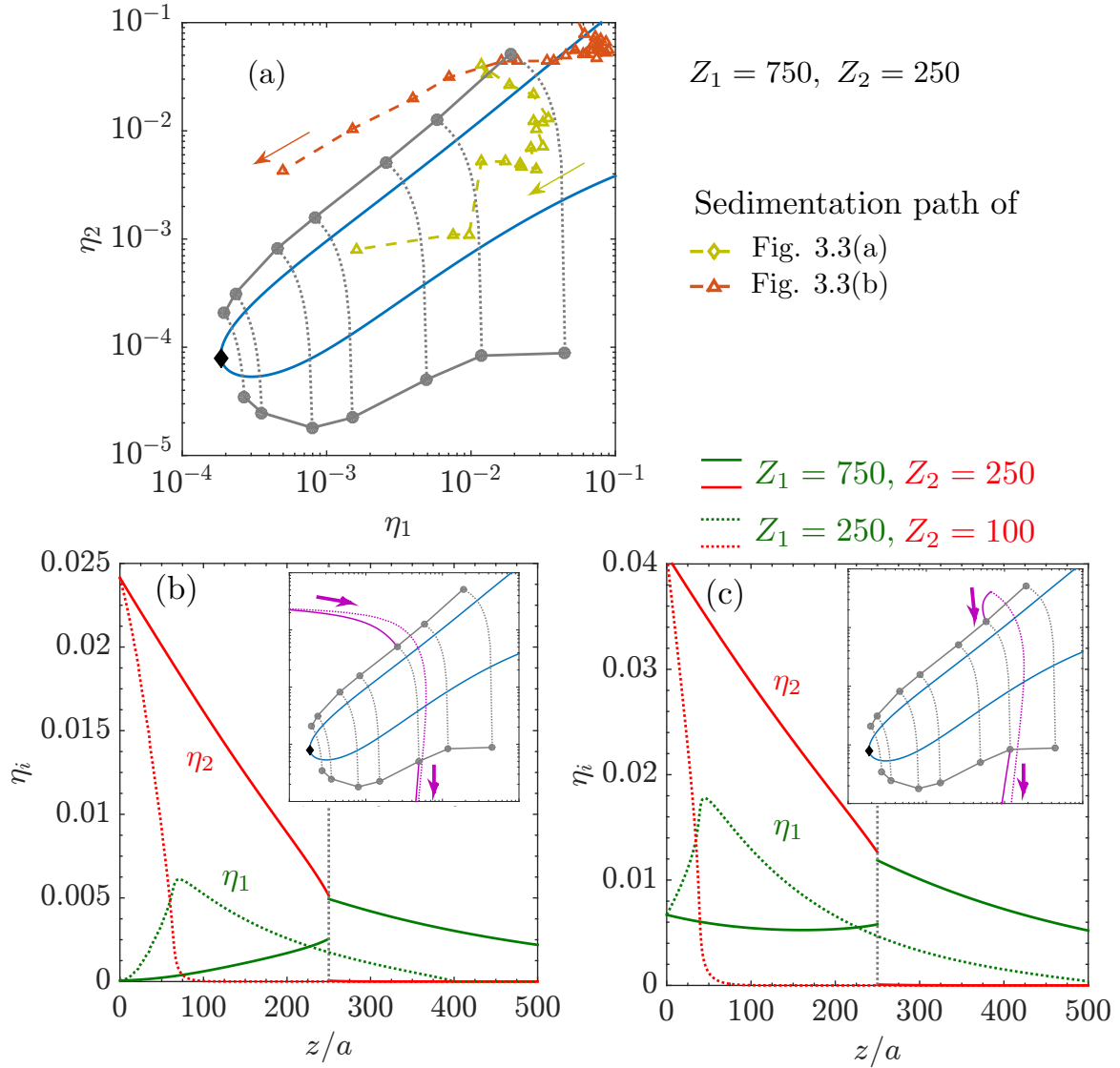
**Figure 3.4:** (a) Same as Fig. 3.2, which shows the spinodal (blue) and the critical point (black diamond) for the CC case where $Z_1 = 750$ and $Z_2 = 250$. For clarity we have not shown the crystallization estimate based on the one-component plasma. Instead we show some of the binodal points (grey circles) and with tie lines (grey dashed). The full grey line is meant to guide the eye. The sedimentation path of Fig. 3.3(a) is shown in (a) in green, and Fig. 3.3(b) is shown in orange. For clarity of presentation, we only include the data for $z > 10~\mu$m. The arrows indicate an increase in height $z$. (b) Sedimentation profiles for gravitational lengths $L_2 = 1.4a$ and $L_1 = 0.7a$ (which means that $i = 1$ is higher charged *and* has a higher buoyant mass than $i = 2$). The dotted grey vertical line is the $z$ for which phase coexistence occurs, which in a local-density approximation results in a discontinuous "jump" in the sedimentation profiles. For the same set of parameters and the same $\eta_{1,2}(z = 0)$ as the full lines, we also plot the sedimentation profiles in the dotted lines for $(Z_1, Z_2) = (250, 100)$, showing that segregation is not necessarily associated with phase separation. The inset shows in purple the sedimentation paths, the dotted ones correspond to $(Z_1, Z_2) = (250, 100)$ and the full lines with $(Z_1, Z_2) = (750, 250)$. In (c) we plot the same graph as in (b), but with a different overall density. The parameters in (b) and (c) are indicative for the system of Fig. 3.3 regarding the charges and buoyant masses.

predicted, but also the observation that the lower charged particles are "reentrant" as the majority species at larger $z$ is not reproduced for suspensions at a larger overall volume fraction, compare Figs. 3.4(a) and (b). Including charge regulation cannot amend this problem (at least within the LDA), since the demixing regions are similar to the the CC case. We note that the comparisons with the CP case should only be made in the region where there is a well-defined demixing, which can be seen from the shape of the iso-$\Pi$ lines, as was discussed in the previous section.

We reveal the poor performance of the LDA result to explain the experiments of Fig. 3.3 by plotting and comparing the experimental sedimentation paths with the calculated one for $(Z_1, Z_2) = (750, 250)$ in Fig. 3.4(a). We observe a "back-bending" phenomenon in the $(\eta_1, \eta_2)$ plane that extends within the spinodal, which is absent in the LDA result (see insets in Fig. 3.4(b) and (c)). Note that we did not use the exact experimental parameters, which means that the spinodal can be shifted if we would use the exact experimental values for $a_2/a_1$, $\kappa^{-1}$ and $\lambda_B$. However, this would not solve the discrepancy between theory and experiment, since we did not see a large sensitivity of the sedimentation profiles to these parameters. We conclude that the experimentally measured sedimentation profiles cannot be explained on the LDA level. Finally, we note that charge regulation seems to be unimportant within LDA, because sedimentation paths approximately coincide with iso-$Z_i$ lines ($i = 1, 2$), compare Figs. 3.2(b)-(e) with Fig. 3.2(a). Comparison of the experimentally measured sedimentation paths in Fig. 3.4(a) with Figs. 3.2(b)-(e), however, suggests that charge regulation can be important for the experimentally measured profiles.

Based on these discussions, we hypothesize that the LDA breaks down close to a spinodal instability: an interface between the two demixed phases can develop with a correlation length that is between that of the hard-core diameter and the Debye screening length. In the latter case, it is clear why the LDA breaks down, and we therefore suggest to go beyond a local description to describe the experimentally observed sedimentation profiles. However, we have confidence that the LDA is accurate when no demixing occurs, an assertion that is based on successful comparisons of calculated sedimentation profiles within the LDA with experiments of one-component colloidal dispersions [108, 109].

## 3.5 Suggestions on improving the LDA result

In this section we sketch how we can go beyond the LDA for a binary mixture of charge-asymmetric repulsive colloids, and we discuss if the various possibilities are worth investigating. To improve on the LDA result, we consider first the square-gradient approximation, given by the grand potential functional

$$\Omega_{\text{sq}}[\rho_1, \rho_2] = \mathcal{F}_{\text{sq}}[\rho_1, \rho_2] + \sum_{i=1}^{2} \int d\mathbf{r} \rho_i(\mathbf{r})[V_{\text{ext},i}(\mathbf{r}) - \mu_i], \tag{3.16}$$

where the instrinsic Helmholtz free energy functional reads

$$\mathcal{F}_{\text{sq}}[\rho_1, \rho_2] = \int d\mathbf{r} \left[ f(\{\rho_j(\mathbf{r})\}_{j=1}^2) + \sum_{i=1}^2 f_2^{ii}(\{\rho_j(\mathbf{r})\}_{j=1}^2) |\nabla \rho_i(\mathbf{r})|^2 \right]. \qquad (3.17)$$

For demonstration purposes we neglected any coupling of gradients between two different colloid species. Clearly, square-gradient theory goes beyond a local description of the colloids. An expression for the density-dependent square-gradient coefficients $f_2^{ii}$ can be derived by matching the square-gradient theory to linear response theory of small density fluctuations [20], to find

$$\beta f_2^{ii}(\rho_1, \rho_2) = \frac{1}{12} \int d\mathbf{r} \ r^2 c_{ii}^{(2)}(r; \rho_1, \rho_2), \qquad (3.18)$$

for $i = 1, 2$. Here we introduced the direct correlation functions of the uniform fluid $c_{ij}^{(2)}(r; \rho_1, \rho_2)$. It is meaningful to estimate the coefficients $f_2^{ii}(\rho_1, \rho_2)$ because they are a measure for the correlation length for the interface between two demixed phases. We do this by using the binary hard-core Yukawa fluid in the low-density limit. In this case the direct correlation function equals the Mayer function

$$c_{ij}^{(2)}(r; \rho_1, \rho_2) = \exp[-\beta \phi_Y^{ij}(r)] - 1, \qquad (3.19)$$

with pair interaction for a hard-core Yukawa fluid $\phi_Y^{ij}(r)$. Clearly, using Eq. (3.24) in Eq. (3.18) shows that the square-gradient coefficients of a hard-core repulsive Yukawa fluid are negative, and therefore, the square-gradient expansion for such a system is ill defined. Attractions are needed for a well-defined gradient expansion and one could argue that these can be provided by the volume terms known from linear screening theory. However, these terms will give contributions to the direct correlation function multiplied by a Dirac delta function $\delta(r)$, because of their one-body nature. Volume terms will therefore not contribute to Eq. (3.18), showing that the square-gradient theory is also ill defined for the cell model, even when we include corrections from linear screening theory.

In contrast to the cell model, a non-local extension of the linear screening model is, however, more straightforward. Without specifying the precise form of the bulk free energy per unit volume $f_{\text{lin}}$ of the many-body linear screening result, we can write the decomposition [92]

$$f_{\text{lin}}(\rho_1, \rho_2) = w_1(\rho_1, \rho_2) + w_2(\rho_1, \rho_2), \qquad (3.20)$$

where $w_1$ are the volume terms and $w_2$ is a two-body term that consists of the classical trace over the pair potential of a binary hard-core Yukawa fluid. If we use the local density approximation for $w_1$ and the random-phase approximation (RPA) for $w_2$, we find the excess Helmholtz free energy functional

$$\mathcal{F}_{\text{ex}}[\rho_1, \rho_2] = \int d\mathbf{r} \ w_1(\rho_1(\mathbf{r}), \rho_2(\mathbf{r})) + \frac{1}{2} \sum_{i,j} \int d\mathbf{r} \int d\mathbf{r}' \rho_i(\mathbf{r}) \rho_j(\mathbf{r}') \phi_Y^{ij}(\mathbf{r} - \mathbf{r}'). \quad (3.21)$$

The RPA is a standard approximation for long-range pair potentials, however, there is one drawback: within many-body linear screening theory the Yukawa parameters also depend on density [92], and therefore, there is an ambiguity in the interpretation of the second term in (3.21). Moreover, if we evaluate the direct correlation function by functional differentiation of the functional (3.21) with respect to the colloid density profiles,

$$c_{ij}^{(2)}(\mathbf{r} - \mathbf{r}') = -\beta \frac{\delta^2 \mathcal{F}_{\text{ex}}[\rho_1, \rho_2]}{\delta\rho_i(\mathbf{r})\delta\rho_j(\mathbf{r}')}, \tag{3.22}$$

we find that it will not have the correct asymptotic behaviour $c_{ij}^{(2)}(r) \sim -\beta\phi_Y^{ij}(r)$, which can be understood from the non-trivial density dependence of the Yukawa parameters in $\phi_Y^{ij}(r)$. These problems are circumvented if we instead use a density expansion around a reference bulk fluid with bulk densities $\rho_1^b$, $\rho_2^b$ and grand potential $\Omega_b$. Such a procedure is standard in classical DFT [20], and we find

$$\Omega[\rho_1, \rho_2] = \Omega_b + \sum_{i=1}^{2} \int d\mathbf{r} \, V_{\text{ext},i}(\mathbf{r})\rho_i(\mathbf{r}) + \beta^{-1} \sum_{i=1}^{2} \int d\mathbf{r} \left[ \rho_i(\mathbf{r}) \ln \frac{\rho_i(\mathbf{r})}{\rho_i^b} - \rho_i(\mathbf{r}) + \rho_i^b \right]$$
$$- (2\beta)^{-1} \sum_{i,j} \int d\mathbf{r} \int d\mathbf{r}' c_{ij}^{(2)}(\mathbf{r} - \mathbf{r}'; \rho_1^b, \rho_2^b) \left[ \rho_i(\mathbf{r}) - \rho_i^b \right] \left[ \rho_j(\mathbf{r}') - \rho_j^b \right], \tag{3.23}$$

The functional (3.23) turns out to be successful in the description of interfacial and wetting properties of a binary non-additive point Yukawa fluid close to a hard wall, with state points in the vicinity of a fluid-fluid binodal [110]. Now there are no problems with the density dependence of $\phi_Y^{ij}(r)$ in Eq. (3.23), because $c_{ij}^{(2)}(r)$ is evaluated at a bulk reference density. An example of a simple closure for the direct correlation functions is

$$c_{ij}^{(2)}(\mathbf{r} - \mathbf{r}'; \rho_1^b, \rho_2^b) = \frac{\partial^2 \beta w_1(\rho_1^b, \rho_2^b)}{\partial \rho_i^b \partial \rho_j^b} \delta(\mathbf{r} - \mathbf{r}') - \beta\phi_Y^{ij}(\mathbf{r} - \mathbf{r}'; \rho_1^b, \rho_2^b). \tag{3.24}$$

With the closure of Eq. (3.24), the Euler-Lagrange equations read for $i = 1, 2$

$$\rho_i(\mathbf{r}) = \rho_i^b \exp\left\{ -\beta V_{\text{ext},i}(\mathbf{r}) + \sum_{j=1}^{2} \int d\mathbf{r}' c_{ij}^{(2)}(\mathbf{r} - \mathbf{r}'; \rho_1^b, \rho_2^b)[\rho_j(\mathbf{r}') - \rho_j^b] \right\}. \tag{3.25}$$

The reference bulk densities can be found by fixing the overall densities $\bar{\rho}_i$, which equal $\bar{\rho}_i = (1/V) \int d\mathbf{r}\rho_i(\mathbf{r})$. Clearly, the exponent in Eq. (3.25) has a non-trivial density dependence, since its sign not only depends on the sign of Eq. (3.24), but also on the sign of the local-density deviation from the uniform bulk reference densities. Since the transition between a Brazil-nut and non-Brazil nut effect depends crucially on the overall density in the capillary, we believe that Eq. (3.25) is an interesting route to take. Furthermore, the functional (3.23) contains microscopic information of the bulk phase behaviour, because the volume and many-body corrected additive Yukawa terms are used to construct $c_{ij}^{(2)}(r)$. Indeed, Eq. (3.25) is a well-defined non-local extension

beyond the LDA in contrast to the square-gradient expansion. Finally, we note that it is also engaging to make comparisons with non-additive point Yukawa systems, for which a simple RPA closure of the type (3.21) (without the volume term) would suffice. The parameters (the charges and screening length) in such a model are easily corrected for non-linear and many-body effects via the extrapolated point charge method [67] or charge-renormalization methods [58] discussed in Chapter 2, but then applied to the binary cell model.

## 3.6  Conclusions and outlook

We have shown within a binary cell model that phase separation occurs for repulsive charge-asymmetric colloids. The region of phase separation is larger when charge regulation is included, although the spinodal is not well-defined for all volume fractions in the case of constant-potential particles. In the LDA we have seen that phase separation in sedimentation profiles results in a density jump, and we have also seen that segregation of the colloidal species in sedimentation-diffusion equilibrium ("layering") is possible without demixing in the bulk. The LDA, however, cannot explain recent experiments, probably due to an underlying correlation length that is on the order of $\kappa^{-1}$. Therefore, the LDA breaks down if phase separation occurs. We proposed two non-local theories beyond the LDA, by (i) using a density expansion together with linear screening theory, or (ii) using a non-additive hard-core Yukawa model within the RPA corrected by the binary cell model to include many-body, non-linear and, possibly, also charge-regulation effects. For these two routes, it is important to first compare the bulk phase diagram of linear screening theory and the non-additive Yukawa model with the binary cell model to draw meaningful conclusions. This is left for future work.

# 4

# Alternating strings and clusters in suspensions of charged colloids

*We report the formation of alternating strings and clusters in a binary suspension of repulsive charged colloids with double layers larger than the particle size. Within a binary cell model we include many-body and charge-regulation effects under the assumption of a constant surface potential, and consider their repercussions on the two-particle interaction potential. We find that the formation of induced dipoles close to a charge-reversed state may explain the formation of these structures. Finally, we will touch upon the formation of dumbbells and small clusters in a one-component system, where the effective electrostatic interaction is always repulsive.*

## 4.1 Introduction

A common theme in soft condensed matter physics and biological physics is the formation of large ordered structures from smaller building blocks [111, 112] that are sometimes analogs of ordered phases in (hard) condensed matter. These structures can be macroscopic in size, such as bulk (liquid) crystals [26, 113], plastic crystals [114, 115], quasicrystals [116, 117] and ferrofluids [118], but also mescoscopic structures are found, such as the double-stranded helix in DNA molecules [119], the secondary (and ternary) structures in proteins [120], micelles and membranes [111], and periodic structures in block copolymers [121]. In this chapter, we will show that like-charged colloidal spheres can form also mesoscopic structures, such as alternating strings and clusters, which we will investigate both in experiment and in theory.

In general, charged colloidal particles are interesting due to their highly tunable effective interactions [43, 122]. For example, their charge is often highly adaptable since its microscopic origin is due to the ionic adsorption on or desorption from the colloidal surface, a phenomenon called charge regulation [51], and there are many possibilities for tuning the dielectric and screening properties of the surrounding medium [123]. Not

only energetic effects (Coulomb interactions) are thus important, but also the entropic effects of the (adsorbed and bulk) ions, which can be taken into account by integrating them out of the partition sum [64, 78, 124–127]. For low electrostatic potentials, the resulting effective interaction between pairs of colloids is of the Yukawa type, and the strength and range can be tuned by varying temperature, the salt concentration and density of particles. Taken together with the attractive van der Waals force, which can be significantly reduced by matching the dielectric constants of the particles and solvent in the visible range of frequencies [128], the effective pair potential is known as the Derjaguin-Landau-Verwey-Overbeek (DLVO) potential [60, 61].

Just adding an additional colloidal species can already induce local ordered structures in charged colloidal systems, as was shown in Ref. [97] for a binary system of positively charged sub-micron polystyrene and silica spheres. These particles could become negatively charged, however, as a function of surfactant concentration due to charge regulation, but the exact concentration for which this occurs is different for the two species. Hence, clusters were observed when only one of the two species became negatively charged, since opposite charges attract.

If the charge itself is inhomogeneously distributed on the particle surface, it can be shown that the effective interaction can be decomposed in multipoles [129–132], which provide to leading order monopole-monopole (DLVO), monopole-dipole and dipole-dipole interactions. These inhomogeneities can have a large impact on the self-assembly, as we shall see in this chapter. The fact that higher order moments of the charge distribution are important, was already hinted towards in Ref. [133]. Here a binary mixture of colloidal species that are both positively charged was considered such that one expects (at least on the mean-field level) a repulsive effective monopole-monopole interaction. However, when an external electric field is applied, dipoles are induced on these particles, that can drive the formation of various structures, showing that the dipole-dipole interaction can become more important than the monopole-monopole interaction, see for experimental examples Refs. [36, 134]. Moreover, theoretical work shows that a long-range repulsion, combined with a short-distance attraction, can lead to a regime where microphase separation occurs instead of bulk phase separation [135–139], which will be a theme here as well.

An external electric field is not the only way to induce dipole moments in charged colloidal particles. For example, for a binary mixture of oppositely charged particles it is known that dielectric effects can give rise to string formation [140]. In the calculation of Ref. [140], however, salt was not included, which appears to be a severe approximation in systems where charge regulation plays a significant role.

Charge-regulating particles usually discharge when the interparticle distance is reduced [125, 141], which weakens electrostatic repulsion. When the particle surroundings are anisotropic, this will lead to an inhomogeneous charge distribution, and hence to a self-induced dipole moment. The adjective "self" is used here to make a distinction with dipoles that are, for example, induced by an external electric field. Self-induced dipoles will turn out to be important for the formation of alternating strings and clusters in a binary system of colloidal particles. The particles that we will study

are positively charged for one-component suspensions in the low-polar solvent cyclo-hexylbromide (CHB), as was shown earlier by electrophoresis measurements [142]. In low-polar solvents the electrostatic interactions can play an even more important role than in water, since the Coulomb interactions are stronger (dielectric constant is lower) and the screening lengths are longer [123, 143]. We will show that a combination of charge regulation and an asymmetry in the charge distribution of both species can lead to a short-distance attraction on top of the long-range repulsion. This rationalizes the formation of the observed strings, while more compact clusters are formed when one of the two species becomes (almost) negatively charged in bulk. We close this chapter with open questions on the observation of dumbbells in one-component systems [103], that were also earlier observed [144] and for which self-induced dipoles do not seem to give an explanation.

## 4.2 Summary of experimental observations

In this chapter we will investigate a system of binary charged colloids within the spherical-cell and two-body approximation. Our motivation to study these systems stems from recent experiments on binary charged colloids in Chapter 2 of Ref. [103]. Two types of positively charged PMMA particles (dielectric constant $\epsilon_c = 2.6$), which we will denote by green and red because of the dyes used, were suspended in the solvent cyclohexylbromide (CHB) (dielectric constant $\epsilon_o = 7.92$) at room temperature $T$, and at Debye length of $\kappa^{-1} = 6\ \mu$m. The green $(g)$ particles (radius $a_g = 0.99\ \mu$m) are larger than the red $(r)$ particles (radius $a_r = 0.79\ \mu$m). This system is the same as sample 6 in Ref. [142], meaning that the green particles underwent a locking procedure, and hence have a higher charge than the red particles [142]. The measured surface potentials at volume fractions $\eta_r = \eta_g = 0.028$ are $\phi_g = 6.5 \pm 0.1$ and $\phi_r = 3.29 \pm 0.09$ (in units of $k_B T/e$, with $k_B T$ the thermal energy and $e$ the proton charge), with corresponding charges $Z_g = 1015 \pm 40$ and $Z_r = 153 \pm 9$ in units of $e$ [142]. The following observations were made [103]:

(i) In an inhomogeneous mixture of red and green particles, alternating strings consisting of red and green particles were spontaneously formed. It was found that single particles and the strings remain positively charged. In Ref. [103] it was hypothesized that a patch of opposite charge is induced on the lower-charged red particle when a higher-charged green particle approaches, which leads to an effective close-distance attraction. (ii) When the (inhomogeneous) binary suspension is brought into contact with water, the formation of alternating strings was enhanced and they become more rigid. Moreover, alternating clusters were formed close to the CHB-water interface.

These observation are summarized in Fig. 4.1, which we have taken from Ref. [103]. In (a) we clearly see the formation of the alternating strings, and that their formation is enhanced when the suspension is brought into contact with an "ion sink" such as water (Fig. 4.1(b)). Close to the oil-water interface extended, alternating clusters were found (Fig. 4.1(c)).

To model this system, we will consider constant-potential colloids, because these
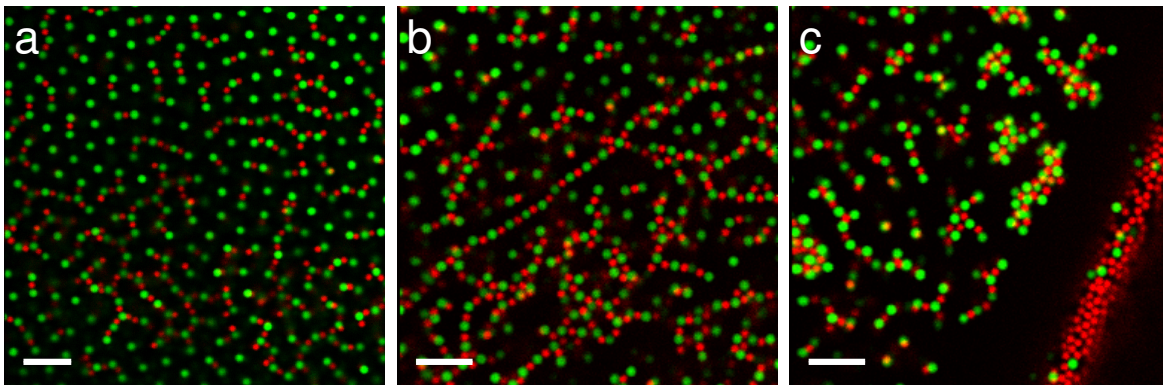
**Figure 4.1:** Alternating strings formed in binary suspensions of large (green, with radius $a_g = 0.99$ $\mu$m) and small (red, with radius $a_r = 0.79$ $\mu$m) particles in CHB (a) without deionised water; two days after mixing, (b) in contact with deionised water; 0.2 mm from CHB-water interface, $\sim 6.5$ hours after mixing, and (c) where extended clusters are found near the CHB-water interface; $\sim 4.5$ hours after mixing. Particles are adsorbed to the CHB-water interface, making the interface visible; the water phase is on the right, the CHB phase, containing the clusters, is on the left. Scale bars indicate 10 $\mu$m. Image taken from Ref. [103].

particles have the largest tendency to discharge as function of density, as was seen in Chapter 2. Therefore, they form a good candidate to study the effective interactions between self-induced dipoles. Also it can be can shown that constant-potential particles can be described by a charge regulation model in which the surface acquires its charge by cationic and anionic adsorption of ions (Chapter 2), and it is known that the particles from Ref. [103] are known to adsorb $H^+$ and $Br^-$ ions that are present in CHB by decomposition of the solvent.

Our approach to describe these experiments will be as follows. First, we will investigate the many-body charging and discharging properties of particles as function of volume fraction and ionic strength within the binary cell model. Next we will investigate the effective interaction potential within the two-body approximation with a special emphasis on the self-induced dipole moments. We will show that many-body corrections, which we will perform by using effective surface potentials, are needed to describe the experiments.

## 4.3 Spherical cell approximation

We will first investigate the charge regulation properties of the binary suspension discussed in Section 4.2 . For this we use the spherical-cell approximation [57, 58, 104, 145, 146]: every colloid of type $i = r, g$ is situated in a spherical cell of type $i$ with radius $R$, and the cells fill the whole system volume, such that $4\pi R^3/3 = V/(N_r + N_g)$, with $N_i$ the particle number of the respective species and $V$ the volume. Consequently, we may relate the volume fraction $\eta_i = N_i(4\pi/3)a_i^3/V$ to the number fraction $x_i = N_i/(N_r + N_g)$ via $\eta_i = x_i(a_i/R)^3$. The ionic density profiles around a particle of species $i$ are described by the Boltzmann distributions $\rho_\pm^i(r) = \rho_s \exp[\mp \phi_i(r)]$, with $2\rho_s$ the ion concentration
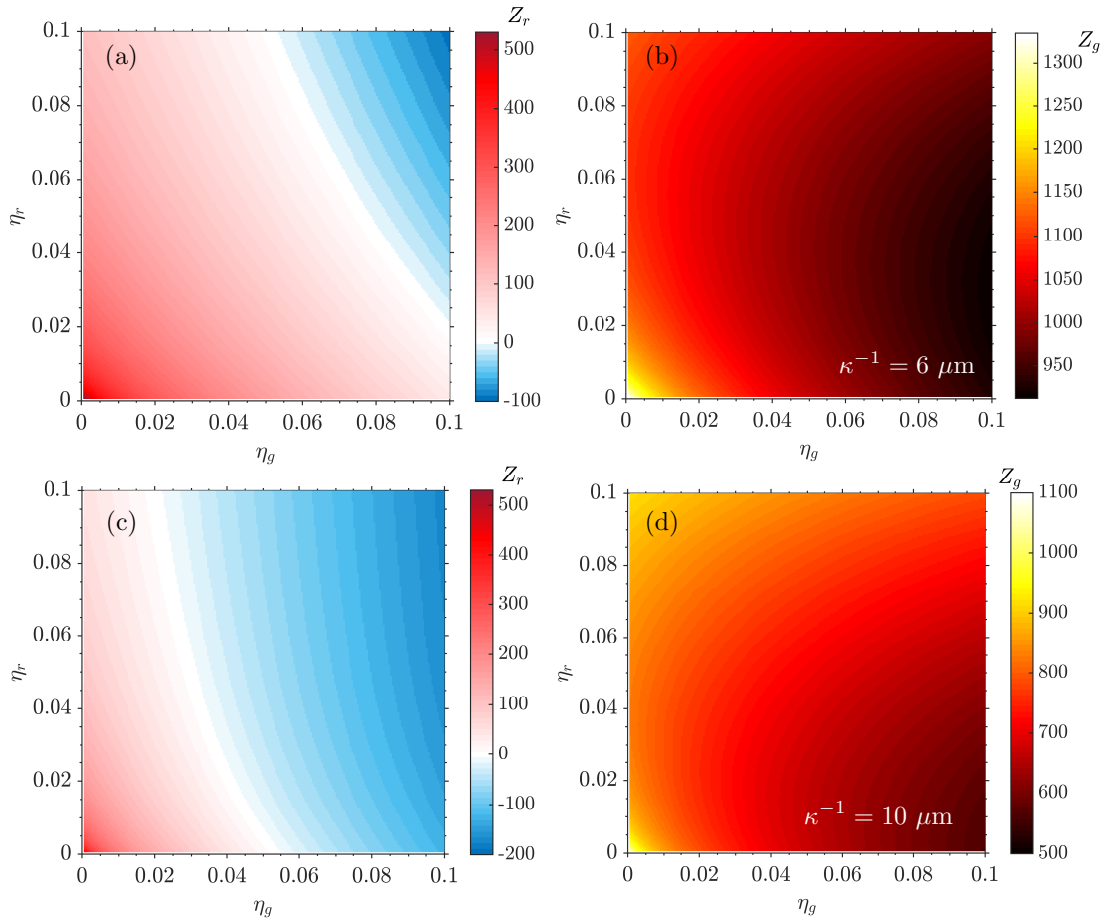
46

**Figure 4.2:** Colloidal charges for the (a) red particles $Z_r$ using a constant surface potential of $\phi_r = 4.4$ and (b) green particles $Z_g$ using a constant surface potential of $\phi_g = 6.7$ at $\kappa^{-1} = 6$ $\mu$m and at a lower ionic strength of $\kappa^{-1} = 10$ $\mu$m in (c) and (d), respectively. We see that the lower charged particle can become negatively charged at sufficiently high packing fractions of both red ($\eta_r$) and green ($\eta_g$) particles, as indicated in blue in (a) and (c). The green particle is always positively charged as can be seen in (b) and (d).

in a (hypothetical) ion reservoir in osmotic contact with the suspension. Together with the Poisson equation for $\phi_i(r)$, it gives the spherically symmetric Poisson-Boltzmann equations

$$\phi_i''(r) + \frac{2}{r}\phi_i'(r) = \kappa^2 \sinh[\phi_i(r)], \quad r \in [a_i, R], \tag{4.1}$$

with $\kappa^{-1} = (8\pi\lambda_B\rho_s)^{-1/2}$ the Debye length and $\lambda_B = e^2/4\pi\epsilon_{\mathrm{vac}}\epsilon_o k_B T$ the Bjerrum length, where $\epsilon_{\mathrm{vac}}$ is the permittivity in vacuum, and $\epsilon_o$ the relative dielectric constant of the oily medium. Throughout this chapter, we will use the value for CHB, $\epsilon_o = 7.92$. Naively, one would argue based on this number that ion-ion correlations are important in this system. However, because the ion density is low ($\sim 10^{-10}$M), we are still in the ideal-gas regime, and therefore Poisson-Boltzmann can be applied without even the need of including Bjerrum pair formation (see, for example Fig. 4 in Ref.

[147]). Denoting $x = x_g$, we express global charge neutrality by the boundary condition $x\phi'_g(R) + (1-x)\phi'_r(R) = 0$. Note that in our formulation a single cell is not necessarily charge neutral, however, the weighted average of two types of cells is neutral, in contrast to the approach in Ref. [105]. This has the added advantage that no minimization to the cell radii is needed and that numerical problems are circumvented when the colloids tend to be oppositely charged. Moreover, we impose the continuity condition $\phi_r(R) = \phi_g(R) \equiv \phi_D$, with $\phi_D/\beta e$ the Donnan potential that is found self-consistently. Finally, we also impose constant-potential boundary conditions: $\phi_i(a_i) = \phi_i$, and by applying Gauss' law, we can evaluate the charge $Z_i = -a_i^2 \phi'_i(a_i)/\lambda_B$. Note that in the constant-potential approximation the colloidal particles resemble active capacitors because they adjust their charge to ensure that their surface potential is constant. Furthermore, assuming a constant potential is a very good approximation for a charge-regulation model for which cations and anions can simultaneously adsorb on the colloidal surface (Chapter 2), which is thought to be relevant for the types of particles that we consider, see Ref. [142].

First, we tried to use the measured values of the surface potentials $\phi_g = 6.5 \pm 0.1$ and $\phi_r = 3.29 \pm 0.09$ at $\eta_r = \eta_g = 0.028$ to determine the dependence of $Z_r$ and $Z_g$ on overall packing fraction and composition. For this condition, we found that $Z_r < 0$, while it was established that all species in the suspension are positively charged at this state point. For this reason, we instead use the experimentally measured charges $Z_r = 153$ and $Z_g = 1015$ at $\eta_r = \eta_g = 0.028$ as known quantities and determine the surface potentials that gave the best correspondence, yielding $\phi_g = 6.7$ and $\phi_r = 4.4$, which is in reasonable agreement with the experimentally determined zeta potentials.

Using these values of $\phi_r$ and $\phi_g$ for all state points we determine $Z_r$ and $Z_g$ as a function of $\eta_r$ and $\eta_g$ from the binary cell model. The resulting $Z_r$ and $Z_g$ are presented in Fig. 4.2, in (a) and (b) for $\kappa^{-1} = 6~\mu$m, and in (c) and (d) for $\kappa^{-1} = 10~\mu$m. We see that the green particle has always a relatively high positive charge, while the red particle can discharge appreciably and even become negative if $\eta_r$ and/or $\eta_g$ are tuned to higher values. Moreover, when the ionic strength is reduced, there is a larger region for which $Z_r < 0$.

For the experimentally reported packing fractions $\eta_r = \eta_g = 0.028$, we show in Fig. 4.3 how the charges $Z_r$ and $Z_g$ vary with ionic strength. We see that charge inversion occurs at $\rho_s \approx 7 \cdot 10^{-11}$ M, which is about three times lower than the initial salt concentration $\rho_s \approx 2 \cdot 10^{-10}$ M. This inversion can also be achieved at a higher $\rho_s$ for larger $\eta_r$ and $\eta_g$, as can be deduced from Fig. 4.2.

## 4.4 Two-body approximation

The spherical symmetry in the cell-model calculations of the previous section cannot directly explain the formation of the alternating strings, since this requires directionality that breaks the spherical symmetry. The simplest extension is the two-body problem, which was investigated earlier within linear Poisson-Boltzmann [148] and later within non-linear Poisson-Boltzmann theory [149]. Therefore, we now consider two colloids
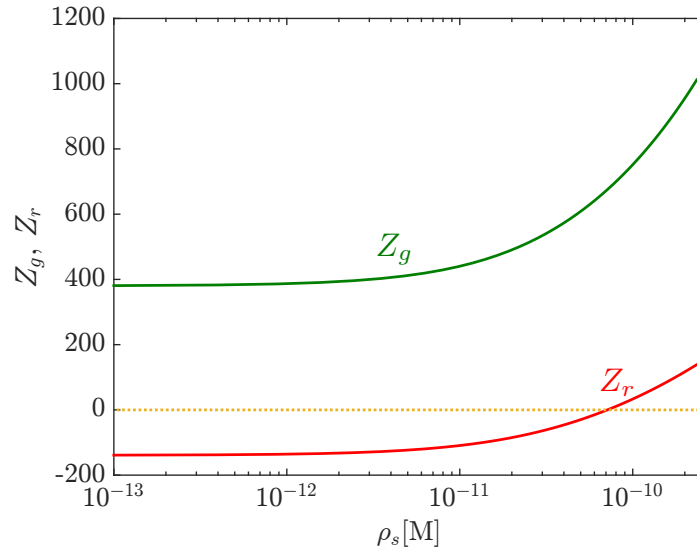
**Figure 4.3:** Colloidal charges for green particles $Z_g$ (radius $a_g = 0.99$ $\mu$m) and red particles $Z_r$ (radius $a_g = 0.79$ $\mu$m) as a function of salt concentration $\rho_s$ at packing fractions $\eta_r = \eta_g = 0.028$ and constant surface potentials $\phi_g = 6.7$ (green particles) and $\phi_r = 4.4$ (red particles). The dotted line indicates the line $Z = 0$. Highest plotted value of $\rho_s$ corresponds with $\kappa^{-1} = 6$ $\mu$m.

with radii $a_i$, surface potentials $\phi_i$ and centre-of-mass coordinates $\mathbf{R}_i$ ($i = r, g$) that are a distance $d = |\mathbf{R}_r - \mathbf{R}_g|$ apart, dispersed in a solvent with monovalent positive and negative ions described by the density profiles $\rho_\pm(\mathbf{r})$. The solvent is again assumed to be in osmotic contact with a reservoir characterized by a total ion concentration $2\rho_s$, with Bjerrum length $\lambda_B$ and Debye screening length $\kappa^{-1}$. When we denote the region outside the two colloids by $\mathcal{R}$, the system is described within mean-field theory by the grand potential density functional

$$\beta\Omega[\rho_\pm; d] = \sum_{\alpha=\pm} \int_{\mathcal{R}} d^3\mathbf{r} \; \rho_\alpha(\mathbf{r}) \left[ \ln\left( \frac{\rho_\alpha(\mathbf{r})}{\rho_s} \right) - 1 \right]$$
$$+ \frac{1}{2} \int_{\mathcal{R}} d^3\mathbf{r} \; Q(\mathbf{r})\phi(\mathbf{r}) - \sum_{i=1}^{2} \phi_i \int_{\Gamma_i} d^2\mathbf{r} \; \sigma_i(\mathbf{r}), \qquad (4.2)$$

with the total charge density (in units of e) $Q(\mathbf{r}) = \rho_+(\mathbf{r}) - \rho_-(\mathbf{r}) + \sum_{i\in\{r,g\}} \sigma_i(\mathbf{r})\delta(|\mathbf{r} - \mathbf{R}_i| - a_i)$ and $e\sigma_i(\mathbf{r})$ the colloidal surface charge density of sphere $i$, and $\phi(\mathbf{r})$ the dimensionless electrostatic potential. Note that we performed a Legendre transformation to an ensemble where the surface potentials $\phi_i$ are fixed, as we will consider constant-potential boundary conditions below. The Euler-Lagrange equations $\delta\Omega/\delta\rho_\pm(\mathbf{r}) = 0$ yield the equilibrium density profiles $\rho_\pm(\mathbf{r}) = \rho_s \exp[\mp\phi(\mathbf{r})]$ for $\mathbf{r} \in \mathcal{R}$. Together with the Poisson equation for the electrostatic potential, this results in the non-linear Poisson-Boltzmann equation

$$\nabla^2\phi(\mathbf{r}) = \kappa^2 \sinh[\phi(\mathbf{r})], \quad \mathbf{r} \in \mathcal{R}, \qquad (4.3)$$

49

together with the constant-potential boundary conditions supplied for the colloidal surfaces $\Gamma_i$ for $i = r, g$,

$$\phi(\mathbf{r}) = \phi_i, \quad \mathbf{r} \in \Gamma_i. \tag{4.4}$$

Far from the colloids we assume that the electric field vanishes, and inside the colloid the Laplace equation $\nabla^2 \phi(\mathbf{r}) = 0$ is to be satisfied. From the solution of the closed set of Eq. (4.3) and (4.4), it is then straightforward to obtain the charge densities $e\sigma_i(\mathbf{r})$ by evaluating

$$\mathbf{n} \cdot [\epsilon_c \nabla \phi|_{\text{in}} - \epsilon_o \nabla \phi|_{\text{out}}]/\epsilon_o = 4\pi \lambda_B \sigma_i(\mathbf{r}), \quad \mathbf{r} \in \Gamma_i, \tag{4.5}$$

with $\mathbf{n}$ the outward-pointing unit surface normal, and $\epsilon_c = 2.6$ the dielectric constant of the colloid (PMMA). Note that for the constant-potential boundary condition that we use, the first term in the square brackets in Eq. (4.5) vanishes. The effective interaction Hamiltonian of the colloidal pair can then be found by

$$H(d) = \varphi_{\text{HS}}(d) + \min_{\rho_\pm} \Omega[\rho_\pm; d], \tag{4.6}$$

where the first term is the bare non-electrostatic colloid-colloid potential, for which we take a hard-sphere potential with contact distance $a_r + a_g$, while the last term is the Legendre-transformed equilibrium ionic grand potential. This leads to

$$\beta H(d) = \beta\varphi_{\text{HS}}(d) - \frac{1}{2}\sum_{i=1}^{2} \phi_i \int_{\Gamma_i} d^2\mathbf{r}\, \sigma_i(\mathbf{r}) + \rho_s \int_{\mathcal{R}} d^3\mathbf{r}\Big\{\phi(\mathbf{r})\sinh\phi(\mathbf{r}) - 2[\cosh\phi(\mathbf{r}) - 1]\Big\}. \tag{4.7}$$

Finally, we calculate the total charge $Z_i$ and the dipole moment $\mathbf{p}_i$ of a colloidal particle with respect to $\mathbf{R}_i$, defined by

$$Z_i = \int_{\Gamma_i} d^2\mathbf{r}\, \sigma_i(\mathbf{r}),$$

$$\mathbf{p}_i = \int_{\Gamma_i} d^2\mathbf{r}\, (\mathbf{r} - \mathbf{R}_i)\sigma_i(\mathbf{r}), \quad i = 1, 2. \tag{4.8}$$

Note that the definition of the dipole moment requires a specific point of reference that we set to $\mathbf{R}_i$, because $\mathbf{p}_i$ is only independent of the reference point for charge neutral particles. In Fig. 4.4 we plot (a) the interaction potential $\Phi(d) = H(d) - H(\infty)$ for the surface potentials $\phi_g = 6.7$ and $\phi_r = 4.4$ that were determined from the cell calculations, and we also show the charge $Z_i$ (left inset in (a)), the dipole moment $\mathbf{p}_i = p_i\hat{\mathbf{z}}$ (right inset (a)), where $\hat{\mathbf{z}}$ is the unit vector pointing in the same direction as $\mathbf{R}_r - \mathbf{R}_g$, and the charge distributions $e\sigma_i(\vartheta)$ for various separations $d$ ((b)-(d)). As can be seen in Fig. 4.4(a), $\Phi(d)$ is repulsive for $d \gtrsim 2\ \mu$m at these parameter values, which is reflected also in the equal sign of the charges $Z_r$ and $Z_g$ for both red and green species for all $d$ and the anti-aligned induced dipole moments (although the red particle does acquire a small negative charge density at its southpole for small enough $d$, which can be seen in Fig. 4.4(b)). Close to the point where both particles touch,
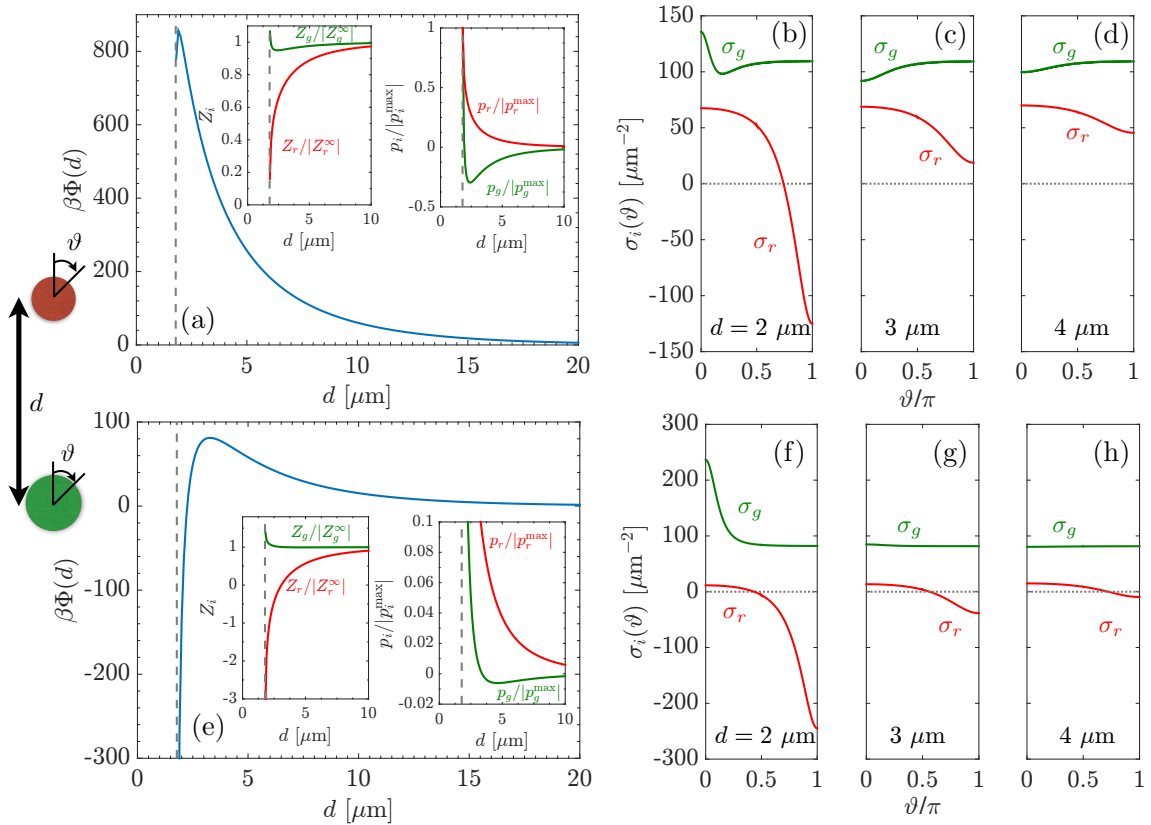
**Figure 4.4:** Interaction potentials between a red and green particle of radius $a_r = 0.79$ $\mu$m and $a_g = 0.99$ $\mu$m, respectively, at Debye lengths $\kappa^{-1} = 6$ $\mu$m as a function of their center-to-center distance $d$ for (a) surface potentials $\phi_g = 6.7$ and $\phi_r = 4.4$ and (e) $\phi_g = 5.5$ and $\phi_r = 1.2$. In the left insets we plot the total charge $Z_i$ ($i = r, g$) normalized by the absolute value of the charge $Z_i^\infty$ at $d \to \infty$. In (a) we have $Z_g^\infty = 1356$ and $Z_r^\infty = 582$ , while in (e) we have $Z_g^\infty = 1005$ and $Z_r^\infty = 152$ for the full lines. In the right inset we plot the dipole moments $p_i$ normalized by the absolute value of the maximum dipole moment $p_i^{\max}$. The corresponding charge distributions are plotted in (b)-(d) for $\phi_g = 6.7$ and $\phi_r = 4.4$ and in (f)-(h) for $\phi_g = 5.5$ and $\phi_r = 1.2$. The dashed vertical grey line in (a) and (e) indicate the distance below which hard-sphere repulsion sets in, while the horizontal dashed grey line in (b)-(d) and (f)-(h) indicates $\sigma_i(\vartheta) = 0$.

$d \lesssim 2$ $\mu$m, we see an attraction that is accompanied by the alignment of the induced dipoles, while the particles remain positively charged.

However, this calculation does not include many-body effects. This can be seen from the observation that for $d$ large the particles have charges $Z_r^\infty = 582$ and $Z_g^\infty = 1356$ which are larger than the charges determined from the cell model at the experimentally measured packing fractions, and these charges are even much higher when $d$ is on the order of the inter-particle distance $d = 3 - 5$ $\mu$m. To include the fact that particles discharge when the density is increased, we set the charges of the pair at infinite distance to coincide with the charges determined from the cell model calculations at $\eta_r = \eta_g = 0.028$ from which we find approximate "effective" surface potentials $\phi_g = 5.5$ and $\phi_r = 1.2$. When we use these parameters to determine $\Phi(d)$ shown in Fig. 4.4(e),
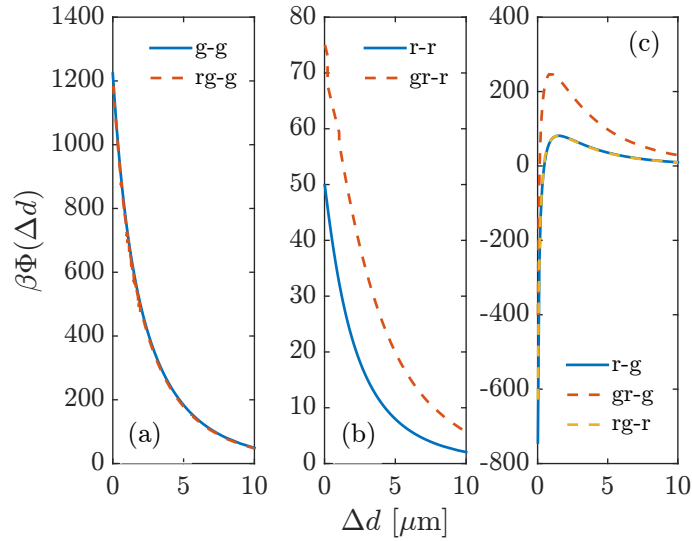
51

**Figure 4.5:** Effective interaction potentials $\Phi$ as a function of surface-to-surface distance $\Delta d$ for various configurations of red particles, with surface potential $\phi_r = 1.2$ and radius $a_r = 0.79$ $\mu$m and green particles with surface potential $\phi_g = 5.5$ and radius $a_g = 0.99$ $\mu$m at Debye length $\kappa^{-1} = 6$ $\mu$m. In (a) we show as the dashed orange line the interaction between a red-green dumbbell and a green particle approaching the green part of the dumbbell. We abbreviate this by rg-g. We compare this effective interaction with the green-green (g-g) repulsion as the full line. Similarly, we show in (b) the r-r and gr-r repulsion and in (c) the effective interactions r-g, gr-g and rg-r that feature short-range attraction and long-range repulsion.

we see a much stronger "short-distance" attraction than in Fig. 4.4(a), which extends to distances on the order of a few microns, beyond which the long-range repulsion sets in. The attraction is again accompanied by the alignment of the induced dipoles, shown in the inset of Fig. 4.4(e). In fact, at lower $d$ we even see that $Z_r < 0$, although $Z_r + Z_g > 0$ at contact, so that the resulting dumbbell is positively charged. We emphasize that although the effective potential of Fig. 4.4(e) resembles in some sense the DLVO potential, the situation here is rather different. The short-distance attraction here is not due to the Van der Waals attraction which is induced by electronic polarization, but occurs here purely due to *ionic* electrostatics. This is also reflected by the micron-range of the present attraction, which is much longer than that of a typical van der Waals attraction.

Finally, we calculated the effective interaction potential between a red-green dumbbell and a red or green particle in Fig. 4.5, with $\phi_r = 1.2$ on the "red" part of the dumbbell and $\phi_g = 5.5$ on a "green" surface. We always let the spherical colloid approach the dumbbell along its symmetry axis, such that we can still exploit cylindrical symmetry. When we determine $\Phi$ as a function of the surface-to-surface distance $\Delta d$ we see in Fig. 4.5(a) that the "rg-g" repulsions between a red-green dumbbell and a green colloid approaching the green part of the dumbbell is little different from the "g-g" (green-green) repulsion. In contrast, the "gr-r" repulsion between a green-red dumbbell and a red particle is rather different: Fig. 4.5(b) shows that red particles are more strongly repelled from the red parts of the dumbbell than the "r-r" repulsion between

two single red particles. The "r-g" attraction between red and green particles shown in Fig. 4.5(c) is however similar to the red-green and red attraction "rg-r", with the only difference that the net free energy gain is larger at contact for the interaction between single red and green particles. The "gr-g" repulsion at large $d$ between a green-red dumbbell and a green particle is, however, stronger than the r-g and rg-r repulsion at large $d$ and the energy barrier is higher. The calculation as presented in this section and the previous one will now be related to the experiments of section 4.2.

## 4.5 Speculation on alternating string and cluster formation in binary systems

Using the results from the binary cell model of section 4.3 and the two-body calculations of section 4.4, we can now give an explanation for the observation of the alternating strings and clusters from section 4.2. In Fig. 4.4(b), we have seen that a short-distance attraction is produced by matching the charges of the two colloids at $d \to \infty$ to the charges as obtained from the binary cell model of Fig. 4.2, emphasizing the important role of many-body effects in this system. The energy barrier is, however, quite high, $\Delta E \sim 80 \, k_B T$. For an attempt frequency per particle of $\nu = 1 \, \text{s}^{-1}$, the production rate of a red-green dumbbell per particle present in the system is $\nu \exp(-\beta \Delta E) \sim 10^{-35} \, \text{s}^{-1}$, which is too low compared to the experimental time scales.

Similar to the reasoning why the short-distance attraction can be enhanced by including discharging due to many-body effects, we hypothesize that the energy barrier can be sufficiently lowered if we allow for variations in the *local* volume fraction. To demonstrate this, we use the charges as obtained from the binary cell model of Fig. 4.2 at $\kappa^{-1} = 6 \, \mu\text{m}$ and $\kappa^{-1} = 10 \, \mu\text{m}$ as function of $\eta_r + \eta_g$ with $\eta_r = \eta_g$. Using effective surface potentials to match the charges of the cell model to the charges within the two-body approximation at $d \to \infty$, we determined $\Delta E$ in Fig. 4.6(a) for various state points. Furthermore, we plot the corresponding (bulk) charges in Fig. 4.6(b). We see that (local) variations in the volume fraction can lower $\Delta E$ through particle discharging, and in particular the energy barrier is lowest when the red particle is close to being charge neutral. If the total (local) volume fraction is twice as large, we find $\Delta E \sim 10 \, k_B T$, with a corresponding production rate per particle of a red-green dumbbell $\sim 10^{-5} \, \text{s}^{-1}$, which means that a single green-red dumbbell is produced within $\sim 6$ hours per particle, close to the experimentally observed time scales. The production rate is even larger at a higher local volume fraction, showing the sensitivity of the energy barrier to the local colloid density. At a slighly lower ionic strength, we see that the energy barrier is even only a few $k_B T$, see Fig. 4.6, and that charge inversion of the red particle occurs above $\eta_r + \eta_g \sim 0.6$.

Because of a short-distance attraction which is accompanied by the alignment of the net dipole moments of the two particles, we speculate that we find strings instead of (spherically symmetric) clusters. Moreover, van der Waals forces are only important on length scales of a few nanometers, which is much smaller than the range of attractions
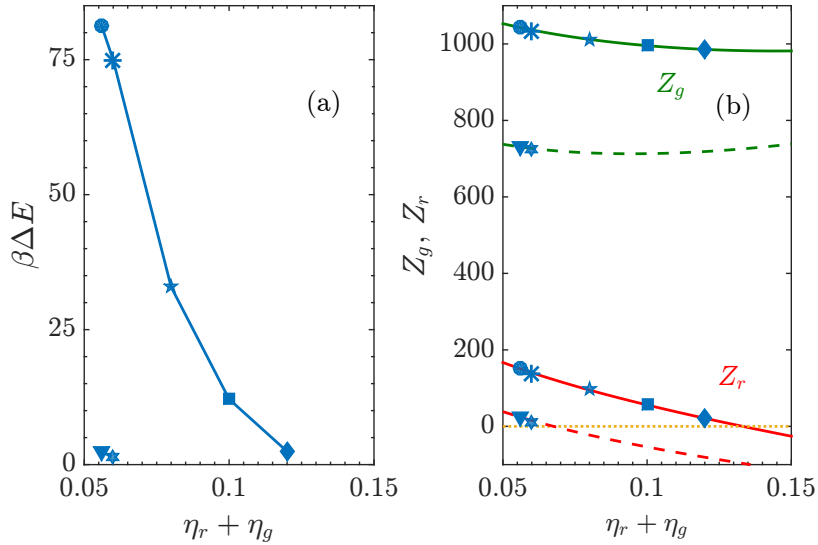
**Figure 4.6:** (a) Energy barrier that separates a regime of short-distance attraction and long-range repulsion for various state points using the bulk charges from the binary cell model of Fig. 4.2 with $\eta_r = \eta_g$. The lines are used to guide the eye. The upper line is for $\kappa^{-1} = 6 \ \mu$m, while the lower one (two points at the bottom) is for a lower ionic strength, $\kappa^{-1} = 10 \ \mu$m, and in (b) we plot the corresponding charges of red ($Z_r$) and green ($Z_g$) particles. The full lines are for $\kappa^{-1} = 6 \ \mu$m and the dashed lines are for $\kappa^{-1} = 10 \ \mu$m, and the symbols match the state points of (a).

set by $\kappa^{-1}$ we observe here. Furthermore, it is important that the alignment of the dipole moments occurs at a larger $d$ than the one for which charge inversion of the red particle takes place, see section 4.3. This implies that the energy barrier for a particle with an aligned dipole moment is lower, and hence, it is more probable for particles approaching an existing dumbbell along its symmetry axis. Other possibilities, say an approach of a particle not exactly along the symmetry axis of an existing dumbbell, can have an energy barrier that is only a few $k_B T$ higher, and may therefore also occur, rationalizing why the bond angle within a string is not always 180 degrees. An ion sink such as water reduces the energy barrier even more (compare bottom symbols and top symbols in Fig. 4.6(a)), explaining the more extended strings in Fig. 4.1(b) compared to Fig. 4.1(a).

Why (extended) clusters are found near the oil-water interface can also be understood from our calculations. Close to the interface, we observed a larger local density, and hence from Fig. 4.6, we find that $\Delta E$ is even lower than it would be in bulk (filled circle). The energy barriers between various angles on which a particle can approach a green-red dumbbells may differ only by a few $k_B T$ and hence all of them can occur within an appreciable timescale, explaining the clusters. We hypothesize that there is still a small energy barrier, because the clusters were linearly extended and not spherically symmetric. Although it is not clear how much the ionic strength is reduced due to the presence of the water phase, our results do suggest that a larger Debye length will indeed promote the formation of the clusters through charge regulation, in line with Ref. [97]. Finally, the relatively favourable rg-r and gr-g interactions support the fact
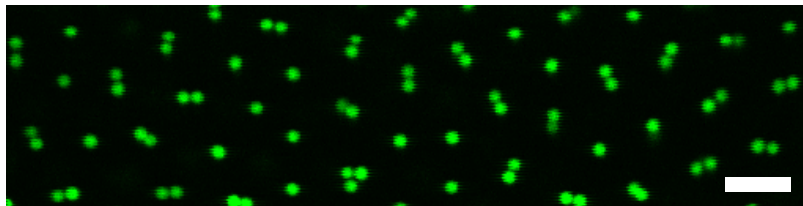
**Figure 4.7:** Clusters (mostly dumbbells) formed in a suspension of locked PMMA particles (radius $a = 1.12\ \mu$m) in CHB at a distance 0.3 mm from CHB-water interface, two days after sample preparation. The scale bar indicates 10 $\mu$m. Image taken from Ref. [103].

that the strings and clusters are alternating, although more calculations are needed to study the height of the barrier that separates the long-range repulsions from the shorter ranged attractions, for example, also within a true three-dimensional geometry, where the cylindrical symmetry cannot be exploited.

## 4.6 Open questions on dumbbell formation in one-component systems

In previous experiments [144] dispersions of sterically stabilized charged PMMA particles in CHB were compressed by centrifugation, and subsequently the system was followed over several months. A significant fraction of the particles was observed to form small clusters during the centrifugation step. The fraction of clustered particles decreased in time due to spontaneous dissociation of the clusters, as the ionic strength in the dispersion increased due to decomposition of the solvent CHB. Similar behaviour (cluster formation and dissociation) was found when the particles were pressed together by an electric field [144].

Interestingly, in a one-component dispersion of green particles with radius $a = 1.12\ \mu$m and surface potential $\phi_0 = 4.6$ (system 7 in Ref. [142]), the formation of dumbbells similarly to the system of Ref. [144] was also observed [103], provided that the system was brought into contact with a water phase, see Fig. 4.7, where a few green-green dumbbells are shown. This observation cannot be explained by the two-body approximation of the previous section, because we found that the r-r and g-g interaction between a pair of the same species is always repulsive. There are now a few possible scenarios that we will consider. The first one is that adding a water phase adjacent to the oil-phase generates a Donnan potential [150] across the oil-water interface due to ion partitioning, and hence a local electric field near the interface is generated that may induce dipole moments on the particles that in turn generate an attraction when these are aligned. However, we do not observe any alignment of the dumbbells in a preferred direction, so this seems an unlikely mechanism.

The second one is that the water phase acts as an ion sink that increases $\kappa^{-1}$ in the oil, leading to discharging of the green particles. The repulsions then become weaker and this may render the van der Waals attraction to be more important, such that the

observed clusters could be a consequence of microphase separation within conventional DLVO theory [138, 139]. To test this hypothesis, we estimate the strength of the van der Waals interaction $\Phi_{\mathrm{VdW}}$ between two equal-sized spheres within Hamaker-de Boer theory, which describes the pair potential (neglecting retardation and screening) as

$$\beta\Phi_{\mathrm{VdW}}(d) = -\frac{A_H}{3}\left[\frac{a^2}{d^2 - 4a^2} + \frac{a^2}{d^2} + \frac{1}{2}\ln\left(1 - \frac{4a^2}{d^2}\right)\right]. \qquad (4.9)$$

As is well known, this expression fails at very short distances $d \approx 2a$ where the atom-atom Born repulsion plays an important role, and for large distances where retardation becomes important due to the finite speed of light. In general, a cutoff for the surface-to-surface distance of 0.16 nm [128] is used to estimate the maximum attraction that is possible due to van der Waals. We approximate the Hamaker constant $A_H$ by the static contribution within Lifschitz theory [151], such that

$$\beta A_H = \frac{3}{4}\left(\frac{\epsilon_o - \epsilon_c}{\epsilon_o + \epsilon_c}\right)^2, \qquad (4.10)$$

which gives the lower bound $\beta A_H = 0.2$, since we neglected the (positive) contribution from the summation over all frequencies . On this basis, we then estimate that the attraction on closest approach $\Phi_{\mathrm{VdW}} \sim -100\ k_BT$. However, the PMMA particles in the experiments have a steric layer that reduces the van der Waals attraction even further (closest approach $\sim 10$ nm), which makes the van der Waals attraction at "contact" even weaker, namely $\sim -2\ k_BT$. To test whether this attraction is strong enough to overcome the electrostratic repulsions, we used for all state points a spherical cell model with a surface potential $\phi_0 = 4.6$ [142]. From it we determined effective surface potentials to be used within the two-body approximation with the condition that the two-body $Z(d)$ coincides with the cell model result for $d \to \infty$. In Fig. 4.8 we show the resulting pair potentials $\Phi(d)$ with the van der Waals attraction of Eq. (4.9) added and with $Z(d)$ in the inset. We see that the screening length in oil must be increased to $\kappa^{-1} \sim 50\ \mu$m for a (metastable) bound state to occur with an energy barrier of $\sim 5\ k_BT$. For a stable bound state the ionic strength must be reduced even further through the uptake of ions by the water phase. In Fig. 4.8 we show for example the resulting $\Phi$ for $\kappa^{-1} = 100\ \mu$m, showing a stable bound state separated from the bulk with an energy barrier of $\sim 1\ k_BT$.

Note that the values of $\kappa^{-1}$ are quite large, but can give still rise to a sufficient charge $Z$ for the colloids within a two-body approximation. One could think that such long Debye lengths are rather unrealistic in a true many-body suspension, where the spheres would be completely discharged at such a state point. However, we stress that $\kappa^{-1}$ is the Debye length of the *reservoir*. We have only performed many-body corrections to the surface potential, but not to the Debye length. In principle, this can be taken into account within the cell model by defining $\bar{\kappa}^2 = \kappa^2 \cosh(\phi_D)$, such that $\bar{\kappa}^{-1}$ is the screening length at the cell boundary. This is also the quantity one needs to use in Debye-Hückel theory to correct for non-linear effects with charge renormalization [58] and $\bar{\kappa}^{-1}$ can therefore be seen as an effective screening length due to double layer
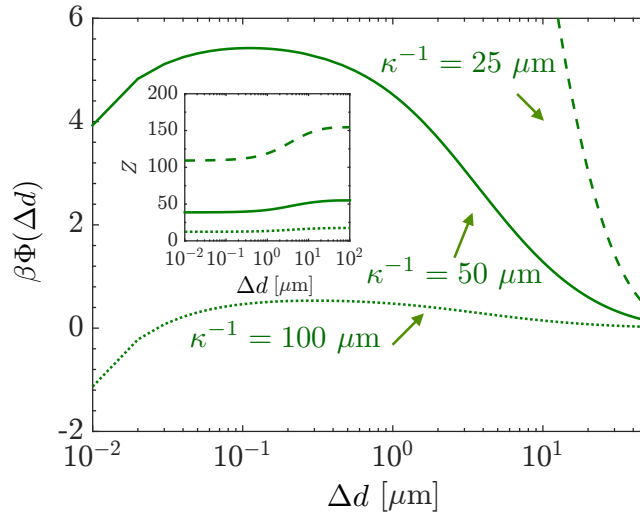
**Figure 4.8:** Colloid-colloid effective pair potentials $\Phi$ as function of surface-to-surface distance $\Delta d$ for two colloids of radius $a = 1.12\ \mu m$ at various Debye screening length $\kappa^{-1}$. A sphere-sphere van der Waals attraction has been added with Hamaker constant $A_H = 0.2\ k_B T$, while for $\Delta d < 10$ nm there is a hard-sphere repulsion to model the effect of steric layer with a thickness of 5 nm. For each $\kappa^{-1}$, we used an effective surface potential that gives a $Z$ that coincides at $\Delta d \to \infty$ with the result of a spherical-cell model where we used a surface potential $\phi_0 = 4.6$ for all state points.

overlaps. Indeed, for a reservoir screening length of $\kappa^{-1} = 100\ \mu m$ at $\eta = 0.02$ and $\phi_0 = 4.6$, we find using the cell model $\bar{\kappa}^{-1} = 13\ \mu m$, a numerical value that is maybe more intuitive in a true many-body system regarding the values of $Z$ involved. Therefore, the calculation as performed in Fig. 4.8 is maybe a poor estimate for the range of the interactions. However, because the charges are not so sensitive to $\rho_s$ in the dilute limit, Fig. 4.8 is a good estimate for the height of the energy barrier, which is more of interest at this stage.

Finally, Fig. 4.7 shows that the dumbbells seem to order in a plastic crystal, at a volume fraction $\eta \sim 0.02$. We test this hypothesis by calculating the OCP coupling parameter $\Gamma$ for this system within a cell model for $\kappa^{-1} = 6\ \mu m$. The procedure for such a calculation can be found in Refs. [54] and in Chapter 2, where it is shown that $\Gamma > 106$ is a reliable freezing criterion. We found that decreasing $\rho_s$ at fixed $\eta_g$ reduces $\Gamma$, so the presence of water will actually impede crystallization. However, we remark that within such a calculation we assume that each lattice point is occupied by a single particle, while dumbbells have a larger charge and hence their existence tends to increase $\Gamma$. In fact, we find that our results are rather sensitive to the precise values of the parameters such as $\kappa^{-1}$, the local colloid density and the charges of the constituent particles. Hence, we could not precisely assess whether the system is in a crystalline state or not within the theory. However, considering the reported surface potential for these particles $\phi_0 = 4.6$ [142] we see that $\Gamma$ varies between $\Gamma = 260$ at $\kappa^{-1} = 6\ \mu m$, to $\Gamma = 137$ at $\kappa^{-1} = 10\ \mu m$ and $\Gamma = 70$ at $\kappa^{-1} = 15\ \mu m$, For the metastable bound state at $\kappa^{-1} = 50\ \mu m$ in Fig. 4.8, however, we find $\Gamma = 3.1$, and hence according to the theory the system is actually far from being crystalline for repulsions that can be overcome

by a small van der Waals attraction of $\sim$-2 $k_B T$. However, given the sensitivity to $\kappa^{-1}$ there is certainly a possibility that the system is close to a crystallization transition. Therefore, another alternative explanation is that the dumbbell formation can be seen as the formation of a Wigner crystal with a double occupancy of particles for some of the lattice sites, which shows a striking resemblance to the one discussed in Ref. [152] for a much shorter-ranged repulsion.

The precise mechanism for the formation of these dumbbells is thus still an open question. However, we are tempted to favour the multiple-occupancy crystal over the formation of a (meta-)stable dimer state by a residual van der Waals attraction. Namely, in the latter case one needs (i) finetuning of the system parameters to enter a regime in which clusters would form and (ii) one would also expect higher order clusters. For a multiple occupancy crystal, however, no finetuning is needed as it can be driven purely by repulsions. Secondly, higher order occupancy of lattice sites is limited in this case by the hard-core and electrostatic repulsion of the particles. It is therefore conceivable that many-body effects not only select the lattice spacing, but also the mean occupancy number of the lattice sites. It is interesting to investigate the dumbbell formation systematically in experiments and theory, which we will both leave for future work.

## 4.7 Discussion and conclusion

We investigated a system of size- and charge- asymmetric colloids with constant-potential boundary conditions. We found that within the two-body approximation it is possible to have a net attraction between the two like-charged particles that induces the formation of alternating strings if (i) the charge of one of the two particles is low enough and (ii) the induced dipole moments are aligned. We studied many-body effects in the effective pair interaction by using effective surface potentials that stem from a spherical-cell model, providing short-distance attractions through charge regulation. Moreover, another additional feature is the formation of aligned induced dipoles that may favor alternating strings over compact clusters. Such strings are not to be expected from standard DLVO theory where the charge is assumed to be spatially constant over the colloidal surface. Moreover, we have shown that enhanced cluster formation is expected to occur upon lowering the ionic strength of the binary suspensions, which enlarges the regime of composition and overall packing fraction in which the colloids are found to be oppositely charged.

It would be interesting to investigate the induced-dipole interactions in a true many-body system, although this is a challenging problem in general. Perhaps an engaging way to tackle this is through the Car-Parinello like simulation techniques first proposed by Fushiki [153] and Löwen *et al.* [154, 155], which offers the possibility to include the effects of deformed ionic screening clouds and the fact that the effective potential between $N$ colloids depends on the many-body configuration of colloids through charge regulation. We hypothesize that these effects are of utmost importance for the formation of alternating strings and clusters in binary suspensions of charged colloids at the

large screening lengths in these systems. This is left for future work. Finally, we have speculated that dimers and trimers found in single-component dispersions of PMMA particles can be seen as the result of a multiple-occupancy Wigner crystal, and also this hypothesis can be tested with the methods of Refs. [153–155].

# 5

# Tuning colloid-interface and colloid-colloid interactions by salt partitioning

*We show that the interaction of an oil-dispersed colloidal particle with an oil-water interface is highly tunable from attractive to repulsive, either by varying the sign of the colloidal charge via charge regulation, or by varying the difference in hydrophilicity between the dissolved cations and anions. In addition, we investigate the yet unexplored interplay between the self-regulated colloidal surface charge distribution with the planar double layer across the oil-water interface and the spherical one around the colloid. Our findings explain recent experiments and have direct relevance for tunable Pickering emulsions.*

## 5.1 Introduction

Colloidal particles experience a deep potential well when they intersect fluid-fluid interfaces. They therefore adsorb strongly to such interfaces, self-assembling into structures such as two-dimensional monolayers [156] or particle-laden droplets in Pickering emulsions [157, 158]. The free energy gain caused by the reduction of the fluid-fluid surface area is $\gamma \pi a^2 (1 + \cos \theta)^2 \simeq 10^3 - 10^7 k_B T$, where $\gamma$ is the fluid-fluid surface tension, the particle radius $a$ is typically between $10 - 10^3$ nm, $\theta$ is the three-phase contact angle and $k_B T$ is the thermal energy [156]. With the exception of nanoparticles [159, 160], the binding is essentially irreversible and hardly prone to physicochemical modifications such as the pH or salt concentration. Only strong mechanical agitation is able to detach micron-sized particles from the interface [161]. However, the recovery of particles from fluid-fluid interfaces is an essential step for the realization of applications, such as in biofuel upgrade [162], "dry water" catalysis [163] and gas storage [164].

An alternative route to overcome the difficulties associated with strong adsorption was offered in Refs. [150, 158], which show that charged poly(methylmethacrylate)

(PMMA) particles that stabilize water-cyclochexylbromide (CHB) Pickering emulsions are (almost) non-wetting ($\cos\theta \to -1$), such that the colloidal particles reside essentially in the oil phase. The crucial ingredient of this system is the relatively "polar" oil which solvates a small but significant amount of charge that stabilizes the colloids [158, 165]. Within a modified Poisson-Boltzmann theory, qualitative agreement was found with the experimental out-of-plane structure of the particles, provided a small degree of wetting was assumed [150, 166].

Very recent experiments on the same system by Elbers *et al.* [167] revealed that the colloidal particles in fact do *not* penetrate the water-CHB interface, but are trapped at a finite $\sim$ nanometer distance [167], completely circumventing the irreversible wetting effects described above. Additionally, these non-touching particles were easily detached from the oil-water interface by the addition of an organic salt [167], while at the same time reversing the sign of the colloidal charge, see Ref. [167]. Interestingly, this tunability offers an appealing route for controlled destabilization of Pickering emulsions. The authors of [167] hypothesized that the trapping mechanism is due to a force balance between an attractive image-charge and a repulsive van der Waals (VdW) force, as proposed by Oettel [168]. While correctly predicting the non-touching behaviour, this argument cannot explain how the particle-interface interaction can be tuned from attractive to long-ranged repulsive by adding salt.

The findings of Ref. [167] show that whether a particle ever *arrives* at the interface is subtle and tunable. In this chapter, we show that the interaction between a charged colloidal particle and the oil-water interface consists not only of well-known image-charge [169, 170] and dispersion forces [168, 171], but also of particle-ion forces that can be tuned between strongly repulsive and strongly attractive by (i) varying the *sign* of the particle charge and (ii) by varying the *difference* between the degree of hydrophilicity of the cations and anions. This difference determines not only the distribution of ions among the water and oil phases ("ion partitioning"), but also the sign of the Donnan potential that spontaneously forms between the water and oil bulk phases (not unlike the potential at a PN junction) [150, 172–176]. In fact, our calculations show contrary to a common assumption [168, 177–179] that the low but non-zero ion concentrations in oil are crucial and should not be neglected [49, 54, 142, 143, 180–182], even if the ions initially present in the oil strongly prefer to be in the water phase [172–176, 183–190]. We explicitly show this not only by investigating colloid-interface interactions for non-touching colloids, but also by investigating the lateral interactions of interfacially trapped colloids using a cylindrical cell model. More specifically, we will evaluate the stress tensor on the cell boundary in Sec. 5.4.

## 5.2 Single-particle model

To describe the coupling between the particle, oil-water interface, and ions, we will focus for simplicity on a single oil-dispersed charged colloidal sphere of radius $a = 1$ $\mu$m, charge $Ze$, and dielectric constant $\epsilon_c = 2.6$ (PMMA) with its center at a distance $d$
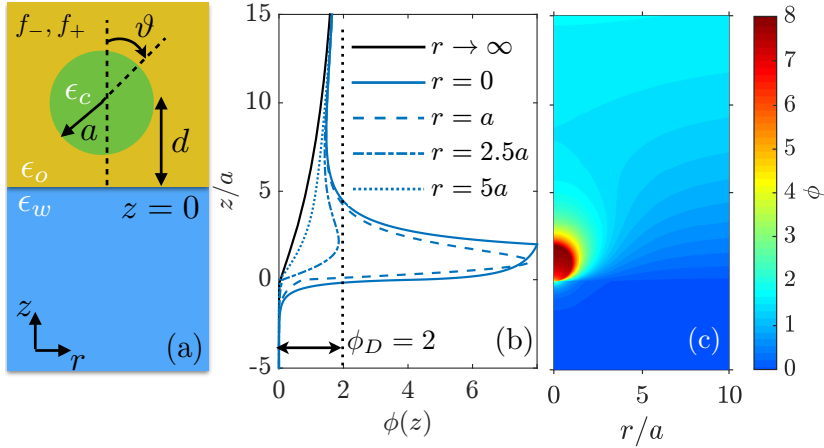
**Figure 5.1:** (a) Geometry of a colloidal sphere with radius $a = 1\ \mu m$ and a dielectric constant $\epsilon_c = 2.6$ at a distance $d$ from an oil-water interface, with the position on the colloidal surface indicated by the polar angle $\vartheta$. The oil and water are characterized by dielectric constants $\epsilon_o = 7.92$ and $\epsilon_w = 80$, respectively. The self-energies $f_- = 10$ and $f_+ = 6$ in units of $k_B T$ determine the degree of ion partitioning of the ions among the two solvents. An exemplary numerical result for the electrostatic potential for a positively charged sphere at $d = a$ is shown along the $z$ direction at fixed $r$ in (b), with the Donnan potential $\phi_D$ indicated, and as a surface plot in (c). We set the charge-regulating equilibrium constant $K_+ a^3 = 1$ ($pK_+ = 8.8$) and the screening length in oil $\kappa_o^{-1} = 10\ \mu m$.

from a planar oil-water interface[1] that separates the oil (CHB) phase ($z > 0$, dielectric constant $\epsilon_o = 7.92$) from the water phase ($z < 0$, dielectric constant $\epsilon_w = 80$), as sketched in Fig. 1(a). Since $\epsilon_c < \epsilon_o < \epsilon_w$, the VdW interaction between particle and the oil-water interface is repulsive [168, 171] for $d > a$. This repulsion is significant only for $d - a \lesssim 10$ nm given the Hamaker constant of $\sim -0.3\ k_B T$ [167]. However, the repulsion is sufficiently strong to impede adsorption to the interface [168]. Since $\epsilon_o < \epsilon_w$ the image charge potential $\Phi_{\text{im}}(d) = -\beta^{-1} Z^2 \lambda_B^o (\epsilon_w - \epsilon_0)/[4d(\epsilon_w + \epsilon_0)]$ (where $\beta^{-1} = k_B T$), which holds in the absence of salt for $\epsilon_c = \epsilon_o$ but which was shown to be accurate within a few percent also for non-index-matched colloidal particles [177], is attractive regardless the sign of $Z$ for oil-dispersed colloidal particles, but is repulsive when the particles are dispersed in the water phase [170]. Here, $\lambda_B^o = \beta e^2/4\pi\epsilon_{\text{vac}}\epsilon_o$ is the Bjerrum length in oil. A force balance between the image and VdW force shows that it is possible to trap the particle at a finite, but small, distance from the interface [167, 168], circumventing the non-tunable nature of the wetting effects. Incorporating the VdW force in our theory (unlike Ref. [150]), we show how screening and ion partitioning makes the trapping mechanism highly tunable.

We use the framework of classical density functional theory to construct the grand potential functional $\Omega[\rho_\pm, \sigma; d]$, with $\rho_\pm(\mathbf{r})$ the density profiles of (non-surface-bound) monovalent ions and $\sigma(\mathbf{r})$ the particle surface charge density. Denoting the region outside the particle by $\mathcal{R}$ and its surface by $\Gamma$, $\Omega$ is given by

---

[1] We neglect any possible interfacial deformations [191]. In the experiments of Ref. [167] no significant interfacial deformation was observed in a two-dimensional setup.

$$\beta\Omega[\rho_\pm, \sigma; d] = \sum_{\alpha=\pm} \int_{\mathcal{R}} d^3\mathbf{r}\, \rho_\alpha(\mathbf{r}) \left[ \ln\left( \frac{\rho_\alpha(\mathbf{r})}{\rho_s^w} \right) - 1 + \beta V_\alpha(z) \right] + \frac{1}{2} \int_{\mathcal{R}} d^3\mathbf{r}\, Q(\mathbf{r})\phi(\mathbf{r}) +$$

$$\tag{5.1}$$

$$\int_{\Gamma} d^2\mathbf{r} \left( \pm\sigma(\mathbf{r}) \left\{ \ln[\pm\sigma(\mathbf{r})a^2] + \ln\left( \frac{K_\pm}{\rho_s^w} \right) + \beta V_\pm(z) \right\} + [\sigma_m \mp \sigma(\mathbf{r})] \ln\left\{ [\sigma_m \mp \sigma(\mathbf{r})]a^2 \right\} \right)$$

The first term is the ideal gas grand potential of the ions coupled to the external potential $V_\alpha(z) = \beta^{-1} f_\alpha \Theta(z)$ ($\alpha = \pm$), with $\Theta(z) = [1 + \tanh(z/2\xi)]/2$, $\xi \sim 10^{-3}a$ the interface thickness and $\rho_s^w$ the bulk density in water. The preference of ions for water or oil is modeled by the energy cost $\beta^{-1} f_\alpha$ to transfer a single ion from the water to the oil phase. To mimic that cations are typically less hydrophilic than anions, we set $(f_+, f_-) = (6, 10)$. The electrostatic energy is described within mean-field theory in the second term, with the total charge density $Q(\mathbf{r}) = \rho_+(\mathbf{r}) - \rho_-(\mathbf{r}) + \sigma(\mathbf{r})\delta(|\mathbf{r} - d\mathbf{e}_z| - a)$, and the electrostatic potential $\phi(\mathbf{r})/\beta e = 25.6\, \phi(\mathbf{r})$ mV. The last term describes the free energy of a two-dimensional binary lattice gas of neutral and (either positively *or* negatively) charged groups, with a maximum charge density $\sigma_m a^2 = 10^6$ (one charged group per nm$^2$). The non-electrostatic free energy of binding an ion is characterized by $k_B T \ln(K_\pm/1\text{ M})$, with equilibrium constant $K_\pm = [\text{S}][\text{X}^\pm]/[\text{SX}^\pm]$ (or $pK_\pm = -\log_{10}(K_\pm/1\text{ M})$) that describes the adsorption of a negative *or* positive ion $\text{X}^\pm$ to a neutral surface site S, i.e. $\text{S} + \text{X}^\pm \leftrightarrows \text{SX}^\pm$.

From the Euler-Lagrange equations $\delta\Omega/\delta\rho_\pm(\mathbf{r}) = 0$ we find the equilibrium profiles $\rho_\pm(\mathbf{r}) = \rho_s(z) \exp[\mp\phi(\mathbf{r}) \pm \Theta(z)\phi_D]$, where $\rho_s(z) = \rho_s^w$ for $z < 0$ and $\rho_s(z) = \rho_s^o$ for $z > 0$, where $\rho_s^o = \rho_s^w \exp[-(f_+ + f_-)/2]$ the bulk ion density in oil. We defined the Donnan potential $\phi_D/\beta e$, with $\phi_D = (f_- - f_+)/2$, which is the potential difference between the bulk oil and water phases due to ion partitioning. Combining our expressions for $\rho_\pm(\mathbf{r})$ with the Poisson equation for the electrostatic potential, we obtain the Poisson-Boltzmann equation for $\mathbf{r} \in \mathcal{R}$,

$$\nabla \cdot [\epsilon(z)\nabla\phi(\mathbf{r})]/\epsilon_o = \kappa(z)^2 \sinh[\phi(\mathbf{r}) - \Theta(z)\phi_D], \tag{5.2}$$

where $\epsilon(z) = (\epsilon_o - \epsilon_w)\Theta(z) + \epsilon_w$. Furthermore, $\kappa(z)^2 = 8\pi\lambda_B^o \rho_s(z)$, with $\kappa^{-1}(z \to \infty)$ the Debye screening length in the bulk oil $\kappa_o^{-1}$. We fix $\kappa_o^{-1} = 10a$, close to typical experimental results, from which the screening length in water follows as $\kappa_w^{-1} = \sqrt{\epsilon_w/\epsilon_o} \exp[-(f_+ + f_-)/4]\kappa_o^{-1} = 0.58a$, which is on the high side but convenient for our numerical calculation, while the precise value of $\kappa_w^{-1}$ is unimportant for the physics in oil discussed below, as we shall see later. Inside the dielectric colloid the Poisson equation reads $\nabla^2\phi = 0$. On the colloidal surface, we have the boundary condition $\mathbf{n} \cdot [\epsilon_c\nabla\phi|_{\text{in}} - \epsilon_o\nabla\phi|_{\text{out}}]/\epsilon_o = 4\pi\lambda_B^o\sigma(\mathbf{r})$, with $\mathbf{n}$ an outward pointing normal vector and where $\sigma(\mathbf{r})$ follows from $\delta\Omega/\delta\sigma(\mathbf{r}) = 0$ [125], resulting for $\mathbf{r} \in \Gamma$ in the Langmuir adsorption isotherm [51],

$$\sigma(\mathbf{r}) = \pm\sigma_m \left\{ 1 + \frac{K_\pm}{\rho_s^o} \exp[\pm(\phi(\mathbf{r}) - \phi_D)] \right\}^{-1}. \tag{5.3}$$

Eqs. ([6.3])-([6.7]) are solved numerically for $\phi(\mathbf{r})$, from which $\rho_\pm(\mathbf{r})$ and $\sigma(\mathbf{r})$ follow, and after insertion in Eq. ([5.1]) the effective colloid-interface interaction Hamiltonian $H(d) := \min_{\rho_\pm,\sigma} \Omega[\rho_\pm, \sigma; d]$, given by

$$\beta H(d) = \int_{\mathcal{R}} d^3\mathbf{r}\ \rho_s(z)\Big\{\phi(\mathbf{r})\sinh[\phi(\mathbf{r}) - \Theta(z)\phi_D] - 2(\cosh[\phi(\mathbf{r}) - \Theta(z)\phi_D] - 1)\Big\}$$
$$- \frac{1}{2}\int_\Gamma d^2\mathbf{r}\ \sigma(\mathbf{r})\phi(\mathbf{r}) - \sigma_m \int_\Gamma d^2\mathbf{r}\ln\left\{1 + \frac{\rho_s^o}{K_\pm}\exp[\mp(\phi(\mathbf{r}) - \phi_D)]\right\}, \quad (5.4)$$

Note that $H(d)$ does not contain the colloid-interface VdW repulsion, which can be added separately, see the end of Sec. [5.3].

## 5.3 Charge regulation and colloid-interface interaction

An example of the resulting potential distribution around a positively charged colloid can be found in Fig. [5.1](b)-(c), which reveals how $\phi(\mathbf{r})$ approaches its asymptotic value $\phi_D$ at $z \to \infty$ for various axial distances $r$ from the colloid, revealing a strong coupling between the spherical and planar geometry of the colloid and the interface, respectively. Since $f_+ < f_-$ (and hence $\phi_D > 0$), the oil side is positively charged and the water side is negatively charged. This strong coupling is further illustrated in Fig. [5.2], where the (scaled) ion density is plotted for distances $d = 10a$, $5a$ and $1.5a$, in (a)-(c) for a positively charged colloid, and in (d)-(f) for a negatively charged colloid. Upon approaching the interface, the colloidal double layer deforms as ions are stripped by the water phase, since they dissolve better in water. As a consequence, the initially planar double layer at the water side strongly deforms as well. This double layer destruction was investigated earlier for a dense laterally averaged monolayer [166], but here we laterally resolve the spatial structure of the double layers for the first time, even with charge regulation taken into account.

Interestingly, the surface charge distributions $\sigma(\vartheta)$ of negative and positive charge regulating colloids, shown in the insets of Fig. [5.2], are *not* related by $\sigma(\vartheta) \leftrightarrow -\sigma(\vartheta)$ because the anti-symmetry is broken by $f_+ \neq f_-$. Here $\vartheta$ is the polar angle defined in Fig. [5.1](a). For $d \gg \kappa_o^{-1}$, the colloidal double layer has spherical symmetry, and $\sigma(\vartheta)$ is constant. Close to the interface, however, we unravel an intricate interplay between mass action and image-charge effects, which for $f_- > f_+$ enhance each other for positive colloids, and counteract each other for negative colloids. The enhanced cation (reduced anion) concentration close to the interface enhances (reduces) $|\sigma(\vartheta)|$ at the south pole $\vartheta = \pi$ for positive (negative) colloids by mass action. The image-charge effect, in contrast, is independent of the charge sign and allows charge-regulating colloids to lower their electrostatic energy by increasing $|Z|$ when the colloid approaches a medium with a higher dielectric constant. Indeed, close to the interface the dielectric effect dominates and for negative colloids the south pole is actually higher charged ($\vartheta = \pi$) than the north pole ($\vartheta = 0$), see inset in Fig. [5.2](f), in contrast to the case farther from the interface (Fig. [5.2](d),(e)). The interplay of mass action and dielectric
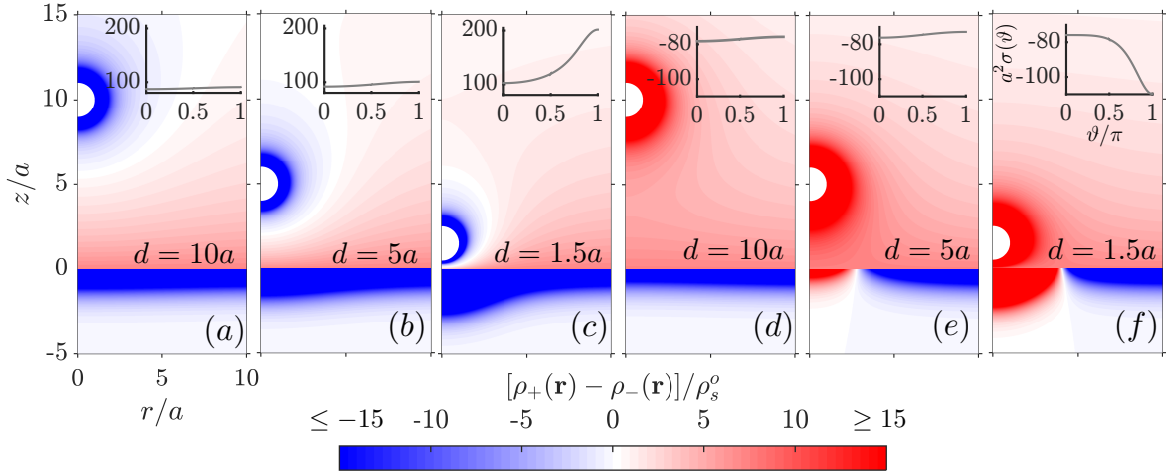
**Figure 5.2:** Double layer destruction for a charged colloid with radius $a = 1$ $\mu$m, with self-energies $(f_+, f_-) = (6, 10)$ and screening length $\kappa_o^{-1} = 10a$. In (a)-(c) the colloid is positively charged ($Z > 0$), and in (d)-(f) it is negatively charged ($Z < 0$). In both cases the equilibrium constant is $K_{\pm} a^3 = 1$ ($pK_{\pm} = 8.8$), and $\rho_s^0 = 9.3 \cdot 10^{-11}$ M and $\rho_s^w = 2.8 \cdot 10^{-7}$ M. We introduced a cut-off for the color coding to make the spatial variation of the scaled net ion density $[\rho_+(\mathbf{r}) - \rho_-(\mathbf{r})]/\rho_s^o$ clearly visible. The insets show the colloidal charge distribution $a^2 \sigma(\vartheta)$.

effects is also seen in the total colloidal charge $Z = \int_\Gamma d^2\mathbf{r} \; \sigma(\mathbf{r})$, which depends on $d$ as shown in the insets of Fig. 5.3 for low and high $|Z|$ in (a) and (b), respectively. This is not only of interest for $(f_+, f_-) = (6, 10)$, but also for $f_+ = f_- = 0$ (blue curves), to isolate the image-charge effects by switching off ion partitioning. Mass action thus increases (decreases) $|Z(d)|$ when $Z > 0$ ($Z < 0$), while dielectric effects always increase $|Z(d)|$. The image-charge effect is weak at low $|Z|$, but strong enough to drive negatively charged colloids even more negative close to the interface. Combined with ion partitioning, this yields a minimum in $|Z(d)|$ for negative colloids if the charge is sufficiently high (Fig. 5.3(b)).

In Fig. 5.3 we plot the colloid-interface interaction potential $\Phi(d) = H(d) - H(\infty)$, which is repulsive for $Z < 0$ (red curve) and attractive for $Z > 0$ (green curve) provided that $f_+ < f_-$. The blue curves, for $f_+ = f_- = 0$, show a much smaller $|\Phi(d)|$, showing that the particle-interface interaction is dominated by ionic rather than image-charge like effects. We also compare $\Phi(d)$ to that of constant-charge particles (dashed-dotted curves), for which the second term in Eq. (5.1) is absent, showing only quantitative differences, meaning that only the sign of the colloidal charge determines the colloid-interface interaction to be attractive or repulsive. Hence, an extended charge regulation mechanism that allows colloids to change the sign of their charge as function of e.g. the salt concentration, allows one to tune attractions into repulsions or vice versa. If the VdW interaction is repulsive, a trapped colloid near the interface can be pushed towards the bulk, because the repulsion has a much longer range $(\kappa_o^{-1})$ than the range of the VdW repulsion. Our calculations also reveal that it is possible to impede adsorption in the case of an attractive VdW interaction, since for $\phi_D > 0$ and $Z < 0$ (or as we
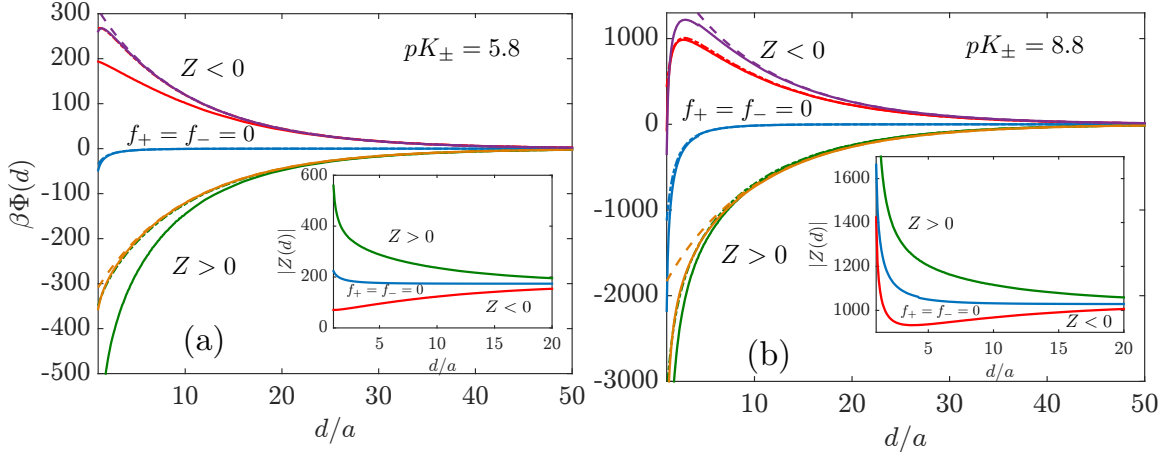
**Figure 5.3:** Colloid-interface potential $\Phi(d)$ for oil screening length $\kappa_o^{-1} = 10a$. The full curves are the results of a charge regulation boundary condition with equilibrium constants (a) $pK_{\pm} = 5.8$ and (b) $pK_{\pm} = 8.8$. The red (green) curves are for a negative (positive) colloid with self-energies $(f_+, f_-) = (6, 10)$, the blue curves are for $f_+ = f_- = 0$ and are independent of the sign of $Z$. The dashed-dotted red and green curves are for constant-charge particles with a charge coinciding with the charge of the full curves at $d \to \infty$. The insets show the absolute charge $|Z(d)|$. The orange ($Z > 0$) and purple ($Z < 0$) full curves show the approximation $\tilde{\Phi}(d)$, the dashed purple and orange curves represent $Z(\infty)\phi_0(d)$, and the blue dashed-dotted curve represent the dielectric contribution $\Phi_{\mathrm{di}}(d)$ (see text).

shall see later also for $\phi_D < 0$ and $Z > 0$) there is a wetting-preventing energy barrier whose location and height can be tuned by the magnitude of $|Z|$ and/or $\phi_D$. This is similar to how water-dispersed colloids are repelled from an oil-water interface by image-charge repulsions, however in this case the strength of the repulsions are only tunable by changing the magnitude of $Z$ [170].

To further analyze the colloid-interface interactions, we consider $\tilde{\Phi}(d) = Z(\infty)\phi_0(d) + \Phi_{\mathrm{di}}(d)$, with $\phi_0(z)$ the (analytically available) Gouy-Chapman-like electrostatic potential without any colloid present [176] (see Appendix) as plotted in Fig. 5.1(b) (black full line), and $\Phi_{\mathrm{di}}(d) = \Phi(d)|_{f_+=f_-=0}$, the purely dielectric numerically obtained interaction potential. In this empirical approximation for $\Phi(d)$, $\phi_0(d)$ acts as an external (electric) potential for a colloid with charge $Z(\infty)$. The full orange and purple curves in Fig. 5.3 show that $\tilde{\Phi}(d)$ is a good approximation for $\Phi(d)$. Hence, $\kappa_o^{-1}$ is the relevant length scale for the colloid-interface interaction, confirming that $\Phi(d)$ is insensitive to the precise value of $\kappa_w^{-1}$. However, the dashed ones, which only represent $Z(\infty)\phi_0(d)$, and thus ignore the image-charge-like effects, are in fact also quantitative, except for charge-regulating particles close to the interface. It turns out that $\tilde{\Phi}$ approximates $\Phi$ for constant-charge particles perfectly if $|Z|$ is low, as is seen in Fig. 5.3(a) from the regime where the full orange and purple curves coincide with the dashed-dotted green and red curves, respectively.

To estimate whether $Z(\infty)\phi_0(d)$ or $\Phi_{\mathrm{di}}(d)$ is dominant, we equate both terms in absolute value at contact, $|Z(\infty)\phi_0(a)| = \Phi_{\mathrm{di}}(a)$, and approximate $\Phi_{\mathrm{di}}(a) \approx \Phi_{\mathrm{im}}(a)$ with $\epsilon_w \gg \epsilon_o$. The latter approximation gives an upper bound for the image-charge attractions, since salt will enlarge screening if no ion partitioning is included. We find

that ion partitioning dominates image charges when $|Z(\infty)|\lambda_B^o/4a$ is small compared to $|\phi_D|$, as is the case in Fig. 5.3(a). In Fig. 5.3(b), we have $|Z(\infty)|\lambda_B^o/4a \sim |\phi_D|$, such that dielectric effects and ion partitioning are both important, although the dielectric effects are significant only for $d < \kappa_o^{-1}$. For $|Z(\infty)|\lambda_B^o/4a \gg |\phi_D|$, dielectric effects would dominate; however, it is hard to enter this regime experimentally, as it would require either fine-tuning the self-energies $f_\alpha$ to obtain extremely small Donnan potentials or particle charges exceeding $\mathcal{O}(10^4)$ in oil. Hence, the tunable Donnan potential is important in most experimental setups, and can be measured [192]. Moreover, we note that changing the sign of $Z(\infty)$ is equivalent to interchanging $f_+ \leftrightarrow f_-$, changing only the sign of $\phi_D$, showing that the nature of the particle-interface interactions can also be tuned by changing the *type* of salt. Finally, when multiple ions are included, $\phi_D$ will depend not only on the self-energies, but also on the bulk ion *concentrations* [176], extending even further the tunability options. We will focus on the influence of multiple ion species in Chapter 6.

Before ending this section, we will comment on how the shape of $\Phi(d)$ changes, when a repulsive VdW interaction is added, given by

$$\Phi_{\text{VdW}}(d) = -\frac{A_H}{6}\left[\frac{1}{d/a - 1} + \frac{1}{d/a + 1} + \ln\left(\frac{d/a - 1}{d/a + 1}\right)\right], \qquad (5.5)$$

for a sphere of radius $a$ at a distance $d$ from a planar interface, with $A_H$ the Hamaker constant [171]. Eq. (5.5) reduces to $\Phi_{\text{VdW}}(d) = -A_H/[6(d/a - 1)]$ for $d/a - 1 \ll 1$. In Fig. 5.4 we show how the results of Fig. 5.3 change with the VdW potential added. As explained before, we indeed see that $\Phi_{\text{VdW}}$ is only important for small $d$, but it is strong enough to impede adsorption of the colloid on the oil-water interface. This also shows that the location of the minimum depends on the magnitude of the colloidal charge, which is also expected when only the image charge potential is taken into account, see Ref. [168], since such a force balance also give rise to a equilibrium distance that depends on $Z$. Moreover, in Fig. 5.4 we see for small $Z$ that there is a no mimimum in $\Phi(d)$. This is because the image forces scale like $Z^2$ while the colloid-ion forces scale like $Z$, therefore the image forces cannot provide enough attraction to overcome the VdW repulsion when $|Z|$ is reduced.
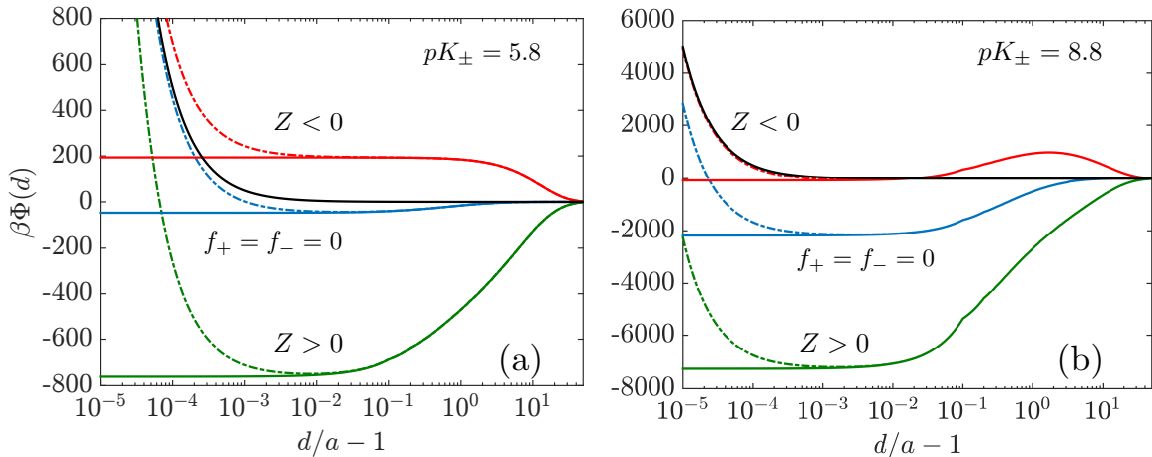
**Figure 5.4:** Contributions to the colloid-interface potential as a function of the surface-to-surface separation $d - a$ in units of the colloidal diameter $a = 1\ \mu$m, where $d$ is the center-to-surface distance between sphere and interface. The full lines are the same colloid-interface potential $\Phi(d)$ as is plotted in Fig. 5.3 for the charge regulation cases. The black full line is the van der Waals interaction $\Phi_{\mathrm{VdW}}$ with Hamaker constant $\beta A_H = -0.3$ and the dashed-dotted lines show $\Phi(d) + \Phi_{\mathrm{VdW}}(d)$, showing that the Van der Waals forces give significant additional repulsion only for $d - a \lesssim 10^{-2}a = 10$ nm, but strong enough to overcome the attractions induced by the Donnan potential for $Z > 0$.

# 5.4 Lateral colloid-colloid interactions of interfacially trapped colloids

Having discussed colloid-interface interactions, we end this chapter with colloids that can penetrate an oil-water interface. A part of the colloidal surface is then exposed to the water phase, while the remaining part is exposed to the oil phase. Such systems have received a great deal of attention in recent years, both in experimental [179, 193–197], and in theoretical work [156, 177, 178, 198–203], showing dipolar interactions between the trapped colloids within Debye-Hückel theory [199], with logarithmic corrections to it when charge renormalization is included [178].

In the theoretical treatments up to now one often neglects the ions in the oil phase, assuming effectively unscreened Coulomb interactions or a vanishingly small surface charge in the oil phase. This approximation is actually more suitable for colloids trapped at an air-water interface, because the small ion concentration in oil cannot always be neglected, as we have seen in the previous section. To our best knowledge, the only work where salt is explicitly taken into account for colloids that penetrate an oil-water interface is Ref. [204], where two colloids within the Derjaguin approximation[2] are studied at an oil-water interface. Although different Debye screening lengths are taken into account for the two media, the Donnan potential across the interface and the dielectric contrast between particle and the two media are not taken into account. Furthermore, in all theoretical approaches the small, but finite width of the interface

---

[2]In this approximation one looks at very small colloid-colloid distances, so that the colloids can be approximated by flat plates [205]

has not been taken into account.

There is ample discussion in the literature whether the interaction goes "through" the oil, or "through the water phase". This nomenclature is often used by saying that if one changes something in phase X (X being either oil or water), which gives some observable effect, one assumes that the interaction "goes through phase X". For example, if a two-dimensional interfacial crystal melts by the addition of salt to the water phase, then one assumes that the interaction is going "through the water phase". Whenever it goes "through" the oil, one attributes this due to the relatively small amount of residual charges on the oil-exposed part of the colloidal surface, which are screened relatively weakly compared to the high surface charge at the water side. For example, for the experimentally observed colloidal Wigner crystals formed at the interface in Refs. [193, 195], it is assumed that the interaction goes through the oil, because these crystals seem to be very robust to changes at the water side of the oil-water interface. However, there is still no consensus regarding this matter, because recent experiments showed a small electrolyte dependence at the water side [179, 206].

This motivates us to investigate whether high surface charges and high screening are important *or* low surface charges and weak screening for the colloid-colloid effective potential. Our goal here is to shed some light on this by a simple calculation within a cylindrical cell model. We not only include ion partitioning, screening of the two phases, and interfacial effects, but also many-body effects within a colloidal monolayer at the interface. Moreover, we consider that the particle may not be positioned necessarily equatorially at the interface, which has not been investigated in detail in the literature up until now.

The PB equation that has to be solved is identical to the one posed in Eq. (5.2), with the main difference that we now solve Eq. (5.2) for a cylinder with a finite radius $R$, but still with an "infinite" length that extends to the bulk oil and water phase. Similarly to the spherical cell model that we have used in the previous chapters of this thesis, $R$ is related to the surface packing fraction via $\varphi = (a/R)^2$. The key quantity that we use to assess the relative importance of oil and water phases is the stress tensor $\sigma_{ij}(\mathbf{r})$, which can, for example, be derived by applying Noether's theorem to Eq. (5.4),

$$\sigma_{ij}(\mathbf{r}) = \sigma_{ij}^{\max}(\mathbf{r}) + \sigma_{ij}^{\mathrm{osm}}(\mathbf{r}), \tag{5.6}$$

where we introduced the Maxwell stress tensor $\sigma_{ij}^{\max}(\mathbf{r})$,

$$\beta\sigma_{ij}^{\max}(\mathbf{r}) = \frac{\epsilon(z)}{4\pi\epsilon_o\lambda_B^o}\left[\partial_i\phi(\mathbf{r})\partial_j\phi(\mathbf{r}) - \frac{1}{2}|\nabla\phi(\mathbf{r})|^2\delta_{ij}\right], \tag{5.7}$$

and the osmotic part $\sigma_{ij}^{\mathrm{osm}}(\mathbf{r})$ given by

$$\beta\sigma_{ij}^{\mathrm{osm}}(\mathbf{r}) = -2\rho_s(z)\{\cosh[\phi(\mathbf{r}) - \phi_D\Theta(z)] - 1\}\delta_{ij}. \tag{5.8}$$

Whereas it is meaningful to talk about the local stress within a cylindrical cell model, we note that the total force acting on a colloid residing in such a cell, which can be found by integrating the stress tensor over a closed oriented surface, equals
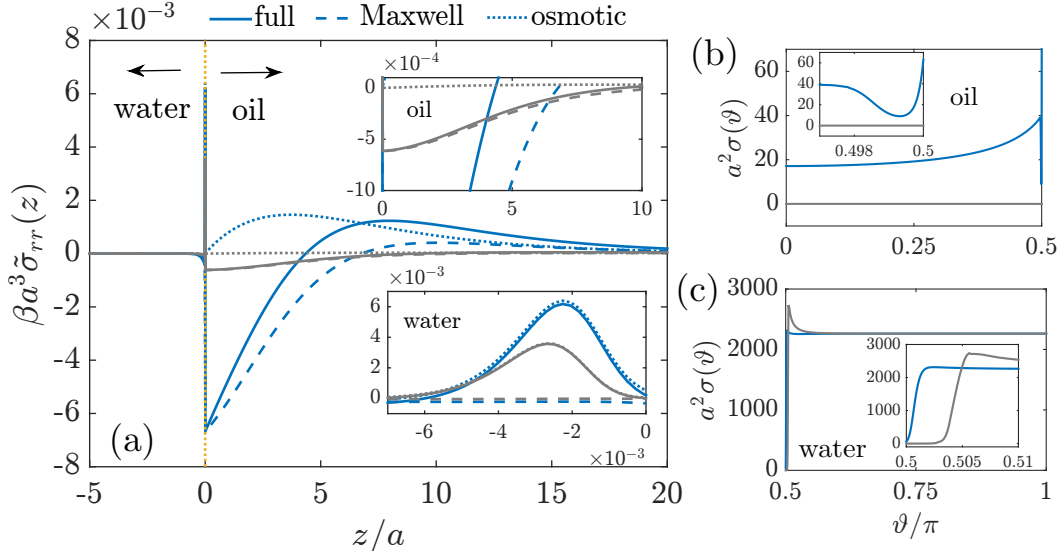
**Figure 5.5:** (a) Various contributions to the reduced stress tensor $\tilde{\sigma}_{rr}(z)$ for a colloidal monolayer described within a cylindrical cell model with surface packing fraction $\varphi = 0.01$. The particles have radius $a = 1$ $\mu$m positioned at $d = 0$ at an interface between oil (dielectric constant $\epsilon_o = 2$) and water (dielectric constant $\epsilon_w = 80$), with a Donnan potential across the interface of $\phi_D/(\beta e) = 2$, and the Debye screening length in water is always $\kappa_w^{-1} = 0.3a$. The oil-exposed side can become positively charged with equilibrium constant $K_o a^3 = 10^2$ for the blue lines at screening length in oil $\kappa_o^{-1} = 10a$, while it is uncharged $K_o a^3 \to \infty$ for the grey lines with $\kappa_o^{-1} = 100a$. The water-exposed side has always an equilibrium constant of $K_w a^3 = 10^4$. We see that the full $\tilde{\sigma}_{rr}$ has an osmotic (dotted) and a Maxwell (dashed) contribution that are both significant in oil, but for the water side only the osmotic part gives a significant contribution (see bottom inset). The osmotic part is reduced almost to zero when no charges in oil are present as seen in the top inset. The vertical dotted yellow line indicates the oil-water interface. In (b) we plot the surface charge density $\sigma(\vartheta)$ for the oil-exposed side, and in (c) for the water-exposed side separately, because of the order of magnitude difference. Furthermore, in order to resolve $\sigma(\vartheta)$ close to the oil-water interface, we show a zoomed-in version of $\sigma(\vartheta)$ in (b) and (c).

zero by the assumption of cylindrical symmetry. Therefore, we choose to investigate at first instance $\sigma_{rr}(r = R, z)$. Upon inspection of Eq. (5.7) we see, however, that the Maxwell stress tensor only contains derivatives with respect to $z$, because a single cell is globally charge neutral by construction. This means that even a colloid-free cell has a non-zero $rr$ component to the stress tensor $\sigma_{rr}^0(r = R, z)$ because of the Donnan potential that is developed across the interface. The back-to-back double layer at the oil-water interface also gives rise to a non-zero osmotic part. These colloid-free contributions to the stress tensor would only lead to a constant as function of colloid-colloid distance in force calculations of colloids within a two-body approximation, and henceforth, we find it more meaningful to investigate instead the reduced stress tensor $\tilde{\sigma}_{rr}(z) = \sigma_{rr}(r = R, z) - \sigma_{rr}^0(r = R, z)$. Similar to Eq. (5.6), we define the reduced Maxwell and osmotic part of $\tilde{\sigma}_{rr}(z)$ by $\tilde{\sigma}_{rr}^{\max}(z)$ and $\tilde{\sigma}_{rr}^{\text{osm}}(z)$, respectively.

In contrast to previous sections, we do not fix $f_+$, $f_-$ and $\kappa_o^{-1}$, but we fix equivalently $\kappa_o^{-1}$, $\kappa_w^{-1}$ and $\phi_D$. We also modify the model in Sec. 5.2 to accomodate for the fact that there is a different equilibrium constant for the colloidal particle in water $K_w$ and

in oil $K_o$. This accounts for non-electrostatic effects in the adsorption process on the colloidal surface which depends on the type of solvent, while the electrostatic ones are taken into account by the difference in dielectric constants between oil and water. We take into account cationic adsorption only, we fix the surface packing fraction $\varphi = 0.01$ and set[3] $\epsilon_o = 2$. Unless stated otherwise, the other parameters are taken the same as in previous sections.

First, we investigate the various contributions to $\tilde{\sigma}_{ij}(z)$ for the parameters $\kappa_o^{-1} = 10a$, $\kappa_w^{-1} = 0.3a$, $\phi_D = 2$ in Fig. 5.5, showing in (a) how the osmotic contribution compares to the Maxwell part for $K_w a^3 = 10^4$ and $K_o a^3 = 10^2$ (blue line) and $K_o a^3 = \to \infty$ (grey line). As one would expect, we see from $\sigma(\mathbf{r})$ that the colloidal surface is more strongly charged in water than in oil, and there are no surface charges at the oil side for $K_o a^3 = \to \infty$. At the water side, the osmotic part gives always the largest contribution. At the oil side it is the Maxwell part, unless the oil-exposed part of the colloidal surface is charged, which gives rise to a significant osmotic part. Close to the oil-water interface $\sigma(\vartheta)$ increases at the oil-exposed side and at the water-exposed side, which can be rationalized according to the dielectric and mass-action effects of the previous section. However, there is also an interfacial effect: close to the interface the oil-exposed side increases in charge because of the dielectric profile that we use, and similar reasonings hold for the water-exposed side.

Although the charge is much lower in oil, the longer screening length gives rise to a larger contribution to the stress in oil than in water, where the screening length is much smaller for a higher charged surface. The stress at the water side seems to be more concentrated close to the interface, while it is more extended in the oil phase. Surprisingly, this still holds in the absence of oil-exposed colloidal surface charges, which can be seen from the grey line in Fig. 5.5(a). In addtition, we find $|\int_{z<0} dz\ \tilde{\sigma}_{rr}(z)| < |\int_{z>0} dz\ \tilde{\sigma}_{rr}(z)|$ suggesting that the electrostatics in oil is more important. Maybe counter-intuitive for no colloidal charges at the oil-exposed side, this has already been suggested by Frydel [178] and later investigated in Ref. [203] to explain the weak electrolyte dependence at the water side on the stability of interfacial colloidal crystals. It was found that electrical field lines that penetrate from the water, through the colloid and to the oil, gives rise to an apparent oil-exposed surface charge, because of the dielectric mismatch of the colloid and the surrounding media. The apparent surface charge is by definition zero for $\epsilon_c \to 0$, however, within our cell model we actually find that in this limit there is still a contribution to $\tilde{\sigma}_{rr}(z > 0)$. This suggests that not only the dielectric mismatches are relevant, but also many-body effects, since they can alter the field line distribution at the oil-exposed colloidal surface. We take this effect into account by using a cell model, in contrast to the single-particle picture of Ref. [203].

Finally, we check the sensitivity of $\tilde{\sigma}_{rr}(z)$ to various parameters in our model, as is shown in Fig. 5.6. In (a) we show the influence of $\kappa_o^{-1}$ revealing that $\tilde{\sigma}_{rr}(z)$ is reduced when less ions are present in the oil. Moreover, the positive contribution that is dominated by the osmotic part is decreased more than the Maxwell part. The water

---

[3]This is a formality to ensure that the colloid can penetrate the interface. Typically this value corresponds to solvents like decane or octane.
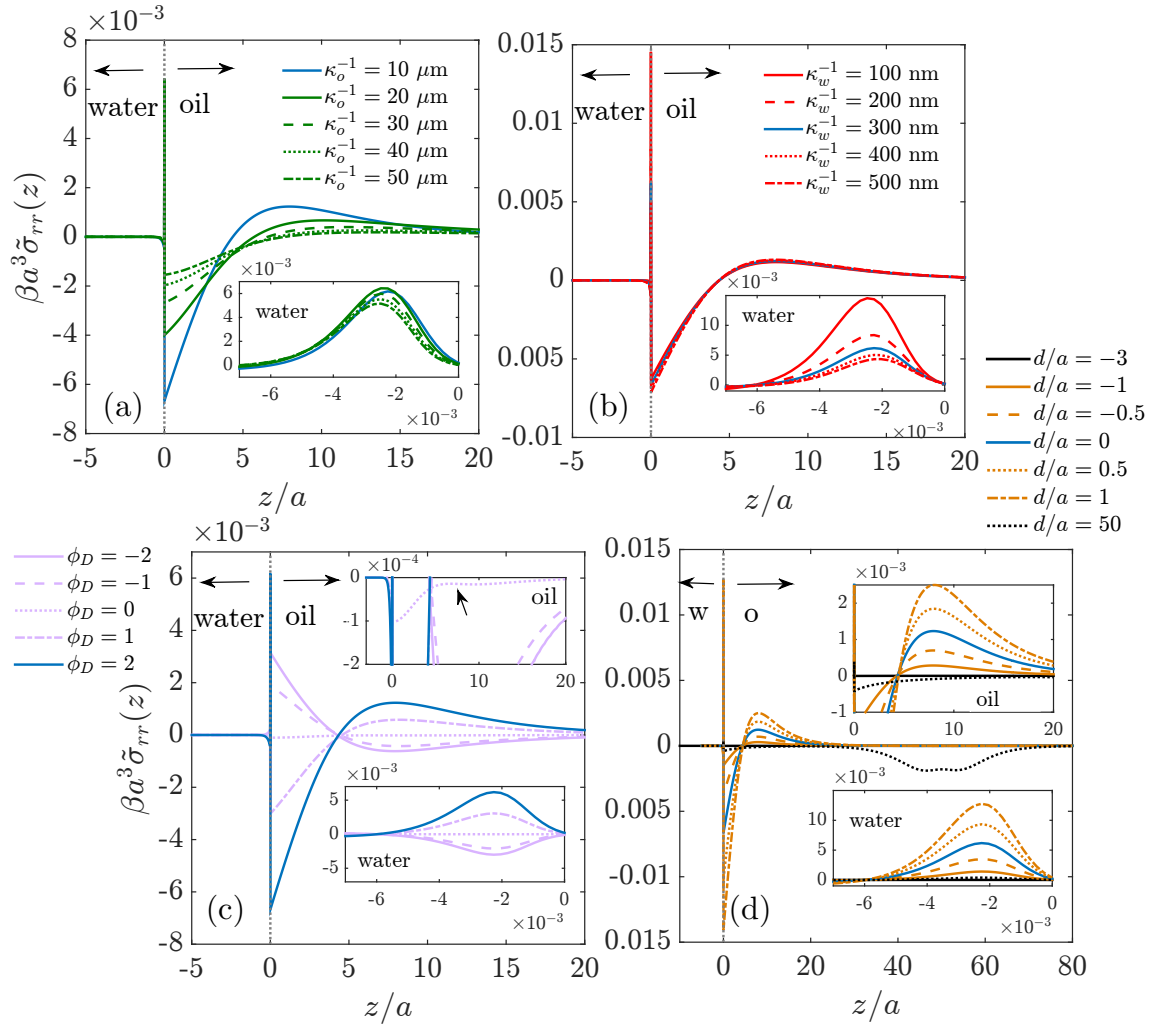
**Figure 5.6:** Same as in Fig. 5.5, but now we vary in (a) the Debye screening length in oil, (b) the Debye screening length in water, (c) the Donnan potential and (d) the position $d$ of the centre-of-mass of particle as measured from the oil-water interface at $z = 0$. Again we zoom in on the water side to resolve the narrow peak close to the oil-water interface in the insets. We also zoom in on the oil side for (c) and (d) in the top insets. In (c) we emphasize the small contribution to $\tilde{\sigma}_{rr}(z)$ at $\phi_D = 0$ indicated by the arrow, which is much higher than at the water side.

side is hardly influenced, as can be seen in the inset. In (b) we show the same plot, but now by varying $\kappa_w^{-1}$, and we observe that only the water side is influenced. In (c) we show that $\phi_D$ can affect the sign of $\tilde{\sigma}_{rr}(z)$. Even when $\phi_D = 0$, we see, however, that the oil side is more important as is shown in the inset by the black arrow. Finally, in (d) we show how $\tilde{\sigma}_{rr}(z)$ changes when the particle is brought from the bulk water, through the interface, to the bulk oil. If the particle is in bulk water, the reduced stress vanishes, but it is increased at the water *and* oil side upon increasing $d$. When the particle is in bulk oil, there is a significant contribution to the reduced stress, because of the long-ranged extension of the colloidal double layer.

Is the interaction going through the oil or through the water? Based on these calculations, it is tempting to say that it goes "through the oil": long screening lengths and thus extended double layers have a stronger influence on the colloid-colloid effective potential than a high surface charge density that is weakly screened. We expect, however, that such a picture would break down if the interparticle separation would be smaller than $\kappa_w^{-1}$. However, this is often a regime with very high surface coverage $\varphi$ and is not expected to be important for long-ranged repulsive colloids.

## 5.5 Conclusions

Our work shows the importance of a low, but non-zero salt concentration in oil for colloidal dispersions in an oil-water medium. We showed that tuning the sign of the colloidal charge or of the Donnan potential can change attractive colloid-interface interactions into repulsions for colloids that cannot penetrate the oil-water interface. This sheds light on the very recent experimental studies by Elbers *et al.* [167, 207], who not only showed that adding a salt with $f_+ < f_-$ to the oil changes $Z > 0$ to $Z < 0$, but also that particles are repelled from the interface to the bulk. Our calculations support this observation, since attractions become repulsions (Fig. 5.3) upon changing the sign of the colloidal charge, if a suitable charge regulation mechanism is provided. We will explore this further in the next chapter. Moreover, the range of the repulsion is of the order $\kappa_o^{-1}$, much larger than the range of the VdW repulsion, that was proposed earlier as the responsible mechanism [168]. Our findings also have a yet unexplored repercussion in the case of a VdW *attraction*, since the Donnan potential impedes adsorption of oil-dispersed colloids by a salt-tunable energy barrier for $Z(\infty)\phi_D < 0$. The Donnan-potential mechanism proposed here should help in designing tunable and reversible Pickering emulsions, which can be applied in drug delivery and food processing [208, 209], but also for novel experiments where an ion flux can induce repulsive or attractive surface-specific interactions depending on the surface chemistry of the suspended particles [210].

Finally, for colloids that can penetrate the oil-water interface, we found that the lateral colloid-colloid effective interactions are dominated by the electrostatics in the oil phase, where we showed also the relevance of many-body effects. For future work, we will focus on the *nature* of the lateral interactions within a cylindrical cell model and the two-body approximation. The first can be, for example, investigated by the $R$

dependence of the grand potential of a cylindrical cell. Within a two-body approach the type of interaction can directly be assessed from the decay of the colloid-colloid effective interaction potential, for which the methods of Chapter 4 can be used. This approach needs, however, a full three-dimensional calculation, since no symmetry can be exploited for two colloids trapped at an oil-water interface[4].

**Acknowledgements** Nina Elbers and Jessi van der Hoeven are thanked for their many discussions on the experiments that they performed, that ultimately led to starting the project on colloid-interface interactions. Sela Samin is thanked for his general insights and collaboration on this project, and his numerical expertise that helped performing the calculations in this chapter.

# Appendix: Some simple analytical solutions

For completeness, we present some simple analytical solutions to the theory of Sec. 5.2.

### No colloids

If there are no colloids, and in the limit that $\xi \downarrow 0$, the Poisson-Boltzmann equation is analytically solvable. The boundary value problem reduces to

$$\phi''(z) = \begin{cases} \kappa_w^2 \sinh[\phi(z)], & z < 0, \\ \kappa_o^2 \sinh[\phi(z) - \phi_D], & z > 0. \end{cases} \tag{5.9}$$

Equivalent to the boundary condition $\phi'(z) = 0$ for $z \to \pm\infty$, we can impose charge neutrality of the bulk fluids, this gives us the boundary conditions $\lim_{z\to-\infty} \phi(z) = 0$ and $\lim_{z\to\infty} \phi(z) = \phi_D$. Together with these boundary conditions, the solution can be found to be

$$\phi(z) = \begin{cases} 2\log\left\{\dfrac{1 + C_w \exp[\kappa_w z]}{1 - C_w \exp[\kappa_w z]}\right\}, & z < 0 \\ 2\log\left\{\dfrac{1 + C_o \exp[-\kappa_o z]}{1 - C_o \exp[-\kappa_o z]}\right\} + \phi_D, & z > 0, \end{cases} \tag{5.10}$$

with integration constants $C_w$ and $C_o$. Moreover, $\phi$ is continuous at $z = 0$ and there is a continuity condition for the dielectric displacements, $\epsilon_w \phi'(0^-) = \epsilon_o \phi'(0^+)$. If we

---

[4]Actually, an attempt to such a calculation has already been performed in Ref. [202], but there the dielectric constant of the colloid, ion partitioning and screening in both media have not been taken into account. What is actually more severe at first sight, is that they only took into account the Maxwell stress tensor and "forgot" the osmotic part in the force calculations. Surprisingly, they did, however, get good agreement with experiment. We can understand this from our calculations, because for non-charged oil-exposed colloidal surfaces, there is only an osmotic contribution at the water side, see Fig. 5.5(a). This stress is very localized, and can therefore be neglected. Their approach, however, breaks down when the oil-exposed side is charged.

define $\chi := \kappa_w \epsilon_w / (\kappa_o \epsilon_o)$, then the integration constants can be compactly written as

$$C_w = \frac{\chi + \cosh(\phi_D/2) - \sqrt{1 + \chi^2 + 2\chi \cosh(\phi_D/2)}}{\sinh(\phi_D/2)}, \tag{5.11}$$

and

$$C_o = \frac{\sqrt{1 + \chi^2 + 2\chi \cosh(\phi_D/2)} - 1 - \chi \cosh(\phi_D/2)}{\chi \sinh(\phi_D/2)}. \tag{5.12}$$

Finally, we find the density profiles

$$\rho_\pm(z) = \begin{cases} \rho_s^w \left[ \dfrac{1 \mp C_w \exp(\kappa_w z)}{1 \pm C_w \exp(\kappa_w z)} \right]^2, & z < 0 \\[2ex] \rho_s^o \left[ \dfrac{1 \mp C_o \exp(-\kappa_o z)}{1 \pm C_o \exp(-\kappa_o z)} \right]^2, & z > 0. \end{cases} \tag{5.13}$$

**Single colloid with a fixed charge, without salt**

The colloid-interface interaction can analytically be derived for a single colloid with fixed charge $Z$ in the limit where $\rho_s = 0$. For $\xi \downarrow 0$ this amounts to solving the Laplace equation $\nabla^2 \phi(\mathbf{r}) = 0$ for $\mathbf{r} \in \mathcal{R} \backslash \Gamma$ together with the boundary condition.

$$\mathbf{n} \cdot \nabla \phi(\mathbf{r}) = -\frac{Z \lambda_B^o}{a^2}, \quad \mathbf{r} \in \Gamma, \tag{5.14}$$

where we assumed that $\epsilon_c = 0$. Taking the correct dielectric contrast into account would give small corrections to the colloid-interface potential close to the interface, as was shown in Ref. [177]. There are continuity conditions $\epsilon_o \partial_z \phi(r, 0^+) = \epsilon_w \partial_z \phi(r, 0^-)$ and $\phi(r, 0^+) = \phi(r, 0^-)$ for all $r$, with $r$ the radial coordinate in cylindrical coordinates. The Laplace equation is then easily solved by the method of images. We place an image charge at $z = -d$ with charge number $Z_{\text{image}} = (\epsilon_o - \epsilon_w)/(\epsilon_o + \epsilon_w)Z$. The solution to the Laplace equation is then

$$\phi(r, z) = \lambda_B^o \left[ \frac{Z}{\sqrt{r^2 + (z-d)^2}} + \frac{Z_{\text{image}}}{\sqrt{r^2 + (z+d)^2}} \right], \tag{5.15}$$

only valid for $d > a$ and $z > 0$. The effective colloid-interface potential in this case is

$$\beta \Phi(d) = \frac{1}{2} \int_\Gamma d^2 \mathbf{r} \ \sigma \phi(r, z) = \frac{Z^2 \lambda_B^o}{4d} \frac{\epsilon_o - \epsilon_w}{\epsilon_o + \epsilon_w}, \quad d > a, \tag{5.16}$$

where we used $\sigma = Z/(4\pi a^2)$ and we ignored an overall constant. Note that the force from such a potential is attractive towards the interface since typically $\epsilon_o < \epsilon_w$.

# 6

# Colloid-interface interactions in the presence of multiple ion species

*We investigate colloid-interface interactions of a non-touching positively charged colloid dispersed in an apolar medium in which multiple types of ions are dissolved. We investigate the effects of various charge-regulation mechanisms on the effective interaction potential, including the influence of multiple ion species in oil and in water. The colloid-ion forces, which can be understood by the ion distributions without any colloidal particle present, are investigated within Poisson-Nernst-Planck theory to qualitatively understand the experimentally observed salt-dependent dynamics of non-touching colloidal particles.*

## 6.1 Introduction

Many electrolyte solutions in living systems contain multiple ion species like $Na^+$, $K^+$, $Mg^{2+}$ and $Cl^-$. The concentration of these ions and their affinity to bind to specific proteins determine the intake of ions from the extracellular space to the intracellular one [112]. In this example the concentration of *multiple* ion species is used to *tune* various biologial processes, however, this scenario is not only limited to living systems, but they can also be important for ionic liquids [211], batteries [212], electrolytic cells [176], and even colloidal systems [167, 207, 213], as we shall show in this chapter.

To be more specific, we will focus on an oil-water system, where oil-dispersed colloids are found to be trapped near the oil-water interface, without penetrating it, due to a force balance between a repulsive van der Waals and an attractive image-charge force between colloid and interface [168, 171]. In Chapter 5 we showed within a single-particle picture that the interaction of such a non-touching colloid with an oil-water interface is highly tunable from attractive to repulsive for large enough distances by changing the sign of the product $Z\phi_D$, where $Ze$ is the colloidal charge and $\phi_D/\beta e$ the

Donnan potential. Tunability of these colloid-ion forces will also be a central subject in this chapter.

Tuning the interaction potential through $Z\phi_D$ is quite general, however, due to global charge neutrality, the salt concentrations in a binary mixture of positive and negative ions cannot be varied independently; in other words, $Z\phi_D$ is always of a definite sign for a given choice of two ions. This motivates us to extend the formalism of Chapter 5 by including multiple ion species. Including at least a second salt compound where one ion species is the same for two salts (*e.g.*, $Cl^-$ in a mixture of NaCl and KCl), allows us to independently vary the ion concentrations. Because of this independence, it is then possible to tune the sign of the colloidal charge by changing the salt concentration of one the two species. Furthermore, for more than two types of ions, the Donnan potential depends not only on the difference in the degree of hydrophilicity between the various species [173], but also on the bulk ion concentrations [176]. This leads to tunability of the magnitude, and possibly even the sign of the Donnan potential. We apply our theory to experiments, where trapped colloids near an oil-water interface could be detached by the addition of an organic salt to the oil phase [167, 207, 213].

As a first step, we will set up the density functional that we will consider in this chapter in Sec. 6.2. We will do this in full generality, by first working out the minimal example of only one salt species, and later, by adding a second salt with an anion that is same as the other salt. In Sec. 6.3 we describe the experiment that we want to explain. In Sec. 6.4, we explore the equilibrium effective colloid-interface interaction potentials as function of salt concentration. In Sec. 6.5, we look at the influence of ion dynamics within Poisson-Nernst-Planck theory and investigate how the system equilibrates if no colloid is present. We conclude this chapter by explaining how our results can explain the recent experiments of Elbers *et al.* [167, 207, 213], where multiple ion species were needed to detach colloids from an interface between cyclohexylbromide (CHB) and water.

## 6.2  Density functional

Consider two halfspaces of water ($z < 0$, dielectric constant $\epsilon_w = 80$) and oil ($z > 0$, dielectric constant $\epsilon_o$) at room temperature $T$. We approximate the dielectric profile by $\epsilon(z) = (\epsilon_o - \epsilon_w)\Theta(z) + \epsilon_w$, with $\Theta(z) = [1 + \tanh(z/2\xi)]/2$ and $\xi$ the interface thickness which is situated at $z = 0$. Since we take $\xi$ to be small, we can interpret $\Theta$ as the Heaviside step function within the numerical accuracy. The $N_+$ species of monovalent cations and $N_-$ species of monovalent anions can either be present as free ions in the two solvents, which can be described by density profiles $\rho_{i,\alpha}(\mathbf{r})$ ($i = 1, ..., N_\alpha$, $\alpha = \pm$) with bulk densities in water (oil) $\rho_{i,\alpha}^w$ ($\rho_{i,\alpha}^o$), or are bound to the surface of a charged colloidal sphere (dielectric constant $\epsilon_c$, radius $a$, distance $d$ from the interface) with areal density $\sigma_{i,\alpha}$. The colloidal surface charge density $e\sigma(\mathbf{r})$ is given by $\sigma = \sum_{i=1}^{N_+} \sigma_{i,+} - \sum_{i=1}^{N_-} \sigma_{i,-}$. The ions can partition among water and oil, which is modeled by the external potentials $V_{i,\alpha}(z) = \beta^{-1} f_{i,\alpha}\Theta(z)$ (where $\beta^{-1} = k_B T$) where the self-energy $f_{i,\alpha}$ is defined as the energy cost in units of $k_B T$ to transfer a single ion from the water to the oil phase.

The effects of ion partitioning and charge regulation can elegantly be captured within the grand potential functional $\Omega$, given by

$$\Omega\left[\{\rho_{i,\pm},\sigma_{i,\pm}\}_{i=1}^{N_\pm};d\right] = \mathcal{F}\left[\{\rho_{i,\pm},\sigma_{i,\pm}\}_{i=1}^{N_\pm};d\right] \tag{6.1}$$

$$-\sum_{\alpha=\pm}\sum_{i=1}^{N_\alpha}\int d^3\mathbf{r}\left[\mu_{i,\alpha}-V_{i,\alpha}(z)\right]\left[\rho_{i,\alpha}(\mathbf{r})+\sigma_{i,\alpha}(\mathbf{r})\delta(|\mathbf{r}-d\mathbf{e}_z|-a)\right],$$

with $\mu_{i,\alpha}=\ln(\rho_{i,\alpha}^w\Lambda_{i,\alpha}^3)$ the chemical potential of the ions, and intrinsic Helmholtz free energy functional $\mathcal{F}$, given by

$$\beta\mathcal{F}\left[\{\rho_{i,\pm},\sigma_{i,\pm}\}_{i=1}^{N_\pm};d\right] = \sum_{\alpha=\pm}\sum_{i=1}^{N_\alpha}\int_\mathcal{R}d^3\mathbf{r}\,\rho_{i,\alpha}(\mathbf{r})\left\{\ln\left[\rho_{i,\alpha}(\mathbf{r})\Lambda_{i,\alpha}^3\right]-1\right\}+\frac{1}{2}\int_\mathcal{R}d^3\mathbf{r}\,Q(\mathbf{r})\phi(\mathbf{r})$$

$$+\sum_{\alpha=\pm}\sum_{i=1}^{N_\alpha}\int_\Gamma d^2\mathbf{r}\left(\sigma_{i,\alpha}(\mathbf{r})\left\{\ln[\sigma_{i,\alpha}(\mathbf{r})a^2]+\ln\left(K_{i,\alpha}\Lambda_{i,\alpha}^3\right)\right\}+ \tag{6.2}\right.$$

$$\left.[\sigma_m\theta_{i,\alpha}-\sigma_{i,\alpha}(\mathbf{r})]\ln\left\{[\sigma_m\theta_{i,\alpha}-\sigma_{i,\alpha}(\mathbf{r})]a^2\right\}\right),$$

where the region outside the colloid is denoted by $\mathcal{R}$ and its surface is denoted by $\Gamma$. The first term is an ideal gas contribution with an external potential. The mean-field electrostatic energy is described by the second term which couples the total charge density $Q(\mathbf{r})=\sum_{i=1}^{N_+}\rho_{i,+}(\mathbf{r})-\sum_{i=1}^{N_-}\rho_{i,-}(\mathbf{r})+\sigma(\mathbf{r})\delta(|\mathbf{r}-d\mathbf{e}_z|-a)$ to the electrostatic potential $\phi(\mathbf{r})/\beta e=25.6\,\phi(\mathbf{r})$ mV. The final term is the free energy of an $(N_++N_-+1)$-component lattice gas of neutral groups and charged groups, with a surface density of chargeable groups $\sigma_m a^2=10^6$ (one chargeable group per nm$^2$) and $\theta_{i,\alpha}$ is the fraction of chargeable groups available for an ion of type $(i,\alpha)$. A neutral surface site $S_{i,\alpha}$ can become charged via adsorption of an ion $X_i^{i,\alpha}$, i.e., $S_{i,\alpha}+X_{i,\alpha}^\alpha\leftrightarrows S_{i,\alpha}X_{i,\alpha}^\alpha$ with an equilibrium constant $K_{i,\alpha}=[S_{i,\alpha}][X_{i,\alpha}^\alpha]/[S_{i,\alpha}X_{i,\alpha}^\alpha]$ and $pK_{i,\alpha}=-\log_{10}(K_{i,\alpha}/1\text{ M})$.

From the Euler-Lagrange equations $\delta\Omega/\delta\rho_{i,\alpha}(\mathbf{r})=0$ we find the equilibrium profiles $\rho_{i,\pm}(\mathbf{r})=\rho_{i,\pm}^w\exp[\mp\phi(\mathbf{r})+f_{i,\alpha}\Theta(z)]$. Combining our expressions for $\rho_{i,\alpha}(\mathbf{r})$ with the Poisson equation for the electrostatic potential, we obtain the Poisson-Boltzmann equation for $\mathbf{r}\in\mathcal{R}$,

$$\nabla\cdot[\epsilon(z)\nabla\phi(\mathbf{r})]/\epsilon_o=\kappa(z)^2\sinh[\phi(\mathbf{r})-\Theta(z)\phi_D], \tag{6.3}$$

where we used bulk charge neutrality to find the Donnan potential $\phi_D/\beta e$ given by,

$$\phi_D=\frac{1}{2}\log\left[\frac{\sum_i\rho_{i,+}^w\exp(-f_{i,+})}{\sum_i\rho_{i,-}^w\exp(-f_{i,-})}\right]. \tag{6.4}$$

We introduced $\kappa(z)^2=8\pi\lambda_B^o\rho_s(z)$, with

$$\rho_s(z)=\frac{1}{2}\sum_{\alpha=\pm}\sum_{i=1}^{N_\alpha}\rho_{i,\alpha}^o\exp[(\alpha\phi_D+f_{i,\alpha})\Theta(-z)], \tag{6.5}$$

where the Bjerrum length in oil is given by $\lambda_B^o = e^2/4\pi\epsilon_{vac}\epsilon_o k_B T$. Notice that $\kappa(z) = \kappa_o$ for $z > 0$, with $\kappa_o^{-1}$ the screening length in oil. Finally, the bulk oil densities are related to the bulk water densities as

$$\rho_{i,\alpha}^w = \rho_{i,\alpha}^o \exp[(\alpha\phi_D + f_{i,\alpha})]. \tag{6.6}$$

Inside the dielectric colloid the Poisson equation reads $\nabla^2\phi = 0$. On the colloidal surface, $\mathbf{r} \in \Gamma$, we have the boundary condition $\mathbf{n} \cdot [\epsilon_c \nabla\phi|_{in} - \epsilon_o \nabla\phi|_{out}]/\epsilon_o = 4\pi\lambda_B^o\sigma(\mathbf{r})$, with a charge density described by the Langmuir adsorption isotherm for $\mathbf{r} \in \Gamma$.

$$\sigma_{i,\alpha}(\mathbf{r}) = \frac{\sigma_m\theta_{i,\alpha}}{1 + K_{i,\alpha}/\rho_{i,\alpha}^o \exp\{\alpha[\phi(\mathbf{r}) - \phi_D]\}}, \tag{6.7}$$

which follows from $\delta\Omega/\delta\sigma_{i,\alpha}(\mathbf{r}) = 0$.

Eqs. (6.3)-(6.7) are solved numerically for $\phi(\mathbf{r})$ using the cylindrical symmetry, and generic solutions were already discussed in the case of a single adsorption model in Chapter 5. From the solution we determine $\rho_\alpha(\mathbf{r})$ and $\sigma(\mathbf{r})$. These in turn determine the effective colloid-interface interaction Hamiltonian

$$H(d) = \Phi_{VdW}(d) + \min_{\{\rho_{i,\pm},\sigma_{i,\pm}\}_{i=1,\ldots,N_\pm}} \Omega\left[\{\rho_{i,\pm},\sigma_{i,\pm}\}_{i=1}^{N_\pm}; d\right], \tag{6.8}$$

for which we also include a van der Waals sphere-plane potential $\Phi_{VdW}$ using macroscopic Lifschitz theory with Hamaker constant $A_H$. Eq. (6.8) can then be evaluated to

$$\beta H(d) = -\frac{\beta A_H}{6}\left[\frac{1}{d/a-1} + \frac{1}{d/a+1} + \ln\left(\frac{d/a-1}{d/a+1}\right)\right] - \frac{1}{2}\int_\Gamma d^2\mathbf{r}\ \sigma(\mathbf{r})\phi(\mathbf{r}) \tag{6.9}$$

$$+ \int_\mathcal{R} d^3\mathbf{r}\ \rho_s(z)\{\phi(\mathbf{r})\sinh[\phi(\mathbf{r}) - \Theta(z)\phi_D] - 2(\cosh[\phi(\mathbf{r}) - \Theta(z)\phi_D] - 1)\}$$

$$- \sum_{\alpha=\pm}\sum_{i=1}^{N_\alpha} \sigma_m\theta_{i,\alpha}\int_\Gamma d^2\mathbf{r}\ln\left(1 + \frac{\rho_{i,\alpha}^o}{K_{i,\alpha}}\exp\{-\alpha[\phi(\mathbf{r}) - \phi_D]\}\right),$$

which we will investigate for experimental parameters of Table 6.1 to be explained in the next section.

Table 6.1: System parameters

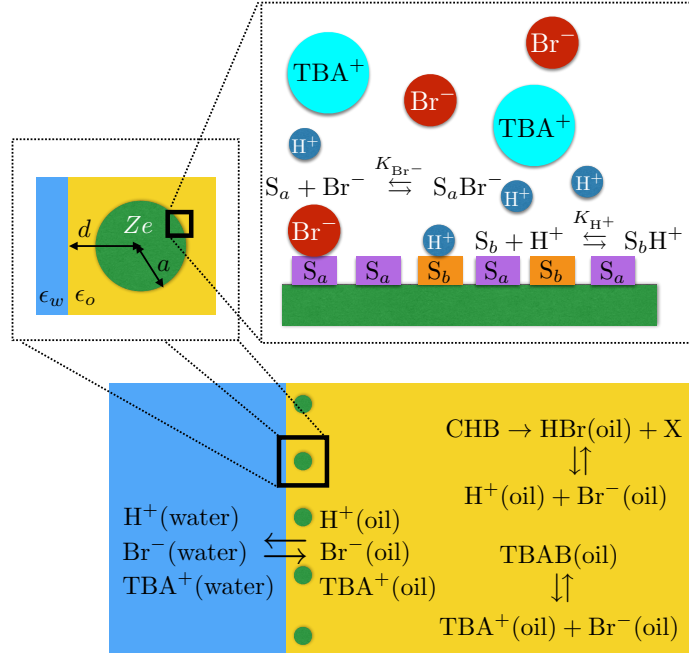| System | $\epsilon_o$ | $\eta$ | $Z$ | $\rho_{TBA^+}\big|_{Z=0}[\mu M]$ | $(\kappa_o\big|_{Z=0})^{-1}[\mu m]$ |
|---|---|---|---|---|---|
| 1 | 7.92 | 0.01 | +930 | 1-5 | $\sim 1$ |
| 2 | 5.6 | 0.01 | -280 | n.a. | n.a. |

**Figure 6.1:** Schematic overview of the experimental system that we will consider. The solvent CHB decomposes giving rise to HBr and a decomposition product X, with HBr in equilibrium with $H^+$ and $Br^-$ ions. In addition to HBr, we also include the organic salt TBAB, so that the concentration of $Br^-$ is not necessarily equal to the $H^+$ concentration. TBAB is in equilibrium with free $TBA^+$ and $Br^-$ ions, and all ions can partition between water and oil. For simplicity we do not take into account the equilibria between the undissociated salts and the free ions. The colloid with radius $a$ and distance $d$ from the interface has a charge $Ze$. On the colloidal surface there are two types of binding sites, $S_a$ and $S_b$, of which the former can bind a $Br^-$ ion with equilibrium constant $K_{Br^-}$ and the latter can bind $H^+$ ion with equilibrium constant $K_{H^+}$. We assume that $TBA^+$ cannot bind to the colloidal surface. There are also colloids in the bulk that are separated from the two-dimensional monolayer at the interface by a zone void of colloids (not shown for clarity).

## 6.3 System and experimental observations

In this chapter, we consider two experimental systems from Ref. [167]. Both systems are suspensions with colloids of $a = 1.4$ $\mu$m and $\epsilon_c = 2.6$. For system 1, the solvent is cyclohexylbromide (CHB), and for system 2, CHB/cis-decalin. There are different colloidal charging mechanims for both systems, such that the particles in system 1 are positively charged, and negatively charged for system 2, see Table 6.1. Here, $\eta$ is the colloidal volume fraction. Finally, we note that CHB is known to decompose in time, producing HBr. HBr can dissociate into $H^+$ and $Br^-$ ions that can adsorb on the surface of the colloidal particles [142]. In a solvent without added salt, $\kappa_o^{-1} = 6$ $\mu$m was estimated for both systems [142], and we will use this value throughout.

The colloids of system 1 are found to reverse the sign of their charge $Z = \int_\Gamma d^2\mathbf{r}\, \sigma(\mathbf{r})$ from positive ($Z > 0$) to negative ($Z < 0$) when the organic salt tetrabutylammonium-bromide (TBAB) is added to the suspension [167]. We list the estimated concentration

of free TBA$^+$ ions $\rho_{\mathrm{TBA}^+}\big|_{Z=0}$ and the resulting Debye length $(\kappa_o\big|_{Z=0})^{-1}$ for which this occurs in Table 6.1. This suggests that H$^+$ and Br$^-$ can both adsorb on the colloidal surface and that the addition of TBAB introduces more Br$^-$ in the system, rendering the colloids of system 1 to become negative for a high enough concentration of TBAB. Such a charge inversion was not likely to occur in system 2.

The suspensions were put into a capillary which was half-filled with deionized water. Such a setup is schematically shown in Fig. 6.1 listing various processes, including the decomposition of CHB, the equilibria of HBr and TBAB with their free ions, and the partitioning of these ions between water and oil. For simplicity, we have not taken these equilibria into account in the theory of Sec. 6.2. However, these Bjerrum pairs could be included in the theory by using the formalism of Ref. [147]. In the upperright inset we show schematically the binding of H$^+$ and Br$^-$ onto the surface of a single colloidal particle.

Both suspensions in Table 6.1 formed two-dimensional monolayers at a distance of a few nanometers from the oil-water interface, separated from a bulk colloidal suspension by a zone void of colloids. The following observations were made: (i) The oil side was negatively charged, while the water phase was positively charged in a system without TBAB. When TBAB was added, we expect a positively charged oil side and a negatively charged water side, because of the hydrophobic nature of TBA$^+$. In other words, we expect $\phi_D < 0$ without TBAB and $\phi_D > 0$ with TBAB. (ii) When TBAB was added to the oil phase, the colloids in system 1 were driven from the interface towards the bulk. Over time, however, the colloids were reattached close to the oil-water interface [213]. (iii) In system 2, the addition of TBAB did not result in particle detachment from the interface. (iv) When TBAB was added to the water phase, colloids from the bulk were actually driven closer to the oil-water interface, producing a denser monolayer at the interface.

We will explain all these observations by applying the formalism of section 6.2. Moreover, we will discuss the differences between a single adsorption model and a binary adsorption model, which is the first logical extension compared to Chapter 5.

## 6.4 Colloid-interface interactions

We will perform calculations with $N_+ = 1, 2$ and $N_- = 1$, where $(1, +)$ corresponds to H$^+$, $(1, -)$ to Br$^-$ and $(2, +)$ to TBA$^+$. To estimate a few of the parameters, we consider their (effective hydrated) ionic radii $a_{\mathrm{H}^+} = 0.28$ nm, $a_{\mathrm{Br}^-} = 0.33$ nm, and $a_{\mathrm{TBA}^+} = 0.54$ nm. This gives the self-energies (in units of $k_B T$) $f_{\mathrm{H}^+} = 11$, $f_{\mathrm{Br}^-} = 10$ and $f_{\mathrm{TBA}^+} = 6$, based on the Born approximation $f_\alpha = (\lambda_B^o/2a_\alpha)(1 - \epsilon_o/\epsilon_w)$. This is a poor approximation for TBA$^+$, because it is known that TBAB is an antagonistic salt, $f_{\mathrm{TBA}^+} < 0$. We will now argue why it is actually not a bad assumption to use the Born approximation for TBA$^+$. From Eq. (6.4), we can obtain the inequality $(f_{\mathrm{Br}^-} - f_{\mathrm{TBA}^+})/2 \leq \phi_D \leq (f_{\mathrm{Br}^-} - f_{\mathrm{H}^+})/2$. As long as $f_{\mathrm{TBA}^+} < f_{\mathrm{Br}^-}$ we thus find that the Donnan potential is varied between a negative value and a positive one by adding TBAB, in line with our expectations. We do not have to assume antagonism

for this. Since we will always fix $\kappa_o^{-1}$ in our calculations, assuming antagonism would only affect the value of $\kappa_w^{-1}$, and we have already shown in Chapter 5 that this parameter is not important for the colloid-interface interaction of oil-dispersed colloids. We therefore use the Born approximation to analyze the qualitative behaviour of the effective interactions, allowing $\phi_D$ to be varied between $-0.5$ and $2$.

Without water the screening length has been approximated to be $\kappa_o^{-1} = 6$ $\mu$m, however, with water this value will become larger, since water acts as an ion sink. In contrast, the charged colloids in the oil will counteract this effect, because these charged species are always accompanied by a double layer, and thus keep the ions in the oil. Because we do not know the exact value of $\kappa_o^{-1}$ in an oil-water system, we will use it as a free parameter and let it vary between 6 $\mu$m and 50 $\mu$m. Note that we work in a single-particle picture, and that many-body effects can, for example, reduce the value of $\kappa_o^{-1}$ by the overlap of double layers. This can be taken into account by introducing an effective Debye length as was done in Chapter 2. Another many-body effect that we do not include is the discharging of particles when the local colloid density is increased. One should keep both these many-body effects in mind when comparing our values of $\kappa_o^{-1}$ to experiment.

### 6.4.1 System without TBAB $N_+ = N_- = 1$

In this subsection we will investigate the systems without added TBAB for two different adsorption models. The first one is a single-ion adsorption model. In this case, system 1 in Table I is described by adsorption of $H^+$, while for system 2 only $Br^-$ can adsorb. We use the values of $Z$ from Table 6.1 to determine the values of the equilibrium constants by using the spherical-cell model in the dilute limit with $\kappa_o^{-1} = 6$ $\mu$m. Within this procedure, we find for system 1 $K_{H^+}a^3 = 165$ and $K_{Br^-} \to \infty$; for system 2 we find $K_{Br^-}a^3 = 2700$ and $K_{H^+}a^3 \to \infty$. The resulting colloid-interface interaction potentials as function of $\kappa_o^{-1}$ are shown in Fig. 6.2 (a) and (c), with $Z(d)$ in the inset. The product $Z\phi_D$ determines the long-distance nature of the colloid-interface interaction: (a) it is repulsive for system 1, since $Z\phi_D < 0$ and (c) attractive for system 2 since $Z\phi_D > 0$ (recall that $\phi_D = -0.5$), see also Chapter 5. At smaller $d$ the image-charge interaction becomes important, which is attractive for both systems. In the nanometer regime the van der Waals repulsion is the most important, and taken together with the image-charge potential, it gives rise to a minimum in $\Phi(d)$, which equals the equilibrium trapping distance of the colloidal particle from the interface.

Increasing $\kappa_o^{-1}$ reduces $|Z|$ and in this case we see that the van der Waals repulsion can overcome the image-charge potential for sufficiently small $d$. However, the reduction in the particle-ion force is much smaller than the reduction of the image force, since the first scales like $\sim Z$, unlike the latter, which scales (approximately) like $\sim Z^2$. In Fig. 6.2(a) we see, for example, that this results in a trapped state near the interface which becomes metastable for large $\kappa_o^{-1}$, with a reduced energy barrier upon increasing $\kappa_o^{-1}$. For system 2, we see that $\Phi$ becomes repulsive for all $d$ for sufficiently large $\kappa_o^{-1}$, because the attractive image charge *and* attractive colloid-ion force are reduced due to
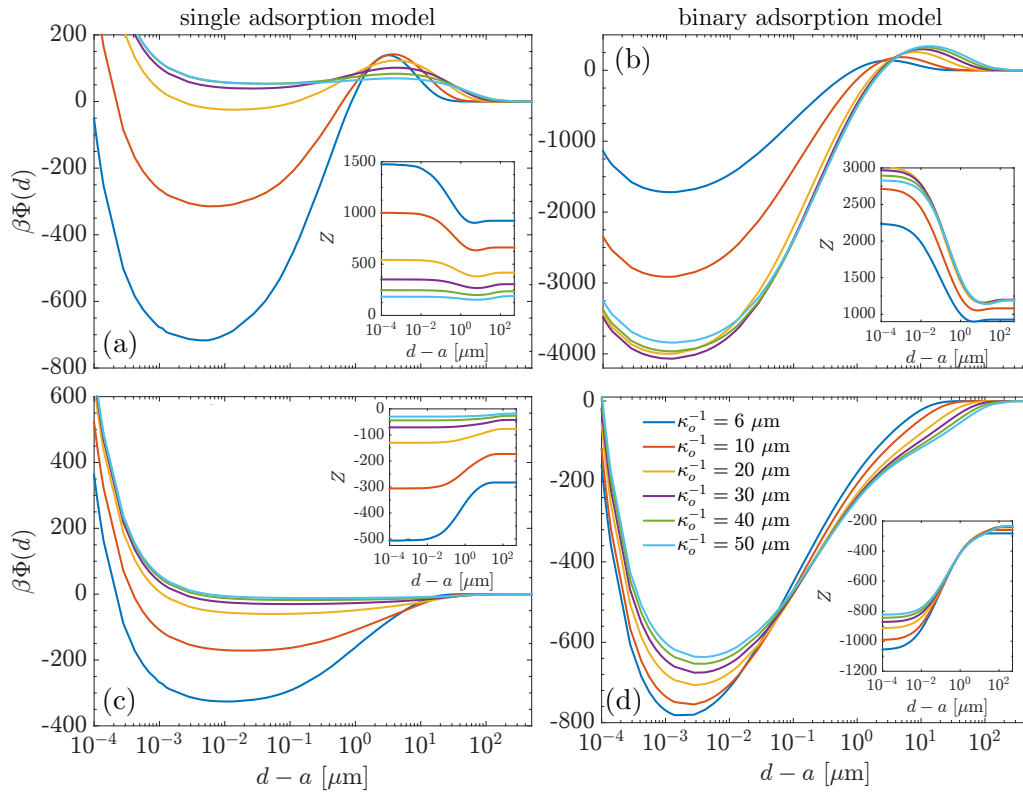
**Figure 6.2:** Colloid-interface interaction potentials for the two different systems in Table 6.1 with the corresponding colloidal charges $Z(d)$ in the insets. System 1 is a CHB system with positively charged colloids and system 2 a CHB/cis-decalin system with negatively charged colloids. We determined the equilibrium constants by matching the charges $Z$ to $d \to \infty$ to the values of $Z$ in Table 6.1 for Debye length in oil $\kappa_o^{-1} = 6$ $\mu$m. For system 1 we consider (a) a single adsorption model where only $H^+$ can attach to the colloidal surface with equilibrium constant $K_{H^+}a^3 = 165$ while $K_{Br^-} \to \infty$ ($Br^-$ cannot adsorb) and (b) a binary adsorption model with $K_{H^+}a^3 = 0.0001$, $K_{Br^-}a^3 = 47$ and fraction of sites available for $Br^-$, $\theta = 0.8$ . For the determination of these values we also used the salt concentration at which $Z$ switches sign by the addition of TBAB. We do similar calculations for system 2, for the single adsorption model in (c) we, however, assume that no $H^+$ can adsorb, but $Br^-$ can with $K_{Br^-}a^3 = 2700$ and (d) in the binary adsorption model we take $K_{H^+}a^3 = 1$ and $K_{Br^-}a^3 = 0.04$, with $\theta = 0.5$ .

particle discharging. This calculation shows that we can also have particle detachment from the interface by removing a sufficient number of ions from the oil phase, and this effect is stronger in the case of (a) than of (c), because the repulsive Donnan-potential mechanism is longer ranged than the van der Waals repulsion. To our best knowledge, both scenarios were not observed in experiment by, for example, adding a sufficient amount of water that acts as an ion sink. Taken together with the fact that positively charged particles can acquire a negative charge, it is clear that systems 1 and 2 are not described by single-adsorption models [167].

With the same procedure as for the single adsorption model, we determined the values of the equilibrium constants in the case of a binary adsorption model. For system 1 we also used the salt concentration $\rho_{TBA^+}\big|_{Z=0}$ for which charge inversion takes place, to find $K_{H^+}a^3 = 0.0001$, $K_{Br^-}a^3 = 47$, and $\theta = 0.8$. Here $\theta = \theta_{Br^-}$ is the fraction

of sites on which anions can adsorb. For system 2, we assumed $\theta = 0.5$ and found $K_{H^+}a^3 = 1$ and $K_{Br^-}a^3 = 0.04$. The short-distance (van der Waals), mid-distance (image charge) and long-distance (Donnan) qualitative behaviour of $\Phi(d)$ do not change when we consider the binary adsorption model, as can be seen in Fig. 6.2(b) and (d). We do, however, see that the trapped state is more "robust" to changes in the ionic strength, because of the much higher values of $|Z(d)|$ involved. This can be understood as follows, for which we consider first system 1. Since $K_{Br^-} > K_{H^+}$, decreasing the salt concentration leads to the negatively charged surface sites to discharge first, which means that the charge initially increases with $\kappa_o^{-1}$. This enhances the image-charge effects, giving rise to a deeper potential well for the trapped state. At even higher $\kappa_o^{-1}$, $|Z(d)|$ will eventually decrease due to cationic desorption, although this is not explicitly shown in Fig. 6.2. A similar reasoning can be found for the negatively charged colloids of system 2, which shows only discharging upon increasing $\kappa_o^{-1}$, but much less compared to the single adsorption model.

The above discussion shows, together with the fact that added TBAB can change the sign of $Z$ of system 1, that the binary adsorption model describes systems 1 and 2 better than the single adsorption model. Note, however, that the large energy barrier between the trapped state and bulk in Fig. 6.2(b), shows that not all the colloids can be trapped near the oil-water interface. This energy barrier explains the experimentally observed zone void of colloids, although one should keep in mind that the charged monolayer will provide extra repulsions which are not taken into account in our single-particle particle. We will come back to this in Section 6.5.1.

## 6.4.2 Systems with added TBAB, $N_+ = 2, N_- = 1$

We now show how the colloid-interface interaction changes in a three-ion system. We focus on the binary adsorption model applied to system 1, because this system has the most rich behaviour. In this case, the addition of TBAB gives rise to two new features. The first one is that it is possible to independently tune $\rho_{Br^-}^o$ and $\rho_{H^+}^o$ under the constraint of bulk charge neutrality, $\rho_{TBA^+}^o + \rho_{H^+}^o = \rho_{Br^-}^o$. By increasing $\rho_{TBA^+}^o$, we find that $Z$ switches sign for

$$\rho_{TBA^+}^o\Big|_{Z=0} = \frac{K_{Br^-}(1-\theta)\rho_{H^+}^o}{(2\theta - 1)\rho_{H^+}^o + \theta K_{H^+}}, \tag{6.10}$$

where we used Eq. (6.7) together with the condition $\sigma_{Br^-} = \sigma_{H^+}$. Secondly, because of the hierarchy $f_{TBA^+} < f_{Br^-} < f_{H^+}$, the Donnan potential can switch from $\phi_D < 0$ to $\phi_D > 0$ at

$$\rho_{TBA^+}^o\Big|_{\phi_D=0} = \rho_{H^+}^o \frac{e^{f_{H^+} - f_{Br^-}} - 1}{1 - e^{f_{TBA^+} - f_{Br^-}}}, \tag{6.11}$$

where we used Eq. (6.4) and (6.6). Note that Eq. (6.11) is weakly dependent on the precise value of $f_{TBA^+}$, since $\exp(f_{TBA^+} - f_{Br^-}) < 0.02$ for $f_{TBA^+} \lesssim 6$ (with 6 being its value within the Born approximation), and hence the second term in the denominator of Eq. (6.11) can be neglected. Using the equilibrium constants of Sec. 6.4.1, we see

from Eq. (6.10) and (6.11) that $\phi_D$ switches sign before $Z$ does upon adding TBAB; i.e., $\rho^o_{\text{TBA}^+}|_{\phi_D=0} < \rho^o_{\text{TBA}^+}|_{Z=0}$.

Since our calculations are performed in the grand-canonical ensemble, we have to specify how we deal with the added TBAB. We choose to fix $\rho^o_{\text{H}^+}$, as was determined from the value at $\kappa^{-1}_o = 10\ \mu$m without added TBAB (blue curve in Fig. 6.2(b)). The resulting colloid-interface interactions are shown in Fig. 6.3(a) and (b), for various values of $\kappa^{-1}_o$, which decreases upon addition of TBAB. The relation between the used screening lengths and $\rho^o_{\text{TBA}^+}$ is shown in Fig. 6.3(c). We can identify four regimes, which are shown in different colours. We start out with a situation with $\phi_D < 0$ and $Z > 0$ (blue), with an energy barrier that separates the trapped state from the bulk state, as was discussed in the previous section. Increasing $\rho^o_{\text{TBA}^+}$, decreases $|\phi_D|$ until ultimately the energy barrier vanishes and $\phi_D$ becomes positive (shown in red). At even larger added TBAB the colloidal particle becomes negative for $d \rightarrow \infty$ as it would be in bulk at the given $\kappa^{-1}_o$ (shown in green).

Interestingly, there is a (small) energy barrier of a different nature than the energy barriers shown until now. Namely, there is a $d^*$ for which $Z(d^*) = 0$ (see insets in Fig. 6.3(b)). Surprisingly, this point of zero charge $d^*$ does not coincide with the location of the maximum in $\Phi(d)$. Furthermore, the result of $\kappa^{-1}_o = 900$ nm does not even show a maximum, although there is a point of zero charge. Both observations can be understood from the fact that although $Z = 0$, the density $\sigma(\vartheta)$ is not spatially constant. In this case, there is still a coupling between bulk and surface ions, that contributes to $\Phi(d)$, see Eq. (5.4).

Finally, at a very high TBAB concentration we find $Z(d) < 0$ for all $d$ (shown in purple). To clarify the difference with the green curves, we show $Z(\infty)$ and $Z(d)$ close to the interface in Fig. 6.3(f). We clearly observe that in the "purple" regime the Donnan potential results in a repulsion for all $d$, and hence particle detachment. Upon decreasing $\kappa^{-1}_o$ this repulsion first becomes stronger, because $\phi_D$ increases from 1.8 to 2. However, increasing $|Z|$ also increases the strength of the image-charge attraction, which eventually results in a small plateau in $\Phi(d)$ between $d - a \sim 10^{-3}\ \mu$m and $d - a \sim 10^{-1}\ \mu$m (compare $\kappa^{-1}_o = 250$ nm with $\kappa^{-1}_o = 400$ nm in Fig. 6.3(b)).

Having focused only on system 1 within a binary adsorption model, we can now also understand how added TBAB would change the colloid-interface interactions in the other cases of Fig. 6.2(a), (c) and (d). In the case of a single adsorption model of system 1 only the Donnan potential switches sign, the energy barrier would vanish and the particles stay trapped. Possibly, some of the particles from the bulk are then moved towards the oil-water interface. For system 2, the addition of TBAB would only introduce an energy barrier separating the trapped state from a bulk state, but no detachment occurs, independent of the investigated adsorption models. This is in line with the experiments of Ref. [207].

From the calculations in Fig. 6.3 we deduce that only significant particle detachment from the interface occurs whenever $Z < 0$ and $\phi_D > 0$. However, the range of the repulsion, which extends up until a micron, is too short to explain the particle detachment found in experiments that may extend up to $> 10\ \mu$m. This can be understood from
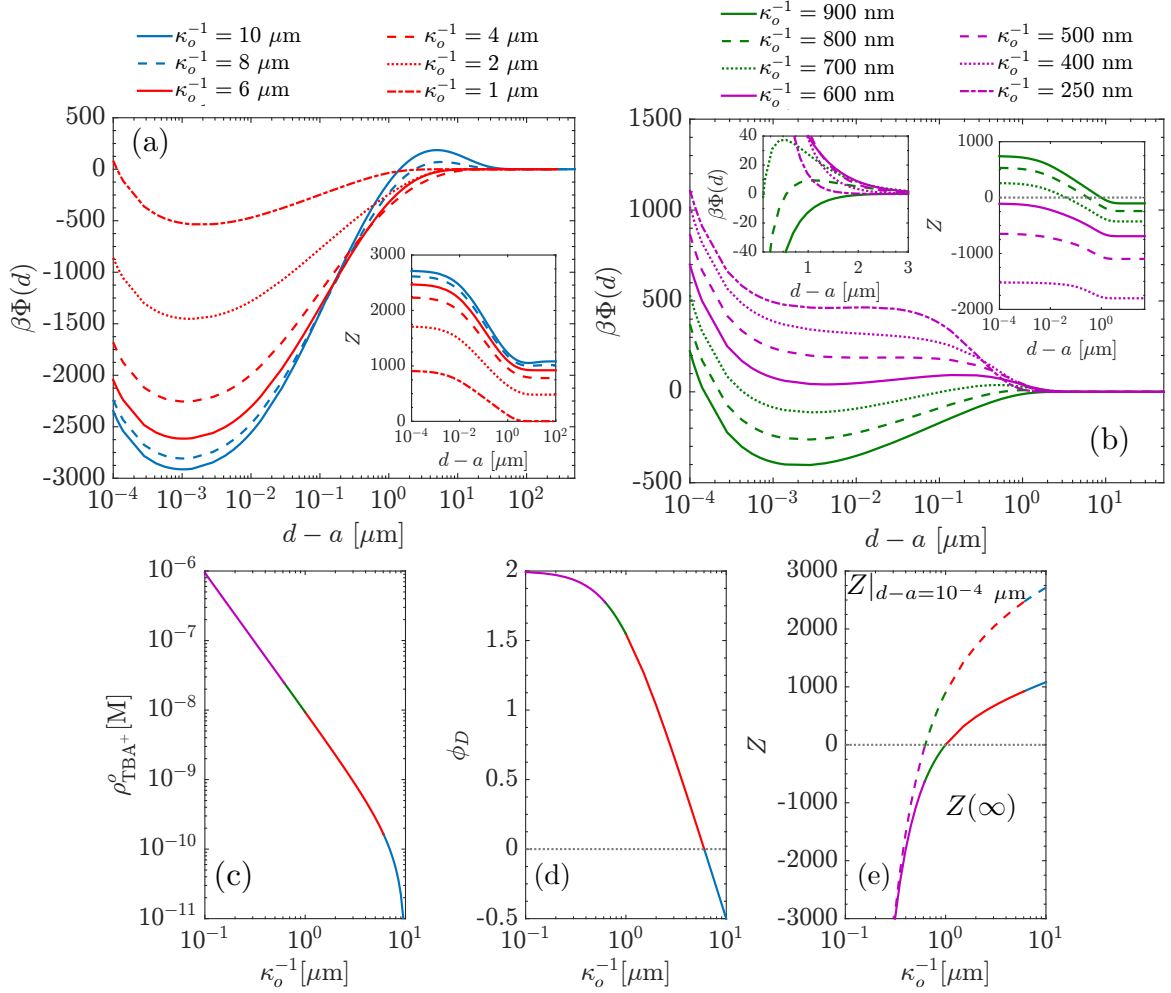
**Figure 6.3:** Colloid-interface interactions for a three-ion model, in which only the ions $H^+$ and $Br^-$ can adsorb with the same equilibrium constants as in Fig. 6.2(b). By fixing $\rho^o_{H^+}$ to the value of the blue full line where $\rho^o_{TBA^+} = 0$ (which is the same as in Fig. 6.2(b)), we show the effect of a decreasing screening length by the addition of $\rho^o_{TBA^+}$ in (a) and (b) with the colloidal charge $Z$ shown in the insets and a zoomed-in version of $\Phi(d)$ in (b) to show more clearly the small maxima that are found for $\kappa_o^{-1} = 700$ nm and 800 nm. In (c) we show how the resulting $\kappa_o^{-1}$ behaves as function of $\rho^o_{TBA^+}$, and changing this density does not only influence the Donnan potential $\phi_D/\beta e$ as shown in (d), but also (e) the charge $Z$ close to the interface as shown as the dashed line in and in the bulk oil as shown by the full line, because more $Br^-$ is available for adsorption. We use different colors to indicate the various regimes: blue is used for $\phi_D < 0$ and $Z > 0$, red for $\phi_D > 0$ and $Z > 0$, green for $\phi_D > 0$ and $Z < 0$ sufficiently far from the interface and purple for $\phi_D > 0$ and $Z < 0$ for all $d$.

the fact that the particle detachment is a non-equilibrium phenomenon, that results from the diffusion of ions from the oil phase to the water phase. This motivates us to have a look at the ion dynamics, to get insights into the time evolution of the colloid-ion forces. Many-body effects can also be important, but these will be left for future work.

## 6.5 Ion dynamics

To describe the ion dynamics, we assume for simplicity that no colloid is present in the system, such that the geometry is one dimensional. This can still provide a lot of insight because we deduced from Chapter 5 that the colloid-ion potential can be approximated by $Z(\infty)\phi_0(d)$, with $\phi_0$ the dimensionless electrostatic potential without any colloids. The theory can be set up from Eq. (5.1), with the second line set equal to zero, and one should keep in mind that for this case $\mathcal{R}$ is the total system volume. It is then possible to derive dynamical equations for $\rho_{i,\pm}(\mathbf{r})$ by using dynamical density functional theory (DDFT) [214][1]. We start with the continuity equation for given and fixed values of $\alpha = \pm$ and $i = 1, ..., N_\alpha$,

$$\frac{\partial \rho_{i,\alpha}(\mathbf{r}, t)}{\partial t} = -\nabla \cdot \mathbf{j}_{i,\alpha}(\mathbf{r}, t), \tag{6.12}$$

with particle currents $\mathbf{j}_{i,\alpha}(\mathbf{r}, t)$ equal to

$$\mathbf{j}_{i,\alpha}(\mathbf{r}, t) = -D_{i,\alpha}(\mathbf{r})\rho_{i,\alpha}(\mathbf{r}, t)\nabla \left( \left. \frac{\delta \beta \mathcal{F}\left[\{\rho_{j,\pm}\}_{j=1}^{N_\pm}\right]}{\delta \rho_{i,\alpha}(\mathbf{r})} \right|_{\rho_{i,\alpha}(\mathbf{r}) \to \rho_{i,\alpha}(\mathbf{r},t)} + \beta V_{i,\alpha}(\mathbf{r}) \right).$$

Explicitly working out the functional derivative gives

$$\mathbf{j}_{i,\pm}(\mathbf{r}, t) = -D_{i,\pm}(\mathbf{r}) \left\{ \nabla \rho_{i,\pm}(\mathbf{r}, t) + \rho_{i,\pm}(\mathbf{r}, t)\nabla[\pm\phi(\mathbf{r}, t) + \beta V_{i,\pm}(\mathbf{r})] \right\}, \tag{6.13}$$

with $D_{i,\alpha}(z) = (D_{i,\alpha}^o - D_{i,\alpha}^w)\Theta(z) + D_{i,\alpha}^w$, with $D_{i,\alpha}^o$ $(D_{i,\alpha}^w)$ the diffusion coefficient of an ion of sign $\alpha$ in bulk oil (water). Here, we have used the Einstein-Smoluchowski relation to relate the electric mobility to the diffusion constant. The time-dependent electrostatic potential $\phi(\mathbf{r}, t)$ satisfies the Poisson equation (neglecting retardation),

$$\nabla \cdot [\epsilon(\mathbf{r})\nabla \phi(\mathbf{r}, t)]/\epsilon_o = -4\pi\lambda_B^o \left[ \sum_{j=1}^{N_+} \rho_{j,+}(\mathbf{r}, t) - \sum_{j=1}^{N_-} \rho_{j,-}(\mathbf{r}, t) \right]. \tag{6.14}$$

Eqs. (6.12)-(6.14) are called the Poisson-Nernst-Planck equations and we solve them under the boundary conditions

$$\left. \begin{array}{l} \mathbf{n} \cdot \mathbf{j}_{i,\alpha}(\mathbf{r}, t) = 0 \\ \mathbf{n} \cdot \nabla \phi(\mathbf{r}, t) = 0 \end{array} \right\} \forall \mathbf{r} \in \partial\mathcal{R}, \ \forall t \in [0, \infty), \tag{6.15}$$

---

[1]An extension of DDFT to go beyond the adiabatic approximation (used to derive DDFT) is available, and is called power functional theory. In this framework the functional also depends on the currents $\mathbf{J}$ [215].

which follow from global mass and charge conservation, respectively. Finally, we have the initial condition

$$\rho_{i,\alpha}(\mathbf{r}, t = 0) = g(\mathbf{r}), \tag{6.16}$$

for a prescribed function $g$.

We estimate the diffusion coefficients by making use of the Stokes-Einstein relation $D_{i,\pm}^j = (6\pi\beta\eta_i a_\pm)^{-1}$ with $\eta_i$ the viscosity of the solvent ($i = o, w$). At room temperature we have $\eta_w = 8.9 \cdot 10^{-4}$ Pa·s, while for CHB we have $\eta_o = 2.269 \cdot 10^{-3}$ Pa·s. From these values we find: $D_{H^+}^w = 8.76 \cdot 10^{-10}$ m²/s, $D_{TBA^+}^w = 4.54 \cdot 10^{-10}$ m²/s, $D_{Br^-}^w = 7.43 \cdot 10^{-10}$ m²/s, $D_{H^+}^o = 3.44 \cdot 10^{-10}$ m²/s, $D_{TBA^+}^o = 1.78 \cdot 10^{-10}$ m²/s and $D_{Br^-}^o = 2.91 \cdot 10^{-10}$ m²/s.

## 6.5.1 The HBr system

We first focus on the colloid-ion forces in a system without added TBAB ($N_+ = N_- = 1$). We model this by investigating the time-dependence of $\phi(z,t)$, with $z$ the direction perpendicular to the oil-water interface. The oil is assumed to reside in a capillary with a linear dimension perpendicular to the oil-water interface of length $L_o = 1$ mm. The value of $L_o$ is ten times smaller than the real experimental setting to facilitate numerical calculations: we need to resolve the width of the interface ($\sim$1 nm) and the width of the Debye screening length which is on the order of microns in oil. The length of the water side of the capillary $L_w$ is also 1 cm in the experiments, but here we take it to be much smaller: $L_w = 100$ $\mu$m. We assume this because there are initially no ions in water, and we expect that water without ions is a much stronger "ion sink" than water with ions. Because real water is hard to deionize completely, we correct for this effect by assuming a much smaller water volume. The disadvantage is that only the ion density profiles in the oil phase are therefore accurate, and more ion species (such as H$^+$ and OH$^-$) in water should be included in the calculations if we want to model the water phase more accurately.

We take an initial condition for $(i, \alpha) = H^+, Br^-$ of the form

$$\rho_{i,\alpha}(z, t = 0) = \rho_0\Theta(z). \tag{6.17}$$

The amplitude $\rho_0$ will be determined from the ionic strength of the suspension before it is brought into contact with a water phase, namely, $\rho_0 = [\kappa_o(t = 0)]^2/8\pi\lambda_B^o$, where $\kappa_o^{-1}(t = 0) = 6$ $\mu$m. Solving Eq. (6.12), (6.13), (6.14), with boundary conditions (6.15) and initial condition (6.17), results in the solutions of $\phi(z,t)$, $\rho_{H^+}(z,t)$ and $\rho_{Br^-}(z,t)$ as given in Fig 6.4. It was convenient in our calculations to express the results in terms of the dimensionless time $\tau = t/t_0$, with time scale $t_0 = L^2/D_{Br^-}^w$. For this specific calculation, we thus find $t_0 = 1.3 \cdot 10^3$ s, which means that the equilibrium state is reached within $\sim 4$ hours, as can be seen in Fig. 6.4. Of course the equilibrium state will be reached later if a larger $L_o$ is chosen.

The time evolution towards equilibrium reveals that $\phi(z,t)$ (Fig. 6.4(a)) always has the same functional form: it always decreases monotonically with $z$ and it goes towards a constant value near $z = L_o$. Furthermore, the range of $\phi(z,t)$ is steadily increased

over time due to the depletion of ions in the oil, because they move towards the water phase. In addition to this effect, $\phi(L_o, t)$ also increases with time, until ultimately $\phi(L_o, t \to \infty) = \phi_D$ is reached.

In Fig. 6.4(b)-(f) we show the time evolution of the concentration of ions in the water phase. The ion concentrations increase with time and the double layer at the water side is always positively charged. At first, the densities of both $H^+$ and $Br^-$ are larger close to the oil-water interface, but after $\tau \sim 0.01$ the concentration of $Br^-$ is reduced near the interface. At this stage, the screening length in water is still low, and $L_w$ is too small to ensure "bulk" charge neutrality until $\tau \sim 1$. For even larger times the form of the profiles do not change, but only the (overall) concentrations increase.

In Fig. 6.4(g)-(k), we show the ion density profiles of $H^+$ and $Br^-$ at the oil side ($z > 0$). At the intial stages of the time evolution, ions are only depleted close to the interface. On the scale of the plots, the $\rho_{H^+}(z, t)$ and $\rho_{Br^-}(z, t)$ look exactly the same, although at very small separations we can see that the density of $Br^-$ is slightly higher, meaning that the oil side is always negatively charged. This can be more clearly seen in Fig. 6.4(j) where the water has taken up a sufficiently amount of ions. The bulk densities $\rho_{i,\alpha}(L_o, t)$ for $\tau \lesssim 5$ are always larger than the densities at the interface as is seen in (g)-(j). Only at very long times (close to or at equilibrium) the bulk density becomes lower for $\rho_{Br^-}(z, t)$ with $z \lesssim \kappa_o^{-1}(t \to \infty)$, as is seen in (k). Here, $\kappa_o^{-1}(t \to \infty) = \rho_{Br^-}(L_o, t \to \infty) + \rho_{H^+}(L_o, t \to \infty)$ and this quantity can be viewed as the equilibrium Debye length in oil. For this particular case, we find $\kappa_o^{-1}(t \to \infty) = 115 \ \mu m$. This is a large value, however, we can go to lower values by choosing a smaller $L_w$. We have performed such calculations, however, we have seen that $L_w$ is then too low to ensure bulk charge neutrality in the water phase, because $L_w < \kappa_w^{-1}(t \to \infty)$. Such a finite-size effect is of course absent in the experiments, where $L_w \gg \kappa_w^{-1}$. For $L_w < 100 \ \mu m$, we see the same qualitative behaviour as in Fig. 6.4, although for some $L_w$ we have seen that $\phi(L_o, t)$ overshoots and becomes more negative than $\phi_D$, before relaxing to the equilibrium state.

Let us now relate the dynamics to the experiments, and in particular to the results on system 1 within a binary adsorption model. In this case particles are always positively charged, and their charge increases initially upon lowering the ionic strength from $\kappa_o^{-1} = 6 \ \mu m$ because of the larger desorption of negative ions than positive ions. Since $Z > 0$ for all times, we conclude from Fig. 6.4 that the colloid-ion force is always repulsive. The question now arises how colloidal particles in the bulk can cross the energy barrier that we have calculated in Fig. 6.2. First of all, we note that the attractive image forces dominate on small distances from the interface. It is an instantaneous effect opposed to the colloid-ion force that takes a few seconds to develop due to the relatively slow ion dynamics. Particles with $d - a = 1 - 10 \ \mu m$ are therefore attracted towards the interface by image forces for all $t > 0$. Other particles at larger distances from the interface would need to cross an energy barrier that for $t \gtrsim 10$ s lies between $50 - 100 \ k_B T$ based on the values of $\phi(L_o, t)$ (which can be a factor 2 lower than $\phi_D$) and Fig. 6.2(b). This barrier can also become smaller when we include many-body particle discharging because of local density variations. Moreover, particles far from the interface are actually lower
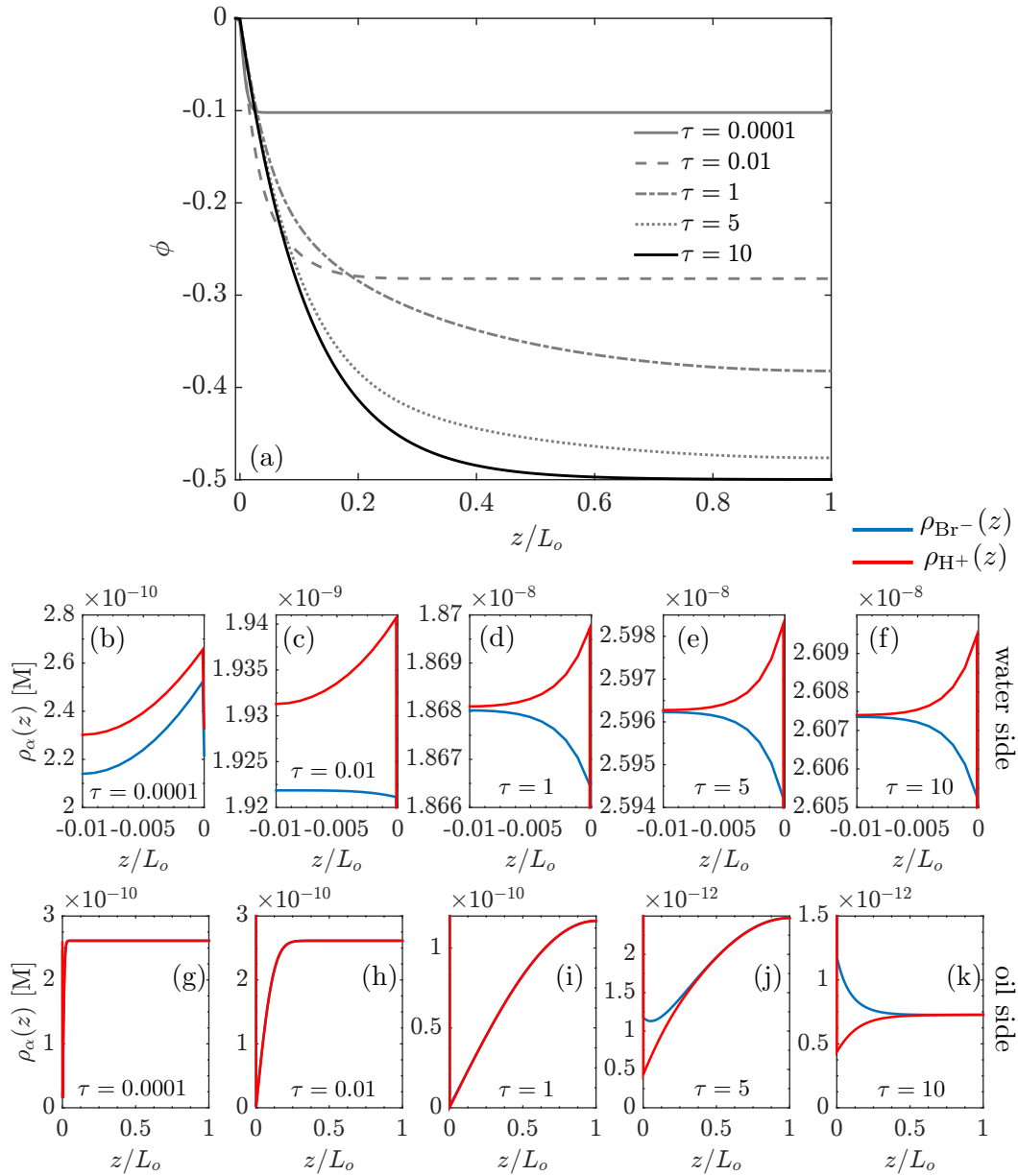
**Figure 6.4:** Time evolution of a system with the ions $H^+$ and $Br^-$ in oil (residing in a capillary with length $L_o = 1$ mm) at an initial Debye length of $\kappa_o^{-1} = 6$ $\mu$m when brought into contact with ionless water (capillary with length $L_w = 10$ $\mu$m). We show (a) the electrostatic potential $\phi(z,t)/(\beta e)$ and the concentration $\rho_{H^+}(z,t)$ and $\rho_{Br^-}(z,t)$, respectively, in water ((b)-(f)) and in oil ((g)-(k)), all in terms of the dimensionless time $\tau = t/t_0$, with $t_0 = L_o^2/D_{Br^-} = 1.3 \cdot 10^3$ s. For $t \to \infty$ the screening length in oil is $\kappa_o^{-1} = 115$ $\mu$m. Note that $Br^-$ and $H^+$ concentrations in oil are essentially identical for $\tau \lesssim 1$.

charged than those close to it, since the ion concentration is higher for $\tau \lesssim 5$, and this could also affect the barrier height. It is therefore a subtle interplay between these various aspects that determine which of the particles are going to be trapped near the interface. The particles that are not able to do so in due time, are eventually prevented from doing so by an energy barrier, separated from the monolayer by a region void of colloids. This depleted zone has also been observed in experiments [150, 158]. Based on the single-particle picture we do not expect many particles in bulk for system 2, because the colloid-ion and image forces are attractive for this case, see Fig. 6.2. In a many-body picture, however, the trapped colloids can repel other colloids from approaching the interface, and this is not taken into account within our calculation. For this, we need a suitable adjustment of the many-body theory presented in Ref. [166] that has been set up for *touching* constant-charge colloids.

## 6.5.2 The TBAB system

The ion dynamics can also provide insights in the experiments where the salt TBAB was added to the oil phase, which resulted in particle dislodgement. The equilibrium calculations of Fig. 6.3 supported this fact by means of a repulsive colloid-ion force. However, due to the large salt concentrations, the range of the repulsive colloid-ion force was deemed to be too small in the parameter regime where the particle was negatively charged (although the range was much larger than the van der Waals repulsion). We will see if this can be resolved when the system is (correctly) viewed out of equilibrium.

In experiment it has been reported that when TBAB was added to the oil, $\kappa_o^{-1}$ can be decreased down to 50 nm. This Debye length is so small that we can (except at the very early stages of the dynamics) neglect the presence of HBr. Again, it is uncertain how many ions are extracted by the water phase. We choose to stay in the regime where the particles are negatively charged for $d \to \infty$ and $t \to \infty$, but they can become positively charged close to the interface. We therefore choose $L_w$ such that a final $\kappa_o^{-1}(t \to \infty) = 979$ nm is reached (the "green" and "purple" regime in Fig. 6.3). Because the Debye lengths are small, we used $L_o = 10$ $\mu$m with $L_w = 100$ nm. It was numerically difficult to perform calculations at even bigger $L_o$ with these screening lengths, but the present parameter settings can still give qualitative insights. Furthermore, we used the Born approximation for all the ions: assuming antagonism for TBA$^+$ would only influence its concentration near the oil-water interface, and we do not expect that the overall qualitative behaviour will change.

In Fig. 6.5 we show the numerical results for $\phi(z,t)$, $\rho_{\text{TBA}^+}(z,t)$ and $\rho_{\text{Br}^-}(z,t)$, in time units of $t_0 = 1.3$ s. We see that the same type of behaviour is found as in Fig. 6.4, with the difference that $\phi(z \to \infty, t)$ evolves towards $\phi_D = 2$, and not to $\phi_D = -0.5$. From Fig. 6.5(a) we see that the water side is always negatively charged (Fig. 6.5(b)-(f)), and the oil side positively charged (Fig. 6.5(g)-(k)). Because of the relative small increase in the Debye length at $t = 0$ compared to Fig. 6.4, bulk charge neutrality cannot be accomodated by the water side, $\kappa_w^{-1}(t \to \infty) > L_w$, and only the ion concentrations in oil are thus representative for the experiment. The nature of
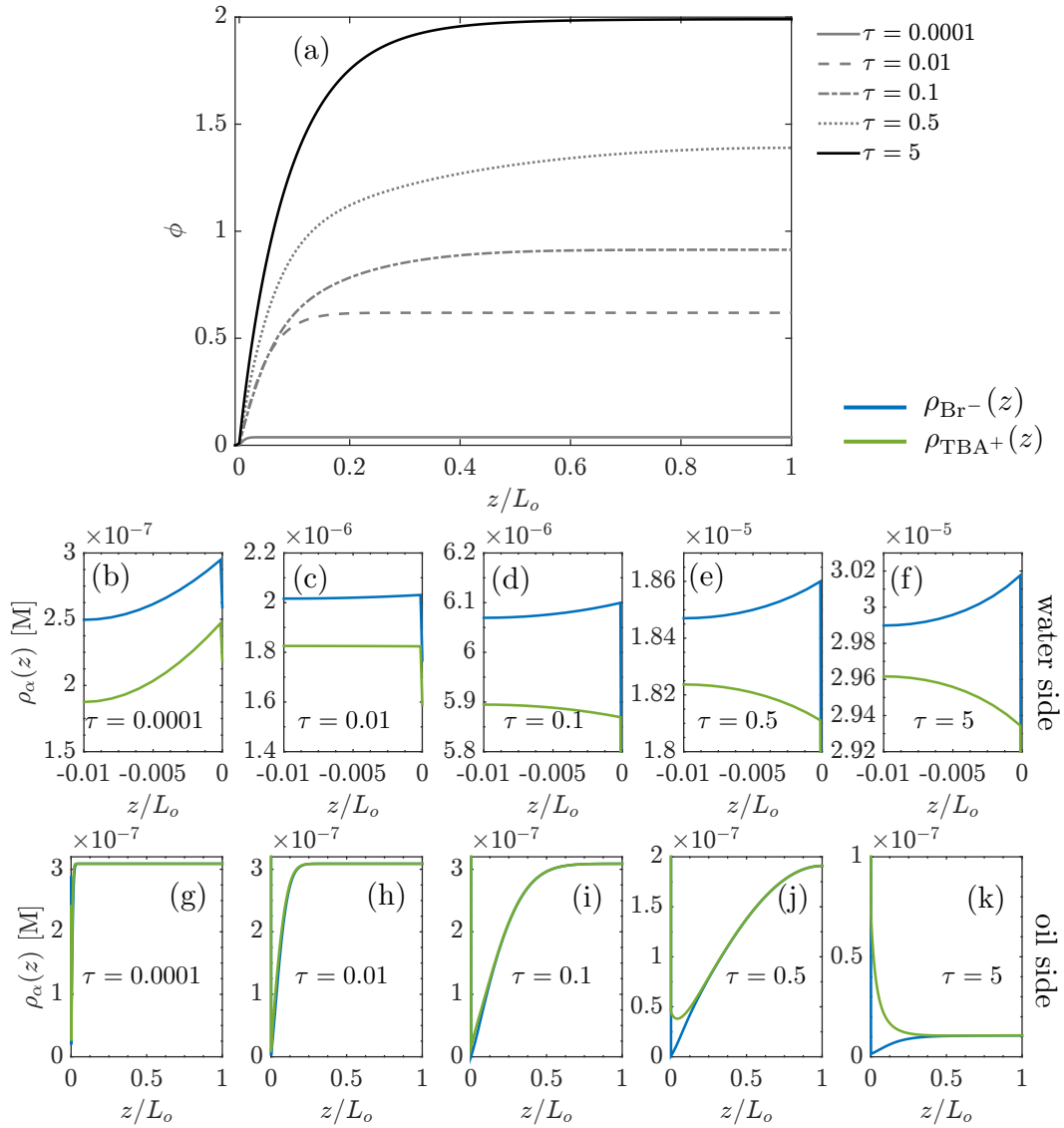
**Figure 6.5:** Time evolution of a system with the ions TBA$^+$ and Br$^-$ in oil (residing in a capillary with length $L_o = 10$ $\mu$m) at an initial Debye length of $\kappa_o^{-1} = 50$ nm when brought into contact with ionless water (capillary with length $L_w = 100$ nm). We show (a) the electrostatic potential $\phi(z,t)/(\beta e)$ and the concentration $\rho_{\text{TBA}^+}(z,t)$ and $\rho_{\text{Br}^-}(z,t)$, respectively, in water ((b)-(f)) and in oil ((g)-(k)), all in terms of the dimensionless time $\tau = t/t_0$, with $t_0 = L_o^2/D_{\text{Br}^-} = 1.3$ s. For $t \to \infty$ the screening length in oil is $\kappa_o^{-1} = 979$ nm.

the colloid-ion forces can also be inferred from Fig. 6.5, but this is more subtle than in the previous section. In the initial state the colloids are negatively charged, and the colloid-ion force is repulsive. Colloids that were initially trapped are then repelled from the interface, but only for surface-interface distances up until a micron, as can be inferred from Fig. 6.3(b). When $t$ increases, we observe that the concentration of Br$^-$ decreases close to the interface. By only including the mass action effect in the charging mechanism (see Chapter 5), we can estimate at which concentration the colloidal particle becomes positively charged, and find $\sim 10^{-8}$ M. This means that for $\tau < 0.5$, the particles are strongly negatively charged, while for $\tau = 0.5$ the particles are negatively charged for $d \gtrsim 1$ $\mu$m. In this case the range of the Donnan potential extends up until $L_o = 10$ $\mu$m (dotted line in Fig. 6.5(a)). This could be an explanation for the range of repulsions being longer than one would expect from the equilibrium calculations. The range of $\phi(z,t)$ is increased because of the depletion of ions near the interface, and by mass action the colloidal charge is (more) negative for large $z$ than close to the interface because of the larger concentration of ions. Particles are therefore repelled by the colloid-ion forces, because it takes time for the bulk ion concentrations to settle. In other words, the range of the interactions is set much faster than that the colloidal charge at large $z$ can "follow". At some point, enough ions are depleted (even for large $z$), the colloids become positively charged and are again attracted towards the interface, as one would expect in equilibrium. This gives a possible explanation for the experimentally observed reattachment after the initial dislodgement.

Finally, we consider the situation where TBAB is added to the water. Again, we neglect HBr, so that the results are only accurate for TBAB concentrations much larger than $10^{-12}$ M, based on the results of Fig. 6.4. We show the results in Fig. 6.6. In (a) we show the time evolution of $\phi(z,t)$ towards its equilibrium profile, and we see that the potential in this time evolution can temporarily become larger than $\phi_D$. The ion densities behave as expected. In (b)-(f) we see that the water side is now depleted from ions, which reduces the screening at the water side until bulk charge neutrality in water cannot be ensured. In (g)-(k) we see that the density of ions is first largest at the interface until, slowly, also the rest of the oil is filled. The oil side of the interface is always positively charged. Finally, the equilibrium situation is identical to the one in Fig. 6.5 by construction.

Based on this calculation, we see that for all times the colloid-ion forces are attractive up until equilibrium is nearly reached. In this case there is a high density of Br$^-$ ions in bulk, such that the particles are negatively charged sufficiently far from the interface. The colloids for small $d$ are, however, positively charged as was explained in Fig. 6.3(b). This explains why colloids are drawn closer to the interface upon adding TBAB in water: the colloids remain mainly positive, but a positive Donnan potential is generated out of a negative one, and hence an attraction towards the interface is induced. This can also be already understood from the equilibrium calculations.

Finally, we note that up until now we considered only quasi-equilibrium effects. What we did not consider up until now are diffusiophoretic effects [216], which is a non-equilibrium process where colloidal particles move along concentration gradients
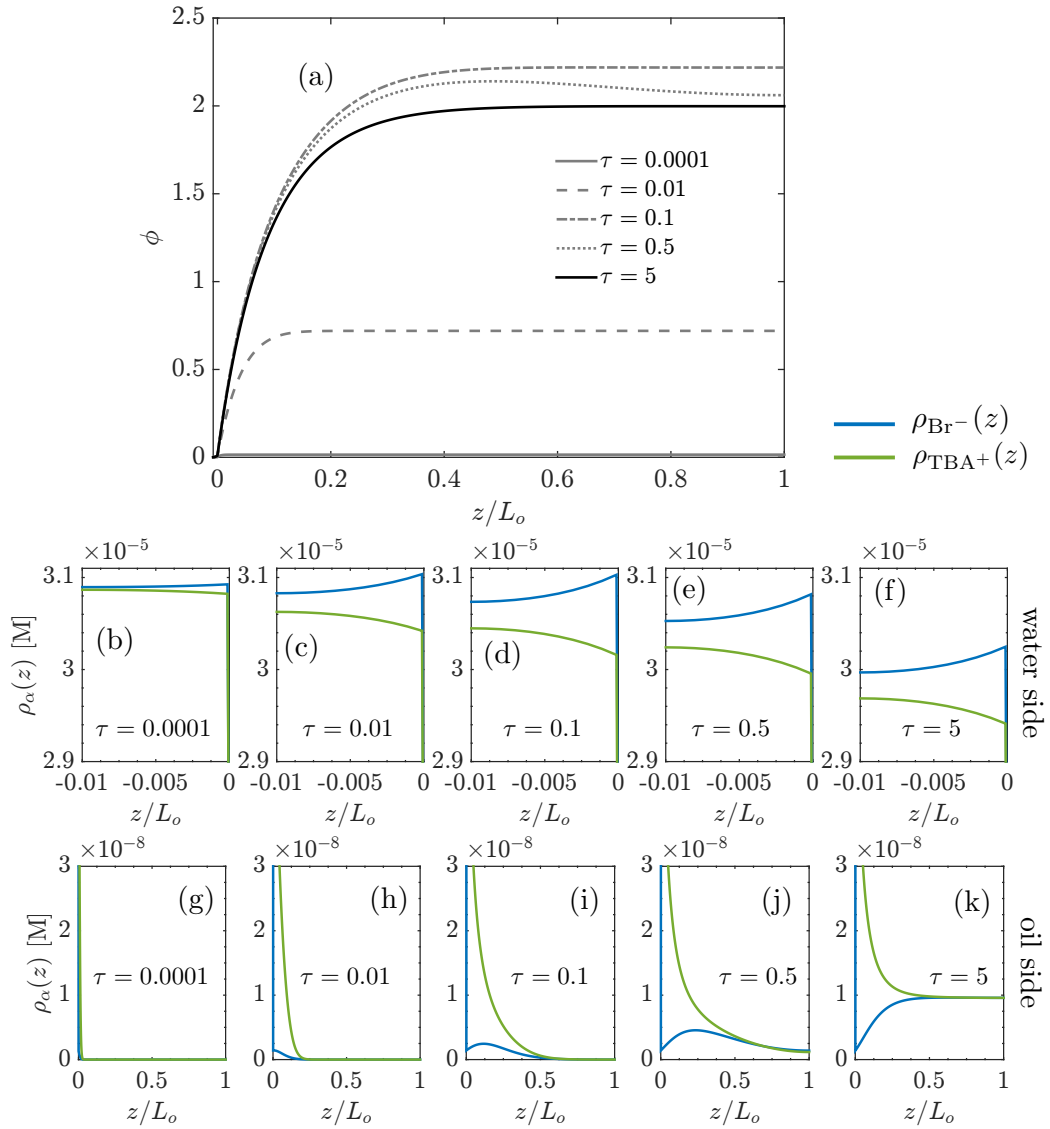
**Figure 6.6:** Same as Fig. 6.5, but now we place all the ions TBA$^+$ and Br$^-$ that were present in the system in Fig. 6.5, as an initial condition in the water phase. The oil resides in a capillary with length $L_o = 10~\mu$m)and the water in a capillary with length $L_w = 100$ nm. We show (a) the electrostatic potential $\phi(z,t)/(\beta e)$ and the concentration $\rho_{\text{TBA}^+}(z,t)$ and $\rho_{\text{Br}^-}(z,t)$, respectively, in water ((b)-(f)) and in oil ((g)-(k)), all in terms of the dimensionless time $\tau = t/t_0$, with $t_0 = L_o^2/D_{\text{Br}^-} = 1.3$ s. For $t \to \infty$ the screening length in oil is $\kappa_o^{-1} = 979$ nm.

of ions. These effects occur even if there is local charge neutrality based on the ion concentrations without any colloidal particle present. Considering that the double layers form faster than that the bulk concentrations of the ions can settle, it is reasonable to expect that diffusiophoretic effects can occur over the whole system volume for a considerable amount of time. However, assessing the direction of the diffusiophoretic force can be highly non-trivial, although we can conclude that this force will work opposite depending on whether TBAB is added to oil or water. Namely, in the first case, there is a positive ion concentration gradient for sufficiently large $z$ at the oil side (see Fig. 6.5), while in the second one it is negative (see Fig. 6.6).

## 6.6 Conclusion and outlook

In this chapter we have looked at colloid-interface interactions and ion dynamics at an oil-water interface, in a system with up to three ion species. We have applied our formalism to recent experiments [167, 207, 213] and have discussed (i) how the charges on the water and oil side of the oil-water interface can change upon addition of salt, (ii) how charge inversion of interfacially trapped non-touching colloidal particles upon addition of salt to the oil phase can drive particles towards the bulk over long distances, followed by reattachment for large times, (iii) that particles that cannot invert their charge stay trapped at the interface and (iv) that colloids in bulk can be driven closer to the interface by adding salt to the water phase. We used equilibrium methods and ion dynamics to show that this is due to a subtle interplay between long-distance colloid-ion forces, mid-distance image forces, and short-distance van der Waals forces. The colloid-ion forces are the most tunable of the three, because they can not only be tuned in the interaction strength, but also in being repulsive or attractive. We have shown this explicitly by including three ion species in the theory and by investigating various charge regulation mechanisms, extending the formalism of Chapter 5.

For future directions we think that it would be meaningful to investigate many-body effects in a similar fashion as in Ref. [166]. There are, however, two drawbacks of the method of Ref. [166] that need to be amended before we could apply it to our system of non-touching colloids. First of all, in Ref. [166] a Pieranski potential [156] was used to ensure the formation of a dense monolayer at the oil-water interface. It would be interesting to see if the trapping of particles near the interface can be found self-consistently by the mechanism presented in this chapter and the previous one, by using a repulsive van der Waals colloid-interface potential. Secondly, the formalism of Ref. [166] was set up for constant-charge particles. In the constant-charge case, it is a good approximation to replace the particle nature of the colloids by a density field. For charge-regulating particles this can be a severe approximation because one needs the surface potential and not the laterally averaged electrostatic potential to determine the colloidal charge.

Investigating many-body effects can be interesting, because colloids present in bulk contribute to the Donnan potential. This is not the case when all the colloids are trapped near the interface: in this case the electrostatic potential generated by the

colloids cannot extend through the whole system volume. Finally, a dense monolayer can provide an extra electrostatic repulsion for colloids, in addition to the repulsive colloid-ion force for $Z(\infty)\phi_D < 0$ and the repulsive van der Waals force. Therefore, we expect that the interplay of the colloidal particles with ions can be very interesting on the many-body level, especially when we include not only image-charge and ion-partitioning effects, but most importantly, also charge regulation. However, it is not trivial to take all these effects into account in a many-body theory. Another direction that we propose is to perform the ion dynamics calculation of Sec. 6.5 in the presence of a single (and maybe stationary) charged sphere near an oil-water interface. This would give insights into the out-of-equilibrium charging of charge-regulating particles, providing not only more information on the tunability of colloidal particles trapped near a "salty" dielectric interface, but also on (out-of-equilibrium) diffusiophoretic effects that were not considered in much detail in this chapter.

# 7

# A Landau-de Gennes theory for hard colloidal rods: defects and tactoids

*We construct a phenomenological Landau-de Gennes theory for hard colloidal rods by performing an order parameter expansion of the chemical-potential dependent grand potential. By fitting the coefficients to known results of Onsager theory, we are not only able to describe the isotropic-nematic phase transition as function of density, including the well-known density jump, but also the isotropic-nematic planar interface. The resulting theory is applied in calculations of the isotropic core size in a radial hedgehog defect, the density dependence of linear defects of hard rods in square confinement, and the formation of a nematic droplet in an isotropic background.*

## 7.1 Introduction

Studying phase transitions involves a careful investigation of the free energy of the system, however, computing it can be very hard, even for the simplest interactions [4]. In the case of symmetry-breaking transitions an order parameter can be defined, which allows one to distinguish a disordered state from an ordered one. From the microscopic Hamiltonian close to a phase transition, a power expansion in terms of this order parameter can often be derived [217], the so-called Landau free energy [218], but it can also be set up phenomenologically based on symmetry grounds. The Landau free energy is usually studied on the level of a saddle-point approximation, such that only polynomial Euler-Lagrange equations have to be solved to understand the phase behaviour, and this procedure has had many successes. Examples include the spontaneous magnetization from a paramagnet to a ferromagnet [219], the gas-liquid transition [220], and the formation of a superconductor from an ordinary metal [221].

For nematic liquid crystals the order parameter is a traceless and symmetric tensor **Q** [222] with components $Q_{\alpha\beta}$ where $\alpha, \beta = 1, 2, 3$ in three-dimensional systems. This tensorial form is chosen because the ordered phase breaks rotational ($SO(3)$-) symme-

try, but there is a residual $\mathbb{Z}_2$, or up-down symmetry, which requires the theory to be invariant under $O(3)$, rather than $SO(3)$. The bulk Helmholtz (or Gibbs) free energy that describes the first order phase transition towards a nematic phase, can then be expanded as

$$\Delta F = A(T - T^*)\mathrm{Tr}(\mathbf{Q}^2) - B\mathrm{Tr}(\mathbf{Q}^3) + C(\mathrm{Tr}\mathbf{Q}^2)^2, \tag{7.1}$$

where $A$, $B$ and $C$ are phenomenological coeffcients, $T$ is temperature and $T^*$ is the temperature of the isotropic spinodal. However, this so-called Landau-de Gennes expansion [222] is only suitable for thermotropics: materials that become liquid crystalline as function of temperature. It has been applied in many situations, ranging from equilibrium [223] to non-equilibrium situations [224], including colloidal particles immersed in a thermotropic nematic [225, 226] and active nematics [227].

In contrast, lyotropic systems, which can consist of hard rods or platelets [228–232], become ordered as a function of density [113], and are not described by the free energy of Eq. (7.1). A simple remedy for this problem would be to replace $T$ in Eq. (7.1) by the density $\rho$, but this cannot capture the density jump that is found in the isotropic-nematic (IN) phase transition, which can be as large as 25% [233]. Most theories for lyotropics, such as Onsager theory [27], do exhibit this density jump, but are difficult to handle numerically in more complex situations or geometries, because one has to solve a complicated non-linear integral equation.

This motivates us to set up a Landau expansion for lyotropics for which we will use the grand potential $\Omega$ rather than the Helmholtz (or Gibbs) free energy $F$ in section II. By using $\Omega$, the expansion parameters will depend on the chemical potential $\mu$ [1], and the density jump will naturally be encoded through the relation $\partial(\Omega/V)/\partial\mu|_{V,T} = -\rho$, with $V$ the volume of the system and $\rho$ the average density. Such a Landau expansion in terms of $\mathbf{Q}$ is different from, for example, the phase-field-crystal method of Ref. [234], which produces terms that also explicitly depend on density. In our description only a single $\mu$-dependent term is needed to describe the density dependence of the IN transition. It is therefore easier to use than the method proposed in Ref. [234], for which also an Euler-Lagrange equation for $\rho$ needs to be solved, in addition to the one for $\mathbf{Q}$. We will explore the bulk properties of such a Landau expansion by fitting and comparing it with Onsager theory, [27] in section III, which is exact in the needle limit [235]. Afterwards, we fit the square-gradient coefficients by using the hard-rod surface tension on parallel and perpendicular anchoring for a planar IN interface in section IV. This approach is similar to the one that is briefly discussed by Wittmann *et al.* in the context of fundamental measure theory [236] . However, we will perform a more thorough analysis of the quality of this theory compared to Onsager theory. Finally, we show some applications: a study of the isotropic core size in a hedgehog defect (section V), linear defects and director textures for rods under confinement (section VI), and the shape and size of a nematic droplet with a homogeneous director field (section VII).

---

[1]Actually, it depends on all intensive variables of the relevant ensemble, in this case not only on $\mu$, but also on $T$. However, we will consider hard particles, hence we do not consider $T$ dependence.

## 7.2 Landau-de Gennes free energy

Let us consider hard rods of length $L$ and diameter $D$ at chemical potential $\mu$ in a macroscopic volume $V$ bounded by a surface $\partial V$. In the Landau grand potential, we will consider terms that depend on $\mathbf{Q}$ and its spatial gradient $\nabla \mathbf{Q}$,

$$\Delta \Omega[\mathbf{Q}] = \int_V d\mathbf{r} \left[\Delta \omega_b(\mathbf{Q}(\mathbf{r})) + \omega_e(\nabla \mathbf{Q}(\mathbf{r}))\right] + \int_{\partial V} dS \, \omega_s(\mathbf{Q}(\mathbf{r})), \tag{7.2}$$

where $\Delta \omega_b$ is the bulk grand potential density with respect to the isotropic state, $\omega_e$ describes elastic deformations and surface tension effects, and $\omega_s$ is an anchoring term that describes the interaction with external walls. All the terms should be invariant under $\mathbf{Q} \to \mathbf{U}^T \mathbf{Q} \mathbf{U}$, with $\mathbf{U} \in O(3)$. We expand the bulk contribution with respect to the isotropic state $\Delta \omega_b$ up until fourth order in $\mathbf{Q}$, which gives us

$$\beta B_2 \Delta \omega_b(\mathbf{Q}(\mathbf{r}); \mu) = \frac{2}{3} a\beta(\mu^* - \mu)Q_{\alpha\beta}Q_{\beta\alpha} - \frac{4}{3}b \, Q_{\alpha\beta}Q_{\beta\lambda}Q_{\lambda\alpha} + \frac{4}{9}d \, Q_{\alpha\beta}Q_{\beta\alpha}Q_{\lambda\rho}Q_{\rho\lambda}, \tag{7.3}$$

where we will use the Einstein summation convention throughout this chapter. The second virial coefficient in the disordered isotropic phase is given by $B_2 = \pi L^2 D/4$ in the limit $L \gg D$, and is included in our definition to render the Landau coefficients $a$, $b$ and $d$ conveniently dimensionless. For simplicity we assume them to be independent of $\mu$. Moreover, $\mu^*$ will turn out to be the chemical potential at the isotropic spinodal. When we assume that the nematic phase is uniaxial, then $\mathbf{Q}$ can be expressed in terms of the scalar order parameter $S(\mathbf{r})$ and the director field $\mathbf{n}(\mathbf{r})$ for $\alpha, \beta = 1, 2, 3$,

$$Q_{\alpha\beta}(\mathbf{r}) = \frac{3}{2}S(\mathbf{r}) \left[n_\alpha(\mathbf{r})n_\beta(\mathbf{r}) - \frac{1}{3}\delta_{\alpha\beta}\right]. \tag{7.4}$$

Notice that the largest eigenvalue of $\mathbf{Q}$ is $S$, while the corresponding (normalized) eigenvector is $\mathbf{n}$. Using that $Q_{\alpha\beta}Q_{\beta\alpha} = (3/2)S^2$ and that $Q_{\alpha\beta}Q_{\beta\lambda}Q_{\lambda\alpha} = (3/4)S^3$, we can express Eq. (7.3) in terms of $S$ as

$$\beta B_2 \Delta \omega_b = a\beta(\mu^* - \mu)S^2 - bS^3 + dS^4. \tag{7.5}$$

For the terms in gradients of $\mathbf{Q}$ we only retain terms up until square gradients in $\mathbf{Q}$ which gives us [2]

$$\beta B_2 \omega_e(\nabla \mathbf{Q}(\mathbf{r})) = \frac{2}{9}\left[l_1(\partial_\alpha Q_{\beta\lambda})(\partial_\alpha Q_{\beta\lambda}) + l_2(\partial_\alpha Q_{\alpha\lambda})(\partial_\beta Q_{\beta\lambda}) + l_3(\partial_\alpha Q_{\beta\lambda})(\partial_\lambda Q_{\beta\alpha})\right], \tag{7.6}$$

where the dimensionfull parameters $l_1$, $l_2$ and $l_3$ are elastic constants for $\mathbf{Q}$. In general, they will depend on $\mu$, but for simplicity, we initially assume them to be constant. Later, in section VII, we will investigate the effect when they are $\mu$-dependent.

---

[2]To show this, recall that $\partial_\alpha$ transforms as a vector, i.e., $\partial_\alpha \to U_{\alpha\beta}\partial_\beta$ for $\mathbf{U} \in O(3)$

It is instructive to work out $\omega_e$ for the uniaxial case of Eq. (7.4). Since the norm of the director is a constant and using the vector identities

$$[\mathbf{n} \times (\nabla \times \mathbf{n})]_\alpha = -n_\beta \partial_\beta n_\alpha, \tag{7.7}$$

$$(\partial_\alpha n_\beta)^2 = (\nabla \cdot \mathbf{n})^2 + [\mathbf{n} \cdot (\nabla \times \mathbf{n})]^2 + |\mathbf{n} \times (\nabla \times \mathbf{n})|^2 - \nabla \cdot [\mathbf{n}(\nabla \cdot \mathbf{n}) + \mathbf{n} \times (\nabla \times \mathbf{n})], \tag{7.8}$$

we can recast $\omega_e$ in the form

$$\begin{aligned}
\beta B_2 \omega_e = &\frac{1}{3}(l_1 + l_s/3)|\nabla S|^2 + \frac{l_s}{3}(\mathbf{n} \cdot \nabla S)^2 \\
&+ \nabla(S^2) \cdot \left[\left(l_1 + \frac{2}{3}l_s\right)(\nabla \cdot \mathbf{n})\mathbf{n} + \left(l_1 + \frac{1}{3}l_s\right)\mathbf{n} \times (\nabla \times \mathbf{n})\right] \\
&+ S^2 \left\{(l_1 + l_s)(\nabla \cdot \mathbf{n})^2 + l_1[\mathbf{n} \cdot (\nabla \times \mathbf{n})]^2 + (l_1 + l_s)|\mathbf{n} \times (\nabla \times \mathbf{n})|^2\right\} \\
&- [l_1 + (l_s - l_a)/2]\nabla \cdot \left\{S^2[\mathbf{n}(\nabla \cdot \mathbf{n}) + \mathbf{n} \times (\nabla \times \mathbf{n})]\right\},
\end{aligned} \tag{7.9}$$

where we introduced $l_s = (l_2 + l_3)/2$ and $l_a = (l_2 - l_3)/2$. We see that $\omega_e$ encodes for surface tension (first line) and elastic deformations (second line) [237]. Eq. (7.9) can be compared with the Frank elastic free energy $F_e$ [238, 239] for a bulk nematic phase with a spatially constant bulk order parameter $S_b$,

$$\begin{aligned}
F_e = \frac{1}{2} \int d\mathbf{r} \{&K_{11}(\nabla \cdot \mathbf{n})^2 + K_{22}(\mathbf{n} \cdot \nabla \times \mathbf{n})^2 + \\
&K_{33}|\mathbf{n} \times (\nabla \times \mathbf{n})|^2 - 2K_{24}\nabla \cdot [\mathbf{n}(\nabla \cdot \mathbf{n}) + \mathbf{n} \times (\nabla \times \mathbf{n})]\},
\end{aligned} \tag{7.10}$$

where the terms in the integrand describe splay, twist, bend and saddle splay deformations, respectively. Up to second order in $S_b$ we find $K_{11} = K_{33} = 2S_b^2(l_1 + l_s)/(\beta B_2)$, $K_{22} = 2S_b^2 l_1/(\beta B_2)$ and $K_{24} = S_b^2[l_1 + (l_s - l_a)/2]/(\beta B_2)$. Within Onsager theory $K_{33} \gg K_{11}$ and $K_{22} = K_{11}/3$ [240], which is not to be expected to hold in the Landau expansion at this order. Finally, notice that the last term of Eq. (7.10) is a surface contribution [3] and that $l_a$ will typically only contribute to the surface free energy [222].

Finally, $\omega_s$ in Eq. (7.2) is an anchoring contribution for external walls, for which we assume the Rapini-Papoular (like), or Nobili-Durand form [242, 243],

$$\frac{\beta B_2 \omega_s}{L} = \frac{w}{2}\left[Q_{\alpha\beta}(\mathbf{r}) - Q_{\alpha\beta}^0(\mathbf{r})\right]^2, \tag{7.11}$$

with $w$ the dimensionless anchoring strength and $\mathbf{Q}^0$ the preferred value of $\mathbf{Q}$ on the surface. Although it is possible to minimize $\Delta\Omega$ with respect to $S$, it is more convenient and more general to directly minimize Eq. (7.2) with respect to $\mathbf{Q}$ when the director field varies as function of position. However, one has to perform the minimization under the constraint that $\mathbf{Q}$ is traceless and symmetric, see for example Ref. [244].

---

[3]Although we say that it is a surface contribution, it does not mean that it cannot have any effect on bulk properties. Actually, it is well known that for certain director field configurations $K_{24}$ can renormalize $K_{11}$, see Ref. [241].

## 7.3 Bulk properties

In bulk, we assume a fully uniaxial nematic phase and hence it is sufficient to investigate Eq. (7.5). The (meta)stable and unstable points are found by the condition $\partial \Delta \omega_b / \partial S = 0$, resulting in the following solutions

$$S_I = 0, \tag{7.12}$$

$$S_N^{\pm} = \frac{3b}{8d} \left( 1 \pm \sqrt{1 - \frac{32ad\beta(\mu^* - \mu)}{9b^2}} \right). \tag{7.13}$$

The stability of these points can be investigated by analyzing the sign of $\partial^2 \Delta \omega_b / \partial S^2$. The isotropic spinodal $\mu^*$ is defined by $\partial^2 \Delta \omega_b / \partial S^2|_{S=S_I} = 0$, while the nematic spinodal $\beta \mu^+ = \beta \mu^* - 9b^2/(32ad)$ is the $\mu$ for which $\partial^2 \Delta \omega_b / \partial S^2|_{S=S_N^+} = 0$. Finally, the binodal $\beta \mu_{IN} = \beta \mu^* - b^2/(4ad)$ is determined from $\Delta \omega_B(S_I) = \Delta \omega_B(S_N^+)$. A stability analysis shows that (i) for $\mu < \mu^+$ the isotropic phase is the stable configuration, (ii) for $\mu^+ < \mu < \mu_{IN}$ we have that $S_N^-$ is absolutely unstable, while $S_N^+$ is metastable and the isotropic phase is stable, and (iii) for $\mu_{IN} < \mu < \mu^*$ we have that $S_N^-$ is absolutely unstable, while $S_N^+$ is stable and the isotropic phase is metastable. (iv) For $\mu > \mu^*$ we have that $S_N^-$ is metastable, while $S_N^+$ is stable and the isotropic phase is unstable. The resulting bifurcation diagram listing the stability of all these branches is shown in the inset of Fig. 7.1, where we indicate with arrows the IN transition as function of $\mu$. Below, we derive the values of the coefficients we used in Fig. 7.1 from fits to Onsager theory.

When $S$ is known for a given $\mu$, one can convert $\mu$ to the dimensionless density $c = B_2 \rho$. For this we introduce the grand potential density of the isotropic state $\omega_I$ and define $\omega := \omega_I + \Delta \omega_b$. Then we find $\partial (B_2 \omega)/\partial \mu = -c$, such that

$$c(\mu) = c_I(\mu) + aS^2, \tag{7.14}$$

where we have defined $c_I(\mu) = -\partial(B_2 \omega_I)/\partial \mu$. Within Onsager theory, we calculate $\omega_I$ by using an isotropic distribution function, such that $\beta \mu(c_I) = \log(c_I/4\pi) + 2c_I$ [28]. By inverting this relation, one obtains $c_I(\mu)$. Together with Eq. (7.14), and $S$ one can determine $c$.

At isotropic-nematic coexistence, we have from Eq. (7.14) and the analysis above that

$$c(\mu_{IN}) = c_I(\mu_{IN}) + aS_{IN}^2, \tag{7.15}$$

$$\beta \mu_{IN} = \beta \mu^* - \frac{b^2}{4ad}, \tag{7.16}$$

$$S_{IN} = \frac{b}{2d}. \tag{7.17}$$

Within Onsager theory, it is known that [28] $c_I(\mu_{IN}) = 3.290$, $c(\mu_{IN}) = 4.191$, $\beta \mu^* = 6.855$, $\beta \mu_{IN} = 5.241$ and $S_{IN} = 0.7922$. Using these values, we find $a = 1.436$, $b = 5.851$
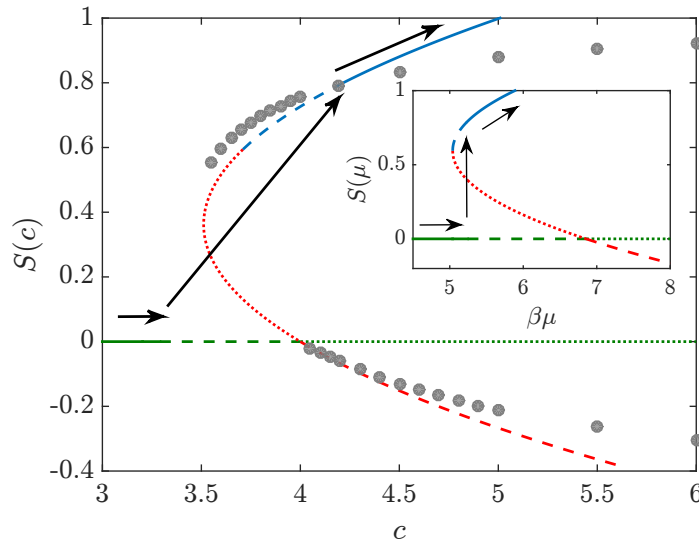
**Figure 7.1:** Bifurcation diagram for the lyotropic Landau-de Gennes (LdG) theory in the density-order parameter $(c, S)$ representation and in the chemical potential-order parameter $(\mu, S)$ representation (inset) by fitting it to coexistence data from Onsager theory. We use green for the isotropic branch $S_I$, blue for the upper nematic branch $S_N^+$, and red for the lower nematic branch $S_N^-$. We use full lines whenever the respective branch is (globally) stable, dashed lines whenever they are metastable and dotted lines whenever they are absolutely unstable. In grey we show data points obtained from Onsager theory and we see that the LdG theory matches well with it. With arrows we indicate the isotropic-nematic transition in both representations, exhibiting a density jump in the $(c, S)$ representation when the ordered phase starts to form.

and $d = 3.693$. With this set of parameters, we determine that $\beta\mu^+ = 5.039$ [4]. We plot the bifurcation diagram in Fig. 7.1, indicating the stable, metastable and unstable regions in the $(c, S)$ representation and in the inset we show the $(\mu, S)$ representation. Arrows indicate the IN transition in both representations, for which the density jump is correctly captured by construction. We also give a comparison with Onsager theory (the grey circles) for which the bifurcation diagram is known [28, 245].

We note that $S_N^+ > 1$ for $c \gtrsim 5$ in Fig. 7.1, which is unphysical. A simple remedy for this problem would be to replace $S^4 \to S^4/(1 - S)$ in Eq. (7.5), which ensures that $S \leq 1$. However, this complicates the free energy, especially when the full **Q**-tensor theory is needed, so it will not be considered here. We have seen in our calculations that this remedy does give better results for the nematic branches at high densities when compared with Onsager theory. However, our calculations show that inhomogeneous Landau theories are less accurate for these expansions, presumably because accuracy in the metastable regime is more important than in the high-density regime.
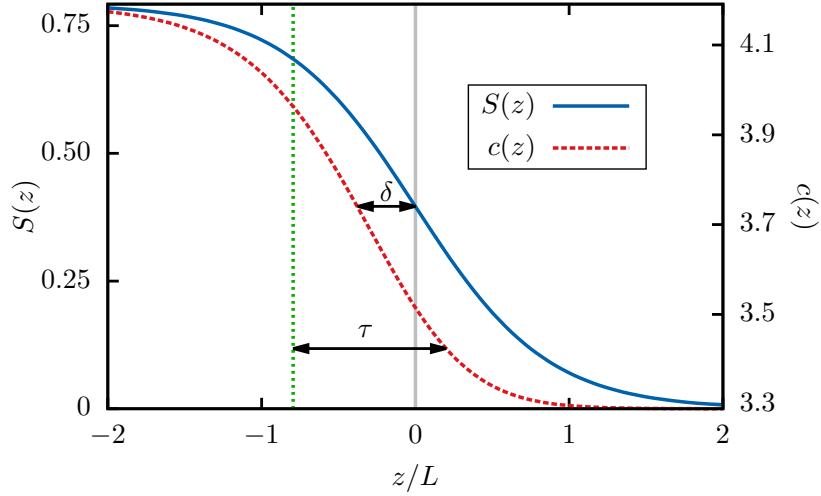
**Figure 7.2:** Interfacial profiles $S(z)$ and $c(z)$ between an isotropic phase and a nematic phase, calculated within the lyotropic LdG theory. Two characteristic distances are defined to quantify the shape of the profiles: $\delta$ is the displacement between the center of the $S$ profile and that of the $c$ profile, where we defined a measure for the interfacial width, $\tau = |z_+ - z_-|$, with $c'''(z_\pm) = 0$.

## 7.4 Isotropic-Nematic interface

Let us now consider an inhomogeneous system that for $z \to \infty$ consists of an isotropic fluid, while for $z \to -\infty$ there is a bulk nematic with order parameter $S_b$. For simplicity, we neglect biaxial effects within our LdG theory, which can be important, but can be included quite easily if necessary [246, 247]. Moreover, we assume homogeneity in the plane perpendicular to the $z$ axis. As a natural consequence a planar interface will develop between the two bulk phases, with an order parameter profile $S(z)$ and a density profile $c(z)$, that can be calculated within our Landau theory. The surface tension for parallel $\gamma_\parallel$ and perpendicular anchoring $\gamma_\perp$ of such a system are known within Onsager theory [248] and these quantities will be used to fit the constants $l_1$ and $l_s = (l_2 + l_3)/2$ from Eq. (7.6). We fix the director field $\mathbf{n}$ to be spatially constant with a specified orientation and let $\alpha$ be the angle of the director with the interface normal. This means that for $\alpha = 0$ ($\alpha = \pi/2$) the rods are aligned perpendicular (parallel) to the interface. With this definition, we can write $\mathbf{n} \cdot \nabla S = S'(z) \cos \alpha$, where henceforth a prime denotes differentiation with respect to $z$.

The Landau grand potential per unit interfacial area $A$ for this geometry is

$$\frac{\Delta\Omega[S]}{A} = \int dz \left[ \frac{m(\alpha)}{2\beta B_2} \left( S'(z) \right)^2 + \Delta\omega_b(S(z); \mu) \right], \tag{7.18}$$

with stiffness constant $m(\alpha) = (2/3)[l_s \cos^2 \alpha + l_1 + l_s/3]$. It is straightforward to rewrite

---

[4]Notice that we could also have used $\mu^+$ to determine the Landau coefficients. However this quantity is hard to determine numerically from Onsager theory.

the Euler-Lagrange equation $\delta\Delta\Omega_{\mathrm{LdG}}[S]/\delta S = 0$, into

$$m(\alpha)S''(z) = \frac{\partial[\beta B_2 \Delta\omega_b(S(z);\mu)]}{\partial S(z)},$$

$$\lim_{z\to-\infty} S(z) = S_b, \ \lim_{z\to\infty} S(z) = 0. \tag{7.19}$$

For our purposes it suffices to consider this equation at coexistence, where $\mu = \mu_{IN}$ and $S_b = S_{IN}$. Multiplying this equation with $S'(z)$ and integration over $z$ gives

$$\frac{m(\alpha)}{2}(S'(z))^2 = dS^2(S - S_{IN})^2, \tag{7.20}$$

where we used that $\beta B_2 \Delta\omega_b(S(z);\mu_{IN}) = dS^2(S - S_{IN})^2$, and where an integration constant vanishes because $S'(z) \to 0$ for $z \to \pm\infty$. Taking the square root of this equation and choosing the positive root since it is consistent with our boundary conditions, it is straightforward to find that the order parameter profile reads

$$S(z) = \frac{S_{IN}}{2}\left[1 - \tanh\left(\frac{z}{2\xi}\right)\right], \tag{7.21}$$

after introducing the correlation length $\xi = [2dm(\alpha)]^{1/2}/b$. The profile for $c(z)$ can be obtained from Eq. (7.14), as

$$c(z) = c_I + \frac{aS_{IN}^2}{4}\left[1 - \tanh\left(\frac{z}{2\xi}\right)\right]^2. \tag{7.22}$$

By definition $\Delta\omega_b(S_{IN}, \mu_{IN}) = 0$, which means that the bulk pressure comes entirely from the isotropic contribution to the grand potential, $\omega_I = -\beta B_2 p_{IN}$. Hence, $\Delta\Omega/A$ is the surface tension when evaluated at coexistence,

$$\beta B_2 \gamma(\alpha) = m(\alpha)\int_{-\infty}^{\infty} dz[S'(z)]^2 = S_{IN}^3\sqrt{\frac{dm(\alpha)}{18}}, \tag{7.23}$$

where we used Eq. (7.20) and we find that $m(\alpha) = 9/(8d)[\pi\beta\gamma(\alpha)LD/S_{IN}^3]^2L^2$ from Eq. (7.23) . From Ref. [248], we know that $\beta\gamma_\parallel LD = 0.156$ ($\alpha = \pi/2$), while $\beta\gamma_\perp LD = 0.265$ ($\alpha = 0$). We thus find $m_\parallel = 0.296L^2$, and $m_\perp = 0.854L^2$. For the perpendicular case ($\alpha = 0$), we plot the profiles $c(z)$ and $S(z)$ in Fig. 7.2, showing that the density profile is shifted with respect to the order parameter profile, which is consistent with Onsager theory and simulations [248]. The same phenomenon is found for $\alpha = 0$, but the interfaces have a smaller width. For the above obtained values of $m_\parallel$ and $m_\perp$, it follows using the relation below Eq. (7.18) that $l_1 = 0.165L^2$ and $l_s = 0.837L^2$. In this case it is not possible to determine $l_a$. Using these values, we find $K_{11}/K_{22} = 6$, which should be contrasted with the exact relation where this ratio should be equal to 3 for $L \to \infty$ [240, 249, 250].

To assess the quality of our calculations, we introduce two characteristic lengths. The first one is defined as $\delta = |z_S - z_c|$, where $S(z_S) = S_{IN}/2$ and $c(z_c) = [c(\mu_{IN}) +$

$c_I(\mu_{IN})]/2$, hence we see that $\delta$ is a measure for the shift of $c(z)$ with respect to $S(z)$. Another length scale is the width of $c(z)$, which can be defined as $\tau = |z_+ - z_-|$, where $z_\pm$ satisfies $c'''(z_\pm) = 0$. For $\alpha = 0$, we find that $\delta_\parallel = 0.223L$ and $\tau_\parallel = 0.586L$, while within Onsager theory the values are $\delta_\parallel^O = 0.45L$ [248] and $\tau_\parallel^O = 0.697L$ [29]. Finally, for $\alpha = \pi/2$, we have determined that $\delta_\perp = 0.378L$ and $\tau_\perp = 0.994L$, however, the values of $\delta_\perp^O$ and $\tau_\perp^O$ are not reported in the literature. Where comparisons are possible, we do see that the LdG results compare quite favourably with Onsager theory, where one should keep in mind the enormously reduced numerical effort of the LdG theory compared to the Onsager theory of the IN interface.

## 7.5 Radial hedgehog defect

In this section, we will study the hedgehog defect, an object that has received much attention in the thermotropic liquid crystal literature [251–254], but for which little is known for lyotropic liquid crystals. To study this type of defect, we assume locally uniaxial symmetry and consider

$$\mathbf{Q}(\mathbf{r}) = \frac{3}{2}S(\mathbf{r})\left(\mathbf{e}_r \otimes \mathbf{e}_r^T - \frac{1}{3}\mathbb{I}\right), \tag{7.24}$$

where $\mathbf{n}(\mathbf{r}) = \mathbf{e}_r$ is the radial unit-vector. If the hedgehog defect would consist of a bulk nematic phase, the elastic free energy density diverges at the centre $r = 0$, and the only way for the system to lower its free energy is by a melting transition of the core to an isotropic phase. Landau theory allows us to determine the internal structure of the resulting defect core, shown schematically in the inset of Fig. 7.3. This calculation would not be possible within continuum theories such as e.g. Eq. (7.10), in which the spatial variation of $S(\mathbf{r})$ is ignored. In such Frank-Oseen theories, a cut-off length is needed to assess the size of the isotropic core, whereas the core size will follow naturally from the regime where $S(\mathbf{r})$ vanishes within our LdG theory. Finally, the rod length $L$ is a natural length scale in our calculations, because we determined the stiffness constants $m_\parallel$ and $m_\perp$ from a microscopic theory. This allows us to estimate the isotropic core size in terms of $L$.

Since we fix the director field to be radial, it suffices to evaluate Eq. (7.5) and (7.9). A radial director field is irrotational, $\nabla \times \mathbf{e}_r = \mathbf{0}$, and has a non-vanishing divergence, $\nabla \cdot \mathbf{e}_r = 2/r$. From Eq. (7.2) and Eq. (7.6) it is then straightforward to derive the grand potential

$$\beta B_2 \Delta\Omega[S] = \int d\mathbf{r}\left[\left(\frac{l_1}{3} + \frac{4l_s}{9}\right)(\partial_r S)^2 + \partial_r(S^2)\frac{2}{r}\left(l_1 + \frac{2}{3}l_s\right) + S^2(l_1 + l_s)\frac{4}{r^2} + \beta B_2 \Delta\omega_b\right], \tag{7.25}$$

for which the Euler-Lagrange equation is

$$S''(r) + \frac{2}{r}S'(r) - \frac{6}{r^2}S(r) = \frac{3\beta B_2}{2m_\perp}\frac{\partial\Delta\omega_b}{\partial S}, \tag{7.26}$$
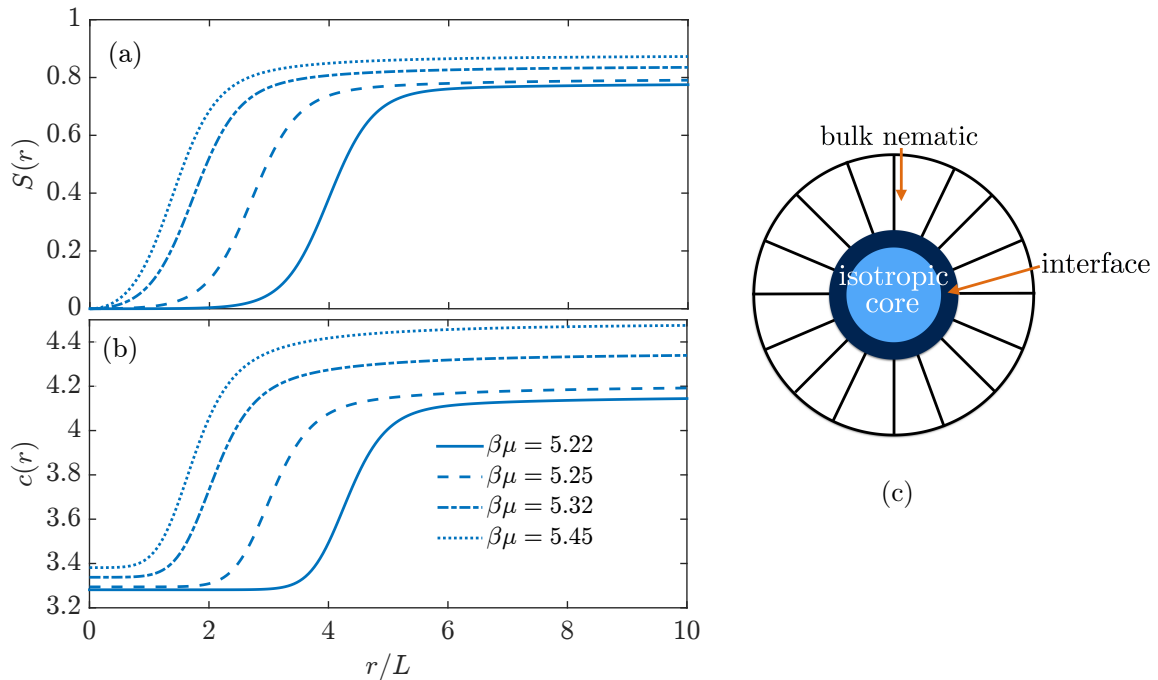
107

**Figure 7.3:** Internal structure of a hedgehog defect for various chemical potentials $\mu$. In (a) the order parameter profile $S(r)$ is shown and in the inset we show a schematic top view of the defect. In (b) we plot the dimensionless local density $c(r)$. The profiles clearly show the structure of an isotropic core centered at $r = 0$.

to be solved for the boundary conditions $S(0) = 0$ and $S(R) = S_N^+(\mu)$. The radius $R$ is the size of the hedgehog defect, which can be thought of as the radius of a finite spherulite or a bulk nematic where there is a finite region of size $R$ where the rods are radially aligned. In our calculations we set $R = 50L$. Notice that the surface term in Eq. (7.6) does not contribute because we consider strong homeotropic anchoring conditions at $r = R$.

Solving Eq. (7.26) for a given $\mu$ gives the structure of a hedgehog defect $S(r)$, shown in Fig. 7.3(a) for several $\mu$. Indeed, an isotropic core centered at the origin is found. For $r \downarrow 0$, the profiles behave locally as $S(r) = \mathcal{O}(r^2)$ and for $r \to \infty$ as $S(r) = S_N^+(\mu) - \mathcal{O}(1/r^2)$, as is well known [251]. Moreover, increasing $\mu$, which is equivalent to setting a higher bulk density, gives rise to a smaller isotropic core size. This behaviour is also observed in thermotropic Landau theory [251], however there are two new features that our version provides. Firstly, as was mentioned earlier, $m_\perp$ is determined by a fit to the Onsager result, and hence the rod length $L$ is an intrinsic (microscopic) length scale of the theory. This allows us to determine the isotropic core size in terms of $L$. We see that the isotropic core size is always $\mathcal{O}(L)$ sufficiently far from the nematic spinodal, in accordance with experiments [255]. This is in sharp contrast with thermotropic liquid crystals, where the isotropic core size is macroscopic in size compared to the microscopic size of the molecules, which have a length on the
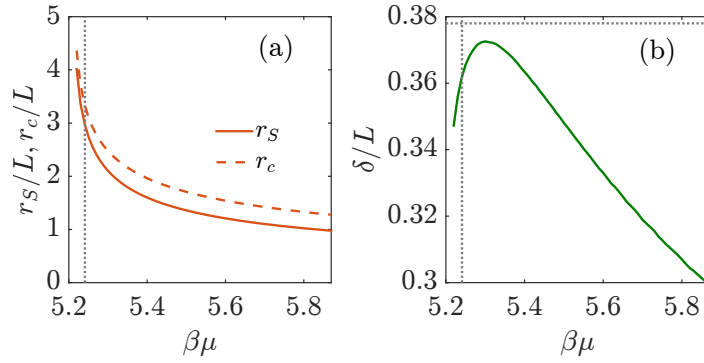
**Figure 7.4:** (a) Isotropic core size measured by the positions $r_S$ and $r_c$ for which the order parameter $S$ and the density $c$ reach the average of their minimum and maximum value, respectively. (b) The interfacial shift $\delta = |r_S - r_c|$ as function of $\mu$. The vertical dotted lines indicate the bulk binodal $\mu = \mu_{IN}$, and the horizontal line in (b) is the shift $\delta_\perp$ in a planar geometry with a fixed director field perpendicular to the interfacial plane, as determined in section IV.

order of $10^{-9}$ m [251]. The reason is that for thermotropics, the binodal lies always close to the isotropic spinodal temperature $T^*$ and the nematic spinodal temperature $T_+$, since typically $T_+ - T^* \lesssim 1$ K [223]. Secondly, from $S(r)$ we can determine the density profiles $c(r)$, for which we show some examples in Fig. 7.3(b) for the same set of $\mu$. Similar to the planar interface case, $c(r)$ is shifted with respect to $S(r)$ towards the region where the bulk nematic phase is found.

The isotropic core size can be characterized by $r_S$ or $r_c$, the positions for which $S(r)$ and $c(r)$ attains the average of their minimum and maximum value, respectively, which we show as a function of $\mu$ in Fig. 7.4(a). We see that both quantities increase with decreasing $\mu$, showing that at low (bulk) densities the rods have a lower tendency to order, which facilitates an isotropic phase. When $\mu$ approaches the nematic spinodal $\mu_+$, the core size diverges, because the nematic phase becomes absolutely unstable. However, it is hard to determine numerically the exact state point for which this happens, because of convergence problems in Eq. (7.26) for $\beta\mu \lesssim 5.22$.

We plot the interfacial shift $\delta = |r_S - r_c|$ in Fig. 7.4(b), revealing a weak (but non-monotonic) variation with $\mu$. As a comparison we indicate $\delta_\perp$, which is the result found in the flat geometry of section 7.4, as the dotted horizontal line. We do not make a comparison with the interfacial width $\tau$ since it is an ill-defined quantity for the hedgehog defect: the equation $c'''(r) = 0$ has only one solution. Finally, we remark that the hedgehog defect can be unstable towards a ring disclination or a split core defect, as was found for thermotropic LdG theory [253]. For hard rods the split core defect has been realized by applying an external magnetic field [256]. Ring disclinations, however, are expected not to occur in hard-rod systems, because, in contrast to molecular systems, we have $K_{11} \gg K_{33}$.
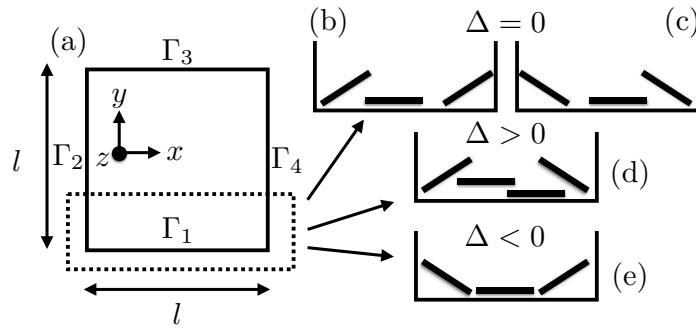
**Figure 7.5:** (a) A rectangular cuboid with a square base of dimensions $l \times l$ in which we confine rods with diameter $D$ and length $L$. Various anchoring boundary conditions at the four walls $\Gamma_1, ..., \Gamma_4$ are investigated. (b)-(c) For $\Delta = 0$ (see Eq. (7.31)) the rods at the corners of the square have the same angle with the bottom wall, while (d) for $\Delta > 0$ the rods always move to the edge farthest from the corner towards the opposing wall or (e) for $\Delta < 0$ the edge closest to the corner is moved towards the opposing wall.

## 7.6 Confined hard rods

An application for which we need the full **Q**-tensor theory is the confinement of rods in a rectangular cuboid. Such a system has been investigated using a mean-field Onsager model [257] and Frank-Oseen model [258], but also using Monte-Carlo simulations [259] and within Landau theory [260]. In the latter case, however, local density variations were *not* considered.

Let us consider a rectangular cuboid with a square base of dimensions $l \times l$ in the $xy$-plane as illustrated in Fig. 7.5(a). To simplify the problem, we take the height equal to the diameter of the rods, such that the rods will necessarily order within the $xy$-plane. We implement this by setting $Q_{zz} = -1/2$ and $Q_{zx} = Q_{zy} = 0$. Following Ref. [259], we use the largest positive eigenvalue $\lambda_+$ of **Q** to determine the degree of order, while the corresponding eigenvector **n** is a measure for the alignment in the $xy$-plane. Observe that $\lambda_+$ is not always the same as the scalar order parameter $S$, which is defined as the absolute largest eigenvalue. We parametrize

$$\mathbf{Q}(x,y) = \begin{pmatrix} \frac{1}{4} + q_1(x,y) & q_2(x,y) & 0 \\ q_2(x,y) & \frac{1}{4} - q_1(x,y) & 0 \\ 0 & 0 & -\frac{1}{2} \end{pmatrix}, \tag{7.27}$$

for which we can derive (see Appendix A) the Euler-Lagrange equations for $\mathbf{q} = (q_1, q_2)$,

$$(l_1 + l_s)\nabla^2 \mathbf{q} = 3a\beta(\mu^* - \mu)\mathbf{q} - \frac{9}{2}b\mathbf{q} + \frac{d}{2}(3 + 16q_1^2 + 16q_2^2)\mathbf{q}, \tag{7.28}$$

with the boundary conditions

$$(l_1 + l_s)(\hat{\boldsymbol{\nu}} \cdot \nabla \mathbf{q}) + \frac{9}{4}w(\mathbf{q} - \mathbf{q}^0) = 0, \tag{7.29}$$

and $\hat{\boldsymbol{\nu}}$ an outward pointing normal vector. Unless stated otherwise, we assume relatively strong anchoring conditions, $w = 10$. Moreover, we assume anchoring conditions at
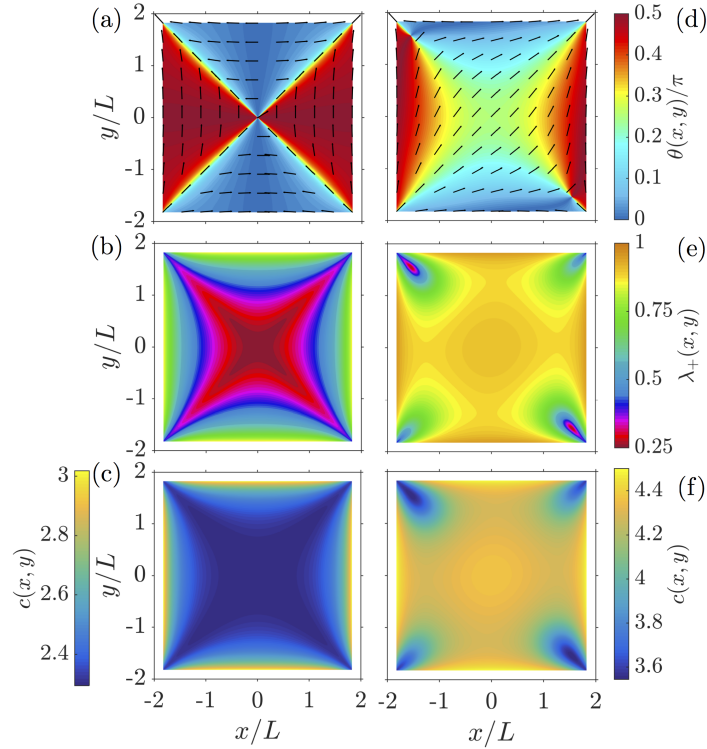
**Figure 7.6:** Profiles of the director angle $\theta(x,y)$ (top), eigenvalue $\lambda_+(x,y)$ (middle) and density $c(x,y)$ (bottom) in a cell of $73/20 \times 73/20$ in units of rod length $L$ and where the height of the slab is chosen to be equal to the diameter $D$ of the rods. We fix the anchoring strength $w = 10$ and anchoring parameter $\Delta = 0.1$, and investigate their effects on an isotropic state (a)-(c) at chemical potential $\beta\mu = 2$, while in (d)-(f) we consider a nematic state $\beta\mu = 5$. The bulk 2D IN transition occurs at $\beta\mu_{IN} = 2.03$ as explained in the text. The ordering effects of the walls can be seen in (a) where $\theta$ is the angle with the $x$ axis, while the degree of ordering is shown in (b) and (e), and the density $c$ in (c) and (f).

the four walls of the form

$$\mathbf{Q}^0(\mathbf{r}) = \frac{3}{2}\left[\mathbf{n}^0(\mathbf{r}) \otimes \left(\mathbf{n}^0\right)^T(\mathbf{r}) - \frac{1}{3}\mathbb{I}\right], \quad \mathbf{r} \in \Gamma_i, \tag{7.30}$$

with a specified director $\mathbf{n}^0$ and $\Gamma_i$ $(i = 1,..,4)$ indicating the four walls. In general, we will assume planar anchoring at the four walls, but we also want to investigate various director configurations at the four corners. For example, for $(x,y) \in \Gamma_1$ we assume

$$n_x^0 = \sqrt{1 - \Delta^2 \sin^2\left(\frac{\pi x}{l}\right)},$$
$$n_y^0 = -\Delta \sin\left(\frac{\pi x}{l}\right), \tag{7.31}$$

with anchoring paramater $\Delta$, which allows us to study metastable states that are otherwise hard to access. For $\Delta = 0$ this gives an equal weight to either of the two configurations shown in Fig. 7.5(b) and (c), whereas a bias in the configurations of the director occurs when $\Delta \neq 0$. For $\Delta > 0$ the configuration of Fig. 7.5(d) is preferred

and for $\Delta < 0$ the configuration of Fig. 7.5(e). Analogous expressions can be derived for the other three boundaries which we can summarize for $(x,y) \in \Gamma_i$ ($i = 1, 2, 3, 4$) as

$$q_1^0 = (-1)^i \frac{3}{4} \left[ 2\Delta^2 \sin^2 \left( \frac{\pi x_i}{l} \right) - 1 \right], \tag{7.32}$$

$$q_2^0 = -\frac{3}{2} \Delta \sin \left( \frac{\pi x_i}{l} \right) \sqrt{1 - \sin^2 \left( \frac{\pi x_i}{l} \right)}, \tag{7.33}$$

with $(x_1, x_2, x_3, x_4) = (x, y, -x, -y)$. Solving the set of equations Eq. (7.28), (7.29), (7.32) and (7.33) gives $\lambda_+(x,y)$ and $\mathbf{n}(x,y)$ [5]. Moreover, within our Landau theory we can extract the density $c(x,y) = c_I(\mu) + (2a/3)\mathrm{Tr}(\mathbf{Q}^2)$. Interestingly, it turns out that $c(x,y)$ is a good measure for the local two-dimensional density $\rho_{2D} = N/A$, with $N = \rho AD$ the number of rods and $A = l^2$ the base area, such that $c = (\pi/4)L^2 \rho_{2D}$, is a natural dimensionless real density.

Note that the present square-gradient theory cannot account for layering at a hard wall, which in principle is present in simulations and theory of these systems [261, 262] although not in a pronounced way given the large particle aspect ratios considered. The extension of the Landau theory to include, for example, a smectic phase in the case of short rods to describe pre-smectic layering for perpendicular anchoring is, however, straightforward [263].

In Fig. 7.6 we show examples of the structures that can be found for $\Delta = 0.1$ and $l/L = 73/20$. The latter system size is chosen because it enables us to compare our results with the simulations of Ref. [259]. We consider $\beta\mu = 2$ (2D isotropic) and $\beta\mu = 5$ (nematic), which should be compared with $\beta\mu_{IN}^{2D} = \beta\mu^* - (3b-d)/(2a) = 2.03$ where the bulk phase transition in this 2D geometry takes place according to our 3D-based LdG theory. In the isotropic state for $\Delta = 0.1$, the rods align along the four walls, while pointing their endpoints towards the corners along the diagonals, as can be seen in Fig. 7.6(a) where we plot the (minimal) angle $\theta$ of $\mathbf{n}$ with respect to the the $x$-axis. Fig. 7.6(b) shows that the core is 2D isotropic since $\lambda_+ = 1/4$, but close to the walls ordering is induced, $\lambda_+ > 1/4$. Furthermore, the density is lowest where the ordering is the smallest, see Fig. 7.6(c). However, a complete study of the wetting and pre-wetting properties of the walls is out of the scope of this chapter, since a more sophisticated surface free energy may be needed [264]. In the nematic state, there is a competition between the ordering effects of the wall and the density-induced order due to the rod-rod interactions. This results in a lens-shaped director field structure (Fig. 7.6(d)), and for this specific boundary condition it results in defects near two of the four corners with an isotropic core shown in red in Fig. 7.6(e), with a reduction in local density shown in blue in Fig. 7.6(f).

The type of possible structures are very sensitive to the boundary conditions that we impose. In Fig. 7.7 we show the various possibilities for different values of $\Delta$ as function of $\mu$. For $\Delta = 0$ we see in Fig. 7.7(a)-(d) that order is always reduced at the four corners, but these isotropic cores become smaller in size for larger $\mu$. The

---

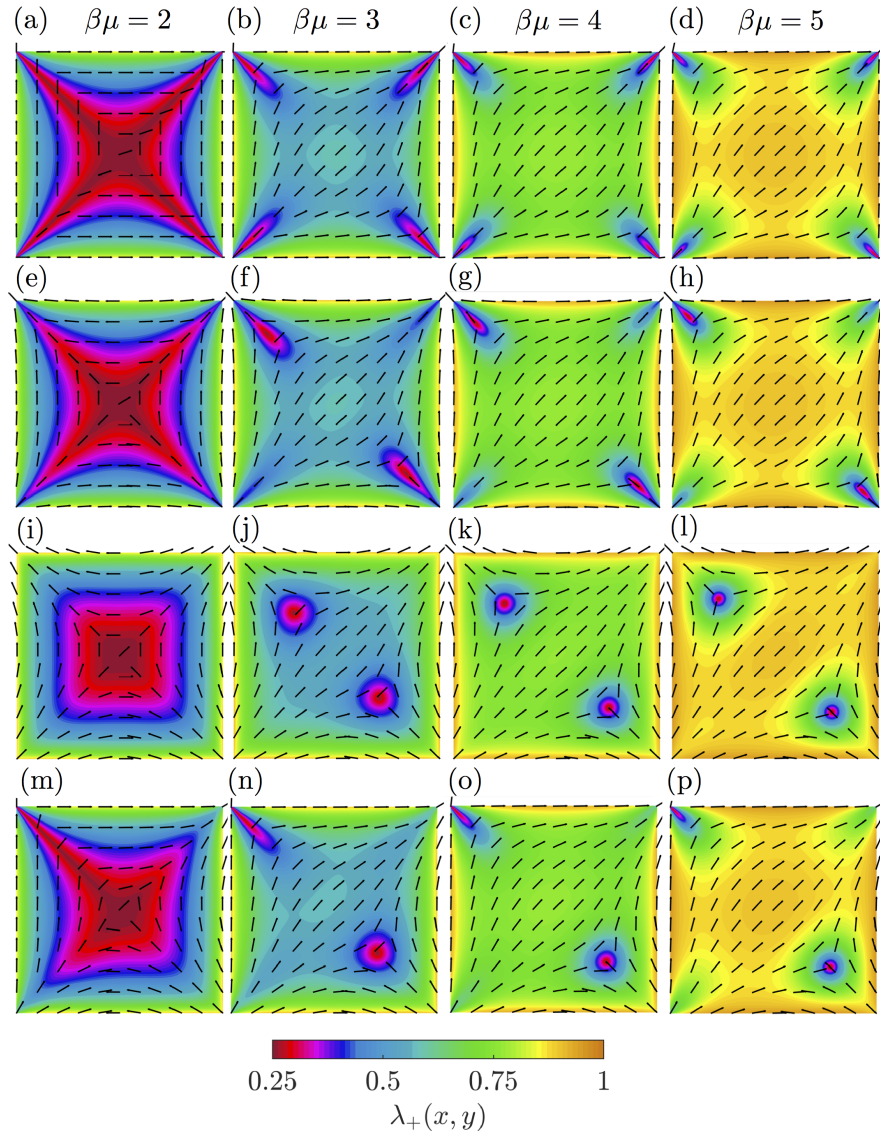[5]Notice that $\mathbf{n}$ is strictly speaking only a well-defined quantity whenever $\lambda_+ > 1/4$

**Figure 7.7:** Nematic director **n** (black lines) and the degree of two-dimensional ordering $\lambda_+(x,y)$ (colormap) for chemical potentials $\beta\mu = 2, 3, 4, 5$ from left to right, for severa; anchoring parameter $\Delta$ (see Eq. (7.31) and Fig. 7.5): (a)-(d) $\Delta = 0$, (e)-(h) $\Delta = 0.1$, (i)-(l) $\Delta = 0.5$ and (m)-(p) $\Delta = 0.5$ on $\Gamma_1$ and $\Gamma_4$, while $\Delta = 0$ on $\Gamma_2$ and $\Gamma_3$. A two-dimensional isotropic state ($\lambda_+ = 1/4$) is colored in red. The cell size is the same as in Fig. 7.6.
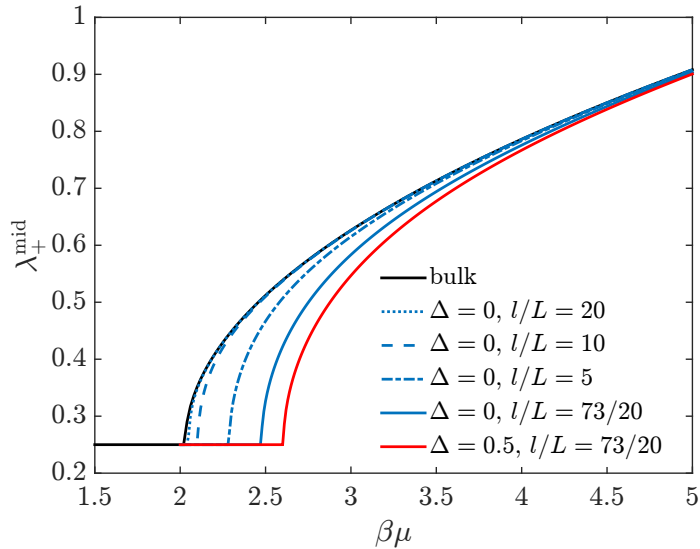
**Figure 7.8:** The 2D order parameter evaluated at the center of the the the cell $\lambda_+^{\text{mid}} = \lambda_+(0,0)$ as function of the chemical potential $\mu$ for various system sizes $l \times l$ and anchoring parameter $\Delta$ (dimensionless anchoring strength $w = 10$). In black we show the 2D bulk phase transition, the 3D IN-transition occurs at $\beta\mu_{IN} = 5.241$ beyond the scale of the plot.

same happens when $\Delta = 0.1$ in Fig. 7.7(e)-(h), although now only in two of the four corners a 2D isotropic phase is found. In Fig. 7.7 (i)-(l) we set $\Delta = 0.5$ and see that two defects are created at the center of the cell, which move apart along the diagonal when the total density is increased. When the center is perfectly ordered, $\lambda_+ = 1$, the defects reside at fixed positions, but not at the corners. A combination of the various structures can be found whenever $\Delta$ is different for the four boundaries. An example is shown in Fig. 7.7(m)-(p) with $\Delta = 0.5$ on $\Gamma_1$ and $\Gamma_4$, and $\Delta = 0$ on $\Gamma_2$ and $\Gamma_3$.

A competition of the wall-induced ordering and the spontaneous nematic ordering always occurs beyond the chemical potential for which the center starts to order. Hence, we investigate $\lambda_+^{\text{mid}} \equiv \lambda_+(0,0)$ as function of $\mu$, shown for various system sizes $l$ and anchoring parameters $\Delta$ in Fig. 7.8. We observe a second-order phase transition at $\mu > \mu_{IN}^{2D}$, with a shift that depends on the system size and on the nature of defects. In our calculations we also observe that a smaller anchoring strength $w$ shifts the phase transition closer to the 2D bulk one, the same as with increasing $l$. This can be understood from the observation that for the formation of a nematic phase in the center, it is necessary to counteract the wall-ordering effects. When the wall-ordering effects are stronger, which happens at larger $w$ or smaller $l$, a larger density and hence a larger $\mu$ is needed to spontaneously order the system. Similar observations were made in a two-dimensional Onsager model [257].

Finally, we make some remarks on the location of the bulk phase transition of the quasi 2D setup that we have investigated here. Converting $\mu_{IN}^{2D}$ to a density, we find that the 2D bulk phase transition takes place at $c^* = 1.95$, which should be compared with $\rho_{2D}^* = 3\pi/2L^2$ or $c^* \approx 4.7$ for the two-dimensional Onsager model [245]. This

significant discrepancy can be understood from the fact that we have not properly included the walls that confine the rods in the $xy$-plane, we simply set $Q_{zz} = -1/2$ and $Q_{zx} = Q_{zy} = 0$. The Landau theory that we use is, however, effectively three-dimensional, and the excluded volume interactions in two dimensions are of a different nature than in three dimensions. A better construction of the LdG theory would include these walls within a three-dimensional calculation. Another alternative is to use a two-dimensional Landau theory where the coefficients are to be determined from the bifurcation diagram of a two-dimensional Onsager theory. We expect that the qualitative features presented in this case, however, will not change.

## 7.7 Nematic droplet

Nematic droplets, or tactoids, differ from droplets of an isotropic fluid because they are elongated rather than spherical in shape. This has been observed in experiments, where the defect structures in the nematic texture have been investigated [265–269], but also in simulations [270], and within the Zwanzig model [271]. The shape of a tactoid can be determined within continuum theory [272] by minimizing the combined elastic and surface free energy

$$F = F_e + \int_{\partial V_{\text{drop}}} dS[\gamma_\parallel + (\gamma_\perp - \gamma_\parallel)(\hat{\boldsymbol{\nu}} \cdot \mathbf{n})^2], \tag{7.34}$$

at a finite and given volume of the droplet $V_{\text{drop}}$. Recall that the Frank elastic free energy $F_e$ is given in Eq. (7.10), and that $\gamma_\parallel$ ($\gamma_\perp$) is the surface tension when the rods are aligned parallel (perpendicular) to the interface. Since the shape is an input parameter in the minimization procedure of Eq. (7.34), one has to impose how the rods align along the interface of the droplet, and this is captured in the second term of Eq. (7.34). Minimization of this free energy has been successful in determining the shapes of tactoids. The surface tensions that are used as fit parameters to match the theory with the experimentally observed shapes, however, disagree with the experimentally measured and theoretically obtained values of the surface tension [29, 241, 248, 269, 273–277]. A hypothesis for this discrepancy is due to the simple choice of the Rapini-Papoular form [242] to describe the anchoring at the IN interface, which is strictly speaking only true for a planar (non-curved) geometry. The question is how much curvature would renormalize the surface tensions of the flat geometry. Our aim is to calculate this within our Landau theory, because the surface effects of Eq. (7.34) should automatically be captured in our treatment. Such a calculation has been briefly touched upon for the thermotropic case in Ref. [278], although only in a two-dimensional $xy$-geometry and with a focus on the time evolution rather than on the equilibrium tactoid sizes and shapes.

For simplicity we focus on tactoids with a homogeneous director field, $\mathbf{n} = \mathbf{e}_z$, with $\mathbf{e}_z$ the unit vector in the $z$-direction. For such a director field all elasticity terms vanish,
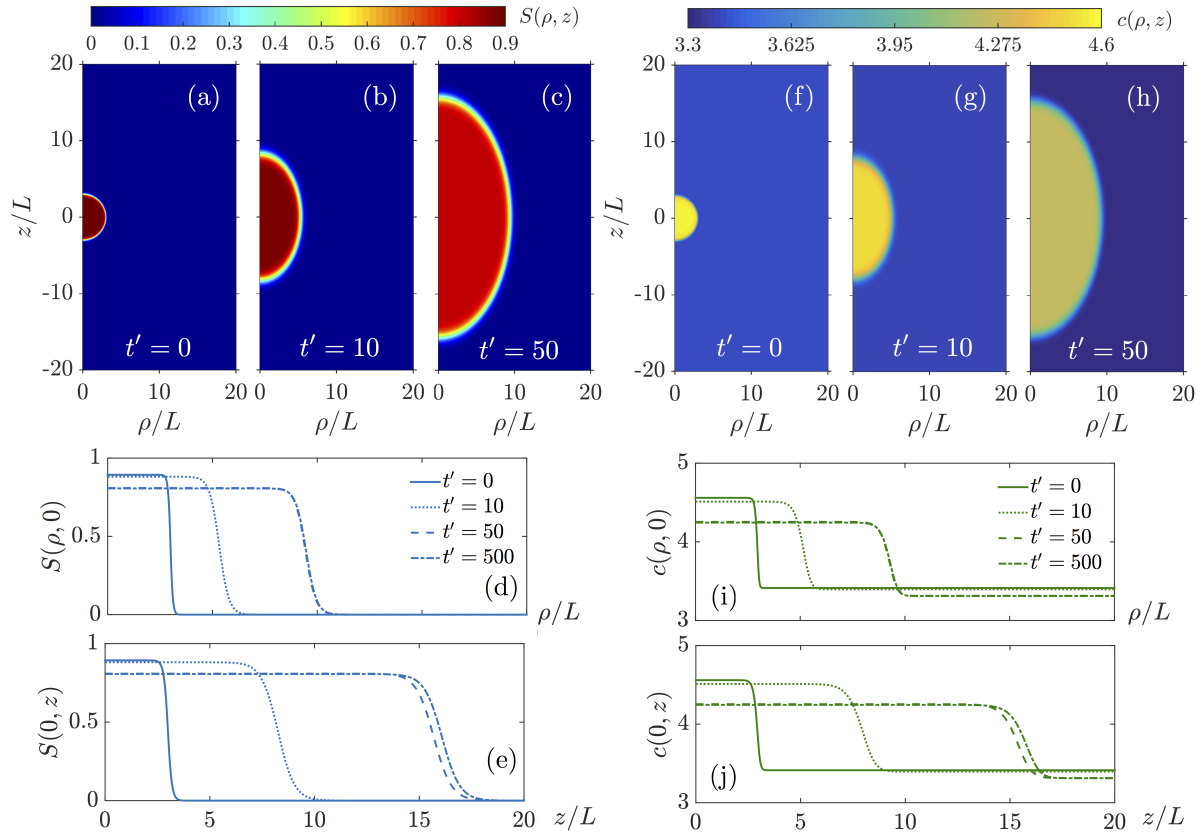
**Figure 7.9:** Relaxation of a spherical liquid crystalline droplet of initial radius $r_0 = 3L$ prepared at $\beta\mu_0 = 5.5$ according to the dynamics of Eq. (7.39) and constraint Eq. (7.40). In (a)-(c) we show snapshots of the order parameter profile $S(\rho, z)$ for various values of dimensionless time $t'$ showing that the spherical droplet becomes elongated over time. In (d) and (e) we show the order parameter profiles along the two symmetry axes of the droplet. In (f)-(h) we show the corresponding snapshots of the local dimensionless density $c(\rho, z)$ and the profiles along the symmetry axes in (i) and (j).

and hence the Landau grand potential is given by

$$\Delta\Omega[S] = \int d\mathbf{r}\left[\frac{m_\parallel}{2\beta B_2}|\nabla S|^2 + \frac{m_\perp - m_\parallel}{2\beta B_2}(\mathbf{n}\cdot\nabla S)^2 + \Delta\omega_b\right]. \tag{7.35}$$

It is easily seen that this free energy mimics the second term in Eq. (7.34), with the identification that the surface normal $\hat{\boldsymbol{\nu}}$ is the same as $\nabla S$ on the surface defined by $S(\mathbf{r}_*) = (1/2)\max_{\mathbf{r}\in V} S(\mathbf{r})$, where we defined the IN interface to be the loci of points for which $S(\mathbf{r})$ attains half its maximum value. Thus, the square gradient term in Eq. (7.35) is a surface tension contribution that results in droplets that tend to minimize their surface area, while the second term favours droplet shapes for which the misalignment between surface normal and director is minimal because $m_\perp > m_\parallel$.

It turns out to be numerically difficult to find non-trivial solutions to the Euler-Lagrange equations of Eq. (7.35) that are spatially inhomogeneous. For this reason we

investigate instead a dynamical equation for $S$ [6] assuming model-A (pseudo-)dynamics [280],

$$\frac{\partial S}{\partial t} = -\Gamma \frac{\delta \Delta\Omega[S;\mu]}{\delta S(\mathbf{r})}, \tag{7.36}$$

and far-field boundary condition

$$\hat{\boldsymbol{\nu}} \cdot \nabla S(\mathbf{r},t) = 0, \quad \mathbf{r} \in \partial V. \tag{7.37}$$

As an initial condition we take a spherical droplet (or "nucleus")

$$S(\mathbf{r}, t=0) = \frac{3}{2} S_N^+(\mu)\Theta(r-r_0), \tag{7.38}$$

where $\Theta$ is the Heaviside step function, $r_0$ is the radius of the initial droplet and $r = \sqrt{\rho^2 + z^2}$, in terms of the cylindrical coordinates $(\rho, z)$. Our goal is to look at a fixed $\mu$ for stationary solutions of Eq. (7.36), since they would also be solutions of the Euler-Lagrange equations. If we use Eq. (7.36) for a fixed $r_0$, we only find solutions for which droplets keep growing if $\mu$ is too large, or droplets that keep shrinking if $\mu$ is too small. Consequently, there must be a critical chemical potential $\mu_c$ for which the droplet neither grows or shrinks when the optimal shape is attained. To find $\mu_c$ for a given shape and droplet volume we fix $\mu_0 = \mu(t=0)$ and evaluate instead of Eq. (7.36),

$$\frac{\partial S}{\partial t} = -\Gamma \frac{\delta}{\delta S(\mathbf{r})} \left[ \Delta\Omega[S;\mu_0] - \frac{\Delta\mu(t)}{\beta B_2} \int d\mathbf{r} \ c(\mathbf{r},t;\mu_0 + \Delta\mu(t)) \right], \tag{7.39}$$

with a Lagrange multiplier $\Delta\mu(t)$ such that conservation of total number of particles

$$\int d\mathbf{r} \ c(\mathbf{r},t;\mu_0 + \Delta\mu(t)) = \int d\mathbf{r} \ c(\mathbf{r},t=0;\mu_0) \tag{7.40}$$

is guaranteed. By definition $\Delta\mu(t=0) = 0$. Working out the above Euler-Lagrange equation gives

$$\frac{\beta B_2}{\Gamma}\frac{\partial S}{\partial t} = m_\parallel \nabla^2 S + (m_\perp - m_\parallel)\frac{\partial^2 S}{\partial z^2} - 2a\beta\{\mu^* - [\mu_0 + \Delta\mu(t)]\}S + 3bS^2 - 4dS^3. \tag{7.41}$$

Moreover, we find that we can approximate $\beta\mu(c_I) \approx Ac_I + B$, with $A \approx 2.25541$ and $B = -2.19865$, with a largest relative error of 0.6% for $c_I \in [3,6]$. Using this approximation the constraint of Eq. (7.40) can be rewritten as

$$\int d\mathbf{r} \left[ \frac{\beta\Delta\mu(t)}{A} + aS^2(\mathbf{r},t) \right] = \int d\mathbf{r} \ aS^2(\mathbf{r},t=0). \tag{7.42}$$

---

[6]We neglect the noise terms in our calculations, since we are only interested in using Eq. (7.36) as a pseudo dynamics to find stationary solutions to the Euler-Lagrange equation of Eq. (7.35). In Ref. [279] it is, however, listed how noise terms for a **Q**-tensor theory can be constructed.

We solve Eq. (7.41) and Eq. (7.42), using the boundary condition Eq. (7.37) and initial condition Eq. (7.38) where we take for the system volume a cylinder of radius $20L$ and height $20L$, using the $xy$-plane as a symmetry plane. When $r_0$ and $\mu_0$ are too small, the initial droplet disappears in time, but when they are chosen too big the droplet will eventually touch the system boundary and a "planar" interface along the radial direction will develop. However, here we will only consider the set of values for $\mu_0$ and $r_0$ that give stable droplets that do not change over time: this defines $\mu_c = \mu_0 + \Delta\mu(t \to \infty)$.

In Fig. 7.9(a)-(c) we show the typical relaxation of a spherical droplet as function of dimensionless time $t' = \Gamma L^3 t/(\beta B_2)$ towards an elongated shape within our LdG theory, with the profiles along the two coordinate axes shown in Fig. 7.9(d) and (e). Our LdG theory allows also for the calculation of $c(\rho, z)$ using Eq. (7.14), which we show in Fig. 7.9(f)-(h) and in Fig. 7.9(i)-(j) along the two symmetry axes. The stationary solution that we find has a higher chemical potential than the bulk binodal, $\mu_c > \mu_{IN}$, which accounts for the Laplace pressure in this ensemble.

Interestingly, the solution found for long times is very similar to the IN planar interface at coexistence. This is indicated by the interfacial shift $\delta$ and interfacial width $\tau$. We find for $S(\rho, 0)$ and $c(\rho, 0)$ that $\delta_\rho = 0.219L$ and $\tau_\rho = 0.576L$ to be compared with the flat plane result of $\delta_\parallel = 0.223L$ and $\tau_\parallel = 0.586L$. Along the $z$ axis we find $\delta_z = 0.372L$ and $\tau_z = 0.978L$ to be compared with $\delta_\perp = 0.378L$ and $\tau_\perp = 0.994L$. This shows that the surface tensions in both directions are effectively reduced for $\mu > \mu_{IN}$, since $\tau$ is smaller. However, from scaling arguments [281], we find that for $\gamma_\perp$ the relevant length scale is $L - (1/2)d^2/L$, with $d$ the possible displacement of the rods given the orientation distribution function. In contrast, for $\gamma_\parallel$ the relevant length scale is $d$. A higher $\mu$ is equivalent to a higher density and hence lower $d$. From the above scaling arguments we deduce that $\gamma_\perp$ should increase with $\mu$ while $\gamma_\parallel$ should decrease, which is not captured in our calculation.

This latter observation is relevant when we investigate the aspect ratio $R_1/R_2$ of the stationary droplets, with $R_1$ the length of the main axis and $R_2$ the one of the minor axis, see the inset of Fig. 7.10(a). It turns out that we always find $R_1/R_2 = 1.7$, which equals the ratio of the surface tensions determined from the planar geometry $\gamma_\perp/\gamma_\parallel = \sqrt{m_\perp/m_\parallel}$, see Eq. (7.23). Starting with different values of $\mu_0$ and $r_0$ (or even changing the aspect ratio of the initial droplet) we observe that $\mu_c$ only depends on $\mu_0$, see Fig. 7.10(a). For small $\mu_c$, and hence lower values of the "Laplace pressure", $\mu_c - \mu_{IN}$, we find larger droplets, as indicated by a larger $R_1$, although the differences are not large among the various final droplet sizes. However, regardless the final size, the aspect ratio is always 1.7, which is illustrated by the various colored lines in Fig. 7.10(b) converging to the dotted grey line. This is only to be expected when curvature effects are not important, which is also found within the macroscopic theory of Eq. (7.34) for homogeneous director fields with $\gamma_\perp$ and $\gamma_\parallel$ constant. However, we expect that $\gamma_\perp$ and $\gamma_\parallel$ depend on curvature. Moreover, in experiments [265–269], it is concluded that (i) the aspect ratio depends on $R_1$, (ii) the aspect ratio can become as large as 4 to 5 and (iii) the experimentally observed shapes have cusps at the endpoints on the axis
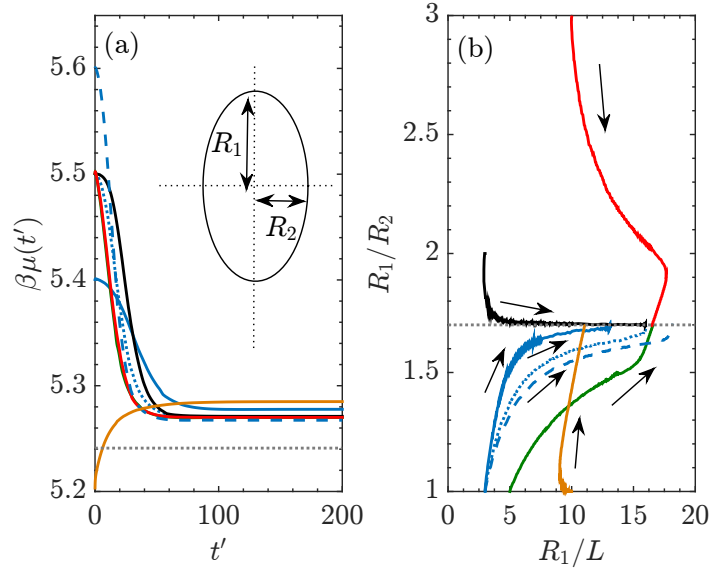
**Figure 7.10:** (a) Time evolution of the chemical potential $\mu(t') = \mu_0 + \Delta\mu(t')$ for various initial droplets and initial chemical potential $\mu_0$. We use the same color for initial droplets of the same $r_0$ and aspect ratio. In the inset we show the shape parameters $R_1$ and $R_2$ that we use to characterize the droplets. In (b) we indicate the time evolution of the aspect ratio $R_1/R_2$ as function of the droplet main axis $R_1$, where the various arrows indicate the flow of time. All lines end on the grey dotted line $R_1/R_2 = 1.7$ where the droplet does not change anymore, while the final droplet size $R_1(t'=\infty)$ depends crucially on $\mu_0$. The dotted blue lines correspond to the results shown in Fig. 7.9.

parallel to the director field when the aspect ratio is larger than 2. Only very large droplets are expected to have an aspect ratio of 1.7.

Interestingly, in simulations $R_1/R_2 \sim 1.7$ is also found [270, 282], in contrast to the experiments where a larger $R_1/R_2$ up to $\sim 5$ has been observed [269]. We note, however, that the rods in these simulations have a smaller particle aspect ratio ($L/D \sim 20$) than in typical experiments ($L/D \sim 1000$). Moreover, rod flexibility, polydispersity and residual Van der Waals forces may be at play, and investigating these effects will be left for future work. In the remainder of the text, we will instead speculate how the present LdG theory can produce $R_1/R_2 > 1.7$. Whether or not these large tactoid aspect ratios can actually be found within Onsager theory remains, however, an open question.

Clearly, increasing the aspect ratio is only possible within our theory by tuning the ratio $m_\perp/m_\parallel$. Indeed, we find in our calculations that we can obtain any desired aspect ratio by varying this quantity. Moreover, to make $R_1/R_2$ depend on the droplet size and hence on $\mu_c - \mu_{IN}$, the coefficients $m_\perp$ and $m_\parallel$ need to depend on $\mu$. This does not come as a surprise, since $l_1$ and $l_s$ are in general $\mu$ dependent. However, since $m_\perp = (2/3)(l_1 + 4l_s/3)$ and $m_\parallel = (2/3)(l_1 + l_s/3)$ we find that the maximal aspect ratio that can be achieved by tuning $l_1$ and $l_s$ is $R_1/R_2 = 2$, while keeping $l_1, l_s > 0$. However, we have to go to extreme limits to achieve this behaviour, $l_1$ should be close to zero or $l_s$ very large.

Another possibility to achieve a higher aspect ratio is by including higher order terms

in the Landau expansion. The next order term has two derivatives and is third order in **Q**. There are many symmetry-allowed terms that satisfy this condition, however, the only one that does not generate any new elasticity contributions and hence the only one that is quadratic in **n** is the term

$$\frac{2}{9}l_4 Q_{\alpha\beta}\partial_\alpha Q_{\rho\sigma}\partial_\beta Q_{\rho\sigma} = \frac{l_4}{2}S(\mathbf{r})\left[(\mathbf{n}\cdot\nabla S)^2 - \frac{1}{3}|\nabla S|^2\right] + \text{elasticity terms}, \qquad (7.43)$$

see Ref. [283], which holds for the uniaxial case. Another motivation why such a term is needed, is that it lifts the degeneracy on $K_{11}$ and $K_{33}$, which is also found within Onsager theory [240], but not in LdG theory if the square gradient terms are only quadratic in **Q**, see section II below Eq. (7.10).

Clearly, including Eq. (7.43) increases $\gamma_\perp$, which is reflected by the positive sign of the first term. In contrast $\gamma_\parallel$ is reduced, since the second term is negative. Consequently, for $l_4 > 0$, the aspect ratio $R_1/R_2$ is increased. To reproduce the flat plane result for large droplets we expand $l_4 = l_4^0(\mu - \mu_{IN}) + \mathcal{O}[(\mu - \mu_{IN})^2]$ with $l_4^0 > 0$, and tried to do the calculation with this contribution [7]. By construction larger droplets will have an aspect ratio closer to $R_1/R_2 = 1.7$, since $\mu_c$ will be closer to $\mu_{IN}$. While it was rather straightforward to get $R_1/R_2 \sim 2$ by tuning $l_4^0$, we found numerical difficulties when we tried to find a larger aspect ratio, because adding Eq. (7.43) introduces extra non-linearities in the Euler-Lagrange equation. Moreover, within all of our calculations, no cusps in the droplet shape were found, while they are always experimentally observed for $R_1/R_2 \gtrsim 2$, see for example Ref. [269]. We hypothesize that for the existence of these cusps is essential to have a large aspect ratio, and we speculate here that we cannot find such solutions due to the adopted square-gradient approximation. Another possibility would be that model-A dynamics is not suitable to find these cusp(-like) solutions. Finally, we neglect any bipolarness in the director-field texture that may also be important [241, 269]. It would be interesting to use the full **Q**-tensor theory to capture this effect, since it is known within the macroscopic theory of Eq. (7.34) that $R_1/R_2$ depends on $R_1$ when bipolarness is included, even when $\gamma_\perp$ and $\gamma_\parallel$ are taken to be constant.

Despite its shortcomings here and there, our theory does show that adding a $\mu$-dependent elasticity term to the free energy allows us to predict an aspect ratio of $R_1/R_2 = 1.7 - 2$ that depends on the droplet size. The larger the droplet, the smaller $R_1/R_2$ since the "Laplace pressure" is smaller. If the elastic coefficients are assumed to be constant, we find no curvature effects on $R_1/R_2$. An improvement of the theory to obtain cusp-like solutions is needed, however. We expect that the cusps have a strong renormalizing effect on the surface tensions so that experimentally observed aspect ratios around 4 can be achieved. The existence of these cusps is expected to be more important than that of the "Laplace pressure", which turns out to be important whenever $R_1/R_2 \sim 2$.

---

[7]In principle the full $\mu$-dependence can be assessed by throughly comparing the Landau coefficients with the results of the elastic constants from Onsager theory [249, 250].

## 7.8 Discussion and conclusions

We have constructed a Landau theory for hard rods by a suitable order parameter expansion of the grand potential in Sec. 7.2. The coefficients are determined by fitting them to the bulk coexistence data and the surface tensions in a planar geometry. This is different from the approach of Ref. [236] where the Frank elastic coefficients from a fundamental measure theory [284] are used to determine the square gradient coefficients. We have compared our results with known properties of Onsager theory, such as the (bulk) bifurcation diagram in Sec. 7.3 and characteristic length scales of the IN interface in Sec. 7.4.

The remainder of the paper was a demonstration of the resulting Landau theory in more complex situations. We gave examples that were investigated before within Landau theory, but not yet within a density-dependent one. In Sec. 7.5 we showed that we can assess the isotropic core size of hedgehog defects in terms of the rod length $L$ and investigated how the isotropic core size depends on the bulk density. Sufficiently far from the spinodal, we found a core size that is on the order of the length of the constituent particles, in contrast to a thermotropic hedgehog defect, which has a core size that is much larger than the length of the constituent molecules. In Sec. 7.6 we studied the evolution of topological defects as function of density in confined quasi two-dimensional geometries and examined the effects of various boundary conditions. Sec. 7.7 describes a novel application to find the curvature dependence of the surface tension in a self-consistent manner to explain the discrepancy between measurements and theoretical predictions of the surface tension for tactoids. Our calculations showed that the "Laplace pressure" renormalizes the surface tensions of the flat geometry for the perpendicular and parallel anchoring conditions, provided that a higher order $\mu$-dependent elastic coefficient is included. However, cusps in the equilibrium shapes of the tactoids are not found, and are expected be important for the renormalization of the surface tensions.

We remark that the construction of the LdG theory is completely general. There are various ways of determining the coefficients, for which we have only shown one example. Moreover, these coefficients do not necessarily need to be fitted to Onsager theory, but can also be determined from comparisons with other theories for (hard) rods, such as fundamental measure theory [236], or experiments and simulations. An interesting application would be to determine the Landau coeffcients from Khokhlov-Semenov theory to describe semi-flexible chains [113, 285, 286]. Furthermore, we only studied the grand-canonical ensemble, however, for bulk systems it is also possible to consider the Gibbs free energy, where the pressure is the relevant intensive variable to be tuned to describe the density-dependent IN transition for hard rods. Ultimately, the final application determines which method is optimal. Finally, we hope that our findings will help to provide (qualitative) insights into problems that can be very hard to tackle within (inhomogeneous) Onsager theory or extensions thereof.

# Appendix: Euler-Lagrange equations for rods in square confinement

In this appendix we derive the Euler-Lagrange equations that we used in section VI. For this we have to minimize $\Delta\Omega$ with respect to $\mathbf{Q}$ while taking into account that $\mathbf{Q}$ is traceless and symmetric, and that the order occurs in the $(x, y)$ plane. Therefore, we introduce the Lagrange multipliers $\lambda^B$, $\kappa_\rho^B$ and $\xi^B$ to ensure these constraints in the bulk, and for the surface we introduce likewise $\lambda^S$, $\kappa_\rho^S$ and $\xi^S$.

We define

$$
\begin{aligned}
\beta B_2 \Delta\tilde{\Omega}[\mathbf{Q}] =& \beta B_2 \Delta\Omega[\mathbf{Q}] - \lambda^B \int_V d\mathbf{r}\,\delta_{\alpha\beta}Q_{\beta\alpha}(\mathbf{r}) - \frac{\kappa_\alpha^B}{2}\epsilon_{\alpha\beta\rho}\int_V d\mathbf{r}[Q_{\beta\rho}(\mathbf{r}) - Q_{\rho\beta}(\mathbf{r})] \\
& - \xi^B \int_V d\mathbf{r}\,\delta_{\alpha z}\delta_{\beta z}\left(Q_{\alpha\beta}(\mathbf{r}) + \frac{1}{2}\right) - \lambda^S L \int_{\partial V} dS\,\delta_{\alpha\beta}Q_{\beta\alpha}(\mathbf{r}) \\
& - \frac{\kappa_\alpha^S L}{2}\epsilon_{\alpha\beta\rho}\int_{\partial V} dS[Q_{\beta\rho}(\mathbf{r}) - Q_{\rho\beta}(\mathbf{r})] - \xi^S L\int_{\partial V} dS\delta_{\alpha z}\delta_{\beta z}\left(Q_{\alpha\beta}(\mathbf{r}) + \frac{1}{2}\right).
\end{aligned}
\tag{7.44}
$$

The Lagrange multipliers $\lambda^B$ and $\lambda^S$ ensure that $\mathbf{Q}$ is traceless in the bulk and surface respectively, while $\kappa_\alpha^B$ and $\kappa_\alpha^S$ ($\alpha = 1, 2, 3$) ensure that $\mathbf{Q}$ is symmetric in the bulk and on the surface respectively. It is then straightforward to find the Euler-Lagrange equations by setting $\delta\Delta\tilde{\Omega}/\delta Q_{\alpha\beta}(\mathbf{r}) = 0$ to find for $\alpha, \beta = 1, 2, 3$ and $\mathbf{r} \in V$

$$
\begin{aligned}
l_1\partial_\lambda^2 Q_{\alpha\beta} + l_2\partial_\lambda\partial_\alpha Q_{\lambda\beta} + l_3\partial_\lambda\partial_\beta Q_{\alpha\lambda} - 3a\beta(\mu^* - \mu)Q_{\beta\alpha} + 9b\,Q_{\beta\rho}Q_{\rho\alpha} - 4dQ_{\lambda\rho}Q_{\rho\lambda}Q_{\beta\alpha} = \\
\lambda^B\delta_{\alpha\beta} + \kappa_\rho^B\epsilon_{\rho\alpha\beta} + \xi^B\delta_{\alpha z}\delta_{\beta z},
\end{aligned}
\tag{7.45}
$$

while for $\mathbf{r} \in \partial V$

$$
\frac{4}{9}[l_1\partial_\lambda Q_{\alpha\beta}\hat{\nu}_\lambda + l_2\partial_\lambda Q_{\lambda\beta}\hat{\nu}_\alpha + l_3\partial_\beta Q_{\alpha\lambda}\hat{\nu}_\lambda] + w(Q_{\alpha\beta} - Q_{\alpha\beta}^0) = \lambda^S\delta_{\alpha\beta} + \kappa_\rho^S\epsilon_{\rho\alpha\beta} + \xi^S\delta_{\alpha z}\delta_{\beta z},
\tag{7.46}
$$

with $\hat{\boldsymbol{\nu}}$ being the unit surface normal. Setting the derivatives with respect to the Lagrange multipliers to zero, gives the constraints

$$
\mathrm{Tr}(\mathbf{Q}) = 0, \quad Q_{\alpha\beta} = Q_{\beta\alpha} \quad (\alpha, \beta = x, y, z), \quad Q_{zz} = -\frac{1}{2}.
\tag{7.47}
$$

The Lagrange multipliers can be determined by evaluating the $zz$ component of Eq. (7.45),

$$
\lambda^B + \xi^B = \frac{3}{2}a\beta(\mu^* - \mu) + \frac{9}{4}b + 2dQ_{\lambda\rho}Q_{\rho\lambda},
\tag{7.48}
$$

while taking the trace of Eq. (7.45) gives

$$3\lambda^B + \xi^B = 2l_s\partial_\rho\partial_\lambda Q_{\lambda\rho} + 9bQ_{\lambda\rho}Q_{\rho\lambda}, \tag{7.49}$$

hence

$$\lambda^B = l_s\partial_\lambda\partial_\rho Q_{\rho\lambda} + \frac{9}{2}b\left(Q_{\lambda\rho}Q_{\rho\lambda} - \frac{1}{4}\right) - \frac{3}{4}a\beta(\mu^* - \mu) - dQ_{\lambda\rho}Q_{\rho\lambda}. \tag{7.50}$$

The effect of the Lagrange multipliers $\kappa_\rho$ is to symmetrize Eq. (7.45) over the indices $\alpha$ and $\beta$. A similar calculation can be performed to determine the surface Lagrange multipliers. Combining Eq. (7.45)-(7.47) and Eq. (7.50) results in the Euler-Lagrange equations Eq. (7.28) and boundary condition Eq. (7.29).

# 8

# **Summary**

In this thesis we investigated various aspects of colloidal dispersions. We not only emphasized the tunability of the particle properties (rods versus spheres, charging properties of the particle surface), but also the properties of the medium in which they reside (oil and/or water). These properties can impact the phase behaviour of colloidal dispersions, and the effective colloid-colloid or colloid-interface interactions. We applied concepts like (long-range) ionic screening, charge regulation, many-body effects, and anisotropy in particle shape, to various dispersions of charged colloidal spheres and hard needles.

In Chapter 2, we studied one-component[1] dispersions of charge-regulating colloidal spheres. These spheres were treated within a spherical-cell model to approximate the many-body environment in which the colloidal particles can reside. This leads, for example, to particle discharging as function of density and salt concentration, and as such, can induce crystallization depending on the (effective) screening length, colloid density and colloidal charge. The type of charge regulation proved to have a large influence on the phase diagram, showing not only a reentrant fluid if the salt concentration is increased (fluid-BCC(-FCC)-fluid), but also if the colloid density is increased (fluid-BCC-fluid) in the case of colloidal spheres that acquire their charge via cationic *and* anionic adsorption. This explained experiments and showed that the macroscopic phase diagram gives insights in microscopic processes such as the charge-regulation properties of a single colloidal particle. Moreover, we compared various crystallization criteria quantitatively by mapping the cell model to inflated hard spheres, point Yukawa systems and the one-component plasma.

We described binary systems of repulsive charge-asymmetric colloidal spheres in Chapter 3. Within the cell approach we calculated thermodynamic properties and looked at spontaneous demixing, which revealed that charge asymmetries between colloidal species can induce a spinodal instability. We constructed phase diagrams and compared various boundary conditions for the colloidal charge. Moreover, we gave estimates on the location of the crystallization transition, by an interpolation between the one-component limits of the suspension. Finally, we looked at the repercussions of

---

[1]The number of components refers to the number of colloidal species.

the phase diagram on sedimentation profiles, revealing that the previously theoretically predicted segregation of the colloidal species is not necessarily associated with phase separation. The results from the local-density approximation that we used were, however, in disagreement with experiment, because non-local contributions can become more important if the system is close to a demixed state.

There is also the possibility for microphase separation in repulsive binary colloidal dispersions, and we investigated this in Chapter 4. Using the binary cell model, we performed many-body corrections to the colloid-colloid effective pair potential by mapping the cell model to a system of two colloidal spheres. This approach revealed the possibility of a directional effective-interaction potential. The directionality stems from the formation of induced dipoles, which depend on the precise local environment of a single colloid. Such effective interactions can explain the experimentally observed formation of alternating strings and extended clusters in binary mixtures of colloids. Furthermore, we ended with open questions on the surprising formation of dumbbells in one-component systems, which is still poorly understood.

In Chapter 5 we considered colloidal particles in a medium that consists of two immiscible solvents, namely oil and water. We showed that so-called non-touching colloids experience an effective interaction potential with the oil-water interface, that is tunable by the Donnan potential and colloidal charge. These colloid-ion forces can not only be tuned in range and strength, but also in being repulsive or attractive at sufficiently large distances from the interface, and should be added to the well-known image-charge and van der Waals potential. Furthermore, we investigated lateral colloid-colloid interactions for colloids that can penetrate the oil-water interface, revealing again the importance of many-body effects, as was also found in other chapters. We suggested that the colloid-colloid lateral interaction is dominated by the small, weakly screened bound charges at the oil-exposed side of the colloidal surface, and these are probably more important than the many highly screened charges at the water-exposed side.

The tunable colloid-interface interaction for non-touching colloids was explicitly compared with experiments in Chapter 6. We considered two salts with the same anion, which enabled us to tune the colloidal charge from negative to positive as a function of ionic strength. We explicitly explained the time-dependent particle detachment and subsequent reattachment from the interface by the addition of an organic salt to the oil phase, by using equilibrium methods and ion dynamics. Furthermore, we explained the Donnan-potential dependence on salt, the robustness of interfacially trapped colloids when the particles cannot switch the sign of their colloidal charge and, finally, the attractive colloid-interface interaction when an organic salt was added to the water side.

Finally, in Chapter 7, we considered the anisotropy in the particle shape in the context of hard needles. These needles were described by a novel Landau-de Gennes theory that accurately mimicks Onsager theory. We tested this theory that is based on the grand-canonical ensemble in bulk and for the isotropic-nematic interface. We applied it subsequently to the hedgehog defect and showed that colloidal systems have an

isotropic core size that is on the order of the particle size. This should be contrasted to molecular (thermotropic) systems where the core size is much larger than the molecular size. Furthermore, we investigated the density dependence of director field textures and their defects for confined rods. Ultimately, we applied our theory to tactoids: liquid crystalline droplets in an isotropic background. The experimentally observed large size aspect ratios of these droplets are, however, not explained in our theory, if we use the surface tensions from Onsager theory, revealing the need of additional ingredients in our model.

# Bibliography

[1] P. W. Anderson, Science **177**, 393 (1972)

[2] A. G. Császár, G. Czakó, T. Furtenbacher, J. Tennyson, V. Szalay, S. V. Shirin, N. F. Zobov, and O. L. Polyansky, J. Chem. Phys. **122**, 214305 (2005)

[3] L. Pauling, J. Am. Chem. Soc. **53**, 1367 (1931)

[4] J.-P. Hansen and I. R. McDonald, in *Theory of Simple Liquids (Third Edition)* (Academic Press, 2005)

[5] T. Graham, Phil. Trans. Roy. Soc. Lond. **151**, 183 (1861)

[6] R. Brown, Phil. Mag. **4**, 161 (1828)

[7] A. Einstein, Annalen der Physik **322**, 549 (1905)

[8] S.-M. Yang, S.-H. Kim, J.-M. Lim, and G.-R. Yi, J. Mater. Chem. **18**, 2177 (2008)

[9] A. Snezhko, M. Belkin, I. S. Aranson, and W.-K. Kwok, Phys. Rev. Lett. **102**, 118103 (2009)

[10] S. Jiang, M. J. Schultz, Q. Chen, J. S. Moore, and S. Granick, Langmuir **24**, 10073 (2008)

[11] L. Hong, A. Cacciuto, E. Luijten, and S. Granick, Nano Lett. **6**, 2510 (2006)

[12] M. M. Moghani and B. Khomami, Soft Matter **9**, 4815 (2013)

[13] A. P. Gantapara, J. de Graaf, R. van Roij, and M. Dijkstra, Phys. Rev. Lett. **111**, 015501 (2013)

[14] I. I. Tarhan and G. H. Watson, Phys. Rev. Lett. **76**, 315 (1996)

[15] M. Faraday, Phil. Trans. Roy. Soc. Lond. **147**, 145 (1857)

[16] S. Eustis and M. A. El-Sayed, Chem. Soc. Rev. **35**, 209 (2006)

[17] A. Badger, W. Weyl, and H. Rudow, Glass ind **20**, 407 (1939)

Bibliography

[18] B. Senyuk, Q. Liu, S. He, R. D. Kamien, R. B. Kusner, T. C. Lubensky, and I. I. Smalyuk, Nature **493**, 200 (2013)

[19] W. T. Irvine and D. Kleckner, Nature materials **13**, 229 (2014)

[20] R. Evans, Advances in Physics **28**, 143 (1979)

[21] R. Netz and H. Orland, Eur. Phys. J. E **1**, 203 (2000)

[22] M. Peskin and D. Schroeder, in *An introduction to quantum field theory* (Westview Press, 1995)

[23] A. G. Moreira and R. R. Netz, Eur. Phys. Lett. **52**, 705 (2000)

[24] L. Šamaj and E. Trizac, Phys. Rev. E **84**, 041401 (2011)

[25] A. Naji, M. Kanduč, J. Forsman, and R. Podgornik, J. Chem. Phys. **139**, 150901 (2013)

[26] P. M. Chaikin and T. C. Lubensky, in *Principles of condensed matter physics* (Cambridge University Press, 2000)

[27] L. Onsager, Ann. NY Acad. Sci. **51**, 627 (1949)

[28] R. van Roij, Eur. J. Phys. **26**, S57 (2005)

[29] K. Shundyak and R. van Roij, Phys. Rev. E **68**, 061703 (2003)

[30] E. Wigner, Phys. Rev. **46**, 1002 (1934)

[31] C. C. Grimes and G. Adams, Phys. Rev. Lett. **42**, 795 (1979)

[32] S. Torquato and F. H. Stillinger, Rev. Mod. Phys. **82**, 2633 (2010)

[33] B. J. Alder and T. E. Wainwright, J. Chem. Phys. **27**, 1208 (1957)

[34] J. Jones, J. Sanders, and E. R. Segnit, Nature **204**, 990 (1964)

[35] P. N. Pusey and W. van Megen, Nature **320**, 340 (1986)

[36] M. E. Leunissen, C. G. Christova, A.-P. Hynninen, C. P. Royall, A. I. Campbell, A. Imhof, M. Dijkstra, R. van Roij, and A. van Blaaderen, Nature **437**, 235 (2005)

[37] R. Williams and R. Crandall, Phys. Lett. A **48**, 225 (1974)

[38] E. B. Sirota, H. D. Ou-Yang, S. K. Sinha, P. M. Chaikin, J. D. Axe, and Y. Fujii, Phys. Rev. Lett. **62**, 1524 (1989)

[39] Y. Monovoukas and A. P. Gast, J. Coll. Int. Sci. **128**, 533 (1989)

[40] T. Okubo, J. Chem. Soc., Faraday Trans. **86**, 2871 (1990)

[41] T. Okubo, J. Chem. Phys. **95**, 3690 (1991)

[42] T. Palberg, W. Mönch, F. Bitzer, P. Lpageserer, L. Belloni, T. Bellini, and R. Piazza, Helv. Phys. Acta **67**, 225 (1994)

[43] A. Yethiraj, Soft Matter **3**, 1099 (2007)

[44] D. M. Herlach, I. Klassen, P. Wette, and D. Holland-Moritz, J. Phys.: Cond. Matt. **22**, 153101 (2010)

[45] H. M. Lindsay and P. M. Chaikin, J. Chem. Phys. **76**, 3774 (1982)

[46] S.-H. Kim, S. Y. Lee, S.-M. Yang, and G.-R. Yi, NPG Asia Materials **3**, 25 (2011)

[47] B. You, N. Wen, L. Shi, L. Wu, and J. Zi, J. Mater. Chem. **19**, 3594 (2009)

[48] L. Shapran, H. J. Schöpe, and T. Palberg, J. Chem. Phys. **125**, 194714 (2006)

[49] C. P. Royall, M. E. Leunissen, A.-P. Hynninen, M. Dijkstra, and A. van Blaaderen, J. Chem. Phys **124**, 244706 (2006)

[50] J. W. Merrill, S. K. Sainis, and E. R. Dufresne, Phys. Rev. Lett. **103**, 138301 (2009)

[51] B. W. Ninham and V. Parsegian, J. Theor. Biol. **31**, 405 (1971)

[52] D. Andelman, in *Introduction to Electrostatics in Soft and Biological Matter* (Taylor and Francis, New York, 2005) pp. 97–122

[53] F. Smallenburg, N. Boon, M. Kater, M. Dijkstra, and R. van Roij, J. Chem. Phys. **134**, 074505 (2011)

[54] T. Kanai, N. Boon, P. J. Lu, E. Sloutskin, A. B. Schofield, F. Smallenburg, R. van Roij, M. Dijkstra, and D. A. Weitz, Phys. Rev. E **91**, 030301 (2015)

[55] C. P. Royall, M. E. Leunissen, and A. van Blaaderen, J. Phys.: Cond. Matt. **15**, S3581 (2003)

[56] I. R. de Anda, A. Statt, F. Turci, and C. P. Royall, Contr. Plasma Phys. **55**, 172 (2015)

[57] S. Alexander, P. M. Chaikin, P. Grant, G. J. Morales, P. Pincus, and D. Hone, J. Chem. Phys. **80**, 5776 (1984)

[58] E. Trizac, L. Bocquet, and M. Aubouy, Phys. Rev. Lett. **89**, 248301 (2002)

[59] A. Diehl and Y. Levin, J. Phys.: Cond. Matt. **17**, S3309 (2005)

[60] B. Derjaguin and L. Landau, Acta Physicochim. URSS **14**, 633 (1941)

[61] E. J. W. Verwey and J. T. G. Overbeek, in *Theory of the Stability of Lyophobic Colloids* (Elsevier, New York, 1948)

[62] H. Löwen, P. Madden, and J.-P. Hansen, Phys. Rev. Lett. **68**, 1081 (1992)

[63] R. van Roij and J.-P. Hansen, Phys. Rev. Lett. **79**, 3082 (1997)

[64] P. B. Warren, J. Chem. Phys. **112**, 4683 (2000)

[65] J.-P. Hansen and H. Löwen, Ann. Rev. Phys. Chem. **51**, 209 (2000)

[66] H. H. von Grünberg, R. van Roij, and G. Klein, Eur. Phys. Lett. **55**, 580 (2001)

[67] N. Boon, G. I. Guerrero-García, R. van Roij, and M. Olvera de la Cruz, Proc. Nat. Acad. Sci. **112**, 9242 (2015)

[68] D. Stigter, Recueil des Travaux Chimiques des Pays-Bas **73**, 593 (1954)

[69] W. van Megen and I. Snook, Chem. Phys. Lett. **35**, 399  (1975)

[70] S. L. Brenner, J. Phys. Chem. **80**, 1473 (1976)

[71] J. A. Beunen and L. R. White, Colloids and Surfaces **3**, 371  (1981)

[72] W. L. Slattery, G. D. Doolen, and H. E. DeWitt, Phys. Rev. A **21**, 2087 (1980)

[73] S. Ichimaru, Rev. Mod. Phys. **54**, 1017 (1982)

[74] O. Vaulina and S. Khrapak, J. Exp. Theor. Phys. **90**, 287 (2000)

[75] S. Hamaguchi, R. T. Farouki, and D. H. E. Dubin, Phys. Rev. E **56**, 4671 (1997)

[76] A.-P. Hynninen and M. Dijkstra, Phys. Rev. E **68**, 021407 (2003)

[77] M. D. Carbajal-Tinoco and P. González-Mozuelos, J. Chem. Phys. **117**, 2344 (2002)

[78] B. Zoetekouw and R. van Roij, Phys. Rev. Lett. **97**, 258302 (2006)

[79] W. Y. Shih, W. Shih, and I. A. Aksay, J. Chem. Phys. **90**, 4506 (1989)

[80] P. Bartlett and A. I. Campbell, Phys. Rev. Lett. **95**, 128302 (2005)

[81] W. Lin, M. Kobayashi, M. Skarba, C. Mu, P. Galletto, and M. Borkovec, Langmuir **22**, 1038 (2006)

[82] E. Sanz, C. Valeriani, D. Frenkel, and M. Dijkstra, Phys. Rev. Lett. **99**, 055501 (2007)

[83] M. Rex and H. Löwen, Phys. Rev. E **75**, 051402 (2007)

[84] M. Bier, R. van Roij, and M. Dijkstra, J. Chem. Phys. **133**, 124501 (2010)

[85] T. Biben and J.-P. Hansen, Phys. Rev. Lett. **66**, 2215 (1991)

[86] A. D. Dinsmore, A. G. Yodh, and D. J. Pine, Phys. Rev. E **52**, 4045 (1995)

[87] M. Dijkstra, R. van Roij, and R. Evans, Phys. Rev. Lett. **81**, 2268 (1998)

[88] A.-P. Hynninen, L. Filion, and M. Dijkstra, J. Chem. Phys. **131**, 064902 (2009)

[89] M. Baus and J.-P. Hansen, Physics Reports **59**, 1 (1980)

[90] P. Hopkins, A. J. Archer, and R. Evans, J. Chem. Phys. **124**, 054503 (2006)

[91] E. Allahyarov and H. Löwen, J. Phys: Cond. Matt. **21**, 424117 (2009)

[92] A. Torres, *Statistical thermodynamics of charge-stabilized colloids, Chapter 5*, Ph.D. thesis, Utrecht University (2008)

[93] A. Meller and J. Stavans, Phys. Rev. Lett. **68**, 3646 (1992)

[94] N. J. Lorenz, H. J. Schöpe, H. Reiber, T. Palberg, P. Wette, I. Klassen, D. Holland-Moritz, D. Herlach, and T. Okubo, J. Phys.: Cond. Matt. **21**, 464116 (2009)

[95] N. J. Lorenz and T. Palberg, J. Chem. Phys. **133**, 104501 (2010)

[96] K. Yoshizawa, N. Wakabayashi, M. Yonese, J. Yamanaka, and C. P. Royall, Soft Matter **8**, 11732 (2012)

[97] Y. Nakamura, M. Okachi, A. Toyotama, T. Okuzono, and J. Yamanaka, Langmuir **31**, 13303 (2015)

[98] A. Esztermann and H. Löwen, Eur. Phys. Lett. **68**, 120 (2004)

[99] J. Zwanikken and R. van Roij, Eur. Phys. Lett. **71**, 480 (2005)

[100] P. M. Biesheuvel and J. Lyklema, J. Phys.: Cond. Matt. **17**, 6337 (2005)

[101] M. Dijkstra, J. Zwanikken, and R. van Roij, J. Phys.: Cond. Matt. **18**, 825 (2006)

[102] J. K. Chung and A. R. Denton, Phys. Rev. E **88**, 022306 (2013)

[103] M. van der Linden, *Long-range repulsive charged colloids in and out of equilibrium*, Ph.D. thesis, Utrecht University (2013)

[104] E. Eggen and R. van Roij, Phys. Rev. E **80**, 041402 (2009)

[105] A. Torres, G. Téllez, and R. van Roij, J. Chem. Phys. **128**, 154906 (2008)

[106] D. de las Heras and M. Schmidt, J. Phys.: Cond. Matt. **27**, 194115 (2015)

[107] R. van Roij, J. Phys.: Cond. Matt. **15**, S3569 (2003)

[108] C. P. Royall, R. van Roij, and A. van Blaaderen, J. Phys.: Cond. Matt. **17**, 2315 (2005)

[109] P. M. Biesheuvel, J. Phys.: Cond. Matt. **16**, L499 (2004)

[110] P. Hopkins, A. J. Archer, and R. Evans, J. Chem. Phys. **129**, 214709 (2008)

[111] R. A. L. Jones, in *Soft Condensed Matter* (OUP Oxford, 2002)

[112] B. Alberts, A. Johnson, J. Lewis, M. Raff, K. Roberts, and P. Walter, in *Molecular Biology of the Cell (5th edition)* (Garland Science, 2007)

[113] G. J. Vroege and H. N. W. Lekkerkerker, Rep. Prog. Phys. **55**, 1241 (1992)

[114] J. Timmermans, J. Phys. Chem. Sol. **18**, 1 (1961)

[115] B. Liu, T. B. Besseling, M. Hermes, A. F. Demirörs, A. Imhof, and A. van Blaaderen, Nature Communications **5**, 3092 (2014)

[116] D. Shechtman, I. Blech, D. Gratias, and J. W. Cahn, Phys. Rev. Lett. **53**, 1951 (1984)

[117] D. Talapin, E. Shevchenko, M. Bodnarchuk, X. Ye, J. Chen, and C. Murray, Nature **461**, 964 (2009)

[118] S. Genc and B. Derin, Curr. Op. Chem. Eng. **3**, 118 (2014)

[119] J. D. Watson, Nature **171**, 737 (1953)

[120] K. A. Dill and J. L. MacCallum, Science **338**, 1042 (2012)

[121] L. Leibler, Macromolecules **13**, 1602 (1980)

[122] W. B. Russel, D. A. Saville, and W. R. Schowalter, in *Colloidal Dispersions* (Cambridge University Press, 1992)

[123] A. Yethiraj and A. van Blaaderen, Nature **421**, 513 (2003)

[124] R. van Roij and J.-P. Hansen, Phys. Rev. Lett. **79**, 3082 (1997)

[125] B. Zoetekouw, *Phase behavior of charged colloids many-body effects, charge renormalization and charge regulation*, Ph.D. thesis, Utrecht University (2006)

[126] H. Löwen, J. Hansen, and P. A. Madden, J. Chem. Phys. **98**, 3275 (1993)

[127] A. R. Denton, Phys. Rev. E **62**, 3855 (2000)

[128] J. N. Israelachvili, in *Intermolecular and Surface Forces (Third Edition)* (Elsevier, 2011)

[129] N. Hoffmann, C. N. Likos, and J.-P. Hansen, Mol. Phys. **102**, 857 (2004)

[130] R. Ramirez and R. Kjellander, J. Chem. Phys. **125**, 144110 (2006)

[131] N. Boon, E. C. Gallardo, S. Zheng, E. Eggen, M. Dijkstra, and R. van Roij, J. Phys.: Cond. Matt. **22**, 104104 (2010)

[132] J. de Graaf, N. Boon, M. Dijkstra, and R. van Roij, J. Chem. Phys. **137**, 104910 (2012)

[133] F. Smallenburg, H. R. Vutukuri, A. Imhof, A. van Blaaderen, and M. Dijkstra, J. Phys.: Cond. Matt. **24**, 464113 (2012)

[134] T. Vissers, A. Wysocki, M. Rex, H. Lowen, C. P. Royall, A. Imhof, and A. van Blaaderen, Soft Matter **7**, 2352 (2011)

[135] R. P. Sear and W. M. Gelbart, J. Chem. Phys. **110**, 4582 (1999)

[136] A. Imperio and L. Reatto, J. Phys.: Cond. Matt. **16**, S3769 (2004)

[137] A. J. Archer and N. B. Wilding, Phys. Rev. E **76**, 031501 (2007)

[138] J. Groenewold and W. K. Kegel, J. Phys. Chem. B **105**, 11702 (2001)

[139] J. Groenewold and W. K. Kegel, J. Phys.: Cond. Matt. **16**, S4877 (2004)

[140] K. Barros and E. Luijten, Phys. Rev. Lett. **113**, 017801 (2014)

[141] T. Vissers, A. Imhof, F. Carrique, Ángel V. Delgado, and A. van Blaaderen, J. Coll. Int. Sci. **361**, 443  (2011)

[142] M. N. van der Linden, J. C. P. Stiefelhagen, G. Heessels-Gürboğa, J. E. S. van der Hoeven, N. A. Elbers, M. Dijkstra, and A. van Blaaderen, Langmuir **31**, 65 (2015)

[143] I. D. Morrison, Coll. Surf. A **71**, 1  (1993)

[144] M. N. van der Linden, D. El Masri, M. Dijkstra, and A. van Blaaderen, Soft Matter **9**, 11618 (2013)

[145] M. Tamashiro, Y. Levin, and M. Barbosa, Eur. Phys. J. B **1**, 337 (1998)

[146] A. R. Denton, J. Phys.: Cond. Matt. **22**, 364108 (2010)

[147] C. Valeriani, P. J. Camp, J. W. Zwanikken, R. van Roij, and M. Dijkstra, Soft Matter **6**, 2793 (2010)

[148] S. L. Carnie, D. Y. C. Chan, and J. S. Gunning, Langmuir **10**, 2993 (1994)

[149] J. Stankovich and S. L. Carnie, Langmuir **12**, 1453 (1996)

[150] M. E. Leunissen, J. Zwanikken, R. van Roij, P. M. Chaikin, and A. van Blaaderen, Phys. Chem. Chem. Phys. **9**, 6405 (2007)

[151] E. M. Lifschitz, J. Exp. Th. Phys. USSR **29**, 94

[152] B. M. Mladek, P. Charbonneau, C. N. Likos, D. Frenkel, and G. Kahl, J. Phys.: Cond. Matt. **20**, 494245 (2008)

[153] M. Fushiki, J. Chem. Phys. **97**, 6700 (1992)

[154] H. Löwen, P. A. Madden, and J.-P. Hansen, Phys. Rev. Lett. **68**, 1081 (1992)

[155] H. Löwen and G. Kramposthuber, Eur. Phys. Lett. **23**, 673 (1993)

[156] P. Pieranski, Phys. Rev. Lett. **45**, 569 (1980)

[157] S. U. Pickering, J. Chem. Soc., Trans. **91**, 2001 (1907)

[158] M. E. Leunissen, A. van Blaaderen, A. D. Hollingsworth, M. T. Sullivan, and P. M. Chaikin, Proc. Nat. Acad. Sci. **104**, 2585 (2007)

[159] M. Luo, G. K. Olivier, and J. Frechette, Soft Matter **8**, 11923 (2012)

[160] F. Reincke, W. K. Kegel, H. Zhang, M. Nolte, D. Wang, D. Vanmaekelbergh, and H. Möhwald, Phys. Chem. Chem. Phys. **8**, 3828 (2006)

[161] V. Poulichet and V. Garbin, Proc. Natl. Acad. Sci. U.S.A. **112**, 5932 (2015)

[162] S. Crossley, J. Faria, M. Shen, and D. E. Resasco, Science **327**, 68 (2010)

[163] B. O. Carter, W. Wang, D. J. Adams, and A. I. Cooper, Langmuir **26**, 3186 (2010)

[164] B. O. Carter, D. J. Adams, and A. I. Cooper, Green Chem. **12**, 783 (2010)

[165] C. P. Kelleher, A. Wang, G. I. Guerrero-García, A. D. Hollingsworth, R. E. Guerra, B. J. Krishnatreya, D. G. Grier, V. N. Manoharan, and P. M. Chaikin, Phys. Rev. E **92**, 062306 (2015)

[166] J. Zwanikken and R. van Roij, Phys. Rev. Lett. **99**, 178301 (2007)

[167] N. Elbers, J. van der Hoeven, M. de Winter, C. Schneijdenberg, M. van der Linden, L. Filion, and A. van Blaaderen, Soft Matter, (2016)

[168] M. Oettel, Phys. Rev. E **76**, 041403 (2007)

[169] J. D. Jackson, in *Classical Electrodynamics (Third Edition)* (Whiley, 1998)

[170] H. Wang, V. Singh, and S. H. Behrens, J. Phys. Chem. Lett. **3**, 2986 (2012)

[171] V. A. Parsegian, "Van der waals forces: A handbook for biologists, chemists, engineers, and physicists," Cambridge Press (2005)

[172] Y. Levin, J. Chem. Phys. **113**, 9722 (2000)

[173] M. Bier, J. Zwanikken, and R. van Roij, Phys. Rev. Lett. **101**, 046104 (2008)

[174] A. Onuki, J. Chem. Phys. **128**, 224704 (2008)

[175] J. Zwanikken, J. de Graaf, M. Bier, and R. van Roij, J. Phys.: Cond. Matter **20**, 494238 (2008)

[176] M. J. E. Westbroek, N. Boon, and R. van Roij, Phys. Chem. Chem. Phys. **17**, 25100 (2015)

[177] K. D. Danov, P. A. Kralchevsky, K. P. Ananthapadmanabhan, and A. Lips, Langmuir **22**, 106 (2006)

[178] D. Frydel, S. Dietrich, and M. Oettel, Phys. Rev. Lett. **99**, 118302 (2007)

[179] C. L. Wirth, E. M. Furst, and J. Vermant, Langmuir **30**, 2670 (2014)

[180] R. R. Netz, Phys. Rev. E **60**, 3174 (1999)

[181] Würger, A., Eur. Phys. J. E **19**, 5 (2006)

[182] G. N. Smith, J. E. Hallett, and J. Eastoe, Soft Matter **11**, 8029 (2015)

[183] M. Bier, A. Gambassi, M. Oettel, and S. Dietrich, Eur. Phys. Lett. **95**, 60001 (2011)

[184] M. Bier, A. Gambassi, and S. Dietrich, J. Chem. Phys. **137**, 034504 (2012)

[185] A. Onuki, Phys. Rev. E **73**, 021506 (2006)

[186] R. Okamoto and A. Onuki, Phys. Rev. E **84**, 051401 (2011)

[187] S. Samin and Y. Tsori, Eur. Phys. Lett. **95**, 36002 (2011)

[188] A. P. dos Santos and Y. Levin, Langmuir **28**, 1304 (2012)

[189] S. Samin and Y. Tsori, J. Chem. Phys. **139**, 244905 (2013)

[190] S. Samin, M. Hod, E. Melamed, M. Gottlieb, and Y. Tsori, Phys. Rev. Appl. **2** (2014)

[191] B. J. Park, M. Lee, B. Lee, and E. M. Furst, Soft Matter **11**, 8701 (2015)

[192] M. Vis, V. F. D. Peters, R. H. Tromp, and B. H. Erne, Langmuir **30**, 5755 (2014)

[193] R. Aveyard, B. P. Binks, J. H. Clint, P. D. I. Fletcher, T. S. Horozov, B. Neumann, V. N. Paunov, J. Annesley, S. W. Botchway, D. Nees, A. W. Parker, A. D. Ward, and A. N. Burgess, Phys. Rev. Lett. **88**, 246102 (2002)

[194] K. Masschaele, B. J. Park, E. M. Furst, J. Fransaer, and J. Vermant, Phys. Rev. Lett. **105**, 048303 (2010)

[195] A. D. Law, M. Auriol, D. Smith, T. S. Horozov, and D. M. A. Buzza, Phys. Rev. Lett. **110**, 138301 (2013)

[196] K. Kim, K. Park, G. Kim, H. Kim, M. C. Choi, and S. Q. Choi, Langmuir **30**, 12164 (2014)

[197] T. Sakka, D. Kozawa, K. Tsuchiya, N. Sugiman, G. Oye, K. Fukami, N. Nishi, and Y. H. Ogata, Phys. Chem. Chem. Phys. **16**, 16976 (2014)

[198] F. H. Stillinger, J. Chem. Phys. **35**, 1584 (1961)

[199] A. J. Hurd, J. Phys. A **18**, L1055 (1985)

[200] K. D. Danov, P. A. Kralchevsky, and M. P. Boneva, Langmuir **20**, 6139 (2004)

[201] D. Frydel and M. Oettel, Phys. Chem. Chem. Phys. **13**, 4109 (2011)

[202] S. Uppapalli and H. Zhao, Soft Matter **10**, 4555 (2014)

[203] G. V. Bossa, J. Roth, K. Bohinc, and S. May, Soft Matter **12**, 4229 (2016)

[204] A. Majee, M. Bier, and S. Dietrich, J. Chem. Phys. **140**, 164906 (2014)

[205] B. Derjaguin, Kolloid-Zeitschrift **69**, 155 (1934)

[206] B. J. Park, M. Lee, B. Lee, and E. M. Furst, Soft Matter **11**, 8701 (2015)

[207] N. Elbers, *Experiments in which oil, water and colloidal particles meet*, Ph.D. thesis, Utrecht University (2015)

[208] Y. Chevalier and M.-A. Bolzinger, Coll. Surf. A **439**, 23 (2013)

[209] J. Tang, P. J. Quinlan, and K. C. Tam, Soft Matter **11**, 3512 (2015)

[210] A. Banerjee, I. Williams, R. N. Azevedo, M. E. Helgeson, and T. M. Squires, Proc. Nat. Acad. Sci. **113**, 8612 (2016)

[211] G. Chatel, J. F. B. Pereira, V. Debbeti, H. Wang, and R. D. Rogers, Green Chem. **16**, 2051 (2014)

[212] A. Guerfi, M. Dontigny, P. Charest, M. Petitclerc, M. Lagacé, A. Vijh, and K. Zaghib, Journal of Power Sources **195**, 845 (2010)

[213] J. E. S. van der Hoeven, *Colloids near oil-water Interfaces: charge regulation, phase behavior and interfacial motion*, Master's thesis, Utrecht University (2014)

[214] U. M. B. Marconi and P. Tarazona, J. Chem. Phys. **110**, 8032 (1999)

[215] M. Schmidt and J. M. Brader, J. Chem. Phys. **138**, 214101 (2013)

[216] J. F. Brady, J. Fluid. Mech. **667**, 216 (2011)

[217] A. Altland and B. D. Simons, *Condensed matter field theory* (Cambridge University Press, 2010)

[218] L. D. Landau, Zh. Eksp. Teor. Fiz. **7**, 19 (1937)

[219] H. T. C. Stoof, K. B. Gubbels, and D. B. M. Dickerschpages, *Ultracold Quantum Fields* (Springer Netherlands, 2009)

[220] P. Hohenberg and A. Krekhov, Physics Reports **572**, 1  (2015)

[221] V. L. Ginzburg and L. D. Landau, J. Exp. Theor. Phys. (U.S.S.R.) **20**, 1064 (1950)

[222] P. G. De Gennes, Mol. Crys. Liq. Crys. **12**, 193 (1971)

[223] E. F. Gramsbergen, L. Longa, and W. H. de Jeu, Physics Reports **135**, 195 (1986)

[224] G. Tóth, C. Denniston, and J. M. Yeomans, Phys. Rev. Lett. **88**, 105504 (2002)

[225] O. Guzmán, E. B. Kim, S. Grollau, N. L. Abbott, and J. J. de Pablo, Phys. Rev. Lett. **91**, 235507 (2003)

[226] A. Nych, U. Ognysta, M. Škarabot, M. Ravnik, S. Žumer, and I. Muševič, Nature Communications **4**, 1489 (2013)

[227] L. Giomi and A. DeSimone, Phys. Rev. Lett. **112**, 147802 (2014)

[228] H. Zocher, Z. Anorg. Chem. **147**, 91 (1925)

[229] F. C. Bawden, N. W. Pirie, J. D. Bernal, and I. Fankuchen, Nature **138**, 1051 (1936)

[230] Z. Dogic and S. Fraden, Phys. Rev. Lett. **78**, 2417 (1997)

[231] F. M. van der Kooij and H. N. W. Lekkerkerker, J. Phys. Chem. B **102**, 7829 (1998)

[232] A. B. D. Brown, S. M. Clarke, and A. R. Rennie, Langmuir **14**, 3129 (1998)

[233] F. M. van der Kooij, K. Kassapidou, and H. N. Lekkerkerker, Nature **406**, 868 (2000)

[234] R. Wittkowski, H. Löwen, and H. R. Brand, Phys. Rev. E **82**, 031708 (2010)

[235] D. Frenkel, J. Phys. Chem. **91**, 4912 (1987)

[236] R. Wittmann and K. Mecke, J. Chem. Phys. **140**, 104703 (2014)

[237] G. Skačej, A. L. Alexe-Ionescu, G. Barbero, and S. Žumer, Phys. Rev. E **57**, 1780 (1998)

[238] C. W. Oseen, Trans. Faraday Soc. **29**, 883 (1933)

[239] F. C. Frank, Discuss. Faraday Soc. **25**, 19 (1958)

[240] J. P. Straley, Phys. Rev. A **8**, 2181 (1973)

[241] P. Prinsen and P. van der Schoot, Eur. Phys. J. E **13**, 35 (2004)

[242] A. Rapini and M. Papoular, J. Phys. Colloques **30**, C4 (1969)

[243] M. Nobili and G. Durand, Phys. Rev. A **46**, R6174 (1992)

[244] N. Schopohl and T. J. Sluckin, Phys. Rev. Lett. **59**, 2582 (1987)

[245] R. F. Kayser and H. J. Raveché, Phys. Rev. A **17**, 2067 (1978)

[246] V. Popa-Nita, T.J. Sluckin, and A.A. Wheeler, J. Phys. II France **7**, 1225 (1997)

[247] S. M. Kamil, A. K. Bhattacharjee, R. Adhikari, and G. I. Menon, Phys. Rev. E **80**, 041705 (2009)

[248] S. Wolfsheimer, C. Tanase, K. Shundyak, R. van Roij, and T. Schilling, Phys. Rev. E **73**, 061703 (Jun 2006)

[249] A. Poniewierski and J. Stecki, Mol. Phys. **38**, 1931 (1979)

[250] J. Stecki and A. Poniewierski, Mol. Phys. **41**, 1451 (1980)

[251] N. Schopohl and T. Sluckin, J. Phys. France **49**, 1097 (1988)

[252] F. Greco and G. Marrucci, Mol. Crys. Liq. Crys. **210**, 129 (1992)

[253] S. Mkaddem and E. C. Gartland, Phys. Rev. E **62**, 6694 (2000)

[254] A. Majumbdar, Eur. J. Appl. Math. **23**, 61 (2012)

[255] J. A. N. Zasadzinski and R. B. Meyer, Phys. Rev. Lett. **56**, 636 (1986)

[256] R. H. J. Otten and P. van der Schoot, J. Chem. Phys. **137**, 154901 (2012)

[257] J. Z. Y. Chen, Soft Matter **9**, 10921 (2013)

[258] A. H. Lewis, I. Garlea, J. Alvarado, O. J. Dammone, P. D. Howell, A. Majumdar, B. M. Mulder, M. P. Lettinga, G. H. Koenderink, and D. G. A. L. Aarts, Soft Matter **10**, 7865 (2014)

[259] I. C. Garlea and B. M. Mulder, Soft Matter **11**, 608 (2015)

[260] C. Tsakonas, A. J. Davidson, C. V. Brown, and N. J. Mottram, App. Phys. Lett. **90**, 111913 (2007)

[261] Y. Mao, P. Bladon, H. N. W. Lekkerkerker, and M. E. Cates, Mol. Phys. **92**, 151 (1997)

[262] M. Dijkstra, R. v. Roij, and R. Evans, Phys. Rev. E **63**, 051703 (2001)

[263] W. L. McMillan, Phys. Rev. A **6**, 936 (1972)

[264] A. K. Sen and D. E. Sullivan, Phys. Rev. A **35**, 1391 (1987)

[265] A. V. Kaznacheev, M. M. Bogdanov, and S. A. Taraskin, J. Exp. Theor. Phys. **95**, 57 (2002)

[266] J. Viamontes, P. W. Oakes, and J. X. Tang, Phys. Rev. Lett. **97**, 118103 (2006)

[267] P. W. Oakes, J. Viamontes, and J. X. Tang, Phys. Rev. E **75**, 061902 (2007)

[268] Y.-K. Kim, S. V. Shiyanovskii, and O. D. Lavrentovich, J. Phys.: Cond. Matt. **25**, 404202 (2013)

[269] V. Jamali, N. Behabtu, B. Senyuk, J. A. Lee, I. I. Smalyukh, P. van der Schoot, and M. Pasquali, Phys. Rev. E **91**, 042507 (2015)

[270] A. Cuetos, R. van Roij, and M. Dijkstra, Soft Matter **4**, 757 (2008)

[271] M. Bier and R. van Roij, Phys. Rev. E **76**, 021405 (2007)

[272] P. Prinsen and P. van der Schoot, Phys. Rev. E **68**, 021701 (2003)

[273] Z. Y. Chen and J. Noolandi, Phys. Rev. A **45**, 2389 (1992)

[274] D. L. Koch and O. G. Harlen, Macromolecules **32**, 219 (1999)

[275] A. V. Kaznacheev, M. M. Bogdanov, and A. S. Sonin, J. Exp. Theor. Phys. **97**, 1159 (2003)

[276] D. van der Beek, H. Reich, P. van der Schoot, M. Dijkstra, T. Schilling, R. Vink, M. Schmidt, R. van Roij, and H. Lekkerkerker, Phys. Rev. Lett. **97**, 087801 (2006)

[277] N. Puech, E. Grelet, P. Poulin, C. Blanc, and P. van der Schoot, Phys. Rev. E **82**, 020702 (2010)

[278] A. K. Bhattacharjee, G. I. Menon, and R. Adhikari, Phys. Rev. E **78**, 026707 (2008)

[279] A. K. Bhattacharjee, G. I. Menon, and R. Adhikari, J. Chem. Phys. **133**, 044112 (2010)

[280] P. C. Hohenberg and B. I. Halperin, Rev. Mod. Phys. **49**, 435 (1977)

[281] P. van der Schoot, J. Phys. Chem. B **103**, 8804 (1999)

[282] Y. Trukhina, S. Jungblut, P. van der Schoot, and T. Schilling, J. Chem. Phys. **130**, 164513 (2009)

[283] K. Schiele and S. Trimper, Physica Status Solidi (b) **118**, 267 (1983)

[284] R. Wittmann, M. Marechal, and K. Mecke, Phys. Rev. E **91**, 052501 (2015)

[285] A. Khokhlov and A. Semenov, Physica A **108**, 546 (1981)

[286] A. Khokhlov and A. Semenov, Physica A **112**, 605 (1982)

# Samenvatting voor iedereen

In het dagelijks leven komen we veelvuldig in aanraking met colloïdale dispersies. Dit soort systemen bestaan in de praktijk uit twee componenten: enerzijds hebben we een medium (gas, vloeistof of vaste stof), en anderzijds hebben we deeltjes die een grootte hebben tussen een nanometer en enkele micrometers (de zogenaamde colloïdale deeltjes), die zelf ook weer gasvormig, vloeibaar of vast kunnen zijn. In principe drinken we dus colloïden (denk aan melk), we maken onze tanden ermee schoon (tandpasta), maar ook ons menselijk lichaam bestaat er uit (denk aan bloed). De colloïdale deeltjes in deze voorbeelden zijn hier respectievelijk vetdruppels, schuurmiddel en rode bloedcellen. Ook hebben colloïdale systemen mogelijke toepassingen als bijvoorbeeld halfgeleiders, wat weer belangrijk is voor de materiaalkunde. In dit proefschrift hebben we echter colloïden vanuit een fundamenteel oogpunt bekeken, waarbij de effectieve wisselwerkingen, het fasengedrag, maar ook de vorm van de deeltjes centraal stonden. Dit hebben we gedaan door naar twee modelsystemen te kijken: elektrisch geladen bolvormige deeltjes en ongeladen harde staven, beiden wanneer ze zich in een vloeistof bevinden.

## Geladen colloïden

Het eerste modelsysteem bestaat uit bolvormige deeltjes met een netto elektrische lading. De effecten van elektrische ladingen kennen we allemaal, denk aan statische elektriciteit, bliksem of stroom die uit je stopcontact komt. Ladingen bevinden zich echter ook in natriumchloride, beter bekend als tafelzout. Wanneer we deze smaakmaker oplossen in water breken de zoutkristallen op in positief geladen natriumionen en negatief geladen chloride-ionen die beiden vrij door het water kunnen bewegen. Er zijn ook andere zouten dan tafelzout, zoals magnesiumcarbonaat, zinksulfaat, waterstofbromide of tetrabutylammoniumbromide (niet allemaal even eetbaar). Wat ze allemaal met elkaar gemeen hebben is dat de ionen waaruit ze bestaan erg klein zijn (0.1-1 nanometer) en in tegenstelling tot colloïdale deeltjes ($\sim$ 1 micrometer) kan je ze niet eens met een optische microscoop zien.

Deze zoutionen kunnen binden aan het oppervlak van colloïdale deeltjes zodat deze zelf ook effectief geladen worden. De hoeveelheid gebonden lading hangt hierbij niet alleen af van de hoeveelheid zout in het systeem, maar ook van bijvoorbeeld de deeltjesdichtheid. De ongebonden ionen kunnen daarentegen vrij door het oplosmiddel bewegen en zullen zich herverdelen rondom de geladen deeltjes volgens het principe dat

ongelijke ladingen elkaar aantrekken, maar gelijke ladingen elkaar afstoten. Hierdoor ontstaat een wolk van negatieve ionen rondom positief geladen deeltjes (en uiteraard een positieve wolk rondom negatief geladen deeltjes). Deze wolk van vrije lading en de gebonden oppervlaktelading vormen samen de elektrische dubbellaag. Wanneer we echter de lading van het colloïdale deeltje van een afstand bekijken, dan is het net alsof de lading lager is dan de daadwerkelijke lading: de tegengesteld geladen wolk schermt de lading van het deeltje af voor de buitenwereld. Deze afscherming is sterker wanneer er meer vrije ionen in het systeem zijn. Er zijn dan immers meer tegenionen beschikbaar om de lading van het colloïdale deeltje "effectief" te neutraliseren; hierdoor kunnen de ionen die hetzelfde ladingsteken hebben als het deeltje dichterbij komen en zijn de dubbellagen kleiner.

Er is daarom een drastisch verschil tussen geladen colloïdale deeltjes in water of in een olie. In olie is het veel moeilijker om vrije ionen te maken: dit kunnen we wederom illustreren met tafelzout, dat veel moeilijker op te lossen is in olijfolie dan in water. Dit levert twee verschillen op tussen een colloïdaal watersysteem en een colloïdaal oliesysteem. Ten eerste zijn de deeltjes lager geladen in olie omdat er minder lading beschikbaar is dat zich aan het oppervlak kan hechten. Het tweede verschil is dat de afscherming van deze lading ook veel zwakker is dan in bijvoorbeeld water, waardoor elektrostatica toch belangrijk is. Olieachtige systemen zijn dus interessant omdat je wel geladen deeltjes kan krijgen, maar de dubbellagen zijn langgerekter. Dit is anders dan in de waterachtige systemen die al uitvoerig bestudeerd zijn in de literatuur. We richten ons daarom voornamelijk op de oliën, alhoewel deze niet altijd direct geschikt zijn voor consumptie.

## Fasengedrag

Het fasengedrag van geladen deeltjes hebben we uitvoerig in kaart gebracht in dit proefschrift. Geladen colloïdale bollen kunnen zich bijvoorbeeld wanordelijk ordenen zoals in een gas of vloeistof. Soms is het echter voor het systeem gunstiger als de deeltjes zich spontaan ordenen in een kristalrooster waardoor de elektrostatische repulsie tussen de deeltjes minimaal is: er wordt dan een zogenaamd Wignerkristal gevormd. Intuïtief gezien zal een dergelijke fase gevormd worden wanneer we de deeltjesdichtheid in het systeem verhogen. Iets soortgelijks vinden we immers ook bij de vorming van edelstenen, een proces dat vaak onder hoge druk en dus hoge deeltjesdichtheid voorkomt. De aanwezigheid van dubbellagen en het feit dat deeltjes kunnen ontladen om repulsies te verminderen, maakt ons systeem echter een stuk complexer. Een ontdekking die we bijvoorbeeld hebben gedaan is dat het mogelijk is om een colloïdaal kristal weer te laten smelten door de dichtheid te verhogen (hoofdstuk 2). Dit blijkt alleen mogelijk te zijn wanneer zowel positieve als negatieve ionen op het colloïdale deeltjesoppervlak kunnen binden, waardoor deeltjes snel genoeg kunnen ontladen.

Voegen we een tweede type deeltjes toe aan het systeem dan krijgt het fasengedrag een extra dimensie. Indien de ladingen van de twee typen deeltjes verschillen in grootte, maar niet van teken, dan kan het systeem ontmengen in een fase die rijk is

aan laag geladen deeltjes en een fase dat rijk is aan hoog geladen deeltjes. Een dergelijk ontmenggedrag zou mogelijk invloed kunnen hebben op het sedimentatieprofiel: de verdeling van deeltjes over de hoogte als we zwaartekracht zijn werk laten doen. Dit kan leiden tot tegenintuïtieve fenomenen zoals het feit dat zware deeltjes boven lichte deeltjes kunnen zweven, puur vanwege het verschil in ladingen en massa. Deze fenomenen hebben we besproken in hoofdstuk 3.

Vloeistoffen en kristallen zijn voorbeelden van macroscopische fasen, we kunnen het verschil tussen deze twee namelijk gewoon met ons blote oog waarnemen. Ordening kan echter ook op een veel kleinere schaal gebeuren, zoals we kunnen lezen in hoofdstuk 4. Deeltjes die verschillen in lading kunnen structuren vormen die alleen onder de microscoop te zien zijn. Zo kunnen deeltjes zich ordenen in een slangachtige structuur waarbij hoog geladen en laag geladen bollen elkaar afwisselen. Dit fenomeen blijkt het gevolg te zijn van een dipoolmoment dat op de deeltjes ontstaat wanneer ze ontladen op het punt waar ze elkaar naderen. Dit elektrische dipoolmoment is vergelijkbaar met een magneet: als twee dipolen oplijnen dan trekken ze elkaar aan, anderzijds stoten ze elkaar af wanneer ze in tegengestelde richting wijzen. Dit is een voorbeeld van een *effectieve wisselwerking*: de manier hoe deeltjes elkaar "voelen" als we de effecten van het medium (olie of water) en de ionen meenemen. Dit is tevens het tweede centrale begrip in dit proefschrift naast de term *fasengedrag*.

## Afstembare effectieve wisselwerkingen

Effectieve wisselwerkingen zijn niet alleen belangrijk voor het fasengedrag van colloïden, maar het blijkt ook belangrijk te zijn bij het vangen van deeltjes nabij een grensvlak. Grensvlakken zijn scheidingen tussen twee fasen van een verschillende aard, zoals een muur met lucht, of een bal in water. Omdat olie en water niet mengen, zal er dus een ook een olie-water grensvlak ontstaan. Het is dan mogelijk om deeltjes te vangen bij een dergelijk grensvlak door het deeltje te laten uitsteken in het water, maar ook een gedeelte te laten uitsteken in de olie. Mocht dit het geval zijn, dan zorgen oppervlaktespanningseffecten ervoor dat het erg moeilijk is om de deeltjes van het grensvlak los te krijgen.

In hoofdstuk 5 en 6 hebben we gekeken naar een mechanisme om deeltjes te vangen nabij een olie-watergrensvlak zonder dat de deeltjes contact hebben met water. Dit is mogelijk omdat de deeltjes Van der Waals krachten ondervinden die de deeltjes van het grensvlak af willen duwen (dit zijn dezelfde krachten waardoor gecko's op muren kunnen klimmen, waar ze overigens attractief zijn). Doordat het geladen deeltje de olie en het water in verschillende mate polariseren, ontstaat er ook een aantrekking op basis van elektrostatica (de spiegelladingattractie), en deze hangt niet af van het teken van de lading. Precies op het punt in de ruimte waar deze afstotende en aantrekkende krachten elkaar opheffen, staan de deeltjes stil en hierdoor worden ze effectief enkele nanometers van het grensvlak gevangen.

Wat echter vaak in de literatuur wordt vergeten is dat er ook nog ionen zijn in het systeem. De ionen verdelen zich over het water en de olie, en zoals we intuïtief wellicht

145

al weten zullen er meer ionen naar de water gaan. Deze scheiding in lading zorgt er uiteindelijk voor dat het grensvlak zelf ook geladen wordt: afhankelijk van het type ionen zal de waterkant positief of negatief opladen, terwijl de oliekant dan respectievelijk negatief of positief geladen wordt. Dit geeft aanleiding tot twee dubbellagen bij het grensvlak (eentje in water en eentje in olie) en deze beïnvloedt de dubbellaag van het deeltje. Echter omdat het grensvlak geladen is, zal er dus ook een potentiaalverschil ontstaan over het grensvlak, en dit potentiaalverschil leidt tot een elektrische kracht die repulsief of attractief is op basis van het teken van het potentiaalverschil (wat afhangt van de type ionen in het systeem), en het teken van de deeltjeslading. Doordat de deeltjes het grensvlak niet doordringen, kunnen we de deeltjes dus van het grensvlak af of er naartoe laten bewegen. Dit allemaal door met de lading van het deeltje of de type ionen in het systeem te spelen. Doordat we deeltjes kunnen vangen dichtbij een grensvlak maar ook ze ervan af kunnen laten duwen, vormt dit fenomeen een interessante mogelijkheid om emulsies te maken waarbij we de stabiliteit ervan kunnen veranderen door middel van zout.

## Anisotropie

Het laatste thema in dit proefschrift gaat over de *anisotropie* in de vorm van colloïdale deeltjes, en in het bijzonder die van (ongeladen) harde staven. We spreken over anisotropie wanneer een bepaalde eigenschap van een specifieke richting afhangt. Om staven te beschrijven hebben we, in tegenstelling tot bollen, twee lengtecoördinaten nodig, zoals de diameter en de lengte. We bekijken hierbij de situatie waarbij de lengte van de deeltjes veel groter is dan de diameter. Deeltjes met een langgerekte vorm hebben de eigenschap dat ze kunnen oplijnen in een specifieke voorkeursrichting zonder dat ze hun massamiddelpunten in een kristalrooster ordenen. In dit geval spreken we van een nematische fase en deze kan in een colloïdaal stavensysteem gevormd worden door de deeltjesdichtheid te verhogen. Een nemaat is een voorbeeld van een vloeibaar kristal: een aggregatietoestand die wel ordening vertoont (de deeltjes wijzen allemaal één kant op), maar de ordening is niet perfect, waardoor het wel bepaalde karakteristieken heeft van een vloeistof. Vloeibare kristallen kennen we het wellicht het beste in dagelijkse leven als toepassing in het LCD (Liquid Crystal Display) scherm. Een andere toepassing is "smart glass": glas dat doorzichtig of ondoorzichtig is, afhankelijk of er een elektrisch veld over heen staat.

In hoofdstuk 7 hebben we colloïdale staven beschreven puur in termen van een ordeparameter (zonder expliciet gebruik te maken van bijvoorbeeld de deeltjesdichtheid). Een ordeparameter is een grootheid waarmee we een geordende fase (nemaat) kunnen onderscheiden van een wanordelijke fase (vloeistof zonder uitgelijnde deeltjes). Het voordeel van een dergelijke beschrijving is dat je makkelijker berekeningen kan doen aan nematische systemen en daardoor dus ook makkelijker voorspellingen kan doen. We hebben de theorie getest door eerst het fasengedrag in kaart te brengen en vervolgens hebben we gekeken naar het grensvlak tussen een "normale" vloeistof en een nemaat.

Omdat de ordening in een nemaat niet perfect is, hebben we ook naar zogenaamde defecten gekeken: fouten in de oplijning van staven in een bepaalde richting. Een voorbeeld is het egeldefect: als de staven radieel uitgelijnd zijn, zal dit ertoe leiden dat de richting in het centrum onbepaald is. Dit brengt enorme energiekosten met zich mee waardoor de kern van een dergelijk defect smelt tot een normale (niet-nematische) vloeistof. We hebben met onze theorie de grootte van een dergelijke kern afgeschat en vergeleken met moleculaire systemen. Tot slot hebben we ook gekeken naar defecten waar de nematische fase in een eindige doos wordt geplaatst, waarbij de staven een voorkeur hebben om parallel uit te lijnen aan de muren.

Het laatste onderwerp in het kader van anisotropie is de vorming van vloeibaar kristallijne druppels, de zogenaamde tactoïden. Deze druppels zijn anders dan waterdruppels omdat ze niet bolvormig zijn, maar langgerekt. We hebben de verhouding tussen de lengte van deze druppels ten opzichte van hun diameter bestudeerd als functie van de tijd, en we hebben gezien hoe we de druppels zo langgerekt mogelijk kunnen maken op basis van de grensvlakspanning en de kromming van de druppel. Kromming bleek hierbij echter weinig invloed te hebben en we concludeerden dat er extra ingrediënten in de theorie nodig zijn om experimenten te verklaren, die nog langgerekter bleken te zijn dan de voorspellingen van de theorie.

## Tot slot

In dit proefschrift hebben we verschillende aspecten van colloïdale dispersies bekeken. Het feit dat de deeltjes zich bevinden in een vloeistof die qua intrinsieke eigenschappen en inhoud (de ionen) veranderd kunnen worden, geeft aanleiding tot een breed scala aan fenomenen. Denk hierbij aan het fasengedrag, maar ook aan de effectieve interacties tussen bijvoorbeeld een colloïdaal deeltje en een olie-watergrensvlak. Het belangrijkste hierbij is dat veel van deze eigenschappen af te stemmen zijn door parameters zoals zoutconcentratie, deeltjesdichtheid, druk of temperatuur te variëren. Alhoewel we dit voornamelijk uit een fundamenteel oogpunt hebben bekeken, zal dit uiteindelijk ook tot meer begrip leiden voor bijvoorbeeld het maken van toepassingen, zoals voedingsmiddelen, materialen, medicijnafgifte en veel meer, aangezien colloïden al heel lang een belangrijke rol spelen in ons dagelijks leven.

# Dankwoord

Een proefschrift maak je niet zomaar, hier gaat veel lezen, schrijven, het doen van berekeningen en het hebben van wetenschappelijke discussies aan vooraf. De belangrijkste schakel in dit alles is zonder twijfel mijn promotor René van Roij. René, ik vond het prettig dat ik altijd bij je kon aankloppen voor mijn vragen of wanneer ik feedback op iets nodig had. Je kon altijd wel iets nuttigs zeggen waardoor ik weer vooruit kon. Ook wil ik je bedanken voor je vele geduld en de vrijheid die je me gaf: een betere begeleider kan je bijna niet wensen! Ik heb veel van je geleerd.

Er waren ook andere personen die me enorm veel hebben geholpen tijdens mijn promotietraject. Eén hiervan is bijvoorbeeld Niels, die tijdens de eerste paar weken van mijn promotie me bij ging praten op verschillende aspecten van geladen colloïden. Niels, ik ben blij dat we uiteindelijk samen ook hebben kunnen publiceren en ik vond je relaxte en open houding erg prettig. Furthermore, I would like to thank my colleague Sela. I benefited a lot from your knowledge on physics and numerics, your help in writing, publishing together, and of course your COMSOL tips and tricks. Thanks! Paul en Melle wil ik graag bedanken voor de discussies en prettige samenwerking (en geduld) met betrekking tot het project over vloeibare kristallen. Finally, I would like to thank Bob Evans for the scientific discussions, you really know how to point out the interesting stuff in physics.

Ook experimentele collega's speelden een essentiële rol in mijn promotieonderzoek. In het bijzonder wil ik hierbij Marjolein vd L., Nina, Jessi en Alfons bedanken. I would also like to thank the people in the group of René for the nice time and many scientific discussions, which include Mathijs, Bram, Ben, Thomas, Simone B., Tara, Giuseppe, Jeroen, Niels en Andreas. For the many useful scientific discussions and a pleasant time together during the conferences in Rome and Lissabon, I would like to thank the colleagues from the Debye institute, Marjolein D., Niko (aka Nick), Simone D., Anjan, Guido, Berend, Wiebke, Henriëtte, Giulia, Rik, Harini, Laura, Vasileios, Chris, Wessel, Da, John, and Ernest.

My "home" during these past four years was the Institute for Theoretical Physics, which was first situated in the Minnaert building and later in the Buys Ballot building. In the first place I would like to thank my past and current office mates (in "chronological" order), Jan, Hedwig, Giuseppe, Leandro and Ben. Betreffende mijn collega's wil ik in het bijzonder Arie-Willem bedanken, voor het luisteren naar mijn vele geklaag en de vermakelijke pauzes. Furthermore, I would like to thank the Italian viking Benedetta, even during the time when you stole my chocolate. It was always great to hear

about your adventures. Vivian, ik wil jou graag bedanken voor het samen werkcollege begeleiden, wat ik altijd als zeer prettig ervaarde. Ik wil ook graag Rembert bedanken waardoor het begeleiden van mijn eerste vak erg ontspannen was. Furthermore, I would like to thank Wellington and Gleb for learning new things during my time as a teaching assistant for the course Quantum Field Theory. Stefan Vandoren bedankt voor het begeleiden van het vak Speciale Relativiteit. Joost, Wanda en Olga wil ik graag bedanken voor de administratieve en organisatorische werkzaamheden afgelopen vier jaar. For the nice breaks, random talk, sushi and nice time on schools, parties and conferences, I would like to thank Rick (Kick), the small wooden frog Jogundas, Dražen, Watse, Laura, Marise, Li'ao, Jules, Huibert, Tycho, Guido, Chiara, Nick, Drian, Niklas, Simonas, Vladimir, Sandeep, Anton, Tatjana, Leihua, Nava, Marco, Stefano, Benedikt, Natália, Olga, Panos, Jiansen, Erik, Riccardo, Aron, Alessandro, Lei, and of course the permanent staff of the ITF (and everyone else I forgot). Tot slot wil ik graag Bram, Didi, Annerieke, Ghislaine, Watse en Yolanda bedanken voor het proofreaden van mijn Nederlandse samenvatting.

Ook buiten het werk om wil ik graag mensen bedanken. Zonder de nodige afleiding buiten het werken om, zou het schrijven van een proefschrift onmogelijk zijn. Op de eerste plaats wil ik paranimfen Jaco en Wout bedanken. Ik heb jullie aan het begin van mijn promotieonderzoek ontmoet en ik vond onze vele (burger)avonturen echt top. Nu ik erover nadank was het eigenlijk jouw schuld, Wout, waardoor ik een salsaverslaving kreeg. Jij begon immers over de Maria, maar je was zelf immuun voor de verslaving die je bij mij startte. Daarop aansluitend wil ik een paar salsamensen bedanken die ik afgelopen jaren heb ontmoet. Ik zal niet iedereen noemen, maar ik wil toch even de krokodillen Jonathan (of toch konijn?), Laurens, Aret en Alex noemen, en daarbij ook de dames Frederique, Annerieke, Ronja, Myrtherds, en Natascha, die ik allen wil bedanken voor de leuke tijd op feesten, festivals en daarbuiten. Brian, bedankt voor de lessen: dit maakte de verslaving nog beter. Ook ex-danspartners Renske en Heleen bedankt voor de donderdagavonden tijdens stijldansen, en nu we het toch erover hebben: Luuk, goede app zeg! Sofferd, bedankt voor de erg geweldige tijd. Ook vrienden Simon, Jipke (aka Niels), Stefan, Battlebeast Kmix (aka Camiel), Bob en Marco, de nodige afleiding enzo waren top.

Tot slot wil ik graag mijn ouders Arfi en Huub, en mijn zus Yolanda bedanken voor de vele steun afgelopen vier jaar (en daarvoor). En ook Land in het bijzonder (met een beetje Kevin) bedankt voor het ontwerpen van de kaft, en ook groetjes aan je robot (je hebt haar/het goed geprogrammeerd).

# About the author

Jeffrey Everts was born on April 1, 1988 in Roermond, the Netherlands. In 2010 he obtained his bachelor degree in Chemical Engineering and Chemistry *(cum laude)* and in Applied Physics *(cum laude)* at the Eindhoven University of Technology. During his studies there, he was a student assistant in the Spinoza lab, where he worked under the supervision of dr. Anja Palmans on the synthesis and characterization of molecular building blocks that could be used in chiral supramolecular self-assembly. After this period, he moved to Utrecht University, where he obtained a master degree in Theoretical Physics *(cum laude)* in 2012, with a master thesis on topological insulators and superfluidity, which was supervised by prof. dr. Cristiane de Morais Smith. His PhD study, carried out under the supervision of prof. dr. René van Roij, dealt with the phase behaviour and effective interactions of charged and uncharged colloidal particles. The most important results of this study are described in this dissertation.